Retinitis Pigmentosa GTPase Regulator Gene Replacement

A POTENTIAL TREATMENT FOR X-LINKED RETINITIS PIGMENTOSA

A thesis submitted for the degree of Doctor of Philosophy

at the University of Oxford during Michaelmas Term 2015

M. Dominik Fischer

Merton College

UNIVERSITY OF OXFORD

Declaration

This thesis is entirely my own work except where otherwise indicated. As such, some experimental work was subcontracted to commercial companies or performed with the help of managers at core facilities of the University of Oxford. Specifically, synthesis of the original plasmids containing wild type and codon optimised RPGR was performed by GenScript, Piscataway, USA. All DNA sequencing was subcontracted to Source BioScience, Department of Biochemistry, University of Oxford, South Parks Road (except the final independent validation of plasmid sequences, which was performed at the National Genetics Reference Laboratory in Manchester). All flow cytometric analyses were done with the kind help of Mr Andrew Worth, Flow Sorting Facility Manager at the The Jenner Institute, University of Oxford. The liquid chromatography-tandem mass spectrometry (LC-MS/MS) experiments and primary data analysis were conducted by Dr. Benjamin Thomas, Central Proteomics Facility Manager at the Sir William Dunn Pathology School, University of Oxford.

06/12/2015 

Date Name

Abstract

X-linked retinitis pigmentosa (XLRP) is the most severe form of retinitis pigmentosa, a neurodegenerative, blinding disorder of the retina. 70% of XLRP cases are due to mutations in the retina-specific isoform of the gene encoding retinitis pigmentosa GTPase regulator (*RPGR*^{ORF15}). Because of the relatively large prevalence and severe clinical phenotype, the responsible gene locus, *RPGR*^{ORF15}, is ideally suited for a tailored gene therapeutic approach. The overall objective of this work therefore was to develop an optimised gene replacement therapy for human XLRP disease.

The human *RPGR*^{ORF15} coding sequence (cds) was codon optimised and both wildtype (wt) and codon optimised (co) sequences were spliced into a specific vector backbone designed for production of adeno-associated virus (AAV). In vitro studies in HEK293T, SHSY-5Y and 661W cell lines showed that the co construct features greater sequence stability and expression levels when compared to the wt construct.

After packaging the superior co construct into AAV8 capsids, subretinal injections were performed in a pilot study on relevant animal models with targeted disruption (*Rpgr*$^{-/y}$) or natural mutation (*C57BL/6J*$^{Rd9/Boc}$) in the murine homologue *Rpgr*. Transgene expression and correct localisation to the physiological subcellular compartment could be demonstrated. A masked, randomised and controlled study in *C57BL6/J* wild type mice was able to show lack of toxic effects while application in *Rpgr*$^{-/y}$ and *C57BL/6J*$^{Rd9/Boc}$ mice led to significant rescue as determined by electroretinography.

Overall the work in this thesis provides the basis for a clinical trial development to treat patients with XLRP due to *RPGR* mutations. A patent application to protect the intellectual property of this work has been filed on behalf of the University of Oxford.

Contents

List of Abbreviations

AAV: adeno-associated virus

AAVSI: Adeno-associated virus integration site I

ACAID: anterior chamber-associated immune deviation

ADK8: Mouse Monoclonal (clone ADK8) to adeno associated virus 8

AdV: adeno virus

AF: autofluorescence

ANOVA: analysis of variance

AMD: age related macula degeneration

ARE: Adenylate-uridylate-rich elements

ARVO: The Association for Research in Vision and Ophthalmology

ART: automatic real time

AU: arbitrary units

bGH: bovine growth hormone

BSA: bovine serum albumin

BSS: balanced salt solution

C57BL/6J$^{Rd9/Boc}$: mouse strain with naturally occurring mutation (32bp insert) in Rpgr

CAAX: motif in primary amino acid sequence, where C is cysteine, A is any aliphatic amino acid, and X is any amino acid

CAG: cytomegalovirus early enhancer and chicken beta-actin hybrid promoter

CAI: codon adaptation index

Cap: capsid proteins VP1-3 (virus protein 1-3)

cc: connecting cilium

CCDS: charge-coupled device sensor

cds: coding sequence

CEP290: centrosomal protein, 290 kilodalton

CG: cytosine-guanine dinucleotide

CpG: cytosine nucleotide occurs next to a guanine nucleotide in the linear sequence of bases

co: codon optimised

chi: crossover hotspot instigator

CORD13: cone-rod-dystrophy-13

Cre: Cre (causes recombination) protein, a recombinase

cSLO: confocal scanning laser ophthalmoscopy

DEPC: Diethylpyrocarbonate

dGTP: Deoxyguanosine triphosphate

dITP: deoxyinosine triphosphate

DNA: deoxyribonucleic acid

DMEM: Dulbecco's modified Eagle's medium

EBSS: Earle's Balanced Salt Solution

ECACC: European Collection of Authenticated Cell Cultures

EDTA: ethylene-diamine-tetra-acetic acid

EGFP: enhanced green fluorescent protein

ELISA: enzyme linked immunosorbent assay

EMA: European Medicines Agency

EMEM: Eagle's minimal essential medium

ERG: electroretinography

EYFP: Enhanced yellow fluorescent protein

FACS: Fluorescence activated cell sorting

FBS: fetal bovine serum

FDA: Food and drug administration

FDR: false discovery rate

FOP: frequency of optimal codons

f1ORI: origin of replication from a f1 phage

GCP: Good clinical practice

GEF: guanine nucleotide exchange factor

GFP: green fluorescent protein

GTPase: guanosine triphosphate hydrolase

HEK293T: human embryonic kidney 293 cell line with T-antigen expression

HPV: human papillomavirus

HRD: hereditary retinal degenerations

HRP: horseradish peroxidase

HSV: herpes simplex virus

Hte: region in the genome of *Escherichia coli* which confers a high efficiency of transformation phenotype

ICC: immunocytochemistry

IFT88: intraflagellar transport protein 88 homolog

IGF: insulin-like growth factor

IHC: immunohistochemistry

IND: investigational new drug

IMP: investigational medicinal product

IPL: inner plexiform layer

IRES: internal ribosome entry site

ITR: inverted terminal repeat

INL: inner nuclear layer

IOP: intraocular pressure

IPL: inner plexiform layer

IR: infrared

IRBP: interphotoreceptor retinoid binding protein

K: total number of nucleotides (in kilobases) of plasmid DNA used in recombinant production of adeno associated virus

kD: kilodalton

LB: Luria broth

LCA: Leber's congenital amaurosis

LGN: lateral geniculate nucleus

MCS: multiple cloning site

MOI: multiplicity of infection

MRC: Medical Research Council (UK)

NA: not applicable

nc: negative control

NCBI: national center for biotechnology information

NGRL: National Genetics Reference Laboratory in Manchester

NPC: nuclear pore complex

NPH6: nephrocystin 6

NPM: nucleophosmin

μ_0: mean of population 0

μ_1: mean of population 1

OCT: optical coherence tomography

OD: *oculus dexter* (right eye)

OMIM: Online Mendelian Inheritance in Man

ONL: outer nuclear layer

OPL: outer plexiform layer

ORF: open reading frame

OS: *oculus sinister* (left eye)

ORI: origin of replication

pA: polyadenylation signal

PAR: pseudoautosomal regions

PBS: phosphate buffered saline

PBS-T: phosphate buffered saline with Triton-X

pc: positive control

PCR: polymerase chain reaction

PDEδ: delta subunit of rod photoreceptor phosphodiesterase (PDE) holoenzyme

PEI: polyethylenimine

PFA: paraformaldehyde

PI: post injection

P21: postnatal day 21

PM2: postnatal month 2

PMMA: Polymethyl methacrylate

PVDF: polyvinylidene difluoride

qPCR: quantitative polymerase chain reaction

rAAV: recombinant adeno-associated virus

R: ratio

RA: retinoic acid

RAN: rat sarcoma (Ras)-related nuclear protein

Ras: rat sarcoma

RCC1: rat sarcoma (Ras)-related nuclear protein guanine exchange factor (RanGEF) regulator of chromosome condensation 1

Rep: replication proteins required for the AAV life cycle

RLD: rat sarcoma (Ras)-related nuclear protein guanine exchange factor (RanGEF) regulator of chromosome condensation 1 (RCC1)-like domain

RGC: retinal ganglion cell

RIPA: radio-immunoprecipitation assay

RK: rhodopsin kinase

RP: retinitis pigmentosa

RPE: retinal pigment epithelium

RPGR: retinitis pigmentosa GTPase regulator [Rpgr is the murine homologue]

RPGRIP: retinitis pigmentosa GTPase regulator interacting protein [Rpgrip is the murine homologue]

RPGRIP1: retinitis pigmentosa GTPase regulator interacting protein 1

Rpgr$^{-/y}$: transgenic mouse line with disruptive insert in murine homologue of RPGR

RT: room temperature

rTPA: recombinant tissue plasminogen activator

σ: common standard deviation

SDS-PAGE: sodium dodecyl sulfate polyacrylamide gel electrophoresis

SNR: signal-to-noise ratio

SOC: super optimal broth with catabolite repression

SPLICE: swift polymerase chain reaction for ligating *in vitro* constructed exons overlap extension polymerase chain reaction

SPSS: statistical package for the social sciences

SV40: Simian (vacuolating) virus 40

T: nucleotide length (in kilobases) of the transgene plasmid

TAE: tris-acetate-ethylene-diamine-tetra-acetic acid

Tm: melting temperature

TPA: tetradecanoylphorbol-13-acetate

Vb: vector backbone

vg: vector genomes

VP1-3: virus protein 1-3

WB: Western blot

WHRN: Whirlin

WPRE: woodchuck hepatitis virus post-transcriptional regulatory element

wt: wild type

XCI: X-chromosome inactivation

XLPRA1: X-linked progressive retinal atrophy 1

XLPRA2: X-linked progressive retinal atrophy 2

XLRP: X-chromosome linked retinitis pigmentosa

List of Tables

List of Figures

CHAPTER 1 GENERAL INTRODUCTION

1.1 The healthy retina

1.1.1 Architecture

The human retina was first described as inner lining of the eye by Democritus around 450 BC and its microscopic architecture detailed by Ramon y Cajal around AD 1900 (**Fig. 1.1**) [1]. A more schematic presentation is given in **Figure 1.2**. The human retina is bordered by the retinal pigment epithelium (**Fig. 1.1A** and **Fig. 1.2a**), a cuboidal epithelial monolayer with many critical functions supporting the retina on the distal side towards Bruch's membrane and the choroid. Towards the pupil, the retina adjoins the posterior hyaloid membrane towards the vitreous body, which fills the eye towards the lens (downward in **Fig. 1.1** and **Fig. 1.2**). With its total area measuring 1cm^2 it contains more than 100

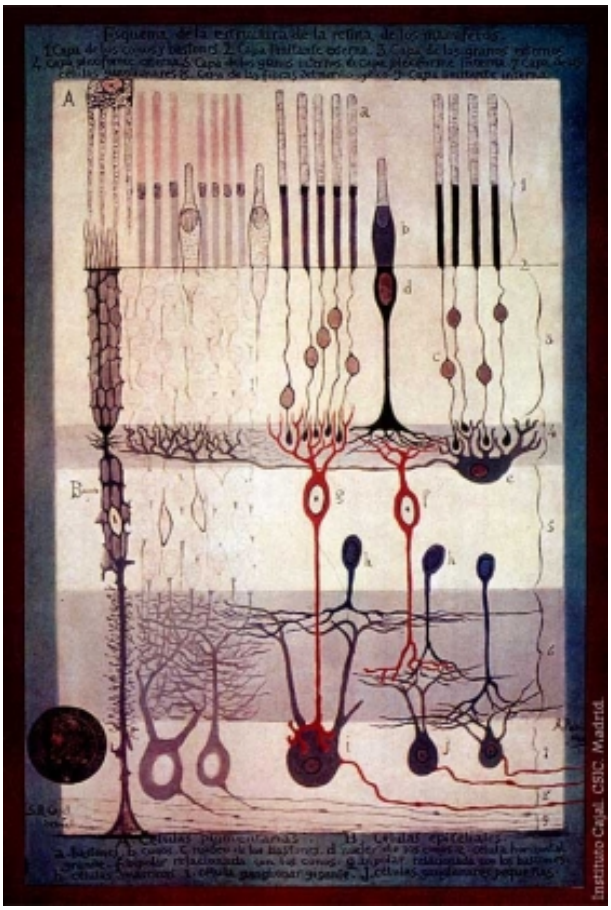

Fig. 1.1 Early drawing from Ramon y Cajal ca. 1901 on the neuronal population of the retina and its laminar architecture. A) Retinal pigment epithelium; B) Soma of Müller glia cell; 1) Rod photoreceptor outer and inner segments; 2) outer limiting membrane; 3) outer nuclear layer; 4) outer plexiform layer; 5) inner nuclear layer; 6) inner nuclear layer; 7) ganglion cell layer; 8) nerve fiber layer; 9) inner limiting membrane. Picture is within the public domain and was reproduced from: https://commons.wikimedia.org/wiki/File:Cajal_Retina.jpg

million photoreceptors converging onto 1 million ganglion cells connecting it to the cortex via the lateral geniculate nucleus of the thalamus [2].

The retina is – as the name suggests – a finely woven net of interconnected neuronal and glia cells organised into layers, which reflect their contribution to the complex process of light capture and image formation. One puzzling characteristic about the human retina is that photons have to traverse the ca. 250µm translucent neuronal tissue before being captured by light sensitive opsin molecules stacked in the outer segments of the photoreceptors (**Fig. 1.1a** and **Fig. 1.2b-c**). Rod photoreceptors (**Fig. 1.1a, c** and **Fig. 1.2b**) are sensitive enough to detect a single photon while cone photoreceptors (**Fig. 1.1b, d** and **Fig. 1.2c**) relay daylight and colour vision due to their different (spectral) sensitivities [3]. Photoreceptor outer and inner segments reach through the outer limiting membrane (OLM, **Fig. 1.2d**, a complex network of tight junctions provided by Müller glia cells (Fig. 1.1B), while the photoreceptor somata (**Fig. 1.1c, d** and **Fig. 1.2e**) form a densely packed outer nuclear layer (ONL). First synapses are formed in the outer plexiform layer (OPL) between photoreceptors and horizontal cells (**Fig. 1.1e** and **Fig. 1.2h**), or different types of cone (**Fig. 1f** and **Fig. 1.2i**), or rod bipolar cells (**Fig. 1.1g**). These second order neurons group their somata in the inner nuclear layer (INL) together with amacrine cells, which likewise extend axons to the inner plexiform layer (IPL, **Fig. 1.2k**). The bipolar and amacrine cells synapse in the IPL with different ganglion cell classes (**Fig. 1.2l**), which project along the optical nerve and chiasm mainly to the lateral geniculate nucleus (LGN) of the thalamus before the signal finally reaches the primary visual cortex (area V1) located in and around the calcarine fissure in the occipital lobe.

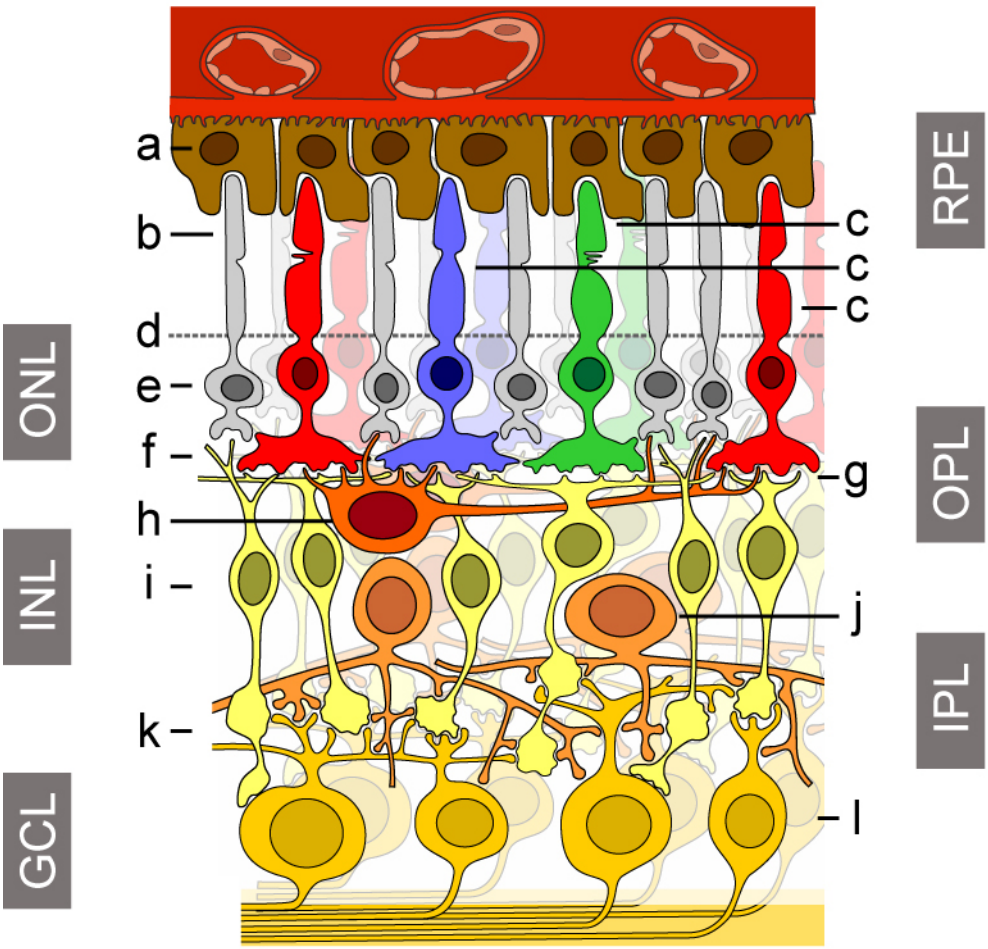

Fig. 1.2 Schematic drawing of the neuroretinal cell population. a) Retinal pigment epithelium (RPE); b) rod photoreceptor; c) cone photoreceptors (green, blue and red cone); d) outer limiting membrane (OLM); e) outer nuclear layer (ONL); f) rod-spherule to bipolar cell synapse in outer plexiform layer (OPL); g) cone-pedicle to bipolar cell synapse; h) horizontal cell i) bipolar cell and j) amacrine cell somata in inner nuclear layer (INL); k) inner plexiform layer with synapses to l) ganglion cells in ganglion cell layer (GCL).

This pattern of stratification is shared among all mammalian species including *Mus musculus*, an important model system for vision research [4]. However, important differences exist between the rodent and primate visual system in general and retinal architecture specifically. Rodents as nocturnal animals largely rely on the

highly sensitive rod system and cone photoreceptors only account for ca. 2% of all photoreceptors found in the mouse retina (vs. 6% in primates) [5]. These cone photoreceptors are distributed across the full retinal field with no clearly specialised region for high resolution, or “area centralis” in mice. This is in stark contrast to the primate retina, which is built around the central fovea, an avascular zone densely packed exclusively with cone photoreceptors for high spatial, temporal and spectral resolution [6]. While cone photoreceptors dominate the very centre, rod photoreceptors dominate the (mid) periphery and add to the lower end of the primate light sensitivity spectrum (night vision) [7]. This differential distribution of rod and cone photoreceptors has important implications for retinal function, disease mechanisms, clinical presentation and treatment strategies as discussed in the following chapters.

1.1.2 Function

The retina perceives light over more than eight orders of magnitude, processes light-induced action potentials with powerful parallel processing circuits and relays that information to the visual cortex for perception and cognitive processing [3]. This process may be initiated by single photons isomerising light-sensitive 11-*cis* retinal (an isomer of retinal with one *cis* double bond between C_{11} and C_{12}) in the visual pigment of a photoreceptor [8], triggering the phototransduction cascade, which amplifies the signal and results in the hyperpolarisation of the membrane potential by opening of cyclic-GMP gated ion channels [9]. Anterograde propagation of the action potential towards the OPL causes reduction of glutamate release at the synaptic ending (cone pedicle or rod spherule) and consecutive changes in membrane potentials of bipolar and horizontal cells [10, 11]. A complex interplay between different types of bipolar cells (4-22 depending on species) and various types of horizontal cells allow for parallel processing of visual components such as movement, directionality, colour or contours [12]. This pre-processed information is then fed into the circuitry of the inner plexiform layer to ganglion cells with additional horizontal processing by different types of amacrine cells before the signal is relayed to the LGN [13]. The parallel-processing power of the mouse retina is exemplified by the fact that each single cone pedicle synapses with ca. 500 dendrites [12]. On the other hand, such a design features a relatively large receptive field size and consequently low spatial resolution. This is confirmed by psychophysical experiments, which indicate a maximal spatial resolution in mice of circa 0.55 cycles per degree [14]. Due to the high density of cones (circa 2.5µm apart) and a one-to-one connectivity of cone to

bipolar to ganglion cell in the human fovea, the human eye can resolve up to 60 cycles per degree [15].

One way to objectively measure retinal function *in vivo* is electroretinography (ERG). In Ganzfeld-ERG defined light stimuli are presented in a way to stimulate the full retina. The resulting sum potential of retinal electrical activity is recorded at the corneal surface (with a strategically placed reference and ground electrode). More than one hundred years of research using ERG [16] has provided valuable insight into the individual contributions of cell classes to this sum potential and protocols have been established to dissect functionality of the rod vs. cone system or outer vs. inner retinal neurons [17]. Moreover, these protocols have been widely used to assess mouse models of retinal dysfunction, a hallmark feature of hereditary retinal disorders.

1.2 Hereditary retinal degeneration

Ophthalmology has played a pioneering role in terms of understanding hereditary conditions ever since the early days of medical genetics for two important reasons. Genetic defects leading to visual dysfunction cause considerable disability, which is readily detected and reported by patients and easily linked to the affected organ by the physician even at times of relatively limited diagnostic resources and before detailed knowledge of genetic mechanisms was available. Secondly, the eye with all its affected structures could be investigated in great detail early on. Since the development of the ophthalmoscope by Hermann von Helmholtz in 1850, Frans Cornelis Donders (1818-1889) in Utrecht, Albrecht von Graefe (1828-1870) in Berlin, Robert Walter Doyne (1857-1916) in Oxford and other early champions of ophthalmology have used the unique advantage of directly observing neuroretinal tissue *in vivo* in microscopic detail to describe pathologic changes in relation to inheritance patterns. As such, the first description of the clinical hallmark features of hereditary retinal degenerations (HRD) was given by Donders in Graefe's Archives as early as 1857 [18].

Different forms of HRD constitute a heterogeneous group of blinding diseases with a considerable burden of visual disability and tremendous socioeconomic impact, yet no cure is currently available. HRD are associated with impaired light sensing and/or signal transmission within the neuroretina, which causes loss of visual acuity, elevation of detection thresholds, defects of the visual field, and/or colour vision. The pathology primarily affects the photoreceptors (rods and/or cones), the retinal pigment epithelium and/or the processing and transmitting second or third order neurons. With

an estimated prevalence of 1:4000, HRD represent a clinically important group of diseases with autosomal recessive, dominant or X-linked inheritance patterns [19, 20]. Between 1980 and 2015, almost 250 retinal disease genes have been identified and additional loci are currently in focus (https://sph.uth.edu/retnet/home.htm; **Fig. 1.3**). The application of next generation sequencing in establishing the genetic diagnosis in HRD patients is likely to further increase the number of known disease-causing mutations over the next few years [21].

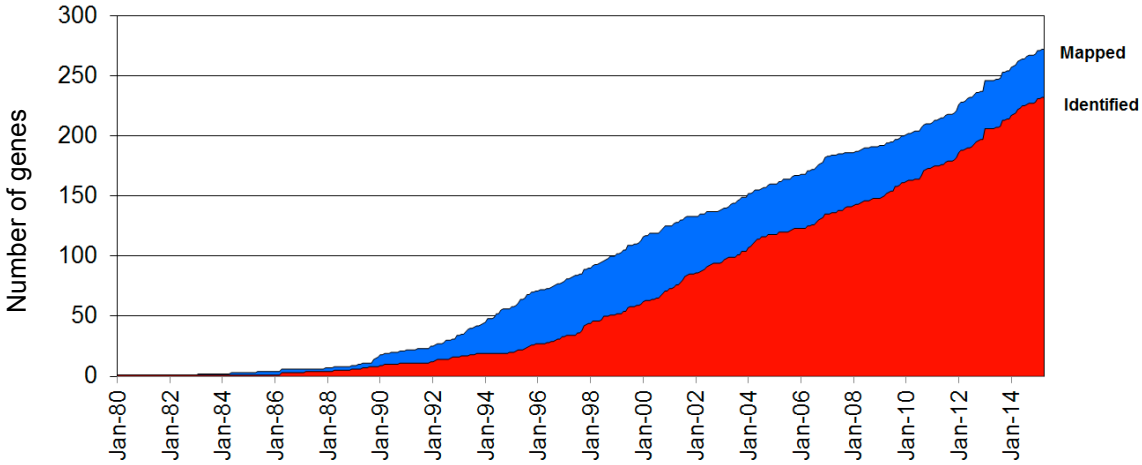

Fig. 1.3 Total number genes associated with retinal disease mapped (blue) and identified (red) by 2015. The abscissa shows time in years and the ordinate gives the number of genes mapped or identified. Graph was produced by Stephen P. Daiger, PhD at The University of Texas Health Science Center, Houston, Texas and is presented at the website: https://sph.uth.edu/retnet/home.htm.

Consequently, the molecular mechanisms involved in HRD are manifold and depend on both the underlying mutation as well as on structural and functional features of the primarily affected cell population [22, 23]. Prominent targets of disease causing mutations include phototransduction, specific metabolic features of photoreceptors and biogenesis of the required components (e.g. transcription, splicing, translation, folding and transport of opsins) [24]. Structural elements of the photoreceptors may also be affected, including the connecting cilium (cc), which is

essential for the crucial transport of proteins from the inner to the outer segment. Since photoreceptors are constantly regenerating their outer segments (~10% per diem), the rate of protein synthesis and transport of outer segment proteins through the cc is among the most demanding subcellular achievements for these primary sensory neurons [25]. Indeed, *de novo* protein synthesis is generally regarded as the most energy-demanding anabolic process in photoreceptors and studies in rabbit retinae showed that 0.55% total cellular protein was replaced per hour, of which the majority would be shuttled through the cc to help renew the outer segment [26]. Not surprisingly, mutations affecting this bottleneck cause photoreceptor dysfunction and/or degeneration.

The multitude of disease mechanisms translates into a range of dynamic phenotypical presentations, which can be hard to strictly categorise in clinical terms. Classical categories typically describe the location or the system primarily involved. Thus, HRD can broadly be divided into macular dystrophies and primary rod- and cone-dystrophies. In macular dystrophies the disease process is generally limited to the macula and might involve retinal pigment epithelium (RPE) as well as both photoreceptor classes in this anatomic region. While this is often the case for example in Stargardt disease, the most prevalent macula dystrophy, extra-macular changes can be observed for example in X-linked juvenile retinoschisis, where retinal splitting can lead to total retinal detachments. A key feature of macular dystrophies is the often dramatic impact on visual acuity and thereby quality of life. This might be surprising as the human macula is a disk of only 3 mm diameter of intense pigmentation with 1mm wider zone of less intense pigmentation and a resulting area of ca. 20 mm^2 compared to the 1094 mm^2 total retinal area. Yet, this fraction of total retinal area has

the highest density of cone photoreceptors (sections 1.1.1 and 1.1.2) and the human visual system heavily relies on the input from the macula. The largest part of the visual cortex is processing information exclusively derived from the macula, further underlining the importance of the information generated in the macula for visual perception in humans.

Mutations primarily affecting cone photoreceptors also lead to an early and substantial reduction of visual acuity. They can be distinguished from macular dystrophies by Ganzfeld-ERG. Where macular dystrophies lead to dysfunction in the full macular photoreceptor population, which is dominated by cones, the extra-macular area still holds the vast majority of the 6.4 million cones. Therefore, Ganzfeld-ERG sum potentials from the cone system reflect generalised cone dysfunction. Some cone dystrophies do also affect rod photoreceptors, while others are generally considered to be 'pure' cone dystrophies. The close interaction of both photoreceptor classes through gap junctions and the early interferential computation of signals from rod and cone pathways by different classes of interneurons provide a good basis for explanations on why any cone photoreceptor dysfunction may also affect the rod system at least on a functional level, even if not necessarily leading to secondary degeneration of the genetically healthy rod photoreceptors.

Rod dystrophies are HRD with primary dysfunction and degeneration of rod photoreceptors. Hallmark features are nyctalopia (night blindness) and (mid-) peripheral visual field restrictions due to dysfunction/degeneration of the rod-rich (mid-) peripheral retina. This (mid-) peripheral degeneration leads to thinning of the retina due to loss of ONL and photoreceptor inner and outer segments along with disintegration of the outer limiting membrane, which forms a tight junction barrier

between Müller glia cells and photoreceptors. As a consequence, inner retinal circulation comes in close proximity of RPE cells, which then proliferate and migrate along the branches of inner retinal vasculature leading to a corrosion cast impression of the capillary network [27]. Morphologically this was termed 'bone spicule' pigmentation as the pattern reminded Frans Donders and colleagues of the aggregates of bony matrix in the skeletal system [18]. The memorable term 'retinitis pigmentosa' then was coined by Donders to reflect this pigmentation pattern and the fact that an inflammatory activity was assumed, supported by the clinical observation of pigment and/or pigmented cells in the vitreous and early development of cataract in these patients.

In most cases, cone photoreceptors are affected secondarily even though they are not genetically dysfunctional *per se*. While the mechanism is not entirely understood, several reasons have been put forward as hypotheses. These generally include loss or downregulation of signals/pathways, which actively support cone survival such as i) the paracrine rod-derived cone viability factor [28], or ii) the intracellular mTOR pathway, which prevents autophagy [29]. Alternatively, iii) an increase of apoptotic signals and/or oxidative stress from dying rods, iv) loss of rod-cone gap junctions, or v) microglia mobilization might induce cell death of cones as genetically healthy bystanders [30]. Given the heterogeneity of causes for the primary rod degeneration, it seems reasonable to assume that a combination of some or all of the above causes might contribute to the secondary cone degeneration, which makes the development of a 'one for all' treatment a challenge. In contrast, strategies like gene therapy offer a curative treatment at the well-understood genetic basis of HRD. It remains to be seen, whether such a causative approach on a genetic level, will limit

the relevance of the downstream mechanisms and of the at times perplexing lack of genotype-phenotype correlation.

1.2.1 X-linked retinitis pigmentosa

The X chromosome features ca. 1100 genes and a disproportionally high number of those are associated with Mendelian diseases [31]. One reason is that hemizygosity of males and X-chromosomal inactivation in females affect almost all genes on the X chromosome and expose recessive phenotypes [32]. Additionally, only very small proportions of the X chromosome termed pseudoautosomal regions (PAR1-3) align with the second sex chromosome during meiosis for potential recombination [33]. Consequently, the largest part of the X chromosome is devoid of a crucial DNA repair mechanism leading to an accumulation of potentially harmful mutations [31, 34].

More than 20 years before the X-chromosome was sequenced, Bhattacharya *et al.* mapped the locus responsible for X-linked retinitis pigmentosa type 2 (XLRP2) and Schwahn et al. isolated it by positional cloning [35, 36]. Methodological advances have quickly helped to identify a large number of other loci and the Retinal Information Network (https://sph.uth.edu/retnet/home.htm) currently lists 20 distinct entities with X-linked gene defects resulting in ocular pathology (**Table 1**). Of these, five can be classified as retinitis pigmentosa-type HRD of which XLRP3 is by far the most prevalent (70-90%) subtype with XLRP2 contributing ca. 10-20% while the loci

for XLRP6, XLRP24 and XLRP34 have no known coding sequence/protein product and have only been described in single cases (XLRP24 and 34) or are even only predicted based on linkage mapping analysis [37-39]. These or still unknown loci may account for the minority of XLRP patients, where mutations in XLRP2 and 3 have been ruled out and next generation sequencing may help to close this gap eventually.

Other retinal diseases originating from mutations on the X chromosome include disorders such as congenital stationary night blindness or colour vision defects such as deuteranopia or tritanopia as well as retinal dystrophies originating from disruption of extracellular components (e.g. RS1). Some can lead to a phenotype with a degree of overlap to XLRP, such as X-linked cone dystrophy or choroideremia. A third group of rare HRDs with X-linked inheritance pattern are vitreoretinal dystrophies with syndromic presentation often affecting the central or peripheral nervous system such as the inner ear. This is interesting as XLRP3 is also regarded by some to lead to sub- clinical syndromic phenotypes reminiscent of ciliopathies, including inner ear defects [40]. This all reflects the challenge to systematically categorise disease entities with heterogeneous and dynamically overlapping clinical phenotypes. However, it remains clear that XLRP type 3 due to mutations in Retinitis Pigmentosa GTPase Regulator (RPGR) is by far the most common cause for X-linked retinal pathology [41].

Table 1 Overview of X-linked ocular pathologies involving the posterior segment of the eye.

Symbols	Location	Gene ID	Protein / Comment	Disease
Retinitis pigmentosa				
XLRP3	Xp11.4	6103	retinitis pigmentosa GTPase regulator, plays role in protein transport at photoreceptor connecting cilium	retinitis pigmentosa (70-90% of XLRP)
XLRP2	Xp11.23	6102	XRP2, a GTPase-activating protein (GAP) involved in trafficking between the Golgi and the ciliary membrane	retinitis pigmentosa (10-20% of XLRP)
XLRP6	Xp21.3-p21.2	6104	unknown	retinitis pigmentosa
XLRP24	Xq26-q27	6116	unknown	retinitis pigmentosa
XLRP34	Xq28-qter	777642	unknown	retinitis pigmentosa
Other hereditary vitreoretinal dystrophies				
NYX, CSNB1, CSNB1A, CSNB4	Xp11.4	60506	nyctalopin, putative involvment in cell adhesion and axon guidance	congenital stationary night blindness
CACNA1F, CORDX3, CSNB2(A),CSNBX2;	Xp11.23	778	voltage-dependent L-type calcium channel subunit alpha-1F	congenital stationary night blindnes, Åland Island eye disease or cone rod dystrophy
COD2, CORDX2	Xq27	1275	unknown	cone dystrophy 2
CHM	Xq21.2	1121	geranylgeranyl transferase Rab escort protein 1	choroideremia
RS1	Xp22.2-p22.1	6247	retinoschisin, plays role in cell adhesion processes	juvenile retinoschisis
OPA2	Xp11.4-p11.2	4977	unknown	optic atrophy 2
PRD	Xp11.3-p11.23	5548	unknown	primary retinal dysplasia
NDP, EVR2	Xp11.3	4693	norrin, transcription factor with central role in retinal vascularization	Norrie disease, familial exudative vitreoretinopathy; Coats disease;
OPN1LW, BCM, CBP, COD5, RCP;	Xq28	5956	red cone opsin	protanopia
OPN1MW, CBD, GCP;	Xq28	2652	green cone opsin	deuteranopia
Hereditary vitreoretinal dystrophies with syndromic phenotype				
OFD1	Xp22.2	8481	centrosomal protein, interacts with LCA5 and SDCCAG8	oral-facial-digital syndrome 1 (Jobert syndrome)
TIMM8A, DDP, DDP2, DFN1	Xq22.1	1678	mitochondrial import inner membrane translocase subunit Tim8 A	Mohr-Tranebjaerg or Jensen syndrome
PRPS1, ARTS, CMTX5, DFNX1	Xq22.3	5631	phosphoribosyl pyrophosphate synthetase 1	optic atrophy and/or retinitis pigmentosa with progressive peripheral neuropathy and/or ataxia and/or hearing loss
DMD	Xp21.2-p21.1	1756	dystrophin, anchors the extracellular matrix to the cytoskeleton via F-actin	Oregon eye disease associated with Duchenne Muscular Dystrophy
PGK1	Xq21.1	5230	phosphoglycerate kinase	retinitis pigmentosa with myopathy (single case)

Table 1 Overview of X-linked ocular pathologies involving the posterior segment of the eye. This list has been adapted from the Retinal Information Network (https://sph.uth.edu/retnet/home.htm).

1.2.2 Mutation in Retinitis Pigmentosa GTPase Regulator (RPGR) cause X-linked retinitis pigmentosa type 3 (XLRP3)

X-chromosomal inheritance is found in ca. 15-30% of all patients with HRD and mutations in the XLRP3 locus (RPGR) account for 70-90% of those. That makes

RPGR mutations the single most prevalent gene defect in HRD patients [42]. RPGR mutations generally lead to a very severe form of retinitis pigmentosa with rapid onset limiting the quality of life in boys as young as 5 years of age [43]. Because of its large impact in terms of incidence and severity, this entity has been studied extensively both clinically as well genetically.

Genetic studies have revealed differently spliced isoforms based on the genomic sequence of RPGR (**Fig. 1.4**). The gene is located on the short arm of the X chromosome (Xp21.1) and spans 172kb [44]. The initially identified transcript of RPGR contains nineteen exons (RPGR^{ex1-19}, also termed the constitutive variant) resulting in a 90kDa protein of unknown function **(Fig. 1.4b and Fig. 1.5)** [45]. Over the years, multiple alternatively spliced transcripts were

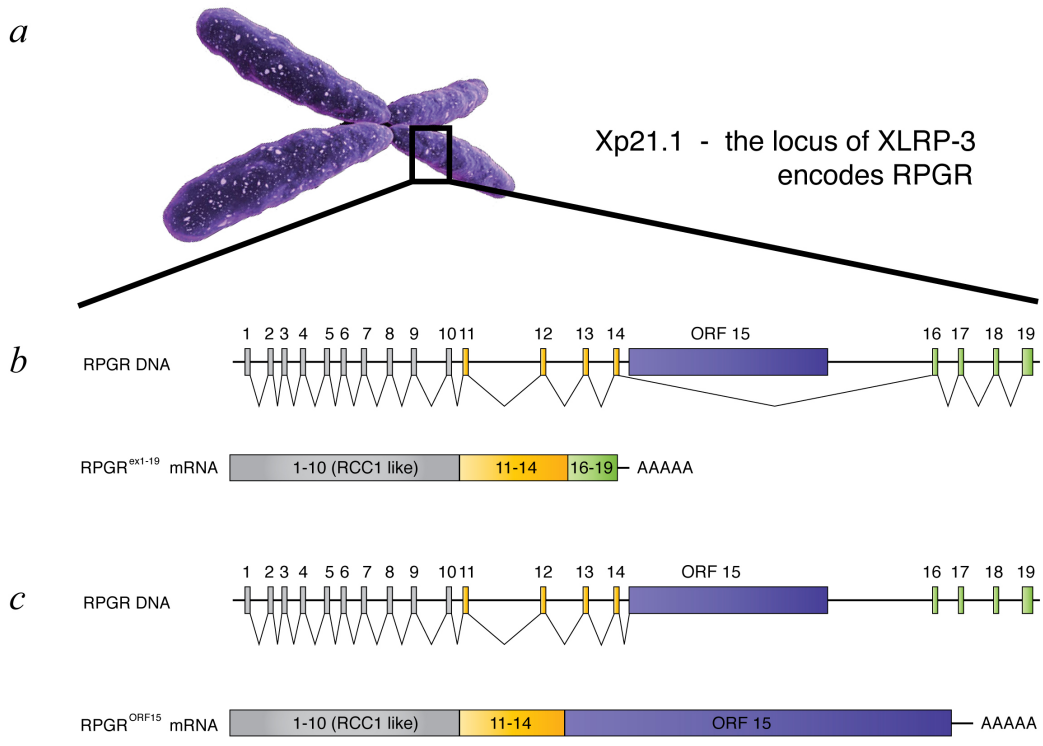

Fig. 1.4 *RPGR* is encoded on the X chromosome and leads to alternatively spliced isoforms. a) The short arm of the X-chromosome harbours *RPGR* at Xp21.1. b) shows the constitutive variant encoded by exons 1-19, while omitting the ORF15 sequence. This transcript is widely expressed throughout the body, while c) the *RPGR*^{ORF15} isoform is primarily expressed in photoreceptor cells and consists of exons 1-14 plus the ORF15 region, which builds the unique C-terminal region. Exons 16-19 are not part of isoform *RPGR*^{ORF15}.

recognized. All isoforms include the (N)-terminal RCC1-like domain (RLD), which is named after the structurally similar RCC1 protein, a guanine nucleotide exchange factor for the small GTP-binding protein, Ran. The first eleven exons encode the RLD, while exons 12-19 translate into the carboxyl (C)-terminal domain [46]. The most relevant transcript regarding photoreceptor viability is $RPGR^{ORF15}$, which is indicated by the fact that all known disease-causing mutations of RPGR are found in the coding sequence of $RPGR^{ORF15}$ [47]. Before splicing is complete, the immature pre-mRNA of $RPGR^{ORF15}$ is 43,155bp long, while the processed mRNA of 4,786bp length includes a capped 196bp 5' UTR with in frame amber stop codon (UAG) at position 28-30 (-141 to -139 from translational start site) and a 1131bp long 3' UTR followed by a AATAAA polyA signal and a poly-A site 17 nt after that.

$RPGR^{ORF15}$ contains exons 1-13 of the constitutive variant but utilizes exon 14 and the open reading frame 15 (ORF15) as a large C-terminal exon encoding 567 amino acids [48]. The full-length human $RPGR^{ORF15}$ isoform encodes an 1152-amino-acid protein (**Fig. 1.5**).

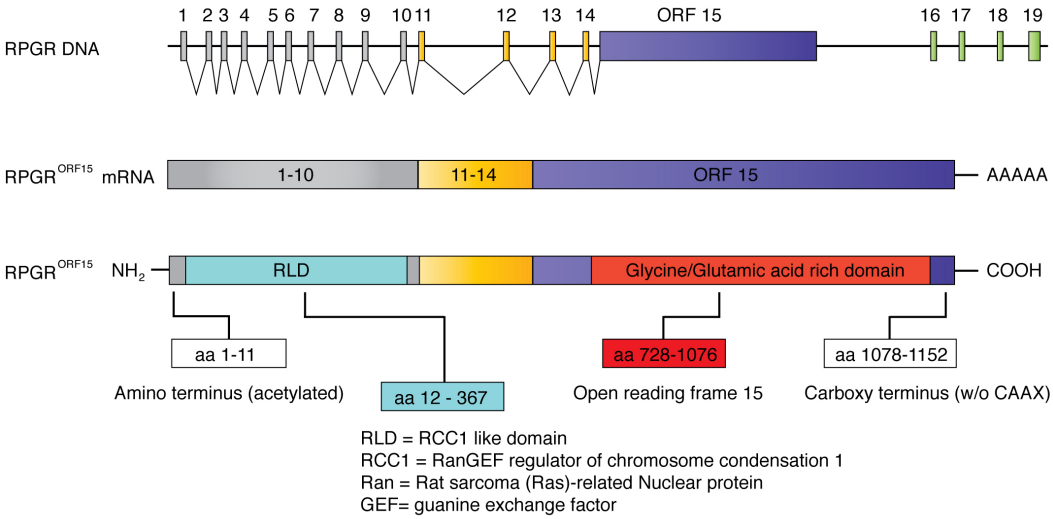

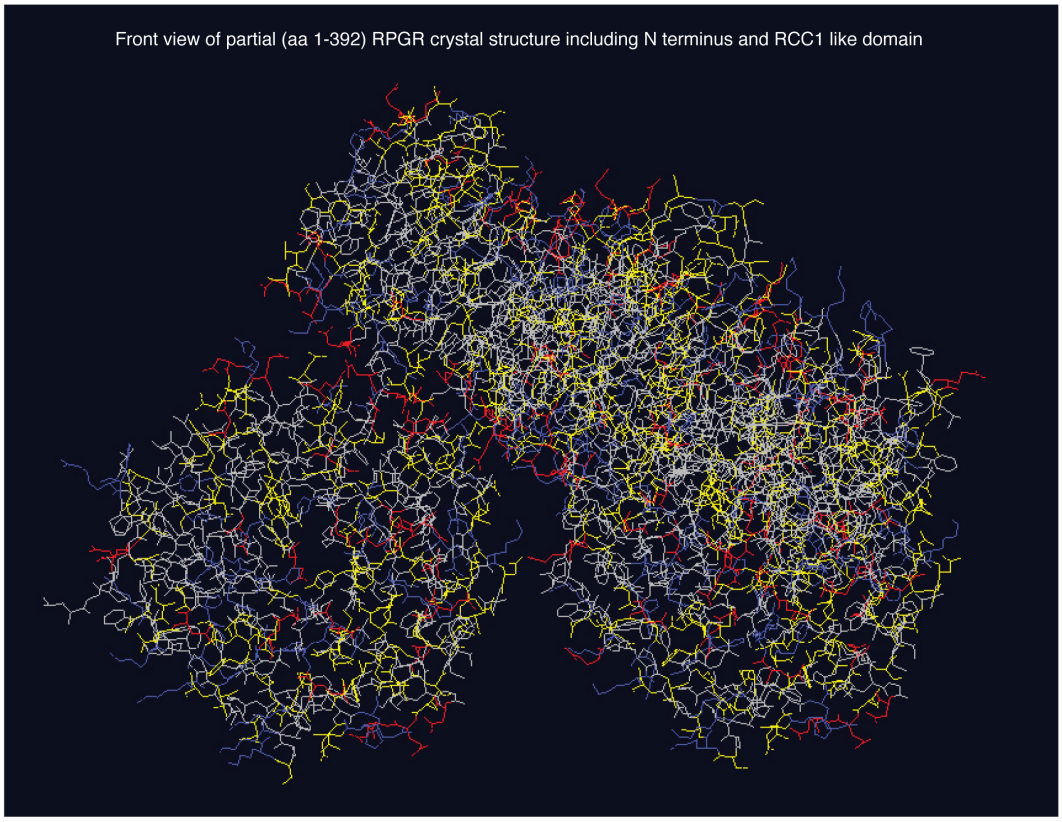

Fig. 1.5 RPGR^{ORF15} encodes for an 1152 amino acid protein with distinct domains. The more N-terminal RCC1-like domain is common to all known RPGR isoforms, while the glycine/glutamic acid rich domain and the carboxy-terminus are unique for RPGR^{ORF15}. Bottom: 3D view of the RCC1-like domain based on X-ray diffraction with 1.7 Å resolution (source data: http://www.ebi.ac.uk/pdbe/entry/pdb/4JHN) produced with the public domain software SwissPdbViewer DeepView v4.1 (http://www.expasy.org/spdbv/).

Circa 250 different mutations have been reported in RPGR and all affect the RPGR^{ORF15} isoform - including shared regions [49]. Indirectly this may indicate that deficiency of the constitutive RPGR isoform is not disease causing and is therefore a likely explanation for the absence of syndromic associations. Two thirds of disease-causing mutations occur in a hot spot region within the open reading frame 15, which features a highly repetitive, purine (guanine & adenine) rich region (**Fig. 1.6**). These mutations are mostly out-of-frame deletions with premature stop codons and since they affect the last exon, production of truncated proteins is more likely than nonsense-mediated decay [50]. In line with this, the clinical phenotype in patients with mutations towards the 3' end of RPGR tends to be less severe [51]. However,

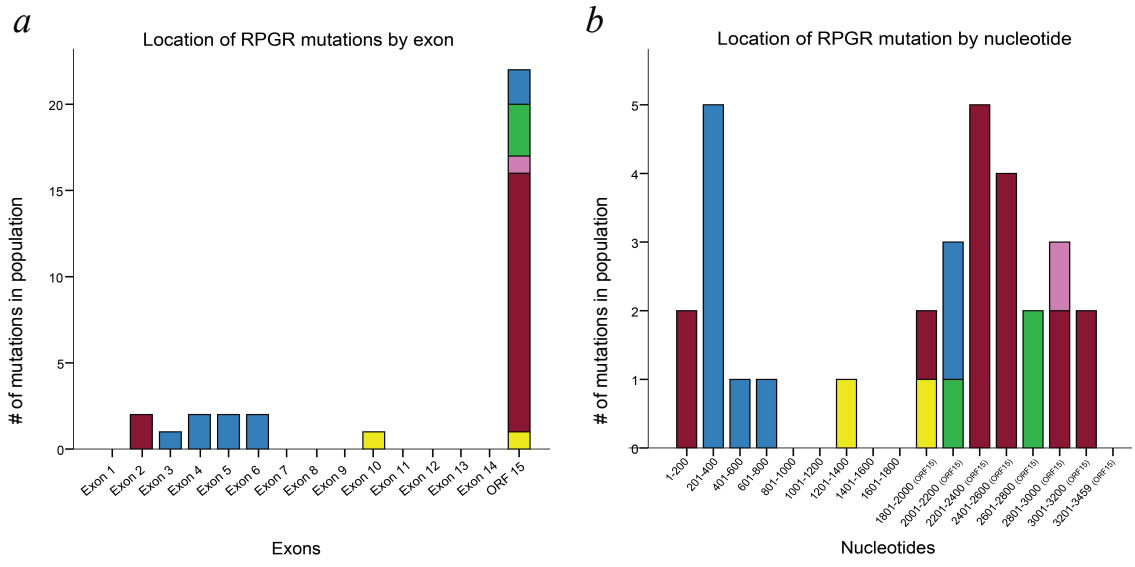

Fig. 1.6 Mutation analysis in a population of 50 XLRP3 patients confirms ORF15 as mutational hotspot within RPGR^{ORF15}. a) shows how numbers of mutations within this cohort are distributed over the exons 1-14 and ORF15. b) shows the distribution by nucleotides. Since ORF15 is by far the biggest exonic sequence, the distribution seems wider as in a). Note the colour coding: Blue=missense, green=nonsense, pink=insertion, maroon=deletion, yellow=duplication. Interestingly, missense mutations are more common in exons 3-6 and deletions more prevalent in ORF15. Data are from Bellingrath *et al.* (unpublished).

several cases and animal models suggest that some mutations may also lead to a dominant negative effect and consequently to even more severe forms of retinal

degeneration [52-54]. Given the complex pattern and the observed variety of RPGR transcription and translation it is not be surprising that general assumptions on genotype-phenotype relationship in XLRP feature many exceptions to the rule.

Indeed, patients with RPGR mutations present with significant phenotypic variability [55]. The presentation can range from atrophic changes confined to the cone-rich macula with preserved rod and cone responses in full field ERG [56], via cone-rod dystrophy to the classical rod-/ or rod-cone dystrophic phenotype mainly referred to by retinitis pigmentosa [43]. The majority of patients with RPGR mutations present with a rod-cone phenotype, where nyctalopia and peripheral visual field restrictions are incidental clinical findings and match elongations in implicit times and amplitude reductions in dark-adapted ERG [57]. The disease in these patients then progresses over time to involve cone driven ERG responses along declining psychophysical measures of cone function such as visual acuity, colour vision and central visual fields. In these patients, 30Hz flicker ERG recordings with Fourier analysis present an objective functional outcome measure of the remaining cone system response until late stages of the disease [58] and Bellingrath *et al.* (unpublished).

Only a minority have a reverse phenotype with predominant cone system involvement leading to early loss of visual acuity, and defects in both colour vision and central visual field and only secondary or simultaneous rod system dysfunction. A presentation with strictly macular dysfunction and degeneration can be regarded as atypical, even though possible [59]. Mechanisms explaining such a restricted distribution theoretically include the principle of dizygotic twin chimerism or *de novo*

mutations during formation of retinal progenitor cells and macular development [6, 60].

Some of this phenotypic variability might be due to mutations in distinct domains of varied importance within RPGR and differences between putative null and gain-of-function mutations. But since significant differences can also be seen among patients with the same mutation (even between fraternal twins with the identical mutation [61]), known unknown factors (e.g. epigenetics, environment) as well as unknown unknowns are likely contributors to the presenting phenotype. Despite this uncertainty in the genotype-phenotype relationship, valuable information e.g. on the rate of progression and concordance of outcome measures has been gained by careful clinical phenotyping and combination of structural and functional diagnostic tools [57, 59], which will be invaluable as benchmarks for and the design of future interventional trials. The molecular viewpoint on the structure and function of RPGR might help to further understand the mechanism of mutations leading to distinct phenotypic presentations and differences in disease progression.

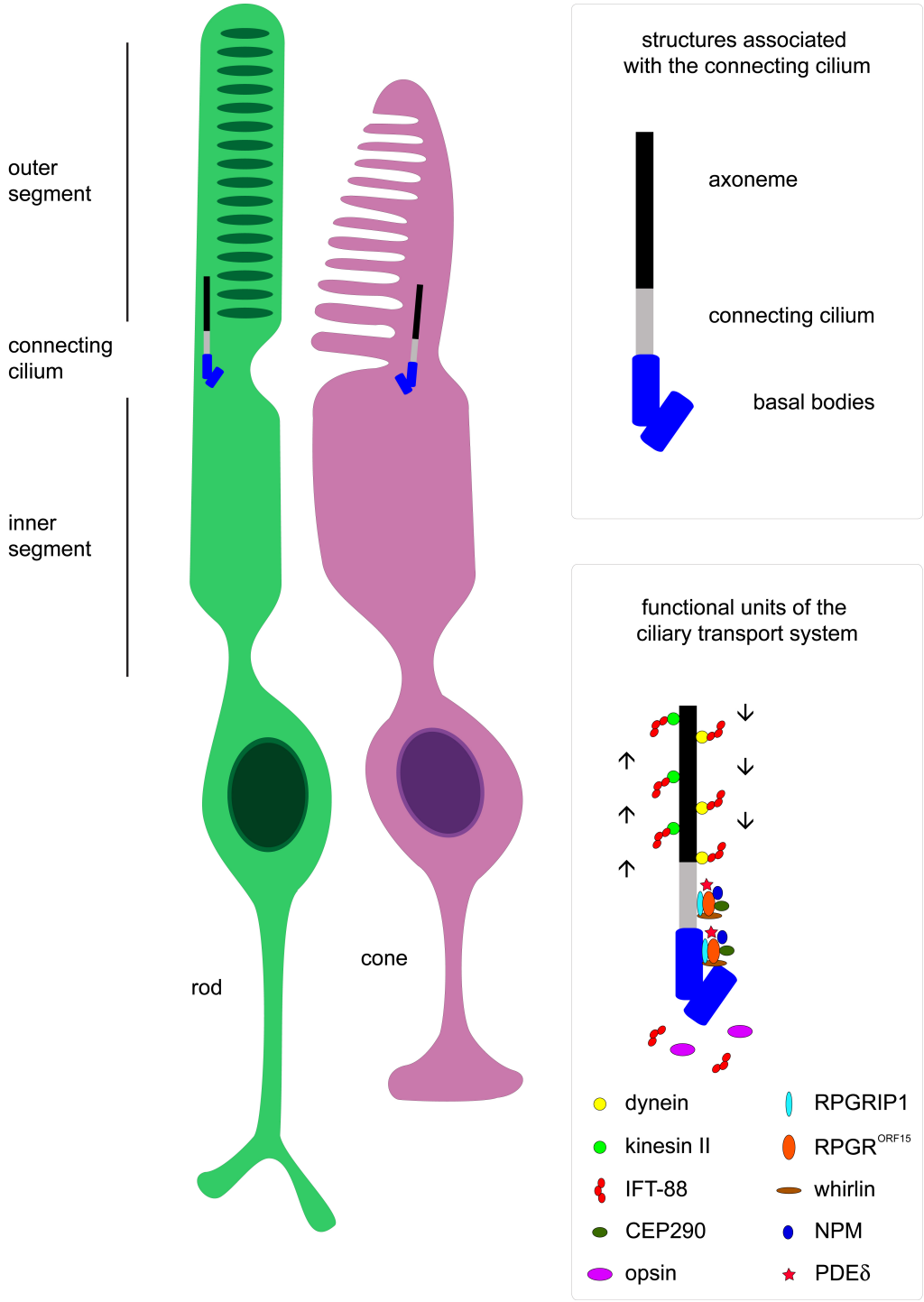

Fig. 1.7 Schematic of rod and cone photoreceptors with detailed drawing of connecting cilium (CC) structures. Core components of the modified sensory cilium are the axoneme, CC and basal bodies. Associated protein complexes facilitate directional transport e.g. of opsins from the inner segment, where opsins are produced, to the outer segment, where opsins are used to catch photons for light detection. $RPGR^{ORF15}$ is tethered to the CC by RPGRIP1 and itself can bind to whirlin, nucleophosmin (NPM), CEP290 (aka nephrocystin 6) and PDE6∂. The precise interaction of this protein complex in its role as facilitator of transport is only incompletely understood. Chapter 1.2.3 gives an overview of what is known and reported in the current literature.

1.2.3 Structure and function of RPGR^{ORF15}

The full length RPGR^{ORF15} isoform encodes an 1152-amino-acid protein with distinct subdomains, which dictate its structure, interaction with other proteins and therefore function at its physiological location, the connecting cilium of photoreceptors (**Fig. 1.7**). The amino-terminal domain is homologous to the Rat sarcoma (Ras)-related nuclear protein guanine exchange factor (RanGEF) regulator of chromosome condensation 1 (RCC1), referred to in short as the RCC1-like domain, or RLD [62]. There is debate about the presumed GEF activity as characteristic structural components required for GEF activity are not found in the RLD and the presumed target Ran-like GTPase RAB8 already has a primary GEF in Rabin8 [49, 63]. However, RAB8 would be a fitting target as it shuttles rhodopsin to the base of the connecting cilium and inhibition of RAB8 leads to rhodopsin mislocalisation, a feature also seen with RPGR^{ORF15} mutations [64]. Other interactions with the RLD are more evident and include RPGR interacting protein 1 (RPGRIP1), nephrocystin 6 (NPHP6/CEP290), and nucleophosmin (NPM) [65]. Mutations in *RPGRIP1* can cause Leber congenital amaurosis type 3 (LCA3) or type 13 cone rod dystrophy (CORD13) [66, 67]. RPGRIP1 tethers RPGR^{ORF15} to the connecting cilium via its C-terminal coiled coil domain and lack of RPGRIP1 results in mislocalisation of RPGR^{ORF15} [68-70]. Mutations in *CEP290* cause impeded intraflagellar transport and retinal degeneration in several (syndromic) ciliopathies: Bardet-Biedl-, Senior-Løken-, Joubert-, or Meckel-Gruber-Syndrome, LCA or nephronophtisis (hence CEP290's synonym NPHP6).

In addition, the RLD interacts with microtubular proteins, such as IFT88, dynein, kinesin II and with PDEδ [65, 71]. X-ray crystal structures of N-terminal RPGR fragments containing the RLD support the notion that RPGR interacts with PDEδ via the RLD and contributes to the movement of farnesylated cargo along the connecting cilium to the photoreceptor outer segment [62].

In contrast to the constitutive variant $RPGR^{ex1-19}$, the $RPGR^{ORF15}$ isoform encodes a repetitive glycine-glutamic acid chain, thought to act as an extended "linker" connecting the globular N- and C-terminal domains. Indeed, the length of this linker region varies among species and an abbreviated form of $Rpgr^{ORF15}$ (the murine homologue) was shown to fully reconstitute retinal function in $Rpgr^{-/Y}$ mice [72].

The C-terminus of the constitutive variant features a CAAX isoprenylation motif and $RPGR^{ex1-19}$ is partly found bound to the membrane of the endoplasmic reticulum [73]. In contrast, the $RPGR^{ORF15}$ isoform ends with a highly conserved 74 amino-acid basic domain, which interacts with NPM and Whirlin (WHRN), but does not feature a CAAX motif for posttranslational farnesyl group addition [74, 75].

Structural and functional analyses of $RPGR^{ORF15}$ have been somewhat hampered due to its highly purine rich, repetitive primary sequence and resulting challenges for cloning, overexpression and purification. As a result, $RPGR^{ORF15}$ function is not completely understood, but all available evidence points towards $RPGR^{ORF15}$ utilising its localisation at the connecting cilium to facilitate micro-tubule-based transport to and from the basal bodies and within photoreceptor axonemes, likely concerned with movement of cargoes between inner and outer segments [46].

1.2.4 Relevant model systems of XLRP

Several principal systems are available to explore the mechanistic basis of HRD originating in individual mutations, and transgenic animal models (e.g. *Rpgr*$^{-/y}$) or strains carrying natural mutations (e.g. *C57BL/6J*$^{Rd9/Boc}$) in target genes have been most helpful not only to dissect the disease mechanism, but also as means for pre-clinical development of therapeutic approaches.

Rpgr is the murine homologue of human *RPGR* and *Rpgr*$^{-/y}$ mice have been engineered by targeted knockout [76]. The resulting retinal phenotype includes opsin mislocalization (normally found only in the photoreceptor outer segment) to the inner segments and proximal synaptic endings, reduced amounts of rod opsin in rod outer segments and abnormal cone outer segment structure. Essentially, this causes comparably slow photoreceptor degeneration with outer nuclear layer reduction by two rows of nuclei and concomitant shortening of photoreceptor outer segments at six months of age. ERG shows ca. 25% reduction of scotopic (rod mediated) a-wave amplitude and ca. 30% of photopic (cone mediated) b-wave amplitude at six and a half months of age. By 24 months of age, *Rpgr*$^{-/y}$ mice feature gross photoreceptor degeneration with only few nuclei remaining [54, 72, 76].

Another mouse model of XLRP, termed *C57BL/6J*$^{Rd9/Boc}$ features a spontaneous 32bp insertion in the ORF15 region introducing a premature stop codon in the murine *Rpgr*^{ORF15} gene [77]. On Western blot, constitutive variant Rpgr^{ex1-19} could be detected, while Rpgr^{ORF15} seemed absent. This was reflected also by immunohistochemical analysis, where no Rpgr^{ORF15} staining could be observed in affected *C57BL/6J*$^{Rd9/Boc}$ mice. Photoreceptor loss as indicated by decline of ONL

thickness appeared only slightly faster than the natural rate during aging in wild type mice with significance levels only met after 12 months and only in three out of four measured quadrants. Functionally, the ERG responses were reduced in the affected mice compared to age matched wild type controls as early as 4 months of age with the difference reaching even more convincing levels at 16 months of age in both dark and light adapted ERG outcome measures [77].

While mouse models have benefits such as short reproductive cycles and relatively small costs per animal, one major drawback is the lack of an area centralis (chapter 1.1) corresponding to the cone rich macula in human patients. Dogs have a visual streak of increased photoreceptor density and their behaviour is generally considered more visually driven then that of nocturnal mice [78]. Zhang *et al.* first described two canine models with naturally occurring mutations in the homologous ORF15 region [79]. The XLPRA1 deletion results in a C-terminal truncation of 230 residues and a slowly progressive rod-cone dystrophy [80]. ONL thickness is significantly thinner compared to wildtype levels at 36 weeks of age, with reduced rod-derived ERG responses and borderline normal cone responses. In contrast, the XLPRA2 deletion causes a shift of the reading frame and isoelectric point of the truncated protein leading to a much more rapid rod-cone dystrophy possibly as result of a negative dominant effect [81]. In this model, ONL thickness is already significantly reduced at 7 weeks of age, coinciding with reduced rod responses in dark-adapted ERG and borderline cone responses, which become pathological after 36 weeks of age. Both models correspond to the disease spectrum of human XLRP3 and can be used to model the first decade of human XLRP, where gene therapy might be most usefully applied in the clinical setting [82].

1.3 Gene replacement therapy in retinal degeneration

Gene replacement has emerged as a potential curative therapeutic strategy for a number of monogenetic diseases involving various organ systems including the eye. The concept of gene transfer arose from the Avery, MacLeod and McCarty studies in the 1940s, which showed that DNA carries all the necessary information needed for the recipient organism to perform a new function [83]. After the discovery that gene transfer was already an established part of nature's repertoire and routinely performed by viral particles [84], Rogers and Pfuderer were among the first to promote the idea of virus mediated gene transfer for therapeutic purposes in the late 1960s [85]. In the following 50 years, the field of gene therapy survived many ups and downs with notable success in the preclinical development of adeno-associated viral vectors (AAVs) for HRDs by Jean Bennett and others [86, 87]. This culminated in landmark clinical trials with first-in-man ocular gene therapy applications [88-90] for mutations primarily affecting the retinal pigment epithelium and subsequent degeneration of photoreceptors. All these trials demonstrated the safety of recombinant AAVs in the eye. The first clinical gene therapy study targeting retinal photoreceptors directly (NCT01461213) was initiated in Oxford in 2011.

1.3.1 Recombinant adeno-associated virus vectors

Adeno-associated viruses (AAV) belong to the genus Dependovirus of the Parvoviridus family [91]. Parvus is Latin for “small”, thus indicating the small size of Parvoviridae. AAV are ca. 20 nm in diameter with a packaging capacity of ca. 4.8kb single stranded DNA. They are free of envelope structures and lack immunogenicity [92]. The recombinant AAV (rAAV) used in this study features elements of two serotypes of human (AAV2) and non-human primate (AAV8) origin. The capsid proteins are derived from the AAV8, while the transgene is flanked by elements of the AAV2 single stranded DNA (ssDNA) genome.

Capsid proteins are the first to interact with target and off-target cells and determine the tissue tropism and infection efficiency. AAV8 capsid proteins were chosen because of their high efficiency to transduce photoreceptors, the target cells for RPGR replacement gene therapy [93-96]. Most of our knowledge about specific capsid protein-host interaction is derived from experiments with rAAV2 virions, which gain entry into target cells by using the cellular receptor heparan sulfate proteoglycan. Internalization is enhanced by interactions with one or more of at least six known co-receptors including αvβ5 integrins, fibroblast growth factor receptor 1, hepatocyte growth factor receptor, αvβ1 integrin, and laminin receptor [97-99]. For rAAV8, a 37 kDa/67 kDa laminin receptor has been identified as receptor, but it is believed that further co-receptors are still to be identified [100].

The infectious, receptor-mediated entry pathway of rAAV has been investigated in HeLa cells [98, 101]. Binding to a cell surface receptor initiates internalization (receptor mediated endocytosis) through clathrin-coated pits. Once internalized, the virus encounters a weakly acidic environment, which is sufficient to allow penetration into the cytosol. rAAV rapidly moves to the cell nucleus and

accumulates perinuclearly within 30 min after the onset of endocytosis. Escape of rAAV from the endosome and trafficking of viral particles to the nucleus are independent from adenoviral co-infection. The majority of the intracellular virus particles remain in a stable perinuclear compartment and slowly penetrate into the nucleus, possibly through the nuclear pore complex (NPC) [101]. Within 2h, viral particles can be detected within the cell nucleus, suggesting that rAAV enters the nucleus prior to uncoating. After entry into the host cell nucleus, wild type AAV can follow either one of two distinct and interchangeable pathways of its life cycle: the lytic or the lysogenic (**Fig. 1.8**).

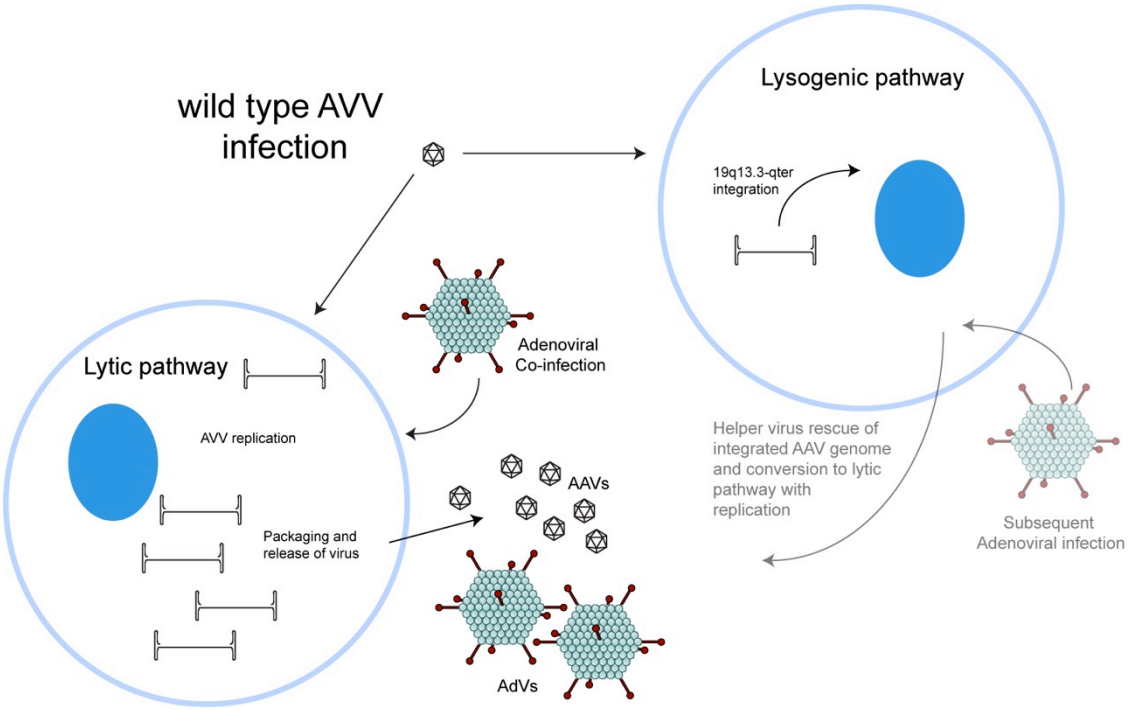

Fig. 1.8 Wild type Adeno associated virus (AAV) life cycle. AAV undergoes productive infection via the lytic pathway in the presence of adenovirus co-infection (left cell). This is characterized by genome replication, viral gene expression, and virion production. In the absence of adenovirus (AdV, right cell), AAV can establish latency via the lysogenic pathway by integrating into chromosome 19. The latent AAV genome can be rescued and replicated upon subsequent infection by adenovirus (bottom right). Both stages of AAV's life cycle are regulated by complex interactions between the AAV genome and AAV, AdV, and host proteins. Note size difference between AAV (ca. 20nm) and AdV (ca. 100nm) particles.

Productive (lytic) infection develops in cells co-infected with a helper virus such as adenovirus [102, 103], Human papilloma virus (HPV) [104-106], vaccinia virus [107] or herpes simplex virus (HSV) [108, 109] to help its replication. In absence of a helper virus a lysogenic state is established with a 1:1000 likelihood of integration of the virus genome into a region of roughly 2-kb on the long arm (19q13.3-qter) of human chromosome 19 [110, 111] designated AAVS1 [112, 113]. The other 99.9 % of AAV DNA persists mainly as monomeric and concatemeric chromatin structures [114, 115].

The AAV genome is approximately 4.7 kilobases long and comprises inverted terminal repeats (ITRs) at both ends of the DNA strand, and two open reading frames (ORFs): rep and cap (**Fig. 1.9**). Both ORFs are composed of multiple overlapping genes. The first ORF encodes Rep proteins required for DNA replication: Rep78, Rep68, Rep52 and Rep40. The two larger Rep proteins (Rep78 and Rep68) also play a crucial role for the site-specific integration reaction at AAVS1 (see above) [116]. The second ORF contains overlapping nucleotide sequences coding for capsid proteins VP1, VP2 and VP3, which interact together to form a capsid of icosahedral symmetry. The partially palindromic wild type ITR sequence of AAV2 comprises 145 bases and contains all *cis*-acting functions required for DNA replication and packaging [117]. Based on these findings, the AAV2 genome was 'gutted' to harness its potential as viral vector: Removal of both ORFs left the ITRs to accept any engineered transgene for packaging into the icosahedral capsid for efficient delivery into target cells. At the same time, this renders rAAV replication-deficient even in presence of wild type helper virus as the genetic information from the Rep ORF and for the production of capsid proteins was lost. Furthermore, in absence of Rep78 and Rep68, crucial

elements for vector genome integration, risk of insertional mutagenesis had become negligible [118] [119]. This is also supported by the observation that rAAVs have been used for more than 20 years in ocular gene transfer studies in animal models and more than 10 year in human clinical trials with no sign of malignant transformation [120].

1.3.1 Gene replacement in relevant model systems of XLRP

After Hong *et al.* created the *Rpgr*$^{-/y}$ mouse model by disruption of the genomic sequence including exons 4 and 5 [76], several studies have been undertaken to attempt replacement gene therapy with the wildtype coding sequence of *Rpgr*, alternate coding sequences mimicking *Rpgr* or *RPGR* as well as full length human *RPGR* using this mouse model [72, 121, 122].

Hong *et al.* provided histopathological, immunocytochemical, and

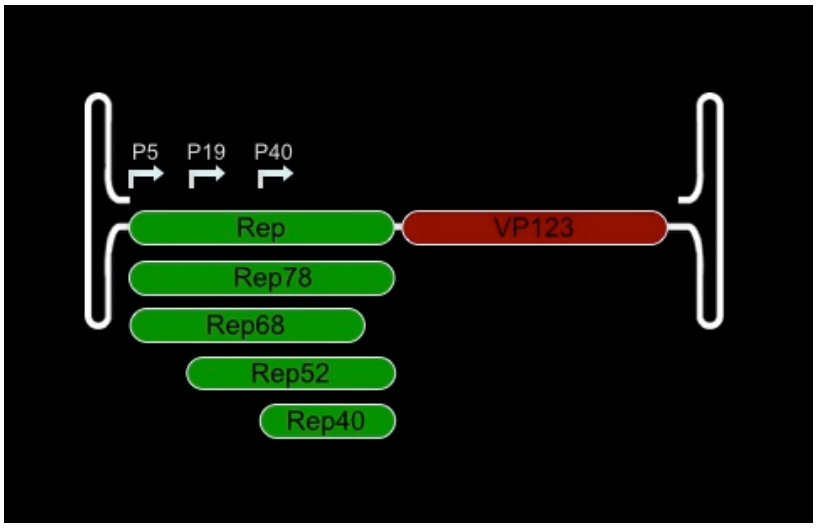

Fig. 1.9 The single-stranded DNA genome of wild type AAV. The inverted terminal repeats (ITRs) flank the two open reading frames rep and cap. The rep gene encodes four nonstructural proteins – Rep78, Rep68, Rep52, and Rep40. The cap gene encodes three structural proteins – VP1, VP2, and VP3. The location of the promoters, p5, p19, and p40 are depicted by arrows.

electrophysiological evidence of a substantial, long-term structural and functional rescue of photoreceptors in *Rpgr*$^{-/y}$ mice expressing a shortened *Rpgr*^{ORF15} transgene [72]. The same author also showed that another truncated version of *Rpgr*^{ORF15} confers a dominant negative effect illustrating the need for cautious and thorough safety studies before moving into clinical trials with RPGR gene replacement therapy [54].

Beltran *et al.* applied vector constructs with a sequence derived from human RPGR^{ORF15} cDNA under two different promoters packaged into recombinant AAV2/5 (rAAV2/5.hIRBP.hRPGRORF15 and rAAV2/5.hGRK1.hRPGRORF15) in the two canine models of XLRP3. The evidence suggested effective preservation of photoreceptor structure and function with rAAV2/5.hIRBP.hRPGRORF15 being the best construct [123]. However, in the downstream development towards a clinical trial application this group found mutations in the coding sequence of the vectors, which alters the primary amino-acid sequence of the translated protein (personal communication with Dr. G. Aguirre). A consequent pre-clinical safety study was published using the same vector with details on the deletions, insertions and missense mutations in the purine rich ORF 15 region of the transgene [122]. This study showed no adverse reactions in a wild type mouse model treated with this vector and the authors argued that the evidence of efficacy in the dog model together with the safety data from the recent work together make a strong case for the safety and potential therapeutic effect of their compound even though the resulting protein is not wild type RPGR^{ORF15}.

Wu *et al.* provide maybe the most promising pre-clinical study on vectors developed with the goal to reach a phase I clinical trial so far [121]. AAV pseudotypes 8 and 9 were manufactured carrying either Rpgr or RPGR driven by the human

rhodopsin kinase (RK) promoter. Good safety was shown over four months for a dose of $1x10^9$ vg, while application of $1x10^{10}$ vg was associated with toxic effects on retinal structure and function. Four dose groups ($1x10^8$, $3x10^9$, $1x10^9$ and $3x10^9$ vg) were tested over 18 months and $1x10^9$ vg demonstrated the best outcome in the *Rpgr*$^{-/y}$ mouse model. However, the purine-rich region of RPGR^{ORF15} again proved prone to deletions and/or rearrangements in the cloning phase of the plasmids and mutations were detected in two out of five AAV vector productions. While precautions were taken to check integrity of AAV production prior to use (band size analysis after PCR), the general instability of the wild-type cds of RPGR^{ORF15} constitutes a significant challenge for any clinical or even commercial AAV production according to good manufacturing practice guidelines.

1.4 Aim and outline of thesis

The overall aim of his work was to develop an optimised gene replacement therapy for X-linked retinitis pigmentosa due to mutations in *RPGR*. This entity is one of the most common and severe forms of HRD. Most patients are affected during childhood and often become legally blind in their 30s. Among ca. 250 disease genes leading to some form of HRD, mutations in RPGR are the single most common gene defect (ca. 20% of all cases) and a successful RPGR gene replacement therapy would benefit a comparably large number of severely affected patients.

To achieve the overall aim, different milestones were identified in the pursuit of an optimised gene replacement therapy for translation into a clinical trial setting. These milestones form individual chapters such as chapter three, where we discuss the optimisation of the expression cassette based on human cDNA sequence of RPGR. Chapter four describes the recombinant production of the optimised viral vector and the *in vitro* assessment of its qualities. In chapter five, we then demonstrate evidence from a pilot trial on the successful subretinal delivery, retinal transduction and transgene expression in relevant animal models of XLRP disease. Two prospective safety and efficacy trials (one masked with sham treatment, one open label unilateral treatment) involving three mouse strains (*C57BL/6J*, *C57BL/6J*$^{Rd9/Boc}$ and *Rpgr*$^{-/y}$) over a 6-month time course build chapter five. The final chapter reflects on the data presented and sets the work in context with the current literature and the wider field of retinal gene therapy.

CHAPTER 2 MATERIALS AND METHODS

2.1 Molecular biology

Standard methods of molecular biological techniques have been applied in a controlled environment. Room temperature (RT) was kept constant at 20 °C and calibrated instruments used throughout. Care was taken to use separate workspace for plasmid DNA, genomic DNA and protein work where possible. A table of all plasmids used in this study is provided below.

Table 2.1 Overview of all plasmids used in the study.

name	**backbone**	**transgene**	**source**
OriGene wtRPGR^{ORF15}	pCMV-XL cloning vector	wtRPGR^{ORF15}	backbone: OriGene Technologies, Rockville, MD, USA; transgene: this study
GenScript wtRPGR^{ORF15}	pUC57 cloning vector	wtRPGR^{ORF15}	backbone: GenScript, Piscataway, NJ, USA; transgene: this study
GenScript coRPGR^{ORF15}	pUC57 cloning vector	coRPGR^{ORF15}	backbone: GenScript, Piscataway, NJ, USA; transgene: this study
CAG.wtRPGR	AAV-CAG	wtRPGR^{ORF15}	backbone: Vector BioLabs, Malvern, PA, USA; transgene: this study
CAG.coRPGR	AAV-CAG	coRPGR^{ORF15}	backbone: Vector BioLabs, Malvern, PA, USA; transgene: this study
RK.wtRPGR	AAV-RK	wtRPGR^{ORF15}	this study
RK.coRPGR	AAV-RK	coRPGR^{ORF15}	this study
control	AAV-CAG	*loxP*.EYFP.*loxP*	gift of Dr. D. Hickey

Table 2.1 Overview of plasmids used in this study. p = plasmid; CMV = cytomegalovirus immediate early enhancer and promoter; pUC57 = common used plasmid cloning vector in *E. coli*; CAG = cytomegalovirus early enhancer and chicken beta-actin hybrid promoter; RK = rhodopsin kinase promoter; wtRPGR^{ORF15} = wild type sequence of RPGR^{ORF15}; coRPGR^{ORF15} = codon optimised sequence of RPGR^{ORF15}; *loxP* = locus of X-over P1 [recognition site for Cre protein (Cre = causes recombination)].

2.1.1 Cloning

XL10-Gold ultracompetent bacteria (Stratagene, Agilent Technologies) were used for cloning purposes due to their high efficiency of transformation. These bacteria exhibit the Hte phenotype, which increases the transformation efficiency of ligated and large DNA molecules. More importantly, they are deficient in all known restriction systems [Δ(mcrA)183 Δ(mcrCB-hsdSMR-mrr)173], deficient of endonuclease (*endA*), and recombination deficient (*recA*), helping to ensure insert stability and improving the quality of miniprep DNA. We followed the manufacturers' instructions with minor modifications to improve yield:

1. One 14 ml BD Falcon polypropylene round-bottom tube was pre-chilled on ice per sample. S.O.C. medium (Gibco) was pre-heated to 37 °C.
2. Cells were thawed on ice, gently mixed and 75 µl of cells transferred into each of the pre-chilled tubes.
3. Three µl of the β-ME mix was provided to each aliquot of cells.
4. The mix in the tube was gently swirled before and every 2' while incubating the cells on ice for 10'.
5. 0.1-50ng of the experimental DNA (or 2 µl of a ligation mixture) was added to one aliquot of cells.
6. The mix in the tube was gently swirled, and then incubated on ice for 30'.
7. Tubes were heat-pulsed in a 42 °C water bath for 30".
8. Tubes were incubated on ice for 2'.

9. 0.9 ml of preheated (37 °C) S.O.C. medium was added and tubes incubated at 37 °C for 1 hour with shaking at 10 x g.

10. 200 µl of the transformation mixture was plated on LB-ampicillin agar plates.

11. Plates were incubated at 37 °C overnight.

After ca. 12-15 h (end of the logarithmic growth phase) plates typically showed 50-200 individual colonies. A subset of these were picked using autoclaved pipette tips and incubated in 4 ml Luria broth (LB) with 8 µl ampicillin (50 µg/ml) in a shaker run at 10 x g and 37 °C for ca. 15 h (end of predicted log phase) before harvesting:

1. Cells were pelleted down at 12,000 x g for 1' at RT.

2. Pellets were subjected to one freeze/thaw cycle (30' at -20 °C).

Lysis of cells and column purification of plasmid DNA were performed using the Sigma GenElute™ Plasmid Miniprep Kit according to the instructions provided by the manufacturer. Total DNA was eluted in 50 µl molecular grade H_2O to have the best efficacy for downstream enzymatic interaction (sequencing, digestions, ligation etc.). Individual minipreparations were then tested for DNA yield and quality using the NanoDrop 1000 Spectrophotometer (Thermo Scientific, Northumberland, UK) and stored at -20 °C unless processed immediately otherwise.

For larger preparations of plasmid DNA the Qiagen® EndoFree® Mega Kit was used according to the instructions provided by the manufacturer. Briefly, single

colonies were picked and incubated as described above (4 ml cultures). After 8 hours, 1 ml aliquots of the culture were transferred to 500 ml of LB with ampicillin in 1l flasks for further incubation under identical conditions. Cells were pelleted down in 500 ml Nalgene flasks in a Avanti J-26XP centrifuge (Beckmann Coulter) for 20 minutes at 4 °C and 8,000 x g, subjected to one freeze/thaw cycle (1h at -20 °C) before following the Qiagen protocol to lyse cells, extract and purify plasmid DNA. Final elution was made with a total of 1.5 ml of elution buffer and yield quantified on the NanoDrop 1000 Spectrophotometer and stored at -20 °C unless processed immediately otherwise.

2.1.2 Transfection

Most transfections (e.g. head to head comparison between wild type and codon optimised *RPGR*^{ORF15}) were performed in 6-well tissue culture plates (Sarstedt Inc., Newton NC, USA) and on HEK293T cells [124](for details on the cell culture see chapter 2.2.1). These transfection experiments were performed using the Mirus *Trans*IT®-LT1 Transfection Reagent (Geneflow Ltd., Lichfield, UK) according to the manufacturer's instructions. Care was taken to have a cell density of ca. 70% confluence at time of transfection, and to use serum/antibiotic free medium for the complex formation step. Best incubation time post-transfection had been established in the lab (personal communication Dr. Michelle McClements).

Approximately 18-24 h before transfection, HEK293T cells were seeded at 2–6 × 10^5 cells/well and incubated overnight. Immediately before transfection, 3 µl

*Trans*IT®-LT1 reagent was added to 250 µl of serum free Opti-MEM (Invitrogen, Carlsbad, CA) substituted with 2mM L-glutamine (Sigma-Aldrich Company Ltd., Dorset, UK). The solution was briefly vortexed and allowed to equilibrate to room temperature (RT) for 10'. Precisely 1 µg of plasmid DNA was mixed into solution to allow complex formation with the liposomes for 20' at RT. The *Trans*IT®-LT1 Reagent-DNA complex was added to the cells in a drop-wise fashion. The culture vessel was gently rocked to allow even distribution of the *Trans*IT®-LT1:DNA complexes before incubation at 37 °C for 48 h. Cells were then harvested and assayed as required.

2.1.3 Recombinant AAV production

To generate rAAVs, HEK293T cells were co-transfected with two plasmids: The appropriate rAAV expression plasmids containing the transgene and a helper plasmid pDP8.ape (PlasmidFactory, Bielefeld, Germany), which encodes Rep and Cap genes of AAV8 and adenoviral helper gene pFΔ6. The transfection protocol in detail was as follows.

1. Seeding HyperFlasks with HEK293T

1.1 Four T75 flasks (Sarstedt Inc.) were each seeded with 1.7 x 10^7 HEK293T cells in culture media (500 ml high glucose DMEM with 10%

FBS [heat-inactivated, non-USA origin, sterile-filtered, suitable for cell culture], 5 ml 200mM L-Glutamine solution, 5 ml Penicillin-Streptomycin [10,000 units penicillin, 10 mg streptomycin/ml]) and incubated at 37 °C, 5% CO_2 for 48 hours.

1.2 Media were removed at ~80% confluency and HEK293T cells were washed with 5 ml PBS. After removing the wash, 2 ml PBS was added and cells incubated at 37 °C, 5% CO_2 for 10'.

1.3 Cells were loosened and resuspended with 8 ml cell culture media by gently pipetting up and down. A further 190 ml of medium was added.

1.4 Two T75 flasks were used to seed one HyperFlask. Two HyperFlasks were used in each rAAV production cycle.

1.5 Cell suspension was transferred from two T75 flasks into one HyperFlask. After the total 400 ml of cell suspension was in the HyperFlask, it was rested on its long, thin side. The cell suspension divided evenly between the layers of the HyperFlask. The HyperFlask was then topped up with media (each HyperFlask held ~560 ml). In order to remove any bubbles, the lid was secured, and HyperFlask first positioned upright, then tilted to one side while tapping slightly to dislodge trapped air. This was repeated on either side until no more bubbles would surface. If required, a final top up with media was performed before laying the HyperFlask down and incubating it at 37 °C, 5% CO_2 for 72 hours.

2. Transfecting HEK293Ts in HyperFlasks

2.1 For each HyperFlask a total of 500 µg DNA was prepared. The ratio was dependent on the size of the plasmids being used:

Table 2.2 Calculations for double transfection experiment.

Plasmid	Size (kb)	Amount per transfection (µg)
pDP8.ape	22.00	22.00 x **R**
pTransgene	T	T x **R**
Total	K	500.00
Ratio (**R**) mass/kb	500/K	

Table 2.2 In order to achieve the optimal ratio of plasmid constructs in the double transfection experiment, genomic size (in kilobases, kb) of the plasmids (e.g. 22kb for pDP8.ape and T for pTransgene) have to be added to give the number of total genomic plasmid DNA used (K). The ratio (R) is defined as 500/K. The resulting number R is then multiplied with the respective genomic plasmid size to yield the amount of plasmid needed (in µg) for one transfection experiment. The total amount of plasmid DNA will amount to precisely 500µg of DNA.

2.2 Plasmids were added to a 50 ml Falcon tube and filled up to 10 ml with NaCl 150mM. In a separate 50 ml Falcon 1.125 ml of 10mM Polyethylenimine (PEI) was added and volume made up to 10 ml with 150mM NaCl.

2.3 DNA and PEI complexes were produced by carefully adding the 10 ml of PEI drop by drop into the tube containing the 10 ml DNA. Solution was incubated at RT for 20'.

2.4 Transfection media was prepared (500 ml high glucose DMEM with 2% FBS [heat-inactivated, non-USA origin, sterile-filtered, suitable for cell culture], 5 ml 200mM L-Glutamine, solution, 5 ml Penicillin-Streptomycin [10,000 units penicillin, 10 mg streptomycin/ml]) and 50 ml of this set aside in a Falcon tube. The DNA/PEI/NaCl complex was poured into the remaining volume of transfection media (~500 ml). Then 20 ml of the 50 ml transfection media aliquot was transferred into the now empty DNA/PEI/NaCl tube to collect any

remaining solution before adding this into the ~500 ml of transfection media containing the DNA/PEI/NaCl.

2.5 HyperFlask was slowly drained before gently adding the transfection media/DNA/PEI/NaCl. The flask was topped up with the remaining 30 ml aliquot of transfection media (if necessary). Bubbles were removed as described above and HyperFlask incubated at 37 °C, 5% CO_2 for 72 hours.

3. Harvesting and lysing transfected HEK293T cells

3.1 200 ml of the HyperFlask media was discarded, the lid secured and the HyperFlask shaken vigorously to mechanically dislodge the cells. Direct viewing under the microscope was used to assess the success of the manoeuvre.

3.2 The cell suspension was poured into a 500 ml flask and centrifuged for 10' at 1,000 x g, 20 °C. During this step 1 ml of Lysis Buffer pH 8.5 was prepared (1M Tris (hydroxymethyl) aminomethane [AnalaR NORMAPUR, VWR], 150mM NaCl [Sigma-Aldrich], molecular biology grade water, DEPC-treated and sterile filtered [Sigma-Aldrich]) with one protease inhibitor pellet (cOmplete mini EDTA-free protease inhibitor cocktail tablets, Roche). This amount was sufficient for two HyperFlask collections.

3.3 Media were removed from the pelleted HEK293T cells and only about 30 ml of media left in the flask to resuspend the cells. This was transferred to a 50 ml Falcon tube, centrifuged as above and media completely removed.

3.4 15 ml of Lysis Buffer was added to the cell pellet (15 ml of Lysis Buffer per HyperFlask) and carefully pipetted up and down to mix. 500 µl of the prepared protease inhibitor cocktail was added and pipetted up and down to mix. The tube was then labelled and place in an -80 °C freezer for 1 hour.

3.5 Lysis sample was placed in a 37 °C water bath for 15' to thaw, and shaken well half way through the incubation time. The tube was placed back in the -80 °C freezer and the freeze/thaw repeated twice more. At the final freeze/thaw, samples were placed at -80 °C and stored until ready to purify.

4. **Isolation of the rAAV particles using an Iodixanol gradient**

4.1 The lysate was thawed at 37 °C for 15' before adding Benzonase (EMPROVE bio Benzonase, Merck Millipore) to the lysate to give a final concentration of 50U/ml, then incubated at 37 °C for a further 45'. Tubes were shaken every 15' during this incubation before spinning them at 3,700 x g for 20' at RT.

4.2 Iodixanol gradients were prepared by layering the different preparations according to the table below: Iodixanol 60% (OptiPrep density gradient medium, Sigma-Aldrich), Phenol Red (Phenol red solution, 0.5% liquid, sterile-filtered, BioReagent, suitable for cell culture, Sigma-Aldrich), 5X PBS-MK (Gibco phosphate buffered saline tablets [Life Technologies], 5mM MgCl2 [Sigma-Aldrich], 12.5mM KCl [Sigma-Aldrich], molecular biology grade water, DEPC-treated and sterile filtered [Sigma-Aldrich]).

Table 2.3 Calculations for iodixanol gradient solutions

Fraction	Iodixanol	5M NaCl	5x PBS-MK	H_2O	Phenol Red
15%	4 ml	3.2 ml	3.2 ml	5.6 ml	-
25%	5 ml	-	2.4 ml	4.6 ml	20 µl
40%	6.7 ml	-	2 ml	1.3 ml	-
60%	10 ml	-	-	-	20 µl

Table 2.3 Calculations for individual solutions of increasing iodixanol concentrations. Solutions were mixed fresh for each rAAV purification step.

4.3 7.2 ml of the 15% preparation was pipetted into OptiSeal 32.4 ml ultracentrifuge tubes. Then, 4.8 ml of the 25% preparation was pipetted into a separate 15 ml Falcon tube and a long neck Pasteur pipette (UV treated beforehand) used to draw up half of the 4.8 ml aliquot. While carefully holding the volume at the tip of the pipette it was gently moved through the 15% iodixanol fraction until the tip touched the bottom of the ultracentrifuge tube. Then, the 25% fraction was carefully layered below the 15% fraction. The Pasteur was carefully withdrawn from the gradient when empty and without drawing up or disturbing the fractions in place. Then the remaining volume of the 25% fraction was pipetted in the same fashion. Once the 25% fraction was in place, this process was repeated to add 4 ml of the 40% preparation beneath the 25% fraction and finished by adding 4 ml of the 60% preparation beneath the 40% fraction.

4.4 The lysate was added drop by drop to the top of the iodixanol gradient. It was ensured that the ultracentrifuge tube was filled to the top (Lysis Buffer was used to top up if necessary).

4.5 OptiSeal 32.4 ml tubes were sealed and transferred into a Rotor 70Ti ensuring they are all were dry and the holes in Rotor were clean and dry.

4.6 Tubes were spun at 358,300 x g for 1 hour and 30 minutes at 20 °C. When centrifuge was done, vacuum was released and centrifuge cap and the tube seal removed. After attaching an 18G needle to a 5 ml syringe, ultracentrifuge tubes were carefully pierced with the needle at the interface between the 60% and 40% phases, while keeping the bevel facing up. As much as possibly of the 40% phase was collected without collecting debris from the 25% phase (bevel was turned sideways towards the end to minimise risk of contamination). Circa 2-3 ml was recovered from each gradient and purified immediately as described below.

5. Purification and concentration of the isolated rAAV vectors

5.1 5 ml PBS was added to an Amicon Ultra 100K filter sitting in a 50 ml Falcon tube and centrifuged at 3,000 x g for 15' at 20 °C. Flow through was discarded. The collected iodixanol fraction was topped up to ca. 10-15 ml total volume with PBS (3 ml -> 10 ml, 6 ml -> 15 ml) and carefully pipetted up and down to mix. The total volume was added onto the filter, which was placed in the centrifuge with its long axis in line with the centrifugal force. The filter was centrifuged at 3,000 x g, 20 °C until the volume was reduced to 500 µl. This took between 1 and 4 hours depending on the fraction. Flow through was discarded.

5.2 15 ml PBS was added again to the filter and carefully pipetted up and down before centrifuging at 3,000 x g, 20 °C until the volume was again reduced to 500 µl. Flow through was discarded.

5.3 Previous step was repeated twice more. On the third and final PBS wash, volume was reduced to ca. 500 µl of purified rAAV solution.

5.4 Using a 200 µl pipette, rAAV solution was drawn up and dispensed back over the filter 20 times on each side to rinse. Appropriate aliquots were prepared and stored (without snap freezing step) at -80 °C until use. 500 µl PBS was used to rinse the filter 20 times on each side for any remaining rAAV particles. Aliquots from this volume had a lower titre than the original aliquots but still contained rAAV (labelled wash).

2.1.4 Quantitative polymerase chain reaction (qPCR)

rAAV vector titre was quantified by using qPCR (ABI Prism 7700; Applied Biosystems, Foster City, CA) to estimate the vector genomes per ml (vg/ml). For this, several primer pairs were designed (Geneious software version 6.1.6 for Mac OS X 10.7.5; Biomatters Ltd, Auckland, New Zealand) to the bovine growth hormone (bGH) polyA sequence at the 3' end of the expression cassette and tested for their efficiency, annealing characteristics and specificity (**Fig. 2.1**). The primer pair with highest efficiency and narrowest peak in the respective melt curve profile was chosen for further experiments:

pA_qPCR_20F	5' – CCAGCCATCTGTTGTTTGCC – 3'
pA_qPCR_91R	5' – GAAAGGACAGTGGGAGTGGC – 3'

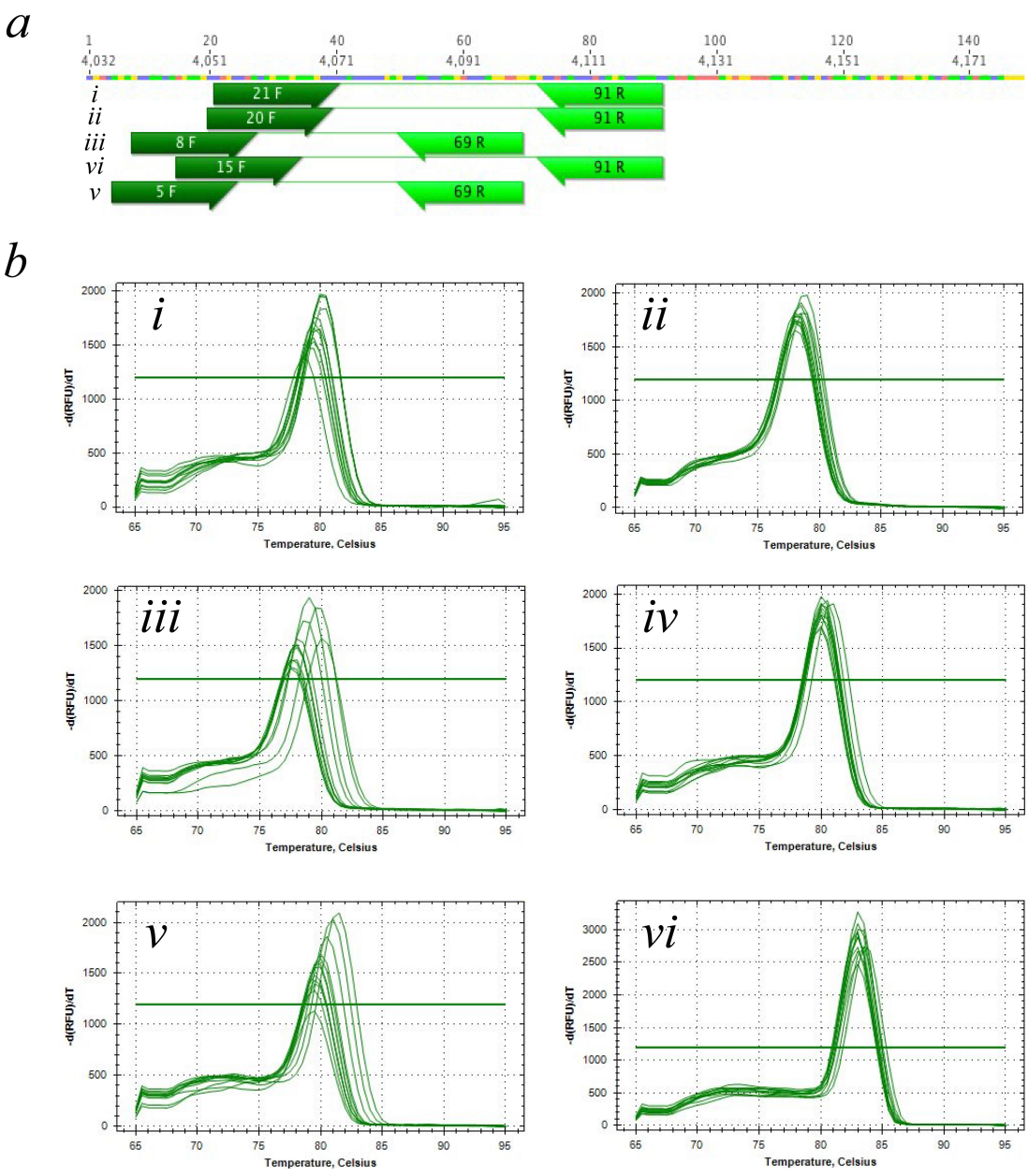

Fig. 2.1 Comparison of melt curves to optimise use of primer pair combinations in vector titre analysis by qPCR. The bovine polyA sequence (a) was used to predict useful primer oligonucleotides for qPCR reactions of rAAV genomes using the Geneious software. Primer pairs *i* - *v* were tested against the established primer pair directed against the rhodopsin kinase promoter (*vi*). b) The primer pair with the closest matching melting curve to the one for *vi* was primer pair *ii* (20F and 91R) as indicated by the graphical output of the proprietary ABI PRISM® 7700 Sequence Detection System software.

For each rAAV titre analysis, 1 µl sample were mixed with 1 µl of DNAse I buffer, 7 µl molecular grade H_2O (SIGMA) and 1 µl of DNAse I (Qiagen) and incubated at RT for 1 h. The DNAse was then heat inactivated and capsids denatured

at 95 °C for 10‘. The sample was then further diluted (1:10) with molecular grade H_2O before use as template in qPCR reactions. Purified, quantified and sequence verified plasmids with the identical expression cassette were used to prepare the standard curve (care was taken to account for the backbone when calculating the number of plasmids in the total mass of DNA).

qPCR reactions were performed in 10 µl of final volume using the 2×SYBR Green qPCR mix (BioRad) supplemented with 100nM each of forward and reverse primer, and 2 µl of template DNA (either plasmid standard or rAAV sample) according to the manufacturer’s instructions. Each plasmid standard, sample and negative control were run in triplicates of 20 µl of reactions in alternate rows of a 96-well optical plate. The PCR profile included an initial denaturation step at 95 °C for 10’ followed by 40 cycles of denaturation at 95 °C for 15” and annealing/extension at 60 °C for 1’, followed by a melt curve stage. Data analysis was performed using the Applied Biosystems StepOne software v2.1 before export to Microsoft Excel.

2.1.5 Enzyme linked immunosorbent assay (ELISA)

Enzyme linked immunosorbent assays were used to estimate the ratio of empty to full capsids. For this purpose, an rAAV8 titration ELISA (PROGEN Biotechnik GmbH, Heidelberg, Germany) was performed according to the instructions provided by the manufacturer. This sandwich ELISA features monoclonal antibodies specific for conformational epitopes on assembled rAAV8 capsids (ADK8) bound to

microtiter strips, which are used to capture rAAV8 particles from the specimen. Captured rAAV particles are detected in two steps. First a biotin-conjugated monoclonal antibody to AAV8 (ADK8) is bound to the immune complex. In the second step streptavidin peroxidase conjugate reacts with the biotin molecules. Addition of substrate solution results in a change in photometrical absorbance of the samples proportional to the amount of specifically bound viral particles. Empty capsid samples provided in the kit are used to provide a standard curve. Briefly, 100 µl of ready-to-use sample buffer (negative control), serial dilutions of kit control (standard) and specimen (rAAV preparation) were added to separate wells of the microtiter strips coated with the monoclonal antibody to AAV8 (ADK8). Strips were sealed with adhesion foil and incubated for 1 h at 37 °C. Wells were carefully emptied and washed twice with 200 µl wash buffer for approximately 5 seconds each. 100 µl biotin conjugate was then added per well, strips sealed and incubated again for 1 h at 37 °C. After the same washing procedure as above, 100 µl of streptavidin conjugate was added and strips sealed and incubated a third time for 1 h at 37 °C. After another round of washing as above, 100 µl colouring substrate as added and reaction stopped after 15' at RT by adding 100 µl of stop solution into each well. Absorbance measurements were taken with a photometer at λ = 450 nm without delay. Absorbance was correlated with known concentrations from the standard sample dilution series. Based on the resulting function the titre in the sample could be derived from the luminescence units measured in the same.

2.2 Cell cultures

Several cell cultures were used e.g. to study levels of $RPGR^{ORF15}$ expression from wild type or optimised sequences and overexpress the protein for sequence analysis (chapter 3). Production of rAAV (chapter 4) involves cell culture work as well as some of the tests for rAAV transduction efficiencies. All relevant cell culture sources and general protocols for maintaining them are described herein.

All cell culture work was performed in regularly serviced class II cell culture hoods and flasks were incubated at 37 °C and 5% CO_2 in a Galaxy R incubator (Eppendorf AG, Hamburg, Germany) unless stated otherwise. All media was freshly prepared and pre-warmed in a water bath to 37 °C unless stated otherwise.

2.2.1 Human embryonic kidney 293 cells

Human embryonic kidney 293 cells (HEK293) [124] were originally derived from human embryonic kidney cells from a healthy, aborted foetus in Alex Van der Eb's lab (University of Leiden, Holland) by Frank Graham. In his 293rd experiment, Dr. Graham successfully transformed the cells using adenovirus 5 leading to a ~4.5 kilobases insertion of viral genome into human chromosome 19 rendering the cell line immortal. Detailed studies conclude that HEK293 most likely originated from embryonic adrenal precursor cells exhibiting adrenal and neuronal properties [125]. Patel and Tikoo modified HEK293 to constitutively express the simian virus 40

(SV40) T antigen [126]. The resulting HEK293T cell line is particularly transfectable with plasmids containing the SV40 promoter and seems to carry further, only partly understood indirect benefits making the production of recombinant virus more efficient [127].

Such HEK293T cells were obtained from the European Collection of Cell Cultures (ECACC) and stored in aliquots of $2x10^6$ cells in 1.5 ml 90%FBS 10% DMSO at -196 °C in liquid nitrogen. Aliquots were resuscitated when needed in 10 ml complete cell culture media [88% DMEM (Invitrogen, Carlsbad, CA) substituted with 2mM L-glutamine, 100I.U./ml Penicillin and 100 µg/ml Streptomycin and 10% fetal bovine serum (all from Sigma-Aldrich Company Ltd., Dorset, UK)] after quickly thawing and mixing them into a single cell suspension. The cells were then spun at 1,200 x g for 5‘ at 4 °C, re-suspended in 1 ml culture media and pipetted to achieve single cell suspension before seeding cells into T75 flasks (Sarstedt Inc., Newton NC, USA) with the required volume of media. Cells were fed fresh media after 24 hours to remove damaged and non-adherent cells and monitored daily until normal proliferation rates were achieved (3-5 days).

Once stable proliferation had been established, HEK293T cells were cultured with freshly prepared media every 2-3 days and passaged at 75-80% confluence: Old medium was removed, and cells washed once with 5 ml pre-warmed 0.01M phosphate-buffered saline (PBS; Invitrogen Life Technologies Ltd., Paisley, UK) before adding 0.25% trypsin (Sigma-Aldrich) in 2 ml of PBS for 2 minutes. Cells were brought into solution and 8 ml of complete cell culture media (see above) added. Two millilitres of this suspension were then transferred to a new T75 flask and 13 ml media added.

2.2.2 Human neuroblastoma derived cells

SH-SY5Y cells are adherent, neuroblast-derived cells [128]. They are subclones from the original SK-N-SH cells, which were isolated from a bone marrow biopsy of a 4 year old female with neuroblastoma [129].

SH-SY5Y cells had been originally obtained from the European Collection of Cell Cultures (ECACC) and stored in aliquots of $2x10^6$ cells in 1.5 ml 90%FBS 10% DMSO at -196 °C in liquid nitrogen. Resuscitation was performed as described for HEK293T cells except the culture media composition was: One to one mixture of Ham's F12 and EMEM (EBSS) with 2mM Glutamine, 1% Non Essential Amino Acids, 15% Foetal Bovine Serum, 100 µg/ml Penicillin and 100 µg/ml Streptomycin (all Sigma-Aldrich). Cells were maintained in T75 flasks and split as sub-confluent cultures (70-80%) in a 1:50 ratio, i.e. seeding at ca. $5x10^4$ cells/cm^2. The splitting was performed again as described for the HEK293T cells except for the constitution of the cell culture medium.

For induction of a neuron-specific differentiation, media was changed to that containing $1.6x10^{-8}$ M Tetradecanoylphorbol-13-acetate (TPA) and 10^{-5} M retinoic acid (RA, both Sigma-Aldrich) 24h after seeding as previously shown [130].

2.2.3 Mouse cone photoreceptor like cells

The 661W cell line was originally cloned from retinal tumours of a transgenic mouse line expressing the simian virus (SV) 40 T antigen under control of the human inter-photoreceptor retinol-binding protein (IRBP) promoter [131]. It is described as 'cone photoreceptor like cell line' as it was reported to demonstrate cellular and biochemical characteristics of cone photoreceptor cells such as expression of short-/ and medium-wavelength sensitive cone opsins.

The cell line was imported as a kind gift from Dr. Muayyad R. Al-Ubaidi (Oklahoma, USA) under a material transfer agreement and cultured strictly according to his suggestions. Aliquots had been cryopreserved for long-term storage and resuscitated when needed as described for the HEK293T and SH-SY5Y cells except for the culture medium composition: DMEM (Gibco, Thermo Fisher Scientific) with 40 µg/l hydrocortisone, 40 µg/l progesterone, 0.032g/l putrescine, 40 µl/l β-mercaptoethanol, 100 mg/l penicillin, 100 mg/l streptomycin (all Sigma-Aldrich) and 7.5% fetal bovine serum (Gibco).

Cells were maintained in T75 flasks and split as sub-confluent cultures (70-80%) at a 1:5 ratio performed again as described for the HEK293T cells except for the constitution of the cell culture medium (above).

2.3 Animals

All animal experiments were performed in compliance with the ARVO Statement for the Use of Animals in Ophthalmic and Vision Research and UK Home Office guidelines. Animals were kept in individually ventilated cages and followed a 12-hour light (<100 lux)/12-hour dark cycle, with food and water available *ad libitum*.

Mice were weaned at P21 and ear notches taken to mark individuals and extract genomic DNA for genotyping using alkaline lysis as originally described by Birnboim and Doly [132]. 100 µl NaOH 0.05M was added to each ear clip before heating tubes to 95 °C for 30min. After vortexing and spinning (9,600 x g) for 30" each, 10 µl neutralisation buffer was added (1M tris 10mM EDTA pH 8.0). After another round of vortexing and spinning (as above), 100 µl supernatant was transferred to a new tube and diluted with 500 µl H_2O for polymerase chain reaction (PCR) based genotyping.

2.3.1 *C57BL/6J* mice

This strain was purchased from the original JAX™ colony from Jackson Laboratory (Bar Harbor, USA) through Charles River Laboratories (Margate Kent, UK) as required and used as wild type control.

2.3.2 *Rpgr*$^{-/y}$ mice

Rpgr knockout mice have been described previously [76] and in chapter 1.2.4. Frozen embryos of *Rpgr*$^{-/y}$ mice were a kind gift obtained under material transfer agreement from Tiansen Li (Neurobiology, Neurodegeneration & Repair Laboratory, NEI, Bethesda, USA). The transgenic line was produced by Hong *et al.* through electroporating a targeting vector into a J1 embryonic stem cell. This vector had been designed to disrupt *Rpgr*, the murine homologue of *RPGR*. It carried the pGT1.8IRESβgeo sequence flanked by fragments from *Rpgr* exons 4 and 6 amplified by PCR from 129/Sv mouse genomic DNA. Linearized vector DNA was electroporated into J1 ES cells, which originated from a male agouti 129/terSv embryo [133]. Clones were microinjected into C57BL/6 blastocysts to generate chimeras and eventually the *Rpgr* knockout strain [76].

The imported frozen embryos were re-derived at the Medical Research Council centre for mouse genetics before import into the Oxford University biomedical services facilities. Circa half of re-derived pups showed agouti coat colour potentially indicating an incomplete backcross onto C57BL/6 background. Therefore, JAX™ C57BL/6J mice were used to set up breeding pairs with homozygote females. Mice were used for experiments only after at least six generations of successive backcrossing.

For genotyping, genomic DNA was extracted from tissue resulting from ear clips (described above). PCR was used to amplify a 138bp region starting 40bp

upstream and extending into exon 6 in case of the wildtype (wt) allele. In the transgenic animals, where this site would instead harbour the disruptive pGT1.8IRESβgeo sequence (literature refers to this model as knock-out), a reverse primer specific to the internal ribosome entry site (IRES) sequence of the target vector would amplify a 290bp product in the absence of a complementary sequence for the wt reverse primer.

Table 2.4 Primers for genotyping *Rpgr*$^{-/y}$ mice.

Forward primers		**Reverse primers**		
name	**sequence**	**name**	**sequence**	**amplicon**
F.Rpgr	5'-GCCCTTTAAAG ACTTTTCTCCC-3'	R.Rpgr.wt	5'-TCCAACAGTCA CTTCATGAGG-3'	138bp wt
F.Rpgr	5'-GCCCTTTAAAG ACTTTTCTCCC-3'	R.Rpgr.co	5'-TCCCCCTGAAC CTGAAACAT-3'	290bp ko

Table 2.4 Primers for genotyping *Rpgr*$^{-/y}$ mice. bp = nucleotide basepair; wt = wild type; ko = knock out.

Each PCR mixture contained 12.5 µl of 2× ImmoMix™ Red (Bioline Reagents Ltd., London, UK), 3 µl of common forward and 1.5 µl of each reverse primer (each at 10µM), 2.5 µl of DNA template, and 4 µl of PCR-grade water in a final volume of 25 µl. Amplification was performed using a T100™ thermal cycler (Bio-Rad). Thermocycling parameters were 95 °C for 10'; 35 cycles of 95 °C for 1', 60 °C for 30", and 72 °C for 1'; and a final step at 72 °C for 5'. The resulting PCR products were analysed via agarose gel electrophoresis using 1% (wt/vol) Hi-Res Standard Agarose (AGCT Bioproducts, Geneflow Ltd., Lichfield, UK). The assay products were run for 1h at 100V in 1× Tris-acetate-EDTA (TAE) buffer (Tris acetate 40mM,

EDTA 1mM [pH 8.0]). DNA was stained with ethidium bromide (0.5 µg/ml), and the gels were imaged under UV light using the U:Genius setup (Syngene UK, Cambridge, UK). PCR amplicon sizes were estimated by comparison to molecular size markers (Hyperladder II; Bioline Reagents Ltd.).

2.3.3 *C57BL/6J*$^{Rd9/Boc}$ mice

Thompson *et al.* first described a strain of C57BL/6J mice with naturally occurring 32bp duplication within the open reading frame 15 (ORF15) of Rpgr (chapter 1.2.4). This frame-shift mutation introduces a premature stop codon and leads to undetectable levels of Rpgr^{ORF15} protein on Western blot and in immunohistochemical staining of unfixed cryosections [77].

C57BL/6J$^{Rd9/Boc}$ breeding pairs were purchased from The Jackson Laboratory and imported through Charles River Laboratories, where breeding pairs were held in quarantine and screened for relevant specific pathogens before import into the Biomedical Service Centre at the John Radcliffe.

For genotyping, PCR was used to amplify a 2225bp region of wild-type Rpgr including the location of the 32bp insertion in the affected animals, thus resulting in a 2257bp product in case of amplifying an Rd9 allele.

Table 2.5 Primers for genotyping *C57BL/6J*$^{Rd9/Boc}$ mice.

Forward primers		**Reverse primers**		
name	**sequence**	**name**	**sequence**	**amplicon**
F.Rd9	5'- GAGAAAGTGATGGAA AGTACACCGTGCAC -3'	R.Rd9	5'- GAGATGACTTCCCTG TTACTTCAATTCCAG -3'	2225bp wt 2257bp Rd9

Table 2.5 Primers for genotyping *C57BL/6J*$^{Rd9/Boc}$ mice. bp = nucleotide basepair; wt = wild type; Rd9 = *C57BL/6J*$^{Rd9/Boc}$ mice.

PCR was performed as described above except both primers were given at equal molarity (1.5 µl at 10mM), annealing temperature was 59 °C and extension time 60sec. An aliquot of the PCR product was analysed by agarose gel electrophoresis as described for Rpgr-ko mouse genotyping (2.2.2) except using 2% (wt/vol) Hi-Res Standard Agarose for added resolution of small fragment size differences.

The rest of the PCR product was processed to purify amplicons before sequencing using PCR primers and additional sequencing primers (F208: 5'-ACGGGGATCAAATCTGTGAG-3' and R1476: 5'-TGTGCCATGTCTGCCATA TT-3'). Sequencing reactions contained 6.8 µl of purified PCR product eluted in H_2O and 3.2 µl of 1µM primer solution. Sanger sequencing was contracted to Source BioScience UK Ltd. and performed at the Biochemistry Department, University of Oxford. Resulting chromatogram files (*.abi) were imported into Geneious and regions with more than 5% chance of error calls trimmed at both, the 5' and 3' ends. Remaining sequencing data were aligned in a pairwise fashion with the NCBI GenBank reference DNA sequence of *Rpgr* (Reference: GRCm38.p1 C57BL/6J; NC_000086.7, residues 10158216 to 10216795.) using following default settings of the Geneious alignment algorithm: Cost Matrix 65% similarity (5.0/-4.0); gap open penalty = 12; gap extension penalty = 3. Animals with pathogenic 32bp insertion were

identified as having a fourth repeat of 5'-AGGAAGAAGGGGAGGGAGAGGA AGAGGGGGAG-3' without the four nucleotide (5'-GGAG-3') sequence linking the three previous repeats in the reference sequence.

2.4 Surgery

In order to transduce photoreceptor cells efficiently, the optimal route of application is by subretinal injection. Due to the particular anatomy of the mouse eye with a disproportionately large lens and very narrow pars plana, an *ab externo* approach was chosen as described in more detail below.

2.4.1 Anaesthesia

Mice were weighed and a mix of the NMDA receptor antagonist ketamine (80 mg/kg) and the α_2 adrenergic receptor agonist xylazine (10 mg/kg) was administered by intraperitoneal injection using a 1 ml insulin syringe with 29G needle (Myjector, Terumo N.V., Leuven, Belgium) at 0.1 ml per 10 grams of body weight. This 'induction-solution' was prepared as follows: Mix 0.8 ml Vetalar™ V (100 mg/ml ketamine; Zoetis UK Ltd, London, UK) and 0.5 ml Rompun® (20 mg/ml xylazine; KVP Pharma + Veterinärprodukte GmbH, Kiel, Germany) in 8.7 ml sterile H_2O. The anaesthesia usually took effect within 5 and then lasted for ca. 45 minutes.

In case of ocular surgery, the procedure typically lasted only 5-10 minute and a 'reversal-solution' with the α_2 adrenergic receptor atipamezole (2 mg/kg) was given upon completion of surgery and postsurgical care (see below) to reverse the effects of xylazine by competitive antagonism. This 'reversal-solution' prepared and applied as follows: Mix 0.4 ml Antisedan® (5 mg/ml atipamezole; Elanco Animal Health,

Basingstoke, UK) with 9.6 ml sterile H_2O. This solution was given at 0.1 ml per 10 grams of body weight and reversed the effects of xylazine but had no influence on the effects of ketamine (which is short-lived in itself).

2.4.2 Paracentesis of the anterior chamber

Mouse pupils were dilated with Mydriaticum (1% tropicamide) and phenylephrine (2.5% phenylephrine hydrochloride) and anaesthetised with MINIMS® (0.4% oxybuprocaine hydrochloride) eye drops (all from Bausch & Lomb, Kingston-on-Thames, UK). The fully anaesthetised and dilated animal was carefully placed on a custom-made foam mat to allow ergonomically optimal access for the surgeon and comfort/protection for the animal.

Using notched forceps the rotational stability of the eye was ensured while a shallow, self-sealing paracentesis was applied using a 33G hypodermic needle (TSK Laboratory, The Hague, Netherlands) just anterior of the limbus in the inferior-nasal quadrant. The escape of anterior chamber fluid during the paracentesis lowered the intraocular pressure (IOP), while the self-sealing nature of the incision ensured stable IOP development post surgery.

2.4.3 Subretinal injection

The eye was covered with Viscotears® Liquid Gel (0.2 mg/g polyacrylic acid; Alcon Laboratories (UK) Ltd., Camberley, UK) and a round cover slip of 6mm diameter (VWR International, East Grinstead, UK) was placed on the eye for direct view of the fundus via a Leica operating microscope (Leica Biosystems, Newcastle Upon Tyne, UK). The NanoFil subretinal injection Kit (WPI, Hitchin, UK) equipped with a 34 gauge bevelled needle with a 25 ° tri-surface bevel optimised for microinjection was used for the injection.

Under direct visual guidance, the needle was advanced *ab externo* to penetrate the sclera, choroid and retinal pigment epithelium (RPE) posterior to the equator. As the tip of the needle became visible through the RPE, the penetration angle (retina : needle) was further reduced to allow placement of the bevel in the subretinal space without penetrating the neuroretina. As soon as the full bevel opening was visible in the subretinal space, the complete volume of ca. 1.5 µl was injected to raise a hemiretinal detachment. The needle was retracted swiftly after ensuring the intraocular pressure was sufficient to allow good intraocular perfusion and would not force subretinal fluid to reflux through the injection canal. The cover slip and Viscotears® Liquid Gel was carefully removed and a drop of antibiotic applied (0.5% w/v chloramphenicol; Mercury Pharmaceuticals Ltd, Croydon, UK).

2.5 Electroretinography

Prior to testing all animals were dark-adapted for >2h. Animal preparation was conducted under dim red illumination and included anaesthesia and pupil dilation as described for surgery above. Body temperature was maintained at 38 °C on a heated platform using a circulating pump-water bath. All recordings were made in a custom, light-tight Faraday cage using an Espion E2 system (Diagnosys LLC, Cambridge, UK).

Electroretinogram (ERG) was recorded from DTL-type silver-coated nylon thread active electrodes modified to include a custom-made contact lens of optically clear Aclar film and placed on the corneal apex with hypromellose eye drops (Hypromellose BPC 1%; Matindale Pharmaceuticals, Romford, UK) pre-applied. This technique was originally described by Sagdullaev *et al.* [134]. Platinum needles were placed subcutaneously over the frontal/nasal bone (in midline between eyes) and at the base of the tail as reference and ground electrodes respectively. Signals were differentially amplified and digitized at a rate of 5 kHz. A notch filter was used to remove 50 Hz line noise and a band-pass filter at 1.25Hz – 1kHz. At each intensity, up to 30 responses were computer averaged. The stepwise protocol was as follows:

Table 2.6 Electroretinography (ERG) protocol.

Step	Trials	inter-sweep delay (s)	sweep length (s)	total step length (s)	inter-step-delay (s)	Description	log
0					**600**	**DA**	
1	16	0	3000	48000	10	Single 0.5Hz 1E-6 cd.s/m^2	-6
2	16	0	3000	48000	30	Single 0.5Hz 1E-5 cd.s/m^2	-5
3	9	1000	3000	35000	30	Single 0.5Hz 0.0001 cd.s/m^2	-4
4	9	1000	3000	35000	60	Single 0.5Hz 0.001 cd.s/m^2	-3
5	9	5000	3000	67000	60	Single 0.5Hz 0.01 cd.s/m^2	-2
6	4	13000	3000	51000	120	Single 0.5Hz 0.1 cd.s/m^2	-1
7	4	29000	3000	99000	120	Single 0.5Hz 1 cd.s/m^2	0
8	4	61000	3000	195000	180	Single 0.5Hz 10 cd.s/m^2	1
9	1	0	3000	3000	60	Single 0.5Hz 25 cd.s/m^2	1.40
10	20	0	500	10000	0	Continuous 0.5Hz 0.01 cd.s/m^2	-2
11	20	0	500	10000	0	Continuous 1Hz 0.01 cd.s/m^2	-2
12	20	0	500	10000	0	Continuous 2Hz 0.01 cd.s/m^2	-2
13	20	0	500	10000	0	Continuous 3Hz 0.01 cd.s/m^2	-2
14	30	0	500	15000	0	Continuous 5Hz 0.01 cd.s/m^2	-2
15	30	0	500	15000	0	Continuous 7Hz 0.01 cd.s/m^2	-2
16	30	0	500	15000	0	Continuous 10Hz 0.01 cd.s/m^2	-2
17	30	0	500	15000	0	Continuous 12Hz 0.01 cd.s/m^2	-2
18	30	0	500	15000	0	Continuous 15Hz 0.01 cd.s/m^2	-2
19	30	0	500	15000	0	Continuous 18Hz 0.01 cd.s/m^2	-2
20	30	0	500	15000	0	Continuous 20Hz 0.01 cd.s/m^2	-2
21	30	0	500	15000	0	Continuous 30Hz 0.01 cd.s/m^2	-2
22	30	0	500	15000	0	Continuous 20Hz 10 cd.s/m^2	1
					600	**LA**	
23	20	0	1000	20000	0	Single 1Hz 0.3 cd.s/m^2	-0.52
24	20	0	1000	20000	0	Single 1Hz 1 cd.s/m^2	0
25	20	0	1000	20000	0	Single 1Hz 3 cd.s/m^2	0.48
26	20	0	1000	20000	0	Single 1Hz 10 cd.s/m^2	1
27	20	0	1000	20000	0	Single 1Hz 25 cd.s/m^2	1.40
28	30	0	500	15000	0	Continuous 20Hz 10 cd.s/m^2	1
		total (min)			**45.68**		

Table 2.6 Electroretinography protocol for mice. DA = dark adaptation; LA = light adaptation. Animals were dark-adapted prior recordings (600 s) followed by a single flash intensity series and a flicker series with fixed intensity. After a period of light adaptation (600 s), a light-adapted single flash intensity series followed by one additional flicker step was recorded. The protocol took ca. 45 minutes per animal (not including preparation time).

Data were exported as tab delimited text files and imported into Excel version 14.1.0 (Microsoft, Redmond, USA) for Macintosh OSX. Custom macros were written in Visual Basic to automate extraction of a- and b-wave amplitudes for single flash recordings and amplitude of flicker recordings. These data were then imported for statistical analysis into SPSS (Statistical Package for Social Sciences version 21 by IBM [SPSS Inc., Chicago, USA]).

2.6 Scanning laser ophthalmoscopy

For *en face* retinal imaging, we used the Spectralis™ HRA device from Heidelberg Engineering (Heidelberg Engineering, Heidelberg, Germany) featuring two diode lasers with emission spectra centred around λ = 488nm and 785nm. Appropriate barrier filters at 500 and 800nm remove the reflected light with unchanged wavelength while recording emissions between ca. 500-700nm in the autofluorescence (AF) channel or above 800nm in the infrared (IR) channel.

Mice were imaged directly after ERG recordings while still under influence of the anaesthesia. Lubricating eye drops (Hypromellose BPC 0.3%; Matindale Pharmaceuticals, Romford, UK) were applied before fitting a contact lens to improve image quality and prevent corneal desiccation and subsequent cataract formation (PMMA mouse lens, back optic zone radius of 1.7 mm, total diameter of 3.2 mm, centre thickness of 0.4 mm, straight sides; Cantor and Nissel, Brackley, UK).

For image acquisition, the animal was placed on a platform mounted on the chin rest of the imaging device so that its eyes were positioned approximately at the level of the marking for a human patients' eye position. The IR mode was used for camera alignment relative to the mouse eye. The first image was recorded after even illumination was achieved and focus set on the nerve fibre layer.

Images were recorded using the automatic real-time (ART) mode, which is able to track slight movements of the fundus (e.g., caused by respiration) based on fundus landmarks with high contrast and thus build an average of n iterative images. This improved signal to noise ratio (SNR), whereby SNR improved by the square root of n (i.e. SNR is tripled with ART set to average n = 9 images). Single-averaged

images were recorded with an intensity resolution of 8 bits/pixel, a 1536 x 1536 pixel spatial resolution, and a frame rate of 4.8 frames/s. The detector sensitivity setting of the Spectralis HRA was set to 50 for IR recordings, but 107 (maximum) for AF recordings as AF levels in mice are low [135].

Images were exported from the Heidelberg Eye Explorer as uncompressed TIF files and processed using ImageJ 1.48v (Wayne Rasband, National Institutes of Health, Bethesda, USA).

For quantitative analysis of hyperfluorescent dots, AF images were converted to 8-bit grey scale and dissected along the horizontal midline into a cropped superior and inferior hemi-retina. Auto-thresholding was applied using the triangle strategy with the option to ignore white, ignore black and ignore white objects on black background. This resulted in a high contrast image with high detection threshold for autofluorescent dots.

2.7 Transgene detection

All antibody based detection methods made use of following primary and secondary antibodies at given dilutions unless otherwise stated. Antibodies were stored as aliquots according to the manufacturers' instructions to avoid freeze-thaw cycles.

Table 2.7 Overview of primary antibodies used in this work.

Antibody	Origin	source / target / clonality	Epitope	Stock [mg/ml]	Dilution used	Technique
C-RPGR^512-531	Aldevron, Freiburg, Germany	rabbit / human / polyclonal	EKSLKLSPVQKQKKQQTIG E	1.28	1:500	WB, ICC, IHC
N-RPGR^19-35/113-129	Aldevron	rabbit / human / polyclonal	KSKFAENNPGKFWFKND / GNNEGQLGLGDTEERNT	1.9	1:500	WB, ICC
Anti-RPGR (N term) antibody	Sigma-Aldrich	rabbit / human / polyclonal	EINDTCLSVATFLPYSSLTS GNVLQRTLSARMRRRERE RSPDSFSMRRTLPPIEGTL GLSACFLPNSVFPRCSERN LQESVLSEQDLMQPEEPD YLLDEMTKEAEIDNSSTVE SLGETTDILNMTHIMSLN	0.2	1:500 (WB), 1:200 (IHC)	WB, ICC, IHC
Anti-RPGR (C term) antibody	Sigma-Aldrich	rabbit / human / polyclonal	C-terminus	0.25	1:500	WB, ICC
Rpgr Antibody (M-20)	Santa Cruz, Heidelberg, Germany	goat / mouse / polyclonal	mouse Rpgr (near C-terminus)	0.2	1:200	IHC
Rpgrip1 Antibody (E14)	Santa Cruz	goat / mouse / polyclonal	mouse Rpgrip1	0.2	1:200	IHC
Anti-GAPDH	OriGene, Cambridge, UK	mouse / human, mouse, rat, dog, monkey / monoclonal	full length human recombinant protein of human GAPDH (NP_002037)	1	1:2,000	WB
Anti-beta actin	Gibco, Life Technologies	mouse / human, mouse / monoclonal	A slightly modified synthetic beta-cytoplasmic actin N-terminal peptide conjugated to KLH		1:1000	WB, ICC

Table 2.7 Overview of primary antibodies used in this work. WB = western blot; ICC = immunocytochemistry; IHC = immunohistochemistry.

Table 2.8 Overview of secondary antibodies used in this work.

IRDye® 680RD	Li-Cor Biotechnologies, Cambridge, UK	donkey / mouse / polyclonal	mouse IgG (H&L)	1	1:10,000	WB, fluorescent
IRDye® 800CW	Li-Cor	donkey / mouse / polyclonal	mouse IgG (H&L)	1	1:10,000	WB, fluorescent
IRDye® 800CW	Li-Cor	donkey / rabbit / polyclonal	rabbit IgG (H&L)	1	1:10,000	WB, fluorescent
IRDye® 680RD	Li-Cor	donkey / goat / polyclonal	goat IgG ((H&L)	1	1:10,000	WB, fluorescent
Donkey Anti-Rabbit HRP	Abcam, Cambridge, UK	donkey / rabbit / polyclonal	rabbit IgG (H&L)	0.5	1:10,000	WB
Donkey Anti-Mouse HRP	Abcam	donkey / mouse / polyclonal	mouse IgG (H&L)	0.5	1:10,000	WB

Table 2.8 Overview of secondary antibodies used in this work. WB = western blot; IgG = immunglobulin G; H&L = heavy and light chains are conjugated.

2.7.1 Immunocytochemistry and flow cytometry

HEK293T cells were used for expression of transgene ($RPGR^{ORF15}$) by transfection with respective expression-plasmids. Indirect labelling of the $RPGR^{ORF15}$ required two incubation steps, firstly with a primary antibody directed against $RPGR^{ORF15}$ then with a compatible secondary antibody with conjugated fluorescent dye (see **tables 2.6 and 2.7**) at the following concentrations:

Table 2.9 Overview of antibodies and concentrations used for immunocytochemistry and flow cytometry.

1° antibody target	species / kind	1° antibody concentration	2° antibody / concentration
RPGR (N-terminal)	rabbit polyclonal	1:500 in PBS-T w/t 1% BSA	donkey anti-rabbit 1:5,000
beta actin	rabbit polyclonal	1:500 in PBS-T w/t 1% BSA	donkey anti-rabbit 1:5,000
GAPDH	rabbit polyclonal	1:5000 in PBS-T w/t 1% BSA	donkey anti-rabbit 1:5,000

Table 2.9 Primary (1°) or secondary (2°) antibodies were diluted in 0.01M phosphate-buffered saline (PBS) with 0.1% Triton -X and 1% bovine serum albumin (BSA).

Forty-eight hours after transfection, cells were washed before resuspension to approximately 1-5 x 10^6 cells/ml in ice cold 0.01M PBS. After fixation in 1% (v/v) paraformaldehyde (PFA) for 10 minutes at 4 °C, cells were gently pelleted down at 120g for 5 minutes at 4 °C. Aqueous solution was carefully aspirated and cells resuspended in blocking solution (10% (w/v) donkey serum in PBS-T [0.1% Triton-X in 0.01M PBS]). After 30 minutes, cells were spun again as above and supernatant removed. Primary antibody solution was added at the appropriate concentration and sample incubated at room temperature for 2h. After three wash steps (cells pelleted down at 120g for 5 minutes at 4 °C, supernatant removed, cells resuspended in ice cold PBS-T), a fluorochrome-labelled secondary antibody (optionally, Hoechst 33342

dye was added to the secondary antibody solution at 1:5000) was added for 30 minutes in the dark at room temperature, followed by the same washing procedure. Cells were kept on ice until further processing on the same day.

Cell suspension was either added drop-wise on a poly-L-lysine coated glass slide (Gerhard Menzel GmbH, Braunschweig, Germany) and mounted in ProLong® Gold (Life Technologies) for fluorescence microscopy. Alternatively, cells were subjected to flow cytometry using a CyAn Advanced Digital Processing (ADP) LX High-Performance Research Flow Cytometer (DakoCytomation, Beckman Coulter Ltd, High Wycombe, UK) at the Flowcytometry Facility of the University of Oxford (The Jenner Institute, Nuffield Department of Medicine). This 9-colour digital flow analyser features three solid-state lasers (488nm, 635nm and 405nm) and analyses up to 500,000 events per second. Gate settings were chosen for a false discovery rate of < 1% for quantitative analysis of positive cells and their median fluorescence intensity.

2.7.2 Liquid chromatography-tandem mass spectrometry

HEK293T cells were used for expression of transgene ($RPGR^{ORF15}$) by transfection with respective expression-plasmids. Forty-eight hours after transfection, cells were washed and brought into suspension with 0.01M PBS before spinning at 120g and 4 °C for 10 min. Centrifugation was repeated after resuspending pellet in 500 µl of 0.01M PBS. Supernatant was discarded and cell pellets subjected to a single

freeze-thaw cycle before adding 200 µl ice-cold Radio-Immunoprecipitation Assay (RIPA) buffer with one dissolved cOmplete mini EDTA-free protease inhibitor cocktail tablet (Roche Products Ltd., Welwyn Garden City, UK) per 10 ml of RIPA buffer. Cell pellets were mechanically disrupted with polypropylene pellet pestles on a motor-driven grinder (Sigma-Aldrich) and cell fragments spun down at 13,800 x g and 4 °C for 30 min. Supernatant was quantified using the Pierce™ bicinchoninic acid (BCA) Protein Assay Kit (Thermo Scientific) according to the manufacturers' instructions. The microplate procedure was used for colorimetric quantitation of total protein: First, the working reagent and nine bovine serum albumin standards were prepared with final concentrations ranging from 25 to 2000 µg/ml. After 25 µl of each standard or unknown sample replicate was pipetted into a white 96 microplate well, 200 µl of the working reagent was added and the plate mixed on a shaker for 30 seconds before incubating at 37 ° for 30 minutes. After the plate cooled to room temperature, the absorbance at 562nm was assessed on a Biochrom EZ Read 400 plate reader.

Samples were diluted to 1 µg/µl total protein concentration and denatured in Laemmli buffer (Sigma-Aldrich) for 20min at RT. Ten µg total protein was loaded per well using 7.5% sodium dodecyl sulfate polyacrylamide gels (Criterion™ TGX™ Precast Gels, Bio-Rad Laboratories Ltd., Hemel Hempstead, UK) for electrophoresis at 100V for 2h (SDS-PAGE). EZBlue™ Gel Staining Reagent (SIGMA) was used to stain proteins according to the manufacturers' instructions: The SDS-PAGE Gel was rinsed three times for 5 minutes each in an excess of water to remove SDS before incubating the Gel in the EZBlue Gel Staining Reagent for 2h at room temperature on a shaker. The gel was then washed in excess water for 2h before an image was taken

and the appropriate bands excised with a disposable scalpel. Bands were transferred to 1.5 ml Eppendorf tubes and stored at 4 °C until further processing at the Proteomics Centre of the University of Oxford (Dunn School of Pathology). Samples were digested using trypsin, lysine C, lysine N, pepsin, formic acid, elastase and/or V8 protease followed by liquid chromatography-tandem mass spectrometry (LC-MS/MS). Peptide fragments were recorded along with their sequence identity and matched to the human proteome.

2.7.3 Western blot

Protein samples were prepared and separated using SDS-PAGE as described above in case of *in vitro* plasmid transfection experiments. In case of *in vivo* experiments, mouse eyes were removed from the eye socket after cervical dislocation and quickly dissected in ice cold 0.01M PBS using a dissection microscope. Whole retina was immediately transferred to 200 µl RIPA lysis buffer with protease inhibitors before subjecting samples to one freeze-thaw cycle. Thawed samples were subject to homogenisation with polypropylene pellet pestles on a motor-driven grinder (Sigma- Aldrich) and cell fragments spun down at 13,800 x g and 4 °C for 30 min. Protein in the supernatant solution was then quantified using the Pierce™ bicinchoninic acid (BCA) Protein Assay Kit (Thermo Scientific) and processed as other protein samples for SDS-PAGE as described above.

Gels were carefully placed onto polyvinylidene difluoride (PVDF) membranes with 0.2µm pore size (Trans-Blot® Turbo™ Midi PVDF, Bio-Rad) and proteins blotted using the Trans-Blot® Turbo™ Transfer Starter System (Bio-Rad) according to the manufacturers' instructions using the midi setting (7min at 25V). PVDF membranes were then cut into sections depending on size of target protein and loading control to stain independently with respective primary and/or secondary antibodies (see **tables 2.6 and 2.7**).

PVDF membranes were blocked, washed and incubated with antibody solutions in the SNAP i.d.™ protein detection system (Millipore (U.K.) Ltd., Feltham, UK) according to instructions by the manufacturer. Briefly, membranes were placed in wells of appropriate size with the protein-loaded side facing up towards the open chamber of the well. 0.01M PBS with 0.1% Triton-X (PBS-T) was combined with 1% bovine serum albumin (BSA). To block unspecific binding, 10 ml PBS-T with 1% BSA was added to each well and vacuum applied to draw solution through PVDF membrane. Primary antibody solution (3 ml) was applied to the well and left to incubate for 10min at RT before applying vacuum followed by washing 3x with ca. 30 ml PBS-T. Incubation with horseradish peroxidase (HRP) linked secondary antibody followed the same steps as with the primary antibody solution. After the final washing step, membranes were removed from wells and incubated with Luminata forte ELISA HRP substrate (Millipore) to allow activation of chemiluminescence. Membrane sections were carefully re-assembled in a BAS cassette 2040 (FUJIFILM UK Ltd., Bedford, UK) for exposure on CL-Xposure™ film (Thermo Scientific) in a dark chamber. Films were developed in a Compact X4 Automatic X-ray Film Processor (Xograph Healthcare, Gloucestershire, UK) and resulting films scanned using an

Epson Perfection V30 flatbed scanner (Epson (UK) Ltd., Hertfordshire, UK) in an uncompressed tagged image file format (TIFF) with 16bit colour depth and 1200dpi resolution.

2.7.4 Immunohistochemistry

For immunohistochemistry of treated or untreated mouse eyes, only unfixed tissue was used in order to detect ciliary proteins, such as $RPGR^{ORF15}$, as antigen detection at the connecting cilium is hampered by the cross-linking activity of fixatives such as PFA. Eyes were harvested as described above, quickly embedded in Tissue-Tek® O.C.T. compound (Sakura Finetek USA Inc., USA) without fixation and/or dehydration and frozen in dry-ice cooled isopentane. Samples were stored at -80 °C until cryosections were prepared at 16µm thickness and collected on a poly-L-lysine coated glass slide (Gerhard Menzel GmbH). Sections were kept within the cryostat at -12 °C until all relevant sections had been prepared. Only then, they were briefly allowed to settle to room temperature to allow the OCT to melt on the glass slide, which prevented mobilisation of the sections during the following steps. Following a brief wash with 0.01M PBS (1 minute), sections were blocked with 10% donkey serum in PBS containing 2% bovine serum albumin for 10 minutes and then incubated with primary antibody diluted in 2% bovine serum albumin for 45 minutes. Sections were washed briefly (1 minute) in PBS before incubating with fluorochrome-conjugated secondary antibodies and Hoechst 33342 dye at 1:5000 for 30 minutes.

Sections were washed again (1 minute) and mounted in ProLong® Gold (Life Technologies) for fluorescence microscopy only minutes to hours later.

Retinal sections were viewed on a confocal microscope (Zeiss LSM710). Flourophore-labelled epitopes were located using epifluorescence illumination before taking a series of XY optical sections. The fluorescence of Hoechst, GFP/Alexa-488, Alexa-555, Alexa-568, and Alexa-635 was sequentially excited using 350-nm UV, 488-nm argon, and the 543-nm HeNe lasers, as appropriate. Stacks were built to give XY projection images where appropriate, and images were processed using Image J.

2.8 Statistical analysis

Data were collated in spread sheets using Excel version 14.1.0 (Microsoft, Redmond, Washington, USA) and analysed using Statistical Package for Social Sciences (SPSS) version 21 by IBM (SPSS Inc., Chicago, IL, USA), both for Macintosh OSX. Statistical significance was defined as $\alpha = 0.05$ for all tests. One asterisk indicates a significance level of < 0.05, while two indicate $\alpha < 0.005$ and three asterisks symbolise $\alpha < 0.0005$ in all figures.

Data were tested for normality of distribution using the Shapiro Wilk test. If the null hypothesis of normality was retained, analysis of variance (ANOVA) or a Student t test was used to test for a significant difference where appropriate. Nonparametric tests such as the Kruskal-Wallis or Mann-Whitney U test were otherwise applied as appropriate.

CHAPTER 3 CODON OPTIMISATION OF RPGR

3.1 Introduction

The coding sequence (cds) of a gene serves as template for translation of nucleic acid sequence into peptides. It involves the cds contained in the mRNA transcript, ribosomal complexes and amino acids, which are bound to tRNA molecules. Three consecutive nucleotides in the cds (e. g. UUA) constitute a codon. tRNA molecules have complementary anti-codon sequences (e.g. AAU), briefly bind to the codon sequence within the ribosomal complex and contribute a single amino acid (e.g. Leucine) they are carrying to the growing chain of amino acids forming the growing peptide encoded by the cds.

With four nucleotides available to encode each of the three positions in a codon, $4^3 = 64$ codons can be formed. Because three combinations encode stop signals (UAA, UAG, UGA) 61 possible combinations are available for 20 amino acids. This redundancy results in multiple codons translating into the same amino acid: Leucine, for example, is added at codon sequences UUA, UUG, CUU, CUC, CUA or CUG.

In the early 1970s, Walter Fiers and colleagues discovered a strikingly non-random pattern of codon usage in a bacteriophage genome and first hypothesised that non-random codon and tRNA frequency might be involved in regulating rates of gene expression [136]. Indeed, highly expressed genes preferentially use so-called major codons, i.e. codons with the highest abundance of matching tRNA molecules to make translation more efficient, a concept called ‘codon bias’. In case of Leucine for example, all six codon sequences (see above) would lead to the correct amino acid being inserted. But if the most abundant tRNA molecule would carry the anti-codon for UUA, this codon would result in more efficient translation than any of the other

nucleotide combinations. This observation was utilized to generate codon adaptation indices (CAI), which aim to reflect the use of high abundance codons in the investigated sequence [137].

Codon frequency varies across species and the strategy of codon optimisation for the intended host organism was adopted to improve expression in heterologous expression systems, for example expressing human insulin like growth factor (IGF) in chloroplasts as potential bioreactors for recombinant protein production [138]. By optimising the cds for the codon frequency in chloroplasts, human IGF was produced much more effectively. Importantly, codon optimisation was also shown to lead to increased expression when applying this concept to mammalian genes in mammalian cells [139].

In the context of gene therapy with rAAV as vector system with its limited packaging capacity, codon optimisation offers the potential to increase transgene expression without additional regulatory elements such as WPRE *in cis*. Moreover, changing the nucleotide sequence without altering the translated amino acid sequence (silent substitutions) of the transgene e. g. allows to change CG content, remove unwanted repeat sequences and/or restriction sites that may interfere with cloning.

However, the most important advantage of optimising codons in difficult sequences such as $RPGR^{ORF15}$ lies in the potential to improve sequence fidelity. Changing nucleotides without changing the resulting amino acid sequence carries the potential to make the sequence more stable and less prone to spontaneous mutations during the production of vectors for gene therapy.

3.2 Aims

The full-length human $RPGR^{ORF15}$ cds encodes an 1152 amino acid protein with a highly repetitive, purine rich mutational hotspot as C-terminal exon. Cloning this isoform without random mutations being introduced is difficult – as is direct sequencing of the adenine/guanine rich regions since polymerases have a tendency to stop at guanine repeats.

The overall aim was therefore to optimise the codon usage of $RPGR^{ORF15}$ cds in order to increase sequence fidelity during the cloning process and provide a construct with the potential to sidestep previous problems in clinical vector design. Additionally, increasing the CAI of $RPGR^{ORF15}$ cds through introducing synonymous major codons where possible might lead to higher transgene expression without the use of accessory regulatory elements in the transgene cassette. This is important as the cds of $RPGR^{ORF15}$ even without promoter or polyadenylation site already fills more then three quarters of the available space between the inverted terminal repeats of the gutted rAAV genome.

3.3 Materials and methods

Geneious software was used to search the consensus coding sequence (CCDS) database of the National Center for Biotechnology Information (NCBI) for the reference human RPGR^{ORF15} nucleotide sequence. The complete cds was subjected to the OptimumGene™ algorithm (GenScript, Piscataway, USA) to optimize a variety of parameters that are critical to the efficiency of gene expression, including codon usage bias, GC content, CpG dinucleotides content, mRNA secondary structure, cryptic splicing sites, premature poly-A sites, internal chi sites and ribosomal binding sites, negative CpG islands, RNA instability motif (ARE), repeat sequences (direct repeat, reverse repeat, and Dyad repeat) and restriction sites that may interfere with cloning. The codon frequency table that was used is displayed in **Fig. 3.1**. The codon optimised human coding sequence (cds) of the retina-specific isoform *RPGR^{ORF15}* was

TTT 16.9(336562)	TCT 14.6(291040)	TAT 12.0(239268)	TGT 9.9(197293)
TTC 20.4(406571)	TCC 17.4(346943)	TAC 15.6(310695)	TGC 12.2(243685)
TTA 7.2(143715)	TCA 11.7(233110)	TAA 0.7(14322)	TGA 1.3(25383)
TTG 12.6(249879)	TCG 4.5(89429)	TAG 0.5(10915)	TGG 12.8(255512)
CTT 12.8(253795)	CCT 17.3(343793)	CAT 10.4(207826)	CGT 4.7(93458)
CTC 19.4(386182)	CCC 20.0(397790)	CAC 14.9(297048)	CGC 10.9(217130)
CTA 6.9(138154)	CCA 16.7(331944)	CAA 11.8(234785)	CGA 6.3(126113)
CTG 40.3(800774)	CCG 7.0(139414)	CAG 34.6(688316)	CGG 11.9(235938)
ATT 15.7(313225)	ACT 12.8(255582)	AAT 16.7(331714)	AGT 11.9(237404)
ATC 21.4(426570)	ACC 19.2(382050)	AAC 19.5(387148)	AGC 19.4(385113)
ATA 7.1(140652)	ACA 14.8(294223)	AAA 24.0(476554)	AGA 11.5(228151)
ATG 22.3(443795)	ACG 6.2(123533)	AAG 32.9(654280)	AGG 11.4(227281)
GTT 10.9(216818)	GCT 18.6(370873)	GAT 22.3(443369)	GGT 10.8(215544)
GTC 14.6(290874)	GCC 28.5(567930)	GAC 26.0(517579)	GGC 22.8(453917)
GTA 7.0(139156)	GCA 16.0(317338)	GAA 29.0(577846)	GGA 16.3(325243)
GTG 28.9(575438)	GCG 7.6(150708)	GAG 40.8(810842)	GGG 16.4(326879)

Fig. 3.1 Codon frequency table for *Homo sapiens* used for codon optimisation of *RPGR^{ORF15}*. Each codon is indicated by the three nucleotide sequence (e.g. TTT), followed by its frequency per 1000 (e.g. 16.9) and the total number (e.g. 336562). The human codon usage table had been calculated from a set of 19250 human genes from the Ensembl database (Release 57) with UniProtKB/SwissProt ID and is available in the public domain : http://genomes.urv.cat/CAIcal/CU_human_nature.html.

synthesised by GenScript. The wild type sequence of *RPGR*^{ORF15} was synthesised by OriGene and provided in the pCMV6-XL vector backbone and by GenScript in a pUC57 vector backbone for cloning.

Sequences were confirmed by Sanger sequencing by Source BioScience services at the Department of Biochemistry, University of Oxford. For this, multiple samples were prepared at 100ng/µl plasmid DNA and appropriate sequencing primers were added at 3.2pmol/µl to initiate reads at various locations along the predicted sequence (**Fig. 3.2**).

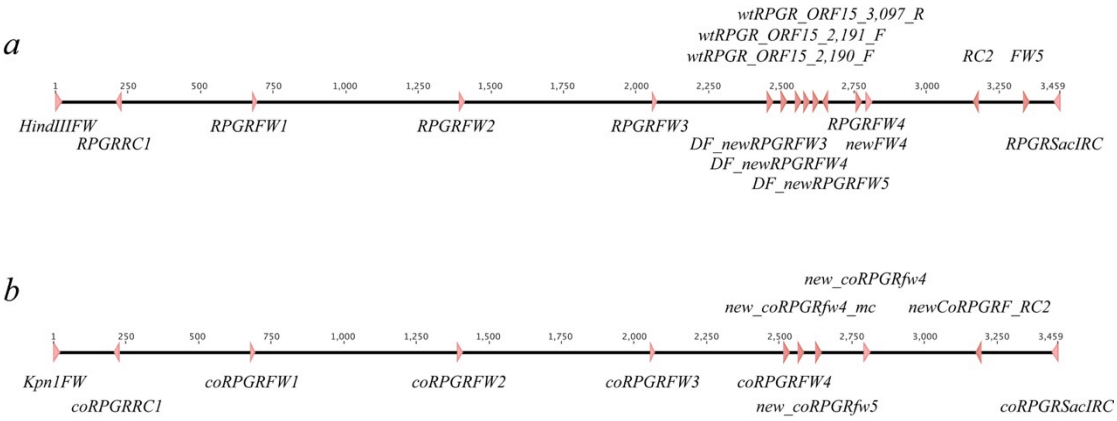

Fig. 3.2 Overview of sequencing primer alignment along (a) *wtRPGR*^{ORF15} and (b) *coRPGR*^{ORF15} coding sequences. Note that more primers needed to be designed and applied within the ORF15 region of the *wtRPGR*^{ORF15} cds in order to achieve full coverage of the sequence. This is due to difficulties in primer annealing and due to frequent premature terminations of sequencing reactions because of poly-G runs in the ORF15 region of *wtRPGR*^{ORF15}.

For the first 13 exons, primers were designed to anneal every ca. 300 bp to allow overlap between readouts and trimming of start and end sequences with poor signal-to-noise ratio. For the purine rich ORF15 region, a multitude of primers were designed for both forward and reverse strand sequencing (**Table 3.1** and **3.2**) as sequence reactions produced much shorter readouts and sometimes failed to produce results altogether.

Table 3.1 Overview of primers used to clone and sequence wtRPGR^{ORF15}.

Primers for wtRPGR^{ORF15} [5' to 3']	
RPGRHindIIIFW	ATGAGGGAGCCGGAAGAGCTGA
wtRPGR_ORF15_3,097_R	CCCCCTCTCCTTCCTCCC
wtRPGR_ORF15_2,191_F	GGGGAGGAGGAGCATGGA
wtRPGR_ORF15_2,190_F	AGGGGAGGAGGAGCATGG
RPGRRC1	TGATCCTAATCCTAACTG
RPGRFW4	GAGGAAGGAGAAGGGGAAGGGGAGGAT
RPGRFW3	TAGCAGAGAAGGAAGAAT
RPGRFW2	GACCTCATGCAGCCAGAG
RPGRFW1	ATCAGCTCCTGGGCAATCACA
RC2	TGGCATTTTGGACCTCTGCT
newFW4	AAGCAGAGGTGAGTGAAGGC
FW5	AGCAGAGGTCCAAAATGCCA
DF_newRPGRFW5	AGTGGAAGGGGAGGTGGAAG
DF_newRPGRFW4	TAGAGGGAGGGGAAGTAGAG
DF_newRPGRFW3	TATCAGATGACCTTACAGAC
RPGRSacIRC	TTACTTCAATTCCAAGTAATGTGGT

Table 3.1 Overview of primers used to clone and sequence wtRPGR^{ORF15}.

Table 3.2 Overview of primers used to clone and sequence coRPGR^{ORF15}.

Primers for coRPGR^{ORF15} [5' to 3']	
coRPGRKpnIFW	ATGAGAGAGCCAGAGGAGCTGA
newCoRPGR_RC2	CTCTTCCCTATTTCTCCGGTT
new_coRPGRfw5	AACCGGAGAAATAGGGAAGAG
new_coRPGRfw4	AAGGAGGAAGGAGAACGGAAG
new_coRPGRfw4_mc	CGAGGAAGTGGAAGGCGAGAG
coRPGRRC1	ATCCAAATCTGCTATCTC
coRPGRFW4	AGGCGAGGAAGAGGAAGGCGA
coRPGRFW3	GATGGAACGACCTGGAGAG
coRPGRFW2	ATCTGATGCAGCCAGAGGA
coRPGRFW1	CAGCTGCTGGGCAATCAC
coRPGRSacIRC	TTATTTCAGTTCCAGATAGTG

Table 3.2 Overview of primers used to clone and sequence coRPGR^{ORF15}.

Once the sequences were verified with at least two times coverage, they were PCR amplified with primers designed to add the appropriate restriction sites on both ends of the *RPGR^{ORF15}* coding sequence for subcloning into an rAAV production plasmid vector (pAAV2 from Vector BioLabs, see **Fig. 3.3**). These primers also

introduced a Kozak consensus sequence (5'-GCCACC-3') immediately upstream of the start codon to improve efficiency of ribosomal binding and initiation of translation in eukaryotes as shown in **Table 3.3** and **3.4**.

Table 3.3 Primers used to introduce Kozak consensus sequence in wtRPGR^{ORF15}.

Primers for wtRPGR^{ORF15}	
RPGR_HindIII_FW	ATGAGGGAGCCGGAAGAGCTGA
RPGR_SacI_RC	TTACTTCAATTCCAAGTAATGTGGT

Table 3.3 Primers used to introduce Kozak consensus sequence in wtRPGR^{ORF15}.

Table 3.4 Primers used to introduce Kozak consensus sequence in coRPGR^{ORF15}.

Primers for coRPGR^{ORF15}	
CORPGR_KpnI_FW	ATGAGAGAGCCAGAGGAGCTGA
CORPGR_SacI_RC	TTATTTCAGTTCCAGATAGTG

Table 3.4 Primers used to introduce Kozak consensus sequence in coRPGR^{ORF15}.

PCR products were tested for appropriate size (i.e. to exclude larger deletions) using 1% agarose gel electrophoresis. Appropriate bands were documented, excised for gel extraction and eluted DNA preparations digested using sequence specific restriction enzymes (*HindIII* and *SacI* for wtRPGR^{ORF15}; *KpnI* and *SacI* for coRPGR^{ORF15}; all New England Biolabs). Digestion reactions were again purified by agarose gel electrophoresis, appropriate bands were documented and excised for subcloning the construct into the multiple cloning site of an appropriately pre-digested pAAV2 vector backbone (**Fig. 3.3**).

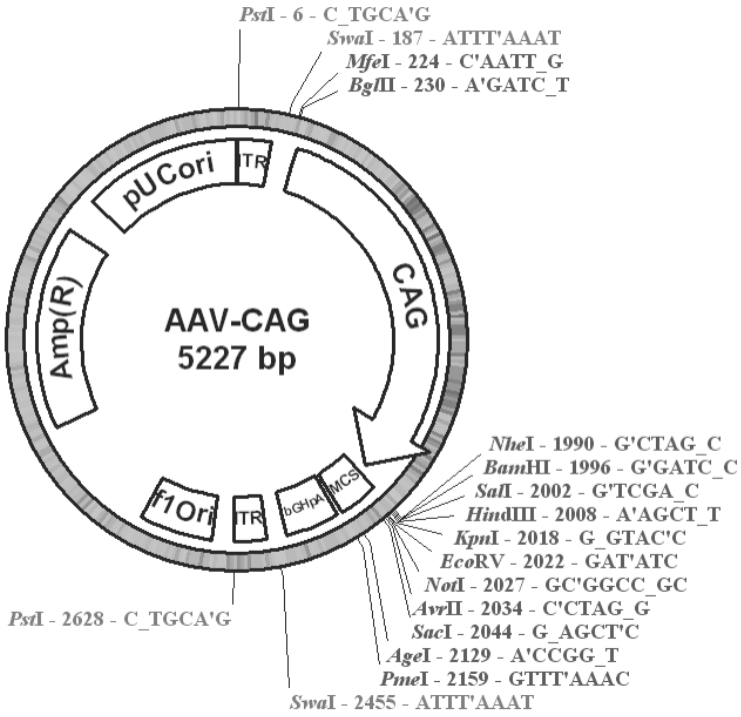

Fig. 3.3 Map of the commercial vector backbone pAAV2 from Vector BioLabs. Both coding sequences *wtRPGR*^{ORF15} and *coRPGR*^{ORF15} were subcloned using this vector by inserting them in the multiple cloning site (MCS).

This plasmid features an AAV2 internal terminal repeat (ITR) sequence followed by the ubiquitous cytomegalovirus early enhancer and chicken beta-actin hybrid promoter (CAG), which is known to drive high expression levels in a number of cell classes in the retina including photoreceptor cells [140]. The promoter sequence is followed by a multiple cloning site (MCS), a downstream polyadenylation (pA) signal from the bovine growth hormone (bGH) and a second AAV2 ITR sequence. The backbone contains an f1 origin of replication (ORI) that allows for the packaging of ssDNA into phage particles (position 4576-4882). Furthermore, the backbone features an ampicillin resistance gene (5401-6258) of 858bp, which is driven by an upstream 29 bp promoter sequence (5331-5359). A pUC57 ORI (6409-

7076) just 5 bp upstream of the initial ITR sequence allows for replication in bacterial hosts. The following plasmids were therefore engineered:

I. ITR.CAG.Kozak.wtRPGR^{ORF15}.bGHpA.ITR (referred to as CAG.wtRPGR)

II. ITR.CAG.Kozak.coRPGR^{ORF15}.bGHpA.ITR (referred to as CAG.coRPGR)

XL10-Gold ultracompetent bacteria (Stratagene, Agilent Technologies) were transformed with the above plasmids as detailed in section 2.1.3. For minipreparations, single colonies were picked and processed as detailed in section 2.1.1. Resulting plasmid DNA preparations were digested in 5 µl aliquots with the appropriate restriction enzymes (*HindIII* and *SacI* for CAG.wtRPGR and *Kpn1* and *SacI* for CAG.coRPGR) and subjected to electrophoresis on 1% agarose gels to confirm presence of the transgene cassette and test for variations in fragment length (i.e. deletions). Promising candidates were then sequenced again to confirm integrity of the construct with at least two times coverage.

Once sequence was confirmed, another round of propagation in XL10-Gold ultracompetent bacteria was performed to allow a larger preparation (mega-preparation) of plasmid DNA using the Qiagen® EndoFree® Mega Kit according to the instructions provided by the manufacturer and detailed in section 2.1.1. These mega-preparations were then sequenced again to confirm integrity of the construct with at least two times coverage before testing for transgene expression levels (this chapter) or other downstream applications such as production of rAAV (next chapter).

3.4 Results

The result of the database query for human RPGR^{ORF15} was a 3459bp long coding sequence (CCDS 35229.1) known as X-linked retinitis pigmentosa GTPase regulator isoform C, transcribed and spliced from gene ID 6103 on the minus strand of the X chromosome at Xp21.1.

The sequence featured a well-balanced GC content of 47.2% and a Tm at 84.1 °C, but an overabundance (72%) of purines vs. pyrimidines with 36% adenine and 35.5% guanine. This imbalance was even most pronounced regionally within the coding sequence. In one particular 959 base pair fragment (**Fig. 3.4**) of the central ORF15 region 93% of nucleotides were purines (56% guanine > 37% adenine >> 6% cytosine > 1% thymidine).

Fig. 3.4 Example of highly repetitive and purine (adenine/guanine) rich sequence within ORF15 of *wtRPGR*^{ORF15}. This 959bp fragment holds 93% purines and only 6% cytosine and 1% thymidine nucleotides. It illustrates the repetitive nature of the ORF15 sequence, which is known as mutational hotspot. G = guanine (yellow); A = adenine (red); C = cytosine (blue); T = thymidine (green).

This limited variability leads to high rate of repetitions of 15-33bp long nucleotide sequences in the region between 2,458 and 2,799 of the cds and multiple poly-guanine runs (5'-GGGGAGGGG-3'), which are notoriously difficult to sequence as the long run of Gs inhibits the ability of the polymerase to unwind the template.

Another consequence of the repetitive, purine rich nucleotide sequence is a skewing of the amino acid frequency towards glutamic acid (26.6%) and glycine (15.4%) with all 17 other amino acids (not counting methionine) featuring in only 0.7 – 6.6% of the cases.

These particular characteristics of the wildtype human RPGR^{ORF15} coding sequence almost certainly contribute to the genetic instability of the gene thereby leading to the high prevalence of mutations found in patient populations.

3.4.1 An optimised coding sequence for RPGR

Analysis of the codon adaptation index of wtRPGR^{ORF15} showed a moderate CAI of 0.73 with 10% use of minor codons (low abundance codons) but only 32% use of major codons, i.e. codons with the highest usage frequency for a given amino acid in *Homo sapiens*. This frequency of optimal codons (FOP) was changed in favour of higher codon quality groups during codon optimisation: only 1% minor codons were left unchanged and the frequency of major codons was increased to 56%. This improved the CAI to 0.87 for codon optimised RPGR^{ORF15} (coRPGR^{ORF15}).

In addition to increasing the CAI, codon optimisation also removed a *MfeI* restriction site and several *cis*-acting elements such as a potential splice site (GGTGAT), four polyadenylation signals (three AATAAA and one ATTAAA), two polyT (TTTTTT) and one polyA (AAAAAAA) sites. GC content and unfavourable peaks were optimised to prolong the half-life of the mRNA. Secondary structure

formations (stem-loops), which would reduce the chance of ribosomal binding and render mRNA less stable, were disabled. The pairwise % identity between wtRPGR^{ORF15} and coRPGR^{ORF15} was 77.2% with most changes occurring in the ORF15 region (**Fig. 3.5**, next page).

Fig. 3.5 (next page) Codon optimisation of *RPGR^{ORF15}* leads to significant changes in the primary coding sequence. a) shows the GC frequency (%) along the full coding sequence of *RPGR^{ORF15}* with wild type *RPGR^{ORF15}* indicated on the top (black) and codon optimised *RPGR^{ORF15}* (*coRPGR^{ORF15}*) at the bottom (red) with grey breaks indicating the changes from the wild type sequence. b) The full sequence is displayed with *coRPGR^{ORF15}* on top indicating and the silent substitutions indicated in red. The wild type *RPGR^{ORF15}* sequence is displayed as reference below.

a

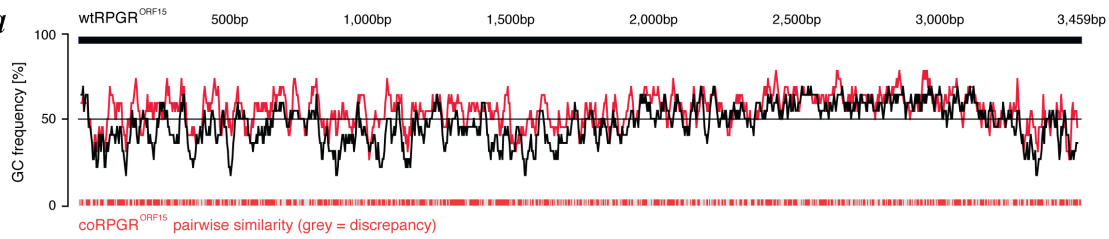

b

```
Optimized    1 ATGAGAGAGCCAGAGGAGCTGATGCCAGACAGTGGAGCAGTGTTTACATTCGGAAAATCT
Original     1 ATGAGGGAGCCGGAAGAGCTGATGCCCGATTCGGGTGCTGTGTTTACATTTGGGAAAAGT

Optimized   61 AAGTTCGCTGAAAATAACCCAGGAAAGTTCTGGTTTAAAAACGACGTGCCCGTCCACCTG
Original    61 AAATTTGCTGAAAATAATCCCGGTAAATTCTGGTTTAAAAATGATGTCCCTGTACATCTT

Optimized  121 TCTTGTGGCGATGAGCATAGTGCCGTGGTCACTGGGAACAATAAGCTGTACATGTTCGGG
Original   121 TCATGTGGAGATGAACATTCTGCTGTTGTTACCGGAAATAATAAACTTTACATGTTTGGC

Optimized  181 TCCAACAACTGGGGACAGCTGGGGCTGGGATCCAAATCTGCTATCTCTAAGCCAACCTGC
Original   181 AGTAACAACTGGGGTCAGTTAGGATTAGGATCAAAGTCAGCCATCAGCAAGCCAACATGT

Optimized  241 GTGAAGGCACTGAAACCCGAGAAGGTCAAACTGGCCGCTTGTGGCAGAAACCACACTCTG
Original   241 GTCAAAGCTCTAAAACCTGAAAAAGTGAAATTAGCTGCCTGTGGAAGGAACCACACCCTG

Optimized  301 GTGAGCACCGAGGGCGGGAATGTCTATGCCACCGGAGGCAACAATGAGGGACAGCTGGGA
Original   301 GTGTCAACAGAAGGAGGCAATGTATATGCAACTGGTGGAAATAATGAAGGACAGTTGGGG

Optimized  361 CTGGGGGACACTGAGGAAAGGAATACCTTTCACGTGATCTCCTTCTTTACATCTGAGCAT
Original   361 CTTGGTGACACCGAAGAAAGAAACACTTTTCATGTAATTAGCTTTTTTACATCCGAGCAT

Optimized  421 AAGATCAAGCAGCTGAGCGCTGGCTCCAACACATCTGCAGCCCTGACTGAGGACGGGCGC
Original   421 AAGATTAAGCAGCTGTCTGCTGGATCTAATACTTCAGCTGCCCTAACTGAGGATGGAAGA

Optimized  481 CTGTTCATGTGGGGAGATAATTCAGAGGGCCAGATTGGGCTGAAAAACGTGAGCAATGTG
Original   481 CTTTTTATGTGGGGTGACAATTCCGAAGGGCAAATTGGTTTAAAAAATGTAAGTAATGTC

Optimized  541 TGCGTCCCTCAGCAGGTGACCATCGGAAAGCCAGTCAGTTGGATTTCATGTGGCTACTAT
Original   541 TGTGTCCCTCAGCAAGTGACCATTGGGAAACCTGTCTCCTGGATCTCTTGTGGATATTAC

Optimized  601 CATAGCGCCTTCGTGACCACAGATGGCGAGCTGTACGTCTTTGGGGAGCCCGAAAACGGA
Original   601 CATTCAGCTTTTGTAACAACAGATGGTGAGCTATATGTGTTTGGAGAACCTGAGAATGGG

Optimized  661 AAACTGGGCCTGCCTAACCAGCTGCTGGGCAATCACCGGACACCCCAGCTGGTGTCCGAG
Original   661 AAGTTAGGTCTTCCCAATCAGCTCCTGGGCAATCACAGAACACCCCAGCTGGTGTCTGAA

Optimized  721 ATCCCTGAAAAAGTGATCCAGGTCGCCTGCGGGGGAGAGCATACAGTGGTCCTGACTGAG
Original   721 ATTCCGGAGAAGGTGATCCAAGTAGCCTGTGGTGGAGAGCATACTGTGGTTCTCACGGAG

Optimized  781 AATGCTGTGTATACCTTCGGACTGGCCAGTTTGGCCAGCTGGGGCTGGGAACCTTCCTG
Original   781 AATGCTGTGTATACCTTTGGGCTGGGACAATTTGGTCAGCTGGGTCTTGGCACTTTTCTT

Optimized  841 TTTGAGACATCCGAACCAAAAGTGATCGAGAACATTCGCGACCAGACTATCAGCTACATT
Original   841 TTTGAAACTTCAGAACCCAAAGTCATTGAGAATATTAGGGATCAAACAATAAGTTATATT

Optimized  901 TCCTGCGGAGAGAATCACACCGCACTGATCACAGACATTGGCCTGATGTATACCTTTGGC
Original   901 TCTTGTGGAGAAAATCACACAGCTTTGATAACAGATATCGGCCTTATGTATACTTTTGGA

Optimized  961 GATGGACGACACGGGAAGCTGGGACTGGGACTGGAGAACTTCACTAATCATTTTATCCCC
Original   961 GATGGTCGCCACGGAAAATTAGGACTTGGACTGGAGAATTTTACCAATCACTTCATTCCT

Optimized 1021 ACCCTGTGTTCTAACTTCCTGCGGTTCATCGTGAAACTGGTCGCTTGCGGCGGGTGTCAC
Original  1021 ACTTTGTGCTCTAATTTTTGAGGTTTATAGTTAAATTGGTTGCTTGTGGTGGATGTCAC

Optimized 1081 ATGGTGGTCTTCGCTGCACCTCATAGGGGCGTGGCTAAGGAGATCGAATTTGACGAGATT
Original  1081 ATGGTAGTTTTTGCTGCTCCTCATCGTGGTGTGGCAAAAGAAATTGAATTCGATGAAATA

Optimized 1141 AACGATACATGCCTGAGCGTGGCAACTTCCTGCCATACAGCTCCCTGACTTCTGGCAAT
Original  1141 AATGATACTTGCTTATCTGTGGCGACTTTTCTGCCGTATAGCAGTTTAACCTCAGGAAAT

Optimized 1201 GTGCTGCAGAGAACCCTGAGTGCAAGGATGCGGAGAAGGGAGAGGGAACGCTCTCCTGAC
Original  1201 GTACTGCAGAGGACTCTATCAGCACGTATGCGGCGAAGAGAGAGGGAGAGGTCTCCAGAT

Optimized 1261 AGTTTCTCAATGCGACGAACCCTGCCACCTATCGAGGGAACACTGGGACTGAGTGCCTGC
Original  1261 TCTTTTTCAATGAGGAGAACACTACCTCCAATAGAAGGGACTCTTGGCCTTTCTGCTTGT

Optimized 1321 TTCCTGCCTAACTCAGTGTTTCCACGATGTTAGCGAGCGGAATCTGCAGGAGTCTGTCCTG
Original  1321 TTTCTCCCCAATTCAGTCTTTCCACGATGTTCTGAGAGAAACCTCCAAGAGAGTGTCTTA

Optimized 1381 AGTGAGCAGGATCTGATGCAGCCAGAGGAACCCGACTACCTGCTGGATGAGATGACCAAG
Original  1381 TCTGAACAGGACCTCATGCAGCCAGAGGAACCAGATTATTTGCTAGATGAAATGACCAAA

Optimized 1441 GAGGCCGAAATCGACAACTCTAGTACAGTGGAGTCCCTGGGCGAGACTACCGATATCCTG
Original  1441 GAAGCAGAGATAGATAATTCTTCAACTGTAGAAAGCCTTGGAGAAACTACTGATATCTTA

Optimized 1501 AATATGACACACATTATGTCACTGAACAGCAATGAGAAGAGTCTGAAACTGTCACCAGTG
Original  1501 AACATGACACACATCATGAGCCTGAATTCCAATGAAAAGTCATTAAAATTATCACCAGTT

Optimized 1561 CAGAAGCAGAAGAAACAGCAGACTATTGGCGAGCTGACTCAGGACACCGCCCTGACAGAG
Original  1561 CAGAAACAAAAGAAACAACAAACAATTGGGGAACTGACGCAGGATACAGCTCTTACTGAA

Optimized 1621 AACGACGATAGCGATGAGTATGAGGAAATGTCCGAGATGAAGGAAGGCAAAGCTTGTAAG
Original  1621 AACGATGATAGTGATGAATATGAAGAAATGTCAGAAATGAAAGAAGGGAAAGCATGTAAA

Optimized 1681 CAGCATGTCAGTCAGGGGATCTTCATGACAGCCAGCCACAACTATTGAGGCTTTTTCA
Original  1681 CAACATGTGTCACAAGGGATTTTCATGACGCAGCCAGCTACGACTATCGAAGCATTTTCA

Optimized 1741 GACGAGGAAGTGGAGATCCCCGAGGAAAAAGAGGGCGCAGAAGATTCCAAGGGGAATGGA
Original  1741 GATGAGGAAGTAGAGATCCCAGAGGAGAAGGAAGGAGCAGAGGATTCAAAAGGAAATGGA

Optimized 1801 ATTGAGGAACAGGAGGTGGAAGCCAACGAGGAAAATGTGAAAGTCCACGGAGGCAGGAAG
Original  1801 ATAGAGGAGCAAGAGGTAGAAGCAAATGAGGAAAATGTGAAGGTGCATGGAGGAAGAAAG

Optimized 1861 GAGAAAACAGAAATCCTGTCTGACGATCTGACTGACAAGGCCGAGGTGTCCGAAGGCAAG
Original  1861 GAGAAAACAGAGATCCTATCAGATGACCTTACAGACAAAGCAGAGGTGAGTGAAGGCAAG

Optimized 1921 GCAAAATCTGTCGGAGAGGCAGAAGACGGACCAGAGGGACGAGGGGATGGAACCTGCGAG
Original  1921 GCAAAATCAGTGGGAGAAGCAGAGGATGGGCCTGAAGGTAGAGGGGATGGAACCTGTGAG

Optimized 1981 GAAGGCTCAAGCGGGGCTGAGCATTGGCAGGACGAGGAACGAGAAGGGCGAAAAGGAT
Original  1981 GAAGGTAGTTCAGGAGCAGAACACTGGCAAGATGAGGAGAGGGAGAAGGGGGAGAAAGAC

Optimized 2041 AAAGGCCGCGGGGAGATGGAACGACCTGGAGAGGGCGAAAAAGAGCTGGCAGAGAAGGAG
Original  2041 AAGGGTAGAGGAGAAATGGAGAGGCCAGGAGAGGGAGAGAAGGAACTAGCAGAGAAGGAA

Optimized 2101 GAATGGAAGAAAAGGGACGGCGAGGAACAGGAGCAGAAAGAAAGGGAGCAGGGCCACCAG
Original  2101 GAATGGAAGAAGAGGGATGGGGAAGAGCAGGAGCAAAAGGAGAGGGAGCAGGGCCATCAG

Optimized 2161 AAGGAGCGCAACCAGGAGATGGAAGAGGGCGGCGAGGAAGAGCATGGCGAGGGAGAAGAG
Original  2161 AAGGAAAGAAACCAAGAGATGGAGGAGGGAGGGAGGAGGAGCATGGAGAAGGAGAAGAA

Optimized 2221 GAAGAGGGCGATAGAGAAGAGGAAGAGGAAAAAGAAGGCGAAGGGAAGGAGGAAGGAGAG
Original  2221 GAGGAGGGAGACAGAGAAGAGGAAGAAGAGAAGGAGGGAGAAGGGAAAGAGGAAGGAGAA

Optimized 2281 GGCGAGGAAGTGGAAGGCGAGAGGGAAAAGGAGGAAGGAGAACGGAAGAAAGAGGAAAGA
Original  2281 GGGGAAGAAGTGGAGGGAGAACGTGAAAAGGAGGAAGGAGAGAGGAAAAAGGAGGAAAGA

Optimized 2341 GCCGGCAAAGAGGAAAAGGGCGAGGAAGAGGGCGATCAGGGCGAAGGCGAGGAGGAAGAG
Original  2341 GCGGGGAAGGAGGAGAAAGGAGAGGAAGAAGGAGACCAAGGAGAGGGGGAAGAGGAGGAA

Optimized 2401 ACCGAGGGCCGCGGGAAGAGAAAGAGGAGGGAGGAGAGGTGGAGGGCGAGAGGTCGAA
Original  2401 ACAGAGGGGAGAGGGGAGGAAAAAGAGGAGGGAGGGGAAGTAGAGGGAGGGGAAGTAGAG

Optimized 2461 GAGGGAAAGGGCGAGCGCGAAGAGGAAGAGGAAGAGGGCGAGGGCGAGGAAGAAGAGGGC
Original  2461 GAGGGGAAAGGAGAGAGGGAAGAGGAAGAGGAGGGAGGGTGAGGGGGAAGAGGAAGGGG

Optimized 2521 GAGGGGGAAGAAGAGGAGGGAGAGGGCGAAGAGGAAGAGGGGGAGGGAAAGGGCGAAGAG
Original  2521 GAGGGGGAAGAGGAGGAAGGGGAGGGGGAAGAGGAGGAAGGAAGGGAAAGGGGAGGAA

Optimized 2581 GAAGGAGAGGAAGGGGAGGGAGAGGAAGAGGGGGAGGAGGGCGAGGGGGAAGGCGAGGAG
Original  2581 GAAGGGGAAGAAGGAGAAGGGGAGGAAGAAGGGGAGGAAGGAGAAGGGGAGGGGAAGAG

Optimized 2641 GAAGAAGGAGAGGGGGAAGGCGAAGAGGAAGGCGAGGGGAAGGAGAGGAGGAAGAAGGG
Original  2641 GAGGAAGGAGAAGGGGAGGGAGAAGAGGAAGGAGAAGGGGAGGGAGAAGAGGAGGAAGGA

Optimized 2701 GAAGGCGAAGGCGAAGAGAGGAGAGGAGGAAGAGAGGAGGGAGGAAGAGGAAGAAGGAAG
Original  2701 GAAGGGGAGGGAGAAGAGGAAGGAGAAGGGGAGGGAGAAGAGGAAGGAGAAGGAAGGAAA

Optimized 2761 GGCGAGGAGGAAGGCGAAGAGGGAGAGGGGGAAGGCGAGGAAGAGGAAGGCGAGGGCGAA
Original  2761 GGGGAGGAGGAAGGAGAGGAAGGAGAAGGGGAGGGGGAAGAGGAAGGAGAAGGAGAAGGGGAA

Optimized 2821 GGAGAGGACGGCGAGGGCGAGGGAGAAGAGGAGGAAGGGGAATGGGAAGGCGAAGAAGAG
Original  2821 GGGGAGGATGGAGAAGGGGAGGGGGAAGAGGAAGGAAGAATGGGAGGGGGAAGAGGAG

Optimized 2881 GAAGGCGAAGGCGAAGGCGAAGAAGAGGGCGAAGGGGAGGGCGAGGAGGGCGAAGGCGAA
Original  2881 GAAGGAGAAGGGGAGGGGGAAGAGGAAGGAGAAGGGGAAGGGAGGAAGGAAGAGGGGAG

Optimized 2941 GGGGAGGAAGAGGAAGGCGAAGGAGAAGAGGGAAGAGGAGGGAGAGGAGGAAGGCGAG
Original  2941 GGGGAAGAGGAGGAAGGAGAAGGGGAGGGGGAAGAGGAGGAAGGGGAAGAAGAAGGGGAG

Optimized 3001 GAGGAAGGAGAGGGGGAGGAGGAGGGAGAAGGCGAGGGCGAAGAAGAAGAGGGAGAAA
Original  3001 GAAGAAGGAGAGGGAGAGGAAGAAGGGGAGGGAGAAGGGGAGGAAGAAGAGGAAGGGGAA

Optimized 3061 GTGGAGGGCGAAGTCGAGGGGGAGGAGGGAGAAGGGAAGGGGAGGAGGAAGAAGAGGAG
Original  3061 GTGGAAGGGGAGGTGGAAGGGGAGGAAGGAGAGGGGGAAGGAGAGGAAGAGGAAGGAGAG

Optimized 3121 GAAGAAGGCGAGGAAAGAGAAAAGGAGGGGAAGGAAGAAAACAGGAGGAACAGAGAA
Original  3121 GAGGAAGGAGAAGAAAGGGAAAAGGAGGGGGAAGGAAGAAAACAGGAGGAACAGAGAA

Optimized 3181 GAGGAGGAAGAGGAAGAGGGAAGTACAGGAGACAGGCGAAGAGGAAAACGAGCGGCAG
Original  3181 GAGGAGGAGGAAGAAGAGGGGAAGTATCAGGAGACAGGCGAAGAAGAGAATGAAAGGCAG

Optimized 3241 GATGGCGAGGAATATAAGAAAGTGAGCAAGATCAAAGGATCCGTCAAGTACGGCAAGCAC
Original  3241 GATGGAGAGGAGTACAAAAAAGTGAGCAAAATAAAAGGATCTGTGAAATATGGCAAACAT

Optimized 3301 AAAACCTATCAGAAGAAAAGCGTGACCAACACACAGGGAATGGAAAAGAGCAGAGGAGT
Original  3301 AAAACATATCAAAAAAAGTCAGTTACTAACACACAGGGAAATGGGAAAAGAGCAGAGGTCC

Optimized 3361 AAGATGCCTGTGCAGTCAAAACGGCTGCTGAAGAATGGCCCATCTGGAAGTAAAAAATTC
Original  3361 AAAATGCCAGTCCAGTCAAAACGACTTTTAAAAAACGGGCCATCAGGTTCCAAAAAGTTC

Optimized 3421 TGGAACAATGTGCTGCCCCACTATCTGGAACTGAAATAA
Original  3421 TGGAATAATGTATTACCACATTACTTGGAATTGAAGTAA
```

3.4.2 Codon optimised RPGR shows higher sequence fidelity than wildtype RPGR

The synthesized sequence of coRPGR^{ORF15} showed no sequence deviation throughout the necessary steps towards successfully subcloning it into the Vector BioLabs pAAV2 plasmid for downstream rAAV vector production. Synthesis of the original plasmid product containing coRPGR^{ORF15} at GenScript took ca. 6 weeks. In contrast, synthesis of a first wtRPGR^{ORF15} sequence by OriGene took more than 5 months due to difficulties in the quality control steps (personal communication with OriGene). Several transformation experiments with XL10-Gold ultracompetent bacteria failed and – once successful – showed a 12 base pair deletion in the ORF15 region in three independent samples stemming from the wtRPGR^{ORF15} plasmid by OriGene (**Fig. 3.6**, next page).

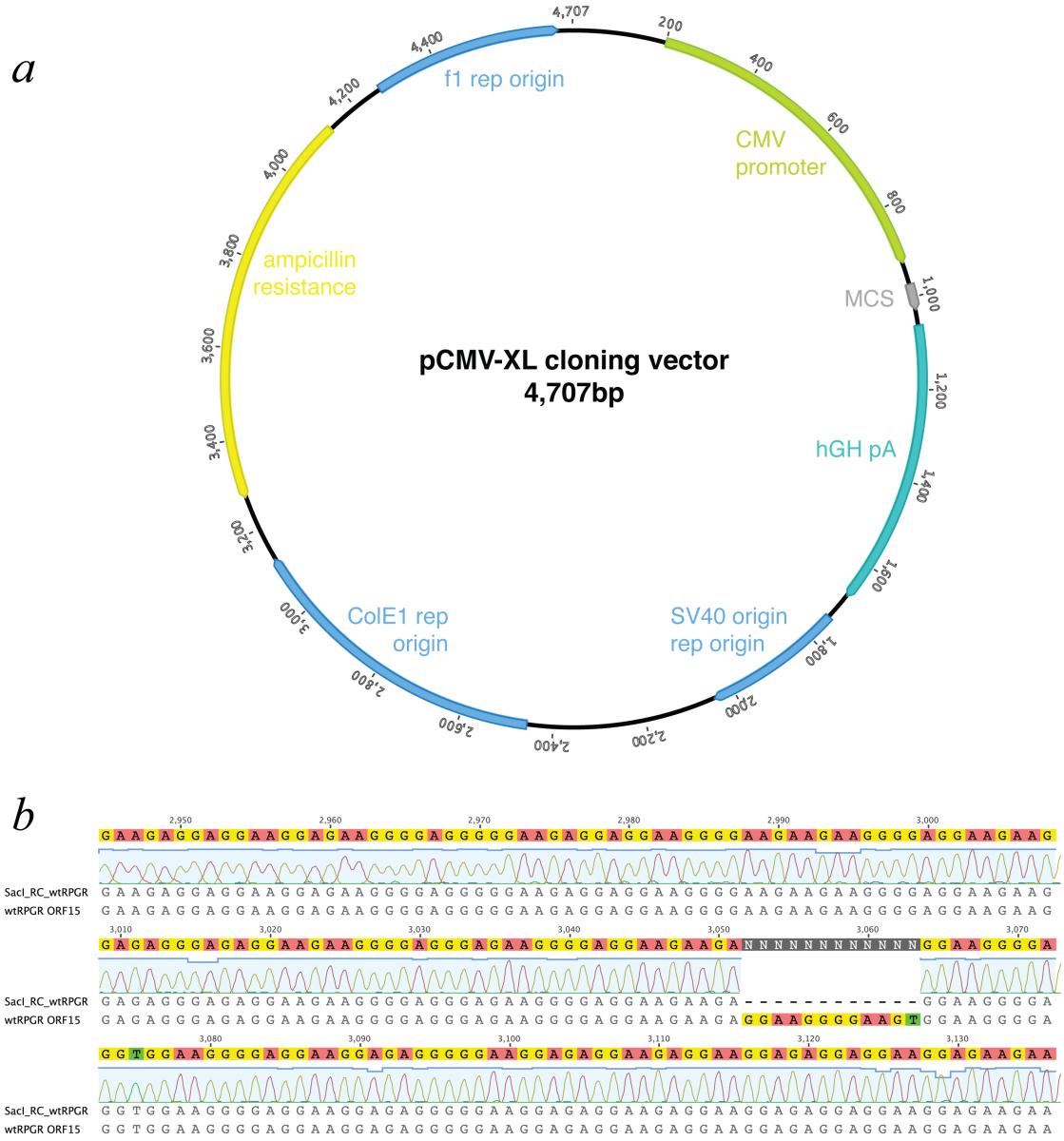

Fig. 3.6 Sequencing of the OriGene *wtRPGR*^{ORF15} containing pCMV-XL cloning vector revealed a 12bp deletion in the ORF15 region. CMV = cytomegalovirus; MCS = multiple cloning site; hGH = human growth hormone; pA = polyA site; SV40 = simian virus 40; rep origin = origin of replication; ColE1 = colicin E1; f1 rep origin = origin of replication from a f1 phage.

Synthesis of a correct version of wtRPGR^{ORF15} by GenScript also took ca. double the time compared with the coRPGR^{ORF15} (ca. 12 weeks). All subsequent steps involving wtRPGR^{ORF15} *en route* to the subcloning into the pAAV2 plasmid showed lower numbers of clones with correct fragment size: out of 24 colonies of XL10-Gold

bacteria following transformation with wtRPGR^{ORF15}, only three samples featured expected fragment sizes (red asterisks in **Fig. 3.7b**). In contrast, cloning of coRPGR^{ORF15} resulted in 18 out of 24 positive clones (red asterisks in **Fig. 3.7d**). Furthermore, plasmid DNA concentration from coRPGR^{ORF15} minipreparations were ca. 50% higher (n = 24, unpaired, two-tailed t-test: p = 0.0004), while 260/280 ratio remained unchanged.

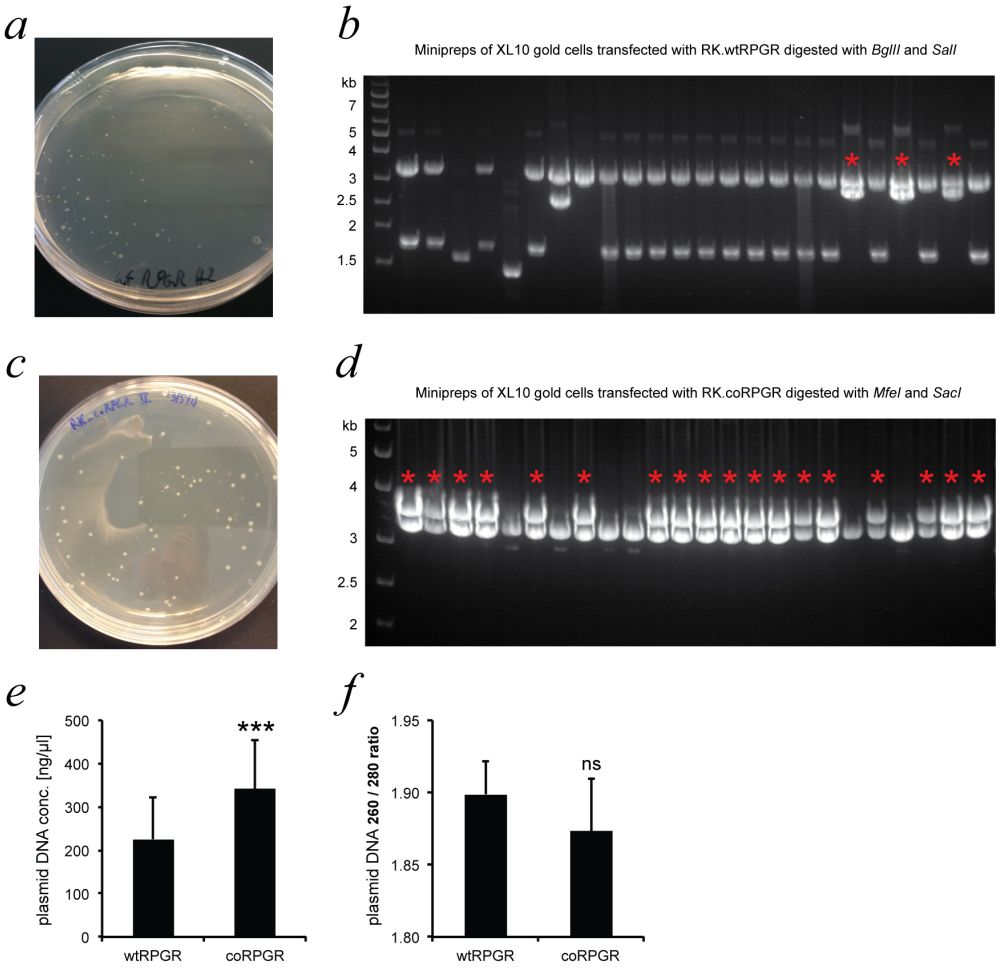

Fig. 3.7 Codon optimisation improves cloning efficiency. Top panel (a-b) shows cloning steps of *wtRPGR*^{ORF15} plasmid. 24 colonies from the plate in a) were grown for minipreparations. Digestion before agarose gel electrophoresis in b) features only three samples with expected product sizes. In contrast, cloning of *coRPGR*^{ORF15} (c) resulted in 18 out of 24 positive clones (d). Furthermore, plasmid DNA concentration of *coRPGR*^{ORF15} minipreparations (e) were significantly higher (n = 24, unpaired, two-tailed t-test: p = 0.0004), while 260/280 ratio remained unchanged (f).

Sequencing the wtRPGR^{ORF15} construct at various stages of the subcloning posed a major challenge due to the repetitive nature and poly-G runs within the ORF15 region. Some regions required use of dGTP sequencing to improve read through in purine rich regions (e.g. **Fig. 3.4**) with long guanine runs. While this technique provides better read-through, it is more likely to introduce band compressions (the reason why in standard Sanger reactions the analogous molecule deoxyinosine triphosphate [dITP] is used instead of deoxyguanosine triphosphate [dGTP]).

In eight independent cloning experiments (n=4 for each construct), an average of 30 sequence runs were necessary to gain full coverage of wild type construct, while a mean of eight sequence runs were sufficient for the coRPGR^{ORF15} sequence. Alignment of sequence data to the reference revealed numerous deletions, insertions, and point mutations of (mostly) single nucleotides in wtRPGR^{ORF15}, but none in coRPGR^{ORF15}.

Table 3.5 Overview of mutations found in plasmid preparations.

	wtRPGR^{ORF15}	**coRPGR^{ORF15}**
deletions [mean (range)]	1.5 (0 - 4)	*nil*
insertions [mean (range)]	0.5 (0 - 1)	*nil*
point mutations [mean (range)]	17.8 (9 - 33)	*nil*
Total [mean (range)]	19.75 (9 - 38)	*nil*

Table 3.5 While all wtRPGR^{ORF15} plasmid preparations featured at least some mutations, none of the coRPGR^{ORF15} plasmid preparations was found to harbour any deletion, insertional- or point mutation.

Key parameters including the Phred quality scores Q20, Q30 and Q40 (Q20 indicates a base call accuracy of 99%, Q30 of 99.9% and Q40 of 99.99%), mean confidence and number of expected errors were significantly weaker in wtRPGR^{ORF15}

vs. coRPGR^{ORF15}. Data are shown as mean ± standard deviation, *p*-values were corrected for multiple comparison using the false discovery rate (FDR) correction method published by Benjamini *et al.* [141].

Table 3.6 Overview of base call accuracy in sequencing wt RPGR^{ORF15} or coRPGR^{ORF15}.

[%] of base calls with a confidence level of at least	**wtRPGR^{ORF15}**	**coRPGR^{ORF15}**	***p* - value** [FDR corrected]
99% (Phred Q20)	91.3 ± 1.0	96.6 ± 0.9	0.0005
99.9% (Phred Q30)	83.1 ± 2.6	90.5 ± 2.6	0.0044
99.99% (Phred Q40)	73.6 ± 3.8	82.3 ± 3.0	0.0054

Table 3.6 Percentage of nucleotides within each plasmid sequence with at least 99% (top row), 99.9% (middle row) or 99.99% (bottom row) base call accuracy. These levels of confidence of individual base calls corresponds to the Phred quality scores Q20, Q30 and Q40 respectively. Numbers are reported as mean ± standard deviation. Statistical analysis was performed with Student's t-test (n=4) and corrected for multiple testing using the false discovery rate method by Benjamini *et al.*

Table 3.7 Mean confidence of call accuracy and number of expected errors in sequencing data from wt RPGR^{ORF15} or coRPGR^{ORF15}.

	wtRPGR^{ORF15}	**coRPGR^{ORF15}**	***p* - value** [FDR corrected]
Confidence Mean	49.1 ± 1.2	52.4 ± 1.0	0.0044
Expected Errors	82.9 ± 25.1	14.4 ± 5.1	0.0023

Table 3.7 Mean confidence level of base call accuracy (top row) and number of expected errors (bottom row) for each plasmid sequence. Numbers are reported as mean ± standard deviation. Statistical analysis was performed with Student's t-test (n=4) and corrected for multiple testing using the false discovery rate method by Benjamini *et al.*

Final proof for the superior sequence fidelity of coRPGR^{ORF15} was given by the National Genetics Reference Laboratory (NGRL) in Manchester. After exchanging the CAG promoter region (1527bp) for the much smaller human rhodopsin kinase promoter (199bp) to aid the recombinant production of AAV (details in chapter 4), both constructs (RK.coRPGR^{ORF15} and RK.wtRPGR^{ORF15}) along with appropriate primers were sent to the NGRL and personnel left masked as to the identity of the sequences. After running 34 sequence reactions on RK.wtRPGR^{ORF15} as template, the cumulative data showed 74 ambiguous nucleotide calls (e. g. equal

signal for guanine and adenine) and six potential in/del mutations (four potential insertions and two potential deletions), all found in the purine rich ORF15 region, the mutational hotspot of RPGR^{ORF15} (**Fig. 3.8**). In contrast, the coRPGR^{ORF15} construct was sequenced with at least 2x coverage with exactly half the number of sequence reactions and no mutations found in the plasmid.

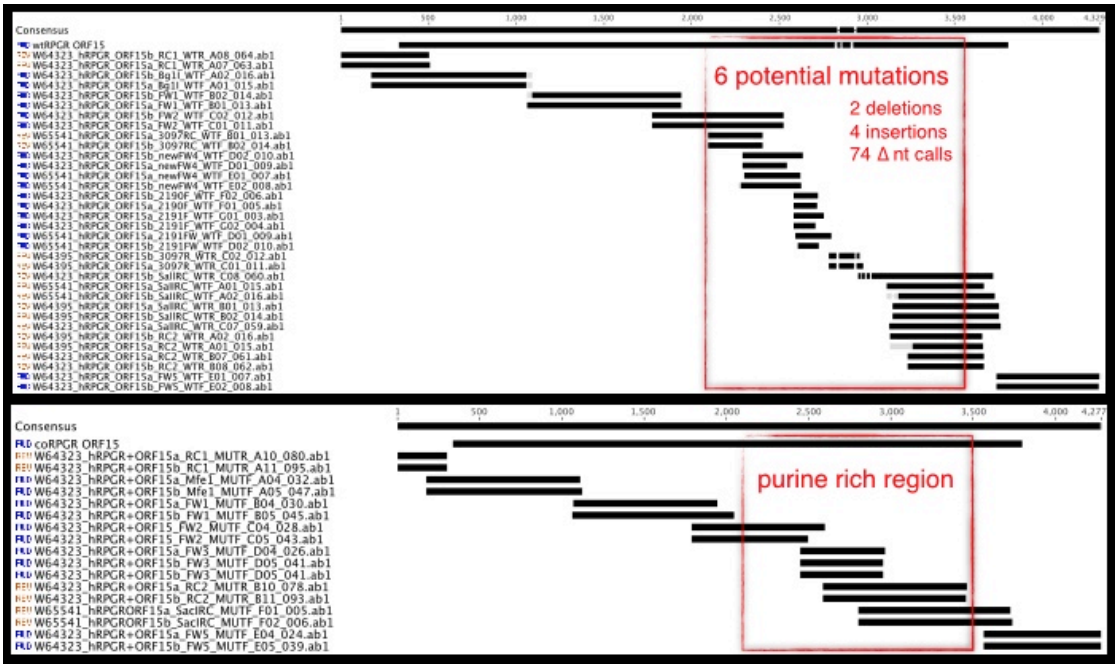

Fig. 3.8 Independent confirmation of superior sequence stability of *coRPGR^{ORF15}*. The National Genetics Reference Laboratory (NGRL) in Manchester identified multiple potential mutations in the *wtRPGR^{ORF15}* construct (top). There were six potential frame shift mutations (two deletions, four insertions) and 74 additional ambiguous base calls. In contrast, the sequence of the *coRPGR^{ORF15}* construct was confirmed to be intact with at least two times coverage (bottom).

3.4.3 Codon optimised RPGR yields higher expression levels than wildtype RPGR

In order to analyse the effect of an increased codon adaptation index (CAI) on the expression levels of $RPGR^{ORF15}$, transfection experiments were performed on HEK293T cells using the CAG.co$RPGR^{ORF15}$ and CAG.wt$RPGR^{ORF15}$ plasmid constructs in head to head comparisons. As detailed in section 2.2.1, HEK293T cells are of human origin and therefore share the species-specific codon frequency distribution, which served as basis for the optimisation for *Homo sapiens*. We hypothesise that cells transfected with CAG.co$RPGR^{ORF15}$ produce more $RPGR^{ORF15}$ than cells transfected with the wild type construct CAG.wt$RPGR^{ORF15}$. To test this hypothesis, several experimental avenues were taken in order to quantify $RPGR^{ORF15}$ in transfected cells. First, HEK293T cells were transfected with CAG.co$RPGR^{ORF15}$ and CAG.wt$RPGR^{ORF15}$ plasmid constructs and processed for immunocytochemistry

(ICC) to establish, whether the transgene detection could be detected by antibody binding. **Fig. 3.9** shows representative images from such an experiment, where cells were transfected with medium only (neg ctrl), CAG.wtRPGR^{ORF15} (wt) or CAG.coRPGR^{ORF15} (co) and stained with anti-RPGR.

Western blot analysis was used to assess expression levels in whole cell lysate from transfected HEK293T cells. Four independent 6-well plate transfections, each with a technical replicate for wt- and coRPGR, produced a total n of eight per construct. Aliquots from these lysates were run on two gels in parallel and mean signal intensities of resulting bands compared (**Fig. 3.10**). The Shapiro-Wilk test retained the null-hypothesis for normality of the data sets (p = 0.06-0.19) and one-way ANOVA showed the statistical significance (p = 0.01, n = 8) of the difference

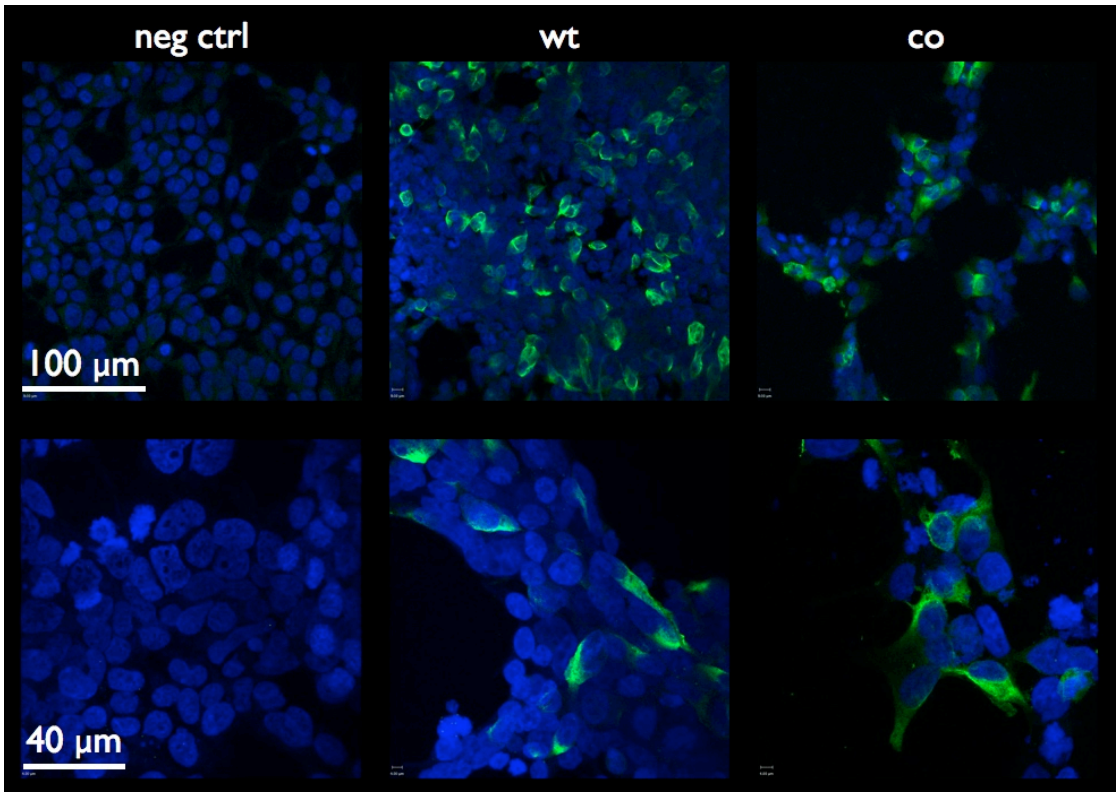

Fig. 3.9 RPGR^{ORF15} transgene expression in HEK293T cells. Cells were transfected with *wtRPGR^{ORF15}* (wt) and *coRPGR^{ORF15}* (co) plasmid constructs or treated with media only (neg ctrl). Confocal microscopy after immunocytochemistry with anti-RPGR (Sigma N-terminal) and Hoechst 33342 demonstrate high levels of RPGR^{ORF15} expression in transfected cells.

between the mean signal intensity reflecting the codon optimised construct = 32.01±8.28 arbitrary units [AU] (mean±standard error) and the signal from cell transfected with the wild type construct = 8.11±1.63 AU.

Fluorescence activated cell sorting (FACS) was also used to measure expression levels of $RPGR^{ORF15}$ in transfected HEK293T cells. In a similar setup as mentioned above, three independent experiments with 6-well plates were conducted each with three technical replicates of wells with HEK293T cells transfected with either CAG.wt$RPGR^{ORF15}$, CAG.co$RPGR^{ORF15}$, CAG.eGFP (as positive control for transfection) or media only (as negative control).

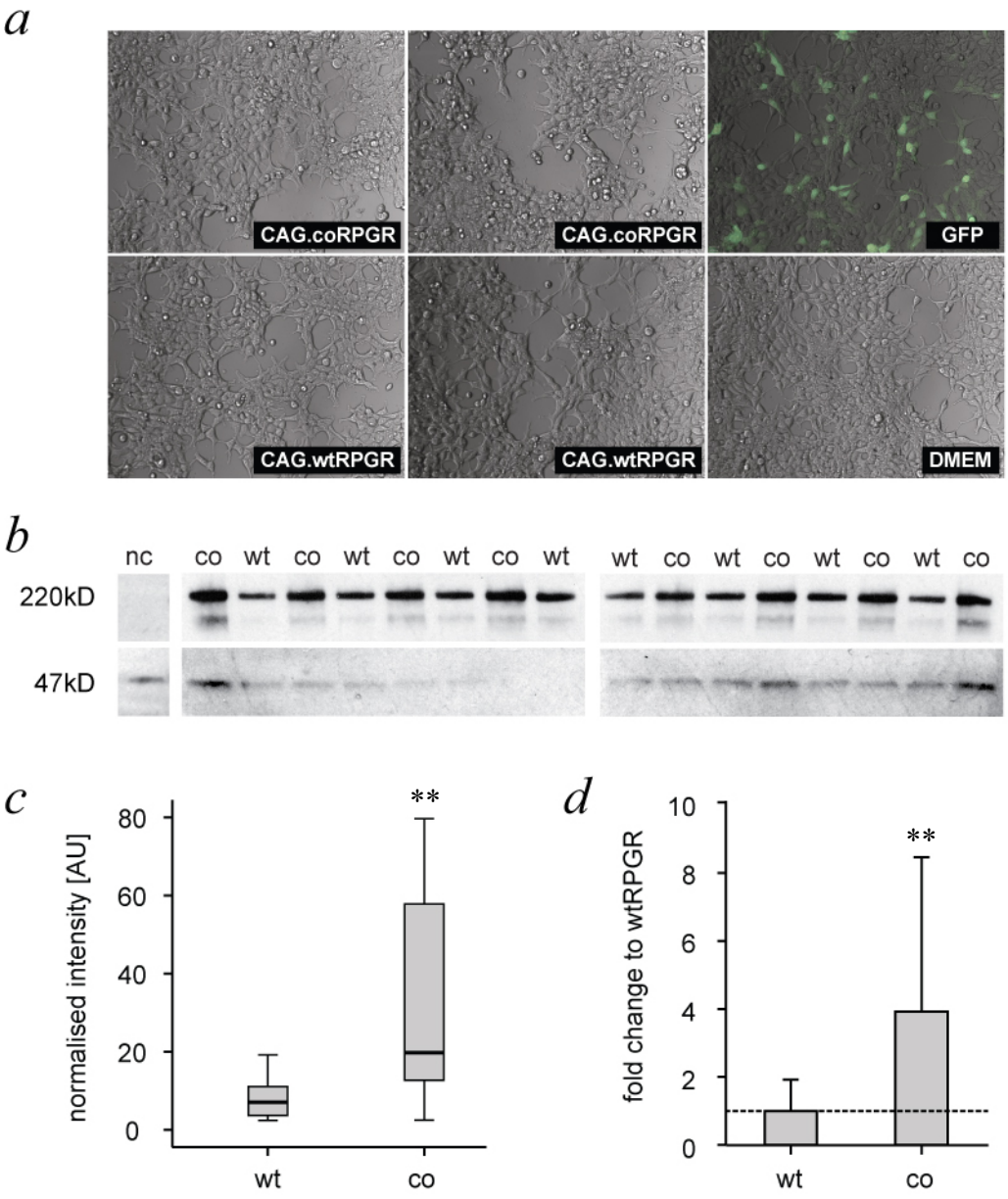

Fig. 3.10 Western blot analysis of RPGR^{ORF15} expression. a) HEK293T cells were transfected with either *wtRPGR*^{ORF15} (wt) or *coRPGR*^{ORF15} (co) plasmid constructs. Control plasmid (GFP) was used to control for transfection (top right) and DMEM was used as negative control (nc). All images in a) were recorded at 10x magnification. b) Western blot of whole protein lysates from transfected cells. DMEM treated cells were used as negative control (nc), which only shows a positive band at 47kD indicating the loading control GAPDH. Codon optimised and wild type plasmid transfected cells were loaded in an alternating fashion and signal intensity of bands at 220kD (indicating RPGR) were quantified (c-d). c) Box plot (median, box delineates lower and upper quartile, whiskers minimum and maximum), of intensities in arbitrary units [AU] after normalisation for loading control (GAPDH). d) Bar graph (mean ± standard deviation) after normalisation to wt levels for a fold change presentation. After confirming the normal distribution of the data set (n = 8), significance was tested by one-way ANOVA. Asterisks indicate $p < 0.005$.

Cells transfected with CAG.eGFP showed eGFP expression at time of harvest indicating that the transfection was successful and that the cells had enough time to produce a plasmid-encoded transgene. After the ICC protocol, these cells were used to set the lower end of the FACS gating for fluorescence in the far-red range as they were incubated with secondary antibody only. The positive controls (naïve HEK293T cells exposed to rabbit anti-βactin and donkey anti-rabbit with conjugated Alexa-Fluor 635) were then used to define the upper end of the fluorescence gate setting. Cells transfected with the CAG.coRPGR^{ORF15} construct showed higher fluorescence intensity then the cells transfected with the wild type construct (**Fig. 3.11**). The Shapiro-Wilk test rejected the null-hypothesis for normality of the data sets ($p < 0.05$) and the Kruskal Wallis non-parametric test demonstrated a robust statistical difference between the cohorts ($p < 0.01$, n = 9).

3.4.4 Codon optimised *RPGR* cds translates into full length RPGR protein

To demonstrate that the substitution of nucleotides with the aim to optimise codon usage and sequence stability does not lead to changes in the amino acid sequence, cryptic epitopes or alternative peptide products, we analysed recombinant RPGR^{ORF15} based on CAG.coRPGR^{ORF15} and CAG.wtRPGR^{ORF15} plasmid expression in HEK293T cells.

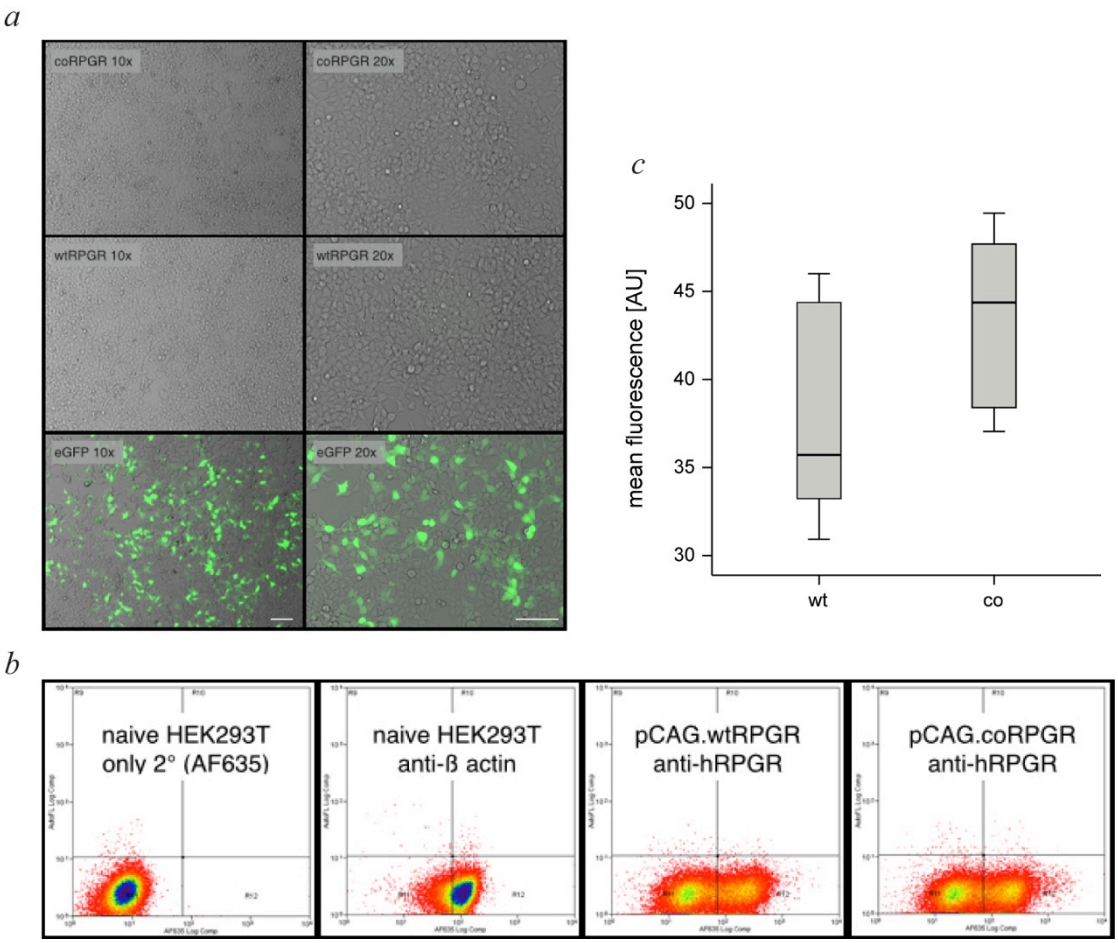

Fig. 3.11 Flow cytometric analysis of RPGR^{ORF15} expression. a) HEK293T cells were transfected with either *wtRPGR*^{ORF15} (wt), *coRPGR*^{ORF15} (co) plasmid constructs. Control plasmid (GFP) was used to control for transfection and DMEM was used as negative control (not shown). Scale bar = 20µm b) First, naïve cells were used to set appropriate sensitivity and specificity thresholds (left). Using these thresholds, test samples transfected with *wtRPGR*^{ORF15} or *coRPGR*^{ORF15} were quantified. c) Box plot (median, box delineates lower and upper quartile, whiskers minimum and maximum) of median fluorescence intensities in arbitrary units [AU] (n = 9).

Following whole cell lysate protein extraction, we separated proteins by SDS-PAGE and demonstrated a single band difference between untransfected (negative control, nc) and transfected HEK293T cell lysates (**Fig. 3.12 a**). The single band was identical in size between cells transfected with either CAG.coRPGR^{ORF15} or CAG.wtRPGR^{ORF15} indicating no difference in migrating pattern between protein products derived from both coding sequences, suggesting a similar if not identical combination of molecular weight, charge and three-dimensional peptide structure.

Bands were excised and analysed by liquid chromatography-tandem mass spectrometry (LC-MS/MS) in order to determine the identity of the protein products derived from CAG.coRPGR^{ORF15} or CAG.wtRPGR^{ORF15} expression plasmids. Both samples showed identical peptide sequences and confirmed the identity of the protein product of coRPGR^{ORF15} cds as human RPGR isoform 6 (aka RPGR^{ORF15}). Slightly more than 80% of all amino acids could be covered by the LC-MS/MS approach (**Fig. 3.12 b**). Not surprisingly, the vast majority of the 228 amino acids, which escaped this approach, originate from the highly repetitive glutamic acid rich ORF15 region. The lack of sites within this peptide sequences that would be recognised by proteolytic enzymes prevented the formation of oligopeptides of the 'correct' size of 6-45 amino acids, which can be detected by LC-MS/MS. Instead either one large peptide of more than 200 amino acids would form or cleavage between glutamic acid and glycine residues would result in peptide lengths below detection threshold of six amino acids. And even if these shorter sequences were detected, the highly repetitive nature of the ORF15 region would make it impossible to determine the precise origin of the peptide within the sequence. The fact that both plasmids resulted in an identical band on SDS-PAGE fits well with the LC-MS/MS evidence. Both suggest that the protein product derived from wild-type and codon optimised RPGR cds is identical to the reference sequence of RPGR^{ORF15}. Even though some of the ORF15 sequence could not be verified by this approach, the intact C-terminal sequence from the LC-MS/MS experiment together with the correct band migration on SDS-PAGE essentially rule out unforeseen side effects due to codon optimisation.

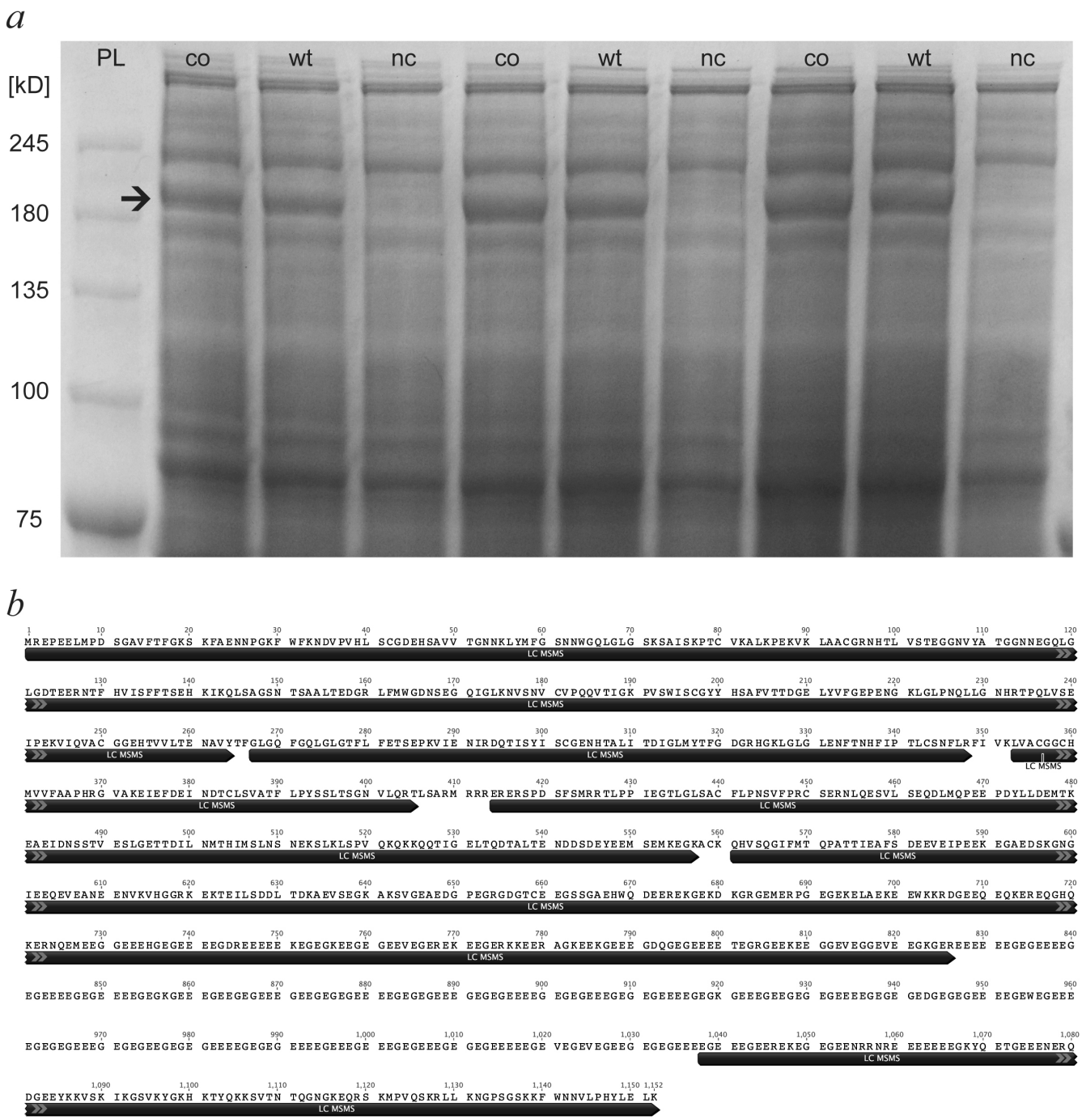

Fig. 3.12 Liquid chromatography-tandem mass spectrometry (LC-MS/MS) of wt- and coRPGR^{ORF15}. a) Following overexpression in HEK293T cells, wt- and coRPGR^{ORF15} was purified from whole cell lysate by SDS-PAGE. In each lane, a single band above 180 kD was identified as RPGR^{ORF15} (arrow). This band was missing in the negative control (nc) lanes. No additional bands are visible, which would be different between wt and coRPGR^{ORF15} lanes. Identified RPGR^{ORF15} bands were then excised for LC-MS/MS analysis (b). More then 80% of peptide sequence could be directly identified (indicated by dark arrows below amino acid sequence). Unidentified amino acids (no black arrows) are largely based in the ORF15 sequence, which escapes LC-MS/MS analysis due to its glutamic acid/glycine rich, repetitive sequence. Note that the C-terminal sequence following the ORF15 region was identified, which rules out premature termination of translation. Together with the identical migration pattern between the wt- and coRPGR^{ORF15} samples in the SDS-PAGE (a), this suggests that codon optimisation does not result in alternative splicing but in a protein product equivalent to the wild type RPGR^{ORF15}.

3.5 Discussion

The data presented here suggest that codon optimisation of *RPGR*^{ORF15} leads to higher expression efficiency and also to greater sequence fidelity, as evident from cloning experiments.

The fact that *E. coli* (XL10-Gold) would clone CAG.coRPGR^{ORF15} with higher efficiency then CAG.wtRPGR^{ORF15} was not necessarily expected, as the codon usage was optimised for *Homo sapiens*, not *Escherichia coli*. However, given the difficult sequence of wtRPGR^{ORF15}, a greater clonal efficiency with CAG.coRPGR^{ORF15} may be explained by additional, species-independent benefits of codon optimisation. These may include a reduced potential for secondary structure formation, reduced number and/or length of poly-guanine runs and a greater balance of nucleotide frequency in general. These mechanisms are also useful in the eukaryotic cell. It becomes evident then that we use the term 'codon optimisation' here in the sense that we have changed the nucleotide sequence to improve protein expression. This includes maximising use of major codons, but also improving protein expression e.g. by stabilising mRNA molecules and minimising G-quadruplex DNA sequences *et cetera*.

At least two resourceful research groups (Dr. Swaroop's laboratory at the NIH, Bethesda, USA and Dr. Aguirre's lab at the University of Pennsylvania, Philadelphia, USA) have been working towards developing gene therapy for patients with mutations in RPGR^{ORF15} for many years. All these programs have experienced serious delays due to the difficult sequence of wtRPGR^{ORF15}, the mutational hotspot responsible for the

high incidence of XLRP3 in the first place. Dr. Swaroop has published extensively in this field with his own group at the National Institute of Health (NIH) and in collaboration with Dr. Aguirre's lab at the University of Pennsylvania. In a paper by Wu *et al.*, Dr. Swaroop's group show safety and efficacy using different vector constructs (rAAV8 and rAAV9) for RPGR gene therapy. However, they also illustrate that two out of five rAAV preparations carrying wtRPGR^{ORF15} present with mutations. This indicates the precarious instability of the wtRPGR^{ORF15} sequence, which constitutes a potential hazard in the translation of these pre-clinical trials into clinical applications.

Dr. Hauswirth's group took a more aggressive line of argument with their vector construct, which was used by Beltran *et al.* in a pivotal dog study and then again by Deng *et al.* to demonstrate safety of a rAAV5 vector construct for RPGR gene therapy [122, 123]. The transgene was originally described as wild type RPGR^{ORF15} in the aforementioned dog study, but Deng *et al.* openly discuss that the sequences found in both rAAV5 vector constructs (two different promoters were tested) harbour numerous in frame mutations, including deletions, insertions and missense mutations in the ORF15 region, which translate into an altered amino acid sequence. Given the proof of efficacy in dogs and the lack of toxic effects on the retina in mice, the authors argue that their constructs may well still be suitable for a clinical safety trial.

In this work we show that optimising the codon usage of *RPGR^{ORF15}* increases the sequence stability during the process of vector construction and enhances the expression of the transgene in human cells. Increased sequence stability translates into

a predictable and reproducible production of rAAV vector, a *sine qua non* for clinical grade vector production. It thereby decreases the risk of new mutations occurring e.g. in the last step or between batches of rAAV production, which have the potential to introduce dominant negative effects [54].

Increased translational efficiency of the codon optimised transgene may reduce the numbers of viral particles necessary to reach a therapeutic effect. This would further decrease any inflammatory potential in the eye and limit the absolute numbers of virions available for unwanted biodistribution and shedding. Also, additional *cis* acting elements such as the woodchuck hepatitis virus post-transcriptional regulatory element (WPRE) can be left out of the expression cassette leading to a cleaner design and higher efficiency in rAAV production cycles as the upper end of the packaging capacity is already reached without the WPRE sequence as explained in more detail in the next chapter.

CHAPTER 4 RECOMBINANT ADENO-ASSOCIATED VIRUS FOR XLRP GENE THERAPY

4.1 Introduction

Recombinant adeno associated virus (rAAV) has become the gold standard of retinal gene therapy leading the way into multiple successful clinical trials over the last decade. The excellent safety profile in pre-clinical models as well as human patients and the versatility of its components to adapt to new target genes are important factors in this success story and reasons why we chose rAAV as our vector system for $RPGR^{ORF15}$ delivery [142-144].

Different rAAV serotypes lead to distinct expression patterns due to specific interactions between rAAV surface proteins and target cell receptors (see chapter 1.3.1). The naturally occurring serotype AAV2 for example is very efficient to transduce retinal pigment epithelium, but less effective in delivering the transgene into photoreceptor cells. In contrast, AAV8 capsid structures lead to rapid and efficient uptake of virions by mammalian photoreceptor cells [96, 145].

Photoreceptors are expressing $RPGR^{ORF15}$ where it localises to the connecting cilium and organises intracellular protein-transport along a bottleneck structure called the connecting cilium (**Fig. 1.6**) [49]. Photoreceptors without functional $RPGR^{ORF15}$ suffer from accumulation of highly expressed proteins such as opsins, which leads to photoreceptor dysfunction and ultimately cell death [76, 146].

With photoreceptors as the target cell population for $RPGR^{ORF15}$ gene delivery, we chose AAV8 capsid proteins as a candidate viral serotype for XLRP gene therapy. With the success of rAAV2 based transgene cassettes in all retinal gene therapy trials, we opted for a pseudotyped construct, rAAV2/8. This combines the AAV8 capsid proteins with the AAV2 based genome (details see chapter 1.3.1). Briefly, the

therapeutic transgene cassette is flanked by AAV2 inverted terminal repeat (ITR) sequences, which coordinate the packaging of the genome during vector production and serve as starting point for the second strand synthesis after successful delivery of the therapeutic transgene into the nucleus of the target cell.

4.2 Aims

The aim of this study was to develop and optimise a gene therapy strategy with the potential to move into a clinical phase I trial in patients with XLRP3. We therefore aimed to engineer a pseudotyped, rAAV vector with the capsid from the AAV8 serotype, while using the well-characterised, gutted genome from AAV2 for an optimised rAAV vector for gene replacement therapy in patients with mutations in $RPGR^{ORF15}$.

4.3 Materials and methods

In order to restrict the expression of RPGR^{ORF15} to the photoreceptors and thereby limit potential off-target effects (e.g. in the retinal pigment epithelium), the plasmid vectors from chapter 3 (CAG.coRPGR^{ORF15} and CAG.wtRPGR^{ORF15}) were modified. Instead of the ubiquitous cytomegalovirus early enhancer and chicken beta-actin, rabbit beta-globin hybrid promoter (CAG), the much shorter and photoreceptor-specific human rhodopsin kinase (RK) promoter was used upstream of the transgene sequences. We deliberately did not include an intron in the RK promoter, due to the possibility of aberrant splicing resulting from combination with AG nucleotides in the RPGR ORF15 region as a cryptic downstream splice acceptor site. It should be noted that ORF15 is identified as an intron in all cells expressing RPGR with the exception of photoreceptors and the splice behaviour of cDNA sequences passed back through the transcriptional machinery via rAAV gene therapy is difficult to predict. This led to the following plasmid constructs:

III. ITR.RK.Kozak.coRPGR^{ORF15}.bGHpA.ITR (henceforth referred to as RK.coRPGR) features no restriction site between RK promoter and Kozak or coRPGR^{ORF15} cds, but was ligated into the vector backbone between the upstream ITR (*Mfe*I) and the downstream MCS (*Sac*I).

IV. ITR.RK.Kozak.wtRPGR^{ORF15}.bGHpA.ITR (henceforth referred to as RK.wtRPGR) as in III, but using restriction sites *Bgl*II after the upstream ITR (wtRPGR^{ORF15} cds features a *Mfe*I restriction site at position 1583-1588) and *Sal*I at the downstream MCS.

In order to exchange the CAG with the RK promoter resulting in RK.coRPGR, a plasmid with the RK promoter sequence (p.RK.ABCA4) was kindly provided by Dr. Michelle McClements, who had designed it based on the work by Khani *et al.* [147]. Several oligonucleotides were then specifically designed to prepare the RK and coRPGR fragments before linking them by the SPLICE technique described by Davies *et al.* [148]. SPLICE stands for swift PCR for ligating *in vitro* constructed exons overlap extension PCR: The forward primer FW_MfeI_RK (see table below) was designed to amplify RK from the p.RK.ABCA4 plasmid while introducing a *Mfe*I restriction site 5' of the RK promoter sequence. The corresponding reverse primer (RC_RK_K_coRPGR, see table below) would add the first six nucleotides of coRPGR and a complementary Kozak consensus sequence (GGTGGC) at the 3' end).

FW_MfeI_RK	5'-ATCAATTGGGGCCCCAGAAGCCTGGTGGTTG-3'
RC_RK_K_coRPGR	5'-CTCTCTCATGGTGGCCCCGGGGCTGACACA-3'

In a second reaction, the forward primer FW_RK_K_coRPGR (see below) was used together with the coRPGRSacIRC sequencing primer (chapter 3.3) to amplify coRPGR while adding the 15 last nucleotides of the RK promoter sequence and the Kozak consensus sequence (GCCACC) to the 5' end.

FW_RK_K_coRPGR	5'-TGTGTCAGCCCCGGGGCCACCATGAGAGAG-3'
coRPGRSacIRC	5'-TTATTTCAGTTCCAGATAGTG-3'

Both PCR reactions were run on temperature gradients for the annealing temperature and PCR products run on an agarose gel. Bands of appropriate size were

excised and DNA extracted from the gel (QIAquick PCR Purification Kit, Qiagen). Overlap extension PCR was then performed using above DNA products as templates and the FW_MfeI_RK forward and coRPGRSacIRC reverse primers, followed by another round of agarose gel electrophoresis for size exclusion and DNA extraction. The new construct was then digested using *Mfe*I and *Sac*I (New England Biolabs) followed by a last purification step by agarose gel electrophoresis and DNA extraction before ligating it back into the commercial vector backbone pAAV2 from Vector BioLabs. For this, the pre-digested (*Mfe*I and *Sac*I) vector backbone was added on equimolar amounts of the new construct along with T4 ligase (New England Biolabs) and the appropriate buffer in a 10 µl reaction. After 8 days at room temperature, 5 µl was then used to successfully transform XL10 gold cells as described in chapter 2.1.1.

The same technique was used to generate the RK.wtRPGR construct, except the added restriction sites for subcloning were *Bgl*II at the 5' end and *Sal*I at the 3' end of the new construct. The respective primers to achieve this were:

F_BglII_RK	5'-ATAGATCTGGGCCCCAGAAGCCTGGTGGTTG-3'
R_RPGR_Kozak_RK	5'-CTCCCTCATGGTGGCCCCGGGGCTGACACA-3'

and

F_RK_Kozak_RPGR	5'-TGTGTCAGCCCCGGGGCCACCATGAGGGAG-3'
RPGR_SalI_RC	5'-AGGTCGACTTACTTCAATTCCAAGTAATGTG-3'

Once both constructs were cloned using XL10-Gold bacteria, respective megapreparations were sequenced to confirm integrity of the complete expression cassette and *Xma*I, *Swa*I, and *Pst*I digestions conducted to validate presence and integrity of ITRs at each end of the transgene (see vector map **Fig.3.3**).

In addition to the potential therapeutic constructs RK.coRPGR and RK.wtRPGR, a third plasmid with the identical backbone and ITR sequences, but with a stuffer sequence (double-floxed and reversed fluorescent protein EYFP) was used to generate a control vector, which would share the same capsid structure with the *verum* preparations:

V. ITR.EF-1a.*loxP*.[EYFP]. *loxP*.WPRE.bGHpA.ITR (henceforth referred to as 'control').

The plasmid was a kind gift from Dr. Doron Hickey. Transfection of HEK293T cells with the plasmid did not produce any transgene (EYFP) in the absence of Cre recombinase. Only co-transfection with a plasmid encoding for Cre led to EYFP production in HEK293T cells (not shown). IHC experiments on cryosections of *verum* or control treated mice also demonstrate lack of transgene expression from this control vector: negative control sections (omission of primary antibody) did not show any EYFP signal as none of the animals have inherent Cre recombinase expression.

To generate pseudotyped rAAV2/8.RK.coRPGR, rAAV2/8.RK.wtRPGR and rAAV2/8.control vectors, HEK293T cells were co-transfected with two plasmids: The appropriate rAAV expression plasmids containing either RK.coRPGR, RK.wtRPGR, or control as transgene and a commercial helper plasmid (pDP8.ape) encoding Rep and Cap genes of AAV8 and an adenoviral helper sequence (PlasmidFactory, Bielefeld, Germany). The transfection protocol and purification steps are detailed in section 2.1.3.

As a first qualitative assessment of the vector production, aliquots of rAAV were heat denatured and peptide solutions analysed by sodium dodecyl sulphate polyacrylamide gel electrophoresis (SDS-PAGE). For this, 20 µl aliquots were dissolved in 1x Laemmli buffer and heat-denatured at 90 °C for 20 minutes before loading the total volume on a 10% SDS PA gel. After one hour at 100V, the gel was subjected to EZBlue staining (detailed protocol see chapter 2.7.2) and resulting staining pattern examined for existence of bands corresponding to molecular weights of 87kD (VP1), 72kD (VP2) and 62kD (VP3) at a ratio of ca. 1:1:10.

rAAV vector titre was quantified using qPCR amplification of the poly adenylation sequence within the expression cassette as detailed in chapter 2.1.4. The structure of the rAAV genome with its palindromic ITR sequences is known to cause variability in determining the exact number of vector genomes (vg). To improve the estimate of the actual titre, we performed three independent qPCR experiments and report the arithmetic mean of the resulting titre calculation as best estimate. This number underestimates the amount of total viral particles in the final vector solution, as iodixanol purification is known to result in large number of empty capsids being harvested along with the capsids containing the transgene cassette.

A second technique was applied to quantify the viral nucleic acid content of the vector preparation. The QuickTiter™ AAV Quantitation Kit (Cell Biolabs, San Diego, USA) measures amounts of vector genomes by fluorescence after denaturing the viral capsid and allowing a fluorophore (CyQuant® GR Dye) to bind to the single stranded DNA. Pre-treatment of samples with a DNase prevents false-high readings from unpackaged nucleic acids in the sample. QuickTiter™ AAV DNA Standard and

an estimation of vector genome size = 5kb are used to calculate the genome copy number per ml.

To estimate the ratio of empty to full capsids in our preparations, an enzyme immunoassay for the quantitative determination of rAAV8 particles was used (rAAV8 Titration ELISA, PROGEN Biotechnik GmbH, Heidelberg, Germany) as detailed in chapter 2.1.5. Specifically, the absorbance measurements from the standard sample dilution series were correlated with known concentrations. Based on the resulting function $y = -1*10^{-18}\ x^2 + 2*10^{-9}x$, the viral particle number (x) could be derived from the luminescence units (y) measured in the sample dilution series.

4.4 Results

Recombinant AAV2/8 was produced to hold genomes containing either RK.coRPGR, RK.wtRPGR, or control expression constructs. To ensure that ITRs were intact for the successful rAAV assembly, AAV2 based ITRs of the expression plasmids were digested with *Xma*I, *Swa*I, and *Pst*I, and products compared to linearized plasmids (*Sac*I, *Sal*I) after agarose gel electrophoresis. All expected band sizes and but no extra bands were detected, suggesting that all ITRs had maintained their integrity during the SPLICE procedure and cloning steps (**Fig. 4.1**).

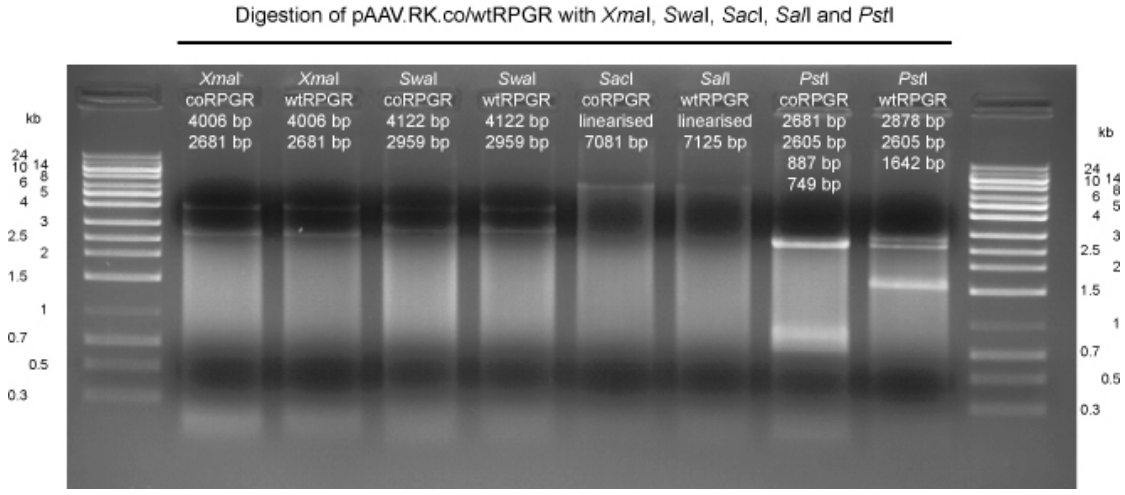

Fig. 4.1 ITR integrity check. Targeted digestion of *Xma*I, *Swa*I, and *Pst*I restriction sites within or close to ITRs showed all expected fragments in agarose gel electrophoresis. Digestions at *Sac*I, *Sal*I sites allow linearization of respective plasmids. Expected band sizes and plasmid are described for each lane. No additional, unexpected bands were observed.

Purification of the cell lysate/rAAV particle mix with iodixanol gradients and ultracentrifugation was followed by a concentration step resulting in ca. 0.5 ml clear solution of 0.01M PBS with high rAAV titres. Samples were inspected for clarity and aliquots of 15-50 µl stored at -80 °C until use.

4.4.1 Qualitative analysis

Each vector production was tested for quality of rAAV capsid protein content by sodium dodecyl sulphate polyacrylamide gel electrophoresis (SDS-PAGE). All three vector productions showed clear bands corresponding to the viral capsid proteins VP1 (87kD), VP2 (72kD) and VP3 (62kD) at a ratio of ca. 1:1:10 (**Fig. 4.2**).

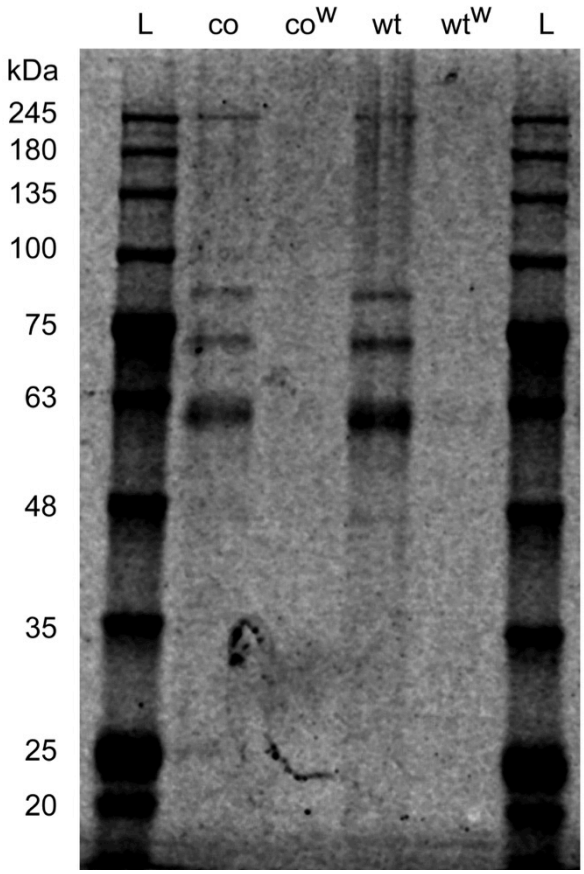

Fig. 4.2 Sodium dodecyl sulphate polyacrylamide gel electrophoresis (SDS-PAGE) of recombinant AAV samples. Following electrophoresis, total protein was stained to detect capsid proteins VP1 (87kD), VP2 (72kD) and VP3 (62kD). The concentrated samples (second and fourth lane) show the predicted ratio of VP1:VP2:VP3 of 1:1:10.

Lanes are:

L = protein ladder
co = AAV2/8.RK.coRPGR
co^{W} = AAV2/8.RK.coRPGR wash
wt = AAV2/8.RK.wtRPGR
wt^{W} = AAV2/8.RK.wtRPGR wash

4.4.2 Quantitative analysis

Titration by qPCR and the QuickTiter™ methods both measured full capsids only and showed overall reasonable agreement on the number of vector genome particles (vg) of around 10^{12} vg/ml. In contrast, the ELISA quantified full and empty capsids and provided evidence of a full to empty particle ratio of between 1:3 and 1:20:

Table 4.1 Overview of results from AAV titre quantification methods.

Method rAAV	qPCR (genome copies/ml)	QuickTiter™ (genome copies/ml)	ELISA (viral particles/ml)
rAAV2/8.RK.wtRPGR	$1.3x10^{12}$	n/a	n/a
rAAV2/8.RK.coRPGR	$1.0x10^{12}$	$3.8x10^{12}$	$2.1x10^{13}$
rAAV2/8.control	$0.7x10^{12}$	$3.2x10^{12}$	$0.8x10^{13}$

Table 4.1 Different methods were used to quantify AAV content in solution. qPCR determines packaged vector genome as the DNAse step in the protocol results in destruction of any unpackaged genome. However, it does not account for (partly) empty or reversely packaged virions in the solution. The higher number of genome copies by the QuickTiter method probably results from additional free nucleotides. The ELISA method quantifies the number of virus particles, but does not specify whether the particles are full or (partly) empty. The difference between the ELISA- and qPCR-based titres partly reflects the full to empty virus particle ratio. n/a = not available.

4.4.3 Functional analysis *in vitro*

In order to provide evidence of a biological infectivity we assessed the potential of the vector productions rAAV2/8.RK.coRPGR and rAAV2/8.RK.wtRPGR to transduce various cell types *in vitro*. For these experiments different cell cultures were harnessed to test the transduction efficiency in human cells of more (SH SY5Y [128]) or less (HEK293T [127]) neuronal type lineage and murine photoreceptor-like

cells (661W [131]). In absence of a fluorescent reporter (which would have made translation into a clinical phase difficult), transduction efficiency was assessed by transgene expression analysis via antibody detection (ICC).

4.4.3.1 Transduction experiments on HEK293T cells

HEK293T cells were seeded in 96-well plates at a density of $2x10^4$ cells/well and transduced using rAAV2/8.RK.coRPGR and rAAV2/8.RK.wtRPGR at a multiplicity of infection (MOI) of 10,000 vg per cell. Control wells were transduced with rAAV2/8 carrying GFP as transgene driven either by the photoreceptor specific rhodopsin kinase promoter (rAAV2/8.RK.GFP) or the stronger, ubiquitous CAG promoter (rAAV2/8.CAG.GFP). Further control wells were transfected with plasmids using the Mirus *Trans*IT®-LT1 Transfection Reagent (Geneflow Ltd., Lichfield, UK) described in detail in chapter 2.1.2. A pRK.GFP expression plasmid was used to control for transfection efficiency and pRK.coRPGR and pRK.wtRPGR expression plasmids were used to control for antigen-detection in the downstream ICC based analysis.

GFP expression was first detected at day 7 and was restricted to few cells treated with the rAAV2/8.CAG.GFP vector. All cells were fixed and processed for transgene expression on day 11 post transfection/-duction (**Fig. 4.3**). Only the cells transfected with pRK.coRPGR showed convincing levels of transgene expression, while the pRK.wtRPGR was almost completely without signal and no signal could be

recorded from any of the transduced cells (except the positive control transduced with the rAAV2/8.CAG.GFP vector).

a

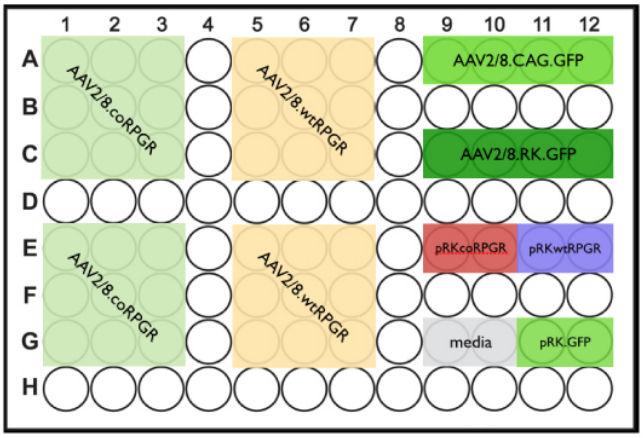

b

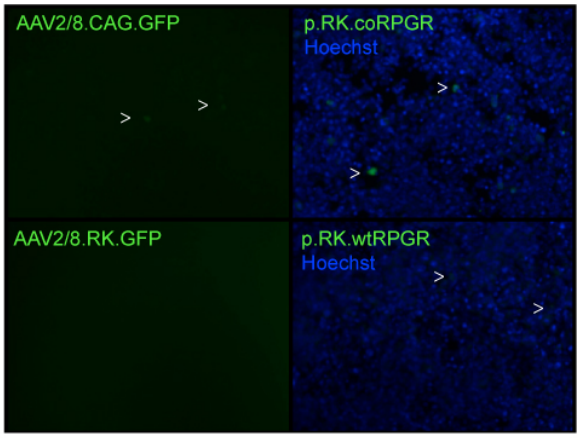

c

	d1	d2	d3	d4	d5	d6	d7	d8	d9	d10	d11	ICC
AAV2/8.coRPGR	-	-	-	-	-	-	-	-	-	-	-	-
AAV2/8.wtRPGR	-	-	-	-	-	-	-	-	-	-	-	-
AAV2/8.CAG.GFP	-	-	-	-	-	-	+	+	+	+	(+)	(+)
AAV2/8.RK.GFP	-	-	-	-	-	-	-	-	-	-	-	-
pRKcoRPGR	-	-	-	-	-	-	-	-	-	-	-	+++
pRKwtRPGR	-	-	-	-	-	-	-	-	-	-	-	+
pRK.GFP	(+)	+	+	+	+	+	+	+	+	+	+	+
RPMI neg control	-	-	-	-	-	-	-	-	-	-	-	-

Fig. 4.3 Transduction of HEK293T cells with different recombinant AAVs. a) The experimental outline is displayed on the 96 well plate. b) Representative recordings of the very weak GFP signals in cells transduced with AAV2/8.CAG.GFP (arrow heads in top left panel) compared to no signal from the corresponding vector with the RK promoter (bottom left). Immunocytochemical staining of RPGR (SIGMA N-terminal) with AlexaFluor 488 as 2° antibody in cells after coRPGR (top) or wtRPGR plasmid transfections (right panels) showed more transgene expression in cells transfected with the codon optimised construct (arrow heads). c) Overview of the readout per category. The results overall suggest that AAV2/8 did not manage to transduce HEK293T cells very well and that the RK promoter additionally limited potential transgene expression.

4.4.3.2 Transduction experiments on SH SY5Y cells

To test whether cells of more neuronal lineage might be more efficiently transduced, SHSY5Y cells (see section 2.2.2) were used. This time, a range of different MOIs (5,000 - 20,000) were applied to see whether this might allow transgene expression based on *in vitro* transduction with AAV2/8.RK.coRPGR and AAV2/8.RK.wtRPGR. Neuron-specific differentiation with RA and TPA was initiated 24h after seeding and transfection/-duction was performed after further 48h. Daily monitoring for GFP fluorescence as surrogate marker for transgene expression only showed positive signal in the pRK.GFP plasmid positive control. Not even cells transduced with the AAV2/8.CAG.GFP demonstrated convincing transgene expression (not shown). ICC on day 14 demonstrated a previously unnoticed punctate staining pattern concordant with inherent RPGR expression: low numbers of cells with this positive staining were found in all wells - including those with negative controls 'treated' with media only. These cells demonstrated two distinct subcellular structures positive for RPGR (**Fig. 4.4**). Given their position relative to the Hoechst staining and the organisational pattern of chromosomal material, the most likely explanation was that the signal derived from inherent RPGR localised to the centrioles [149]. The antibody used in this experiment would pick up the constitutive RPGR$^{ex1\text{-}19}$ variant known to associate with these structures as it targets the common N-terminal sequence of RPGR.

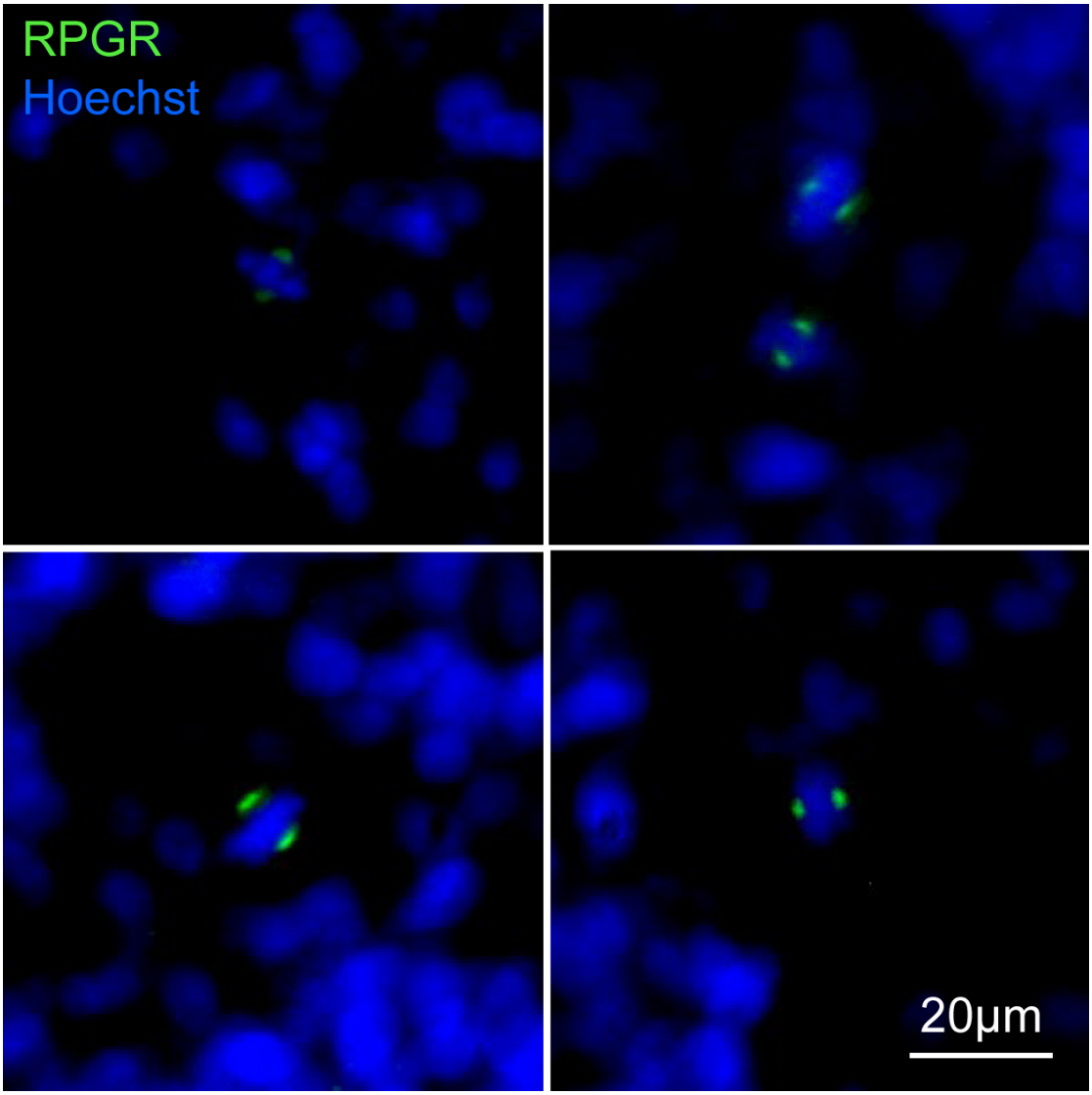

Fig. 4.4 RPGR staining pattern in SHSY5Y cells. Representative images from SHSY5Y cells after immunocytochemical staining with N-terminal anti-RPGR (SIGMA), Alexa Fluor 488 as secondary antibody and Hoechst 33342. Note the distinct bipolar staining pattern in transduced (both left panels) as well as in the naïve (both right panels) SHSY5Y cells alike. This suggests co-localisation of inherent RPGR with centrioles during mitosis.

4.4.3.3 Transduction experiments on 661W cells

We used 661W cells even though they are of murine and not human origin because they are seen as cone photoreceptor like cells (see chapter 2.2.3). Indeed, transduction of these cells with AAV2/8.RK.coRPGR and AAV2/8.RK.wtRPGR resulted in RPGR

transgene expression *in vitro* indicating the infectivity of the AAV vectors and suggesting their ability to lead to transgene expression in photoreceptors (**Fig. 4.5**).

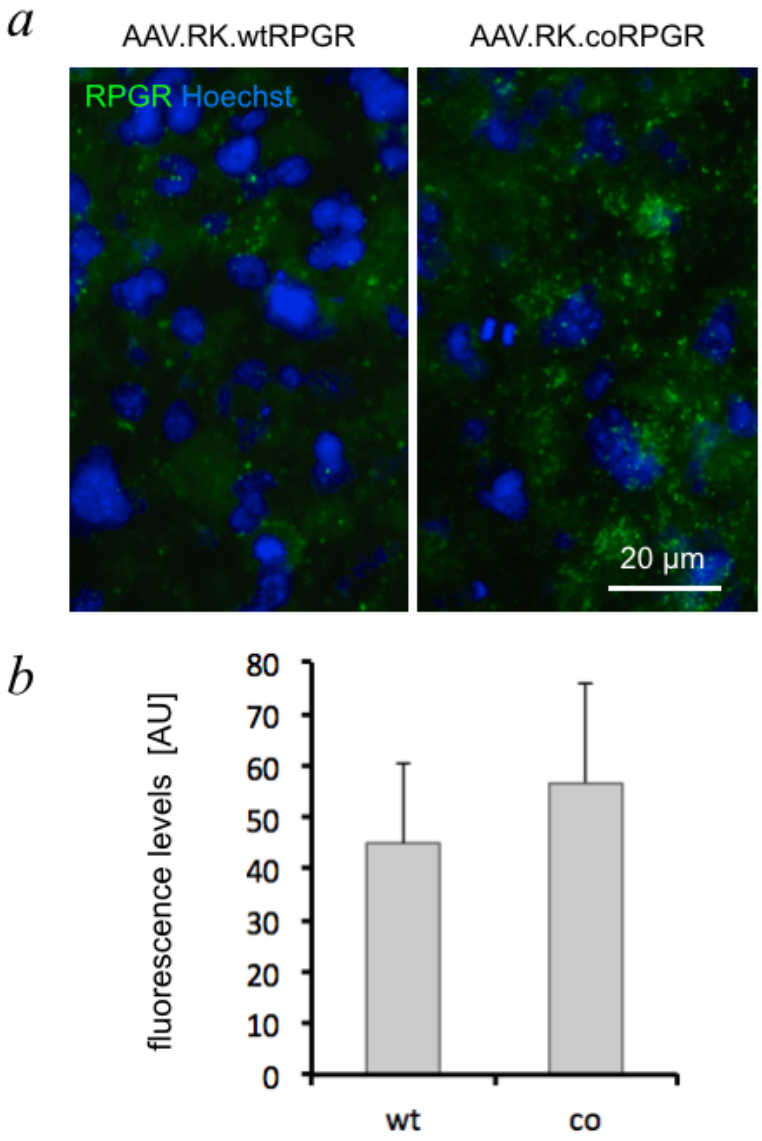

Fig. 4.5 Transduction of 661W cells with AAV.RK.wtRPGR and AAV.RK.coRPGR. a) ICC illustrate punctate signal from anti-RPGR staining in absence of ciliary structures in 661W cells. b) Quantification of fluorescence signal between transductions with wt or coRPGR do not yield a statistical significant difference (box plots show mean and standard deviation), but a trend for higher expression based from the codon optimised construct (Student's t-test; $p = 0.12$; n = 6).

4.5 Discussion

Qualitative analysis by SDS-PAGE showed three clear bands at the expected ratio of 1:1:10 reflecting the protein capsid composition VP1:VP2:VP3 for the AAV8 capsid. There were no additional bands visible indicating a clean production of recombinant AAV ready for *in vitro* and *in vivo* applications.

Three different techniques were used to quantify the vector titre. Traditionally, the titre is estimated by qPCR after DNAse treatment of the sample and reports the calculated number of vector genomes per ml. This test presents the number of DNAse resistant particles (i.e. fully formed capsids), which hold the transgene with the DNA sequence used in the amplification step of the qPCR. As the vector production in HEK293T cells relies on dual transfection with the potential of some cells being transfected with only the rep/cap/helper plasmid or the transgene plasmid, a certain number of empty capsids or free nucleic acid molecules will be purified along with the complete and full virions. Additionally, cells, which were successfully transfected with both plasmids will produce complete and full virus, but might be in the process of doing so at time of harvest. Thus these cells might also contribute empty or partly filled capsids and naked viral genomes. The information of free nucleic acid content and empty capsids in the final vector solution is important because it influences its pharmacology and its potential for negative effects such as immune-reactivity [150].

We showed that the purification technique applied resulted in a ratio of about 1:4 packaged to free nucleic acid content and about 1:10 to 1:20 when comparing full to empty capsids. qPCR only ‘counted’ the full capsids as the preceding DNAse treatment destroyed all heterogeneous nucleic acid fragments derived from the host

cell and helper components such as 'naked' viral genomes and because empty capsids could not contribute to the amplification of viral genome particles in the polymerase chain reaction. The titres from the qPCR assessment were thus the lowest and at the same time the most relevant to determine the MOI for *in vitro* and *in vivo* experiments as neither empty capsids nor naked DNA would effectively contribute to gene transfer.

While AAV2 readily transduces HEK293T cells *in vitro*, its success to transduce photoreceptors *in vivo* is limited. The reverse is true for AAV8, which features different surface proteins in its capsid structure and therefore presents a different tropism. AAV8 readily transduces photoreceptors *in vivo*, but does not seem to favour HEK293T as target cells [96, 145]. This has also been observed by Dr. De Silva (personal communication) and may be explained by the differences in surface receptors between HEK293T and photoreceptor cells. This hypothesis was supported by the fact that transduction was more efficient in 661W photoreceptor-like cells. Beside the question of capsid protein – cell surface receptor interaction, use of the rhodopsin kinase promoter was intended to limit expression to photoreceptor cells *in vivo*. Not surprisingly then, expression from control vectors carrying the ubiquitous CAG promoter (AAV2/8.CAG.GFP) were more successful compared to constructs with the RK promoter in expressing their transgene in the non-photoreceptor cell lines such as SHSY5Y.

The successful production of recombinant AAV led to high titres of AAV2/8.RK.coRPGR, AAV2/8.RK.wtRPGR and AAV2/8.control. Analyses of vector solutions using SDS-PAGE, qPCR, DNA quantification and ELISA provided robust evidence of their quality and quantity. *In vitro* tests in three different cell lines

provided evidence of high specificity of the AAV8 vectors with rhodopsin kinase promoter to transduce photoreceptor-like cells and drive transgene expression in these target cells. These results provide the basis for *in vivo* tests to explore the transduction efficiency of recombinant AAV vectors in relevant mouse models and to see whether transgene expression is followed by correct localisation of RPGR to the connecting cilium in photoreceptor cells lacking inherent Rpgr expression.

CHAPTER 5 PILOT STUDY: RPGR GENE THERAPY

5.1 Introduction

RPGR gene therapy aims to reconstitute RPGR expression in target cells, which harbour a disease causing mutation in *RPGR* leading to a complete loss of RPGR (null-mutations) or a dysfunctional protein. One way of achieving this is by introducing a correct copy of *RPGR* cds, which is then translated to RPGR protein by the target cell's own translational machinery. Such a nucleotide sequence can be introduced by means of transduction with a recombinant AAV.

Here we present data from a pilot trial designed to explore the transduction efficiency of recombinant AAV vectors AAV2/8.RK.coRPGR and AAV2/8.RK.wtRPGR after subretinal injection in mice. To model RPGR gene therapy more closely to the clinical scenario, we used *Rpgr*$^{-/y}$ mice, which lack *Rpgr* expression. *Rpgr* is the murine homologue of *RPGR*, the gene affected in most cases of X-linked retinitis pigmentosa (chapter 1) and transgenic *Rpgr*$^{-/y}$ mice thus mimic null mutations in human patients on a genetic level.

We have shown in previous chapters that codon optimised *RPGR* cds features higher expression levels then wild type *RPGR* cds and – crucially – provides greater sequence fidelity while leading to the identical protein product, RPGR^{ORF15}. We further have demonstrated that recombinant AAV vectors AAV2/8.RK.coRPGR and AAV2/8.RK.wtRPGR are able to transduce photoreceptor like cells *in vitro*.

5.2 Aims

The aim of this study was to explore, whether *RPGR* would be expressed *in vivo* following subretinal injection of AAV2/8.RK.coRPGR or AAV2/8.RK.wtRPGR and whether RPGR would be localised to the connecting cilium in photoreceptor cells lacking inherent *Rpgr* expression.

5.3 Materials and methods

Recombinant AAV solutions containing AAV2/8.RK.coRPGR and AAV2/8.RK.wtRPGR were produced and assessed for quality and titre as described in chapters 2-4. To control for the surgical intervention and photoreceptor transduction by AAV2/8, a third construct was used with GFP as reporter gene under control of the CAG promoter (AAV2/8.CAG.GFP; a kind gift by Dr. McClements).

These vector solutions were quantified by qPCR to calculate the number of vector genomes/ml (for details see chapter 2.1.4). Aliquots stored at -80 °C were thawed on ice immediately before application and diluted in balanced salt solution (BSS®) for vitreoretinal surgery (Alcon Laboratories, Camberley, UK) with 0.001% Pluronic® PF-68 (BASF, Ludwigshafen, Germany) to allow subretinal delivery of 1 x 10^{10}vg in 2 µl volume.

Rpgr$^{-/y}$ mice were used for this pilot study as they lack Rpgr expression (for details see chapter 1.2.4 and 2.3.2) while maintaining a connecting cilium for the potential localisation of the transgene product RPGR. Mice were anaesthetised for subretinal injection of 2 µl AAV solution under the superior hemiretina (for details see chapter 2.4).

Three weeks following the surgery, treated *Rpgr*$^{-/y}$ mice were again anaesthetised for *in vivo* retinal imaging using confocal scanning laser ophthalmoscopy (cSLO) to investigate autofluorescence pattern in the animals, which had received AAV2/8.RK.coRPGR, AAV2/8.RK.wtRPGR, and GFP fluorescence as readout of transduction efficiency in the animals treated with AAV2/8.CAG.eGFP.

Immediately after imaging, mice were sacrificed and quickly enucleated. Whole eyes were rapidly processed for immunohistochemistry without fixation as detailed in chapter 2.7.4. Briefly, 16µm sections of unfixed retinal samples were stained with Hoechst 33342 dye and a polyclonal antibody directed against amino acids 379-509 of RPGR (Sigma, HPA001593). Donkey anti-rabbit with conjugated AlexaFluor 488 (Invitrogen) was used as secondary antibody to indicated RPGR detection. High powered (x63 with oil immersion) optical sections were recorded on a confocal microscope (Zeiss LSM710) to investigate RPGR expression and localisation in photoreceptor cells of treated *Rpgr*$^{-/y}$ mice. Untreated mice served as negative control to test the specificity of the assay.

5.4 Results

5.4.1 Surgical outcome

All animals received the intended dose of AAV solution in the subretinal space (**Fig. 5.1**) and recovered well from anaesthesia. This was made possible by the surgical procedure (detailed in section 2.4), which first reduces the intraocular pressure (IOP) by an anterior paracentesis before creating a hemiretinal detachment with the vector suspension. This technique allowed delivery of up to 2 µl volume without developing corneal edema and/or limiting the intraocular circulation due to high IOP. At the same time, the lowered IOP reduced the risk of reflux of subretinal fluid through the injection canal (i.e. into the choroidal circulation or orbit).

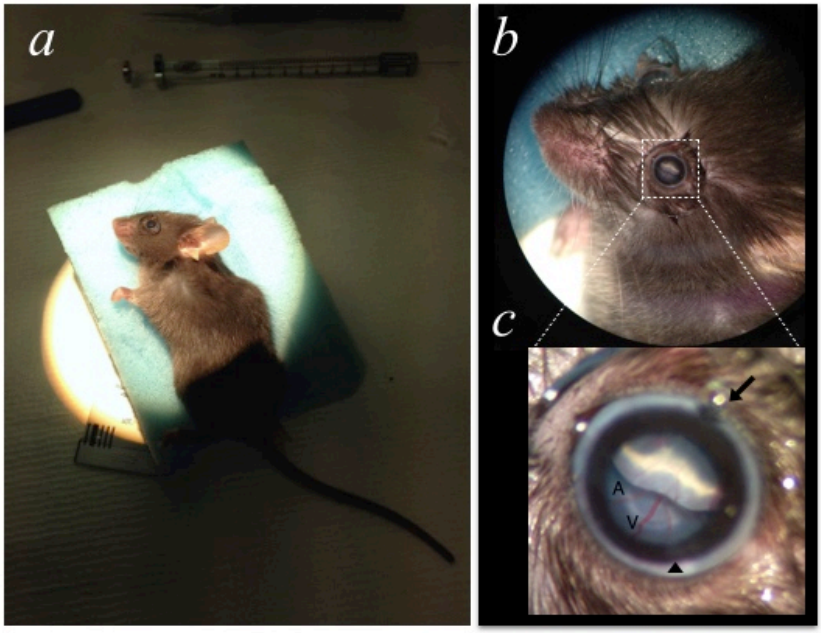

Fig. 5.1 Subretinal delivery of AAV vector solution in mice. a) Anaesthetised mouse under the surgical microscope at the end of surgery. b) View through the microscope at low power provides anatomic overview. c) Detailed recording of the *situs*. Arrowhead indicates site of paracentesis, while needle for subretinal injection was advanced just temporal of the superior rectus muscle (arrow, injection site behind lid). Letters A and V in (c) indicate a retinal artery and vein. Note bullous hemiretinal detachment of the superior retina.

Fundoscopic evaluation of treated mice 24h after the surgery showed complete re-attached retinae in all cases.

5.4.2 Retinal imaging shows safe delivery and reporter gene expression

After 3 weeks, cSLO imaging revealed good optical media with clear view of the fundus in infrared imaging (**Fig. 5.2**). Autofluorescence imaging showed hyperfluorescent dots in treated and untreated eyes of *Rpgr*$^{-/y}$ mice treated with AAV2/8.RK.coRPGR or AAV2/8.RK.wtRPGR. Mice with AAV2/8.CAG.GFP vector application demonstrated strong and ubiquitous GFP derived fluorescence. This indicated robust transgene expression and made it likely that the other recombinant AAV vectors would have had enough time to lead to transgene expression.

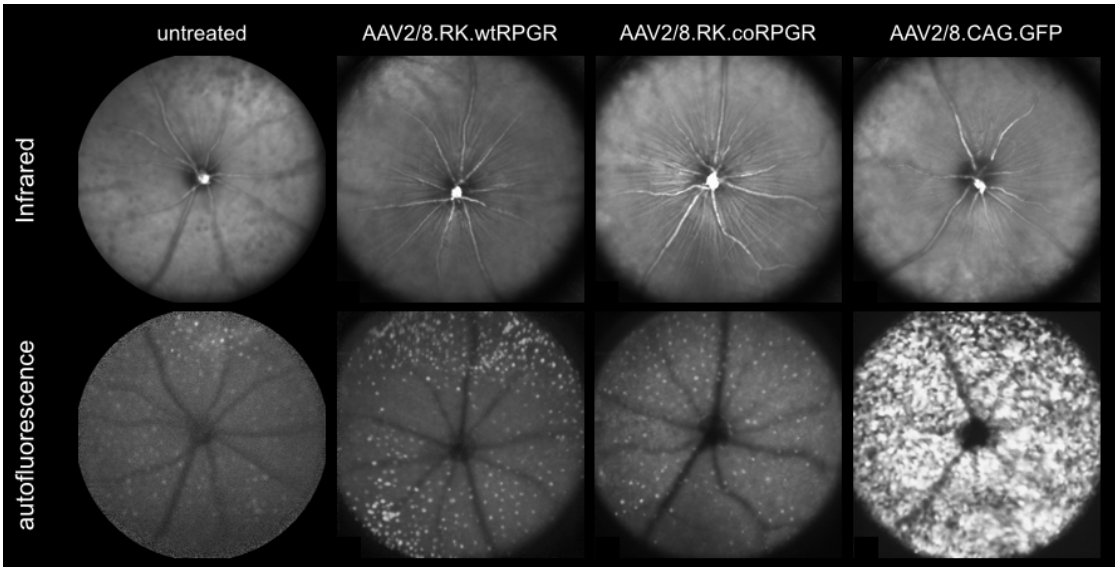

Fig. 5.2 Confocal scanning laser ophthalmoscopy in (un-)treated *Rpgr*$^{-/y}$ mice. Top row shows infrared recordings with focal plane on the inner retina. Bottom row displays recordings in the autofluorescence mode. Untreated (bottom left) and mice treated with AAV.RK.wtRPGR or AAV.RK.coRPGR (bottom middle) all show a punctate pattern of hyperfluorescence. At the same sensitivity setting, the eye treated with AAV.CAG.GFP (bottom right) demonstrates widespread and strong GFP fluorescence beyond the superior hemiretinal detachment indicating successful transduction of cells beyond the site of subretinal vector delivery (Four eyes were treated in treatment cohorts (Table 6.2) with 2µl containing 1 x 10^9 vg per injection).

5.4.3 Immunohistochemistry shows RPGR expression

Despite some technical difficulties related to handling unfixed sections, specific signal could be observed in sections from treated but not in those from untreated mice (**Fig. 5.3**). This signal stems from antibody binding to the RPGR epitope and is consistent with *RPGR* expression due to transduction with an AAV carrying *RPGR* as transgene. The more robust signal was seen in sections from eyes treated with AAV2/8.RK.coRPGR, the AAV carrying the codon optimised cds of *RPGR*.

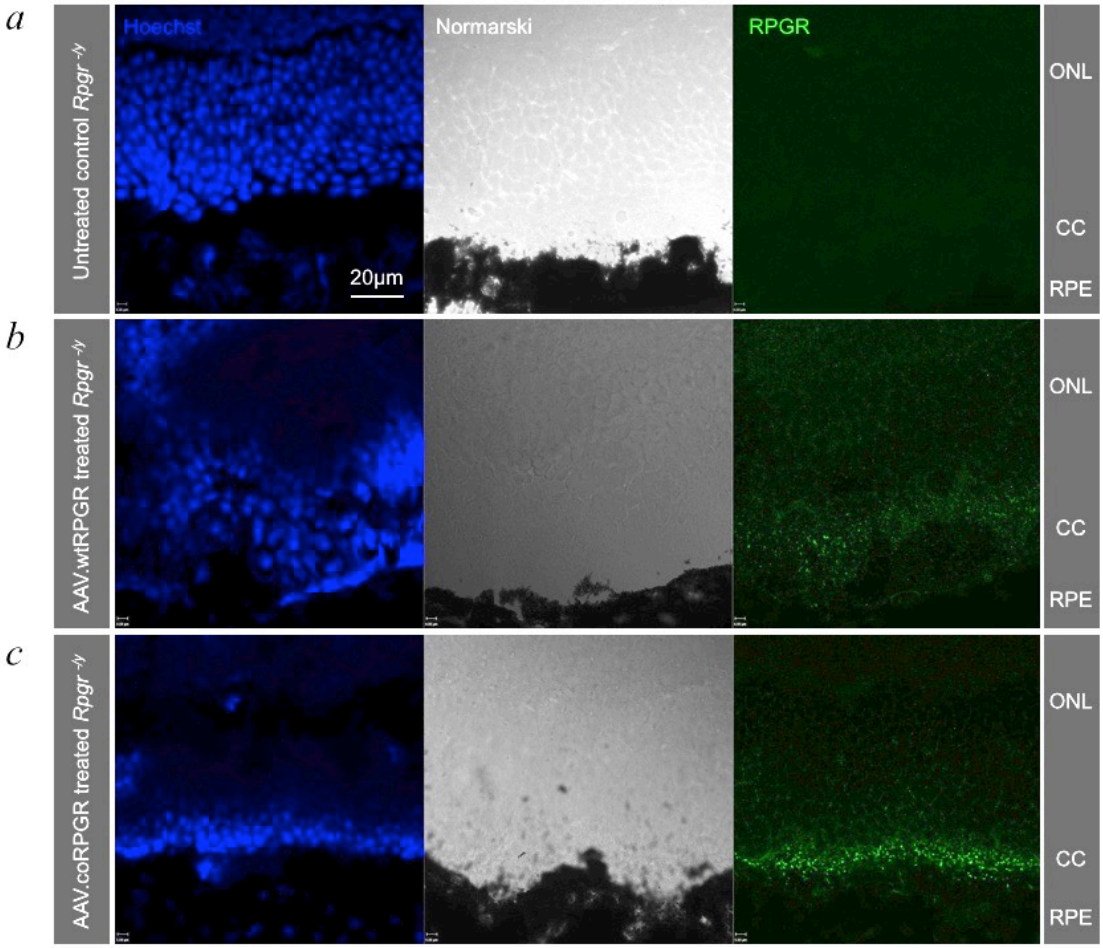

Fig. 5.3 Immunohistochemistry shows RPGR in treated *Rpgr*$^{-/y}$ mice. a) Untreated eye of an *Rpgr*$^{-/y}$ animal shows absence of RPGR staining. b) Single treatment with AAV.RK.wtRPGR results in limited signal, most of which is localised to the region between inner and outer segments (cc = connecting cilium). c) *Rpgr*$^{-/y}$ mice treated with codon optimised vector show the most convincing RPGR expression in this representative section. Four eyes were treated in treatment cohorts (Table 6.2) with 2µl containing 1 x 10^9 vg of AAV.

5.5 Discussion

The surgical technique applied here allowed safe application of up to 2 µl into the subretinal space of mice. The resulting hemiretinal detachment spontaneously re-attached within 24h in all animals and no ocular sequelae were observed. At the same time it prevented (temporary) corneal oedema formation and/or cessation of intraocular circulation as can be observed after subretinal injections without prior paracentesis (unpublished observation). Optical media remained clear for the following 3 weeks and there was no indication of intraocular pathology such as cellular infiltrates, anterior/posterior synechiae of the iris or cataract formation.

Retinal imaging demonstrated robust levels of GFP transgene expression in the control group, which had received AAV2/8.CAG.GFP. Interestingly, the reporter protein GFP was evident across the whole retina, even though the immediate application was limited to the superior hemiretina. This indicates at least some degree of transduction of cells outside the detachment area. One has to bear in mind though, that GFP was driven by the unspecific CAG promoter, which leads to ubiquitous transgene expression not limited to photoreceptors. This is in contrast to the vectors carrying the $RPGR^{ORF15}$ cds, in which the rhodopsin kinase promoter drives photoreceptor specific expression of $RPGR^{ORF15}$.

Eyes treated with AAV2/8.RK.coRPGR or AAV2/8.RK.wtRPGR showed normal retinal vasculature and nerve fibre layer as indicated by the infrared images focused on the inner retina (**Fig. 5.2**). However, their autofluorescence recordings showed hyperfluorescent dots likely corresponding to macrophages loaded with phagocytised autofluorescent photoreceptor debris as a result of the retinal

degeneration due to Rpgr deficiency [151]. In contrast, mice treated with AAV2/8.CAG.eGFP vector demonstrated strong and ubiquitous GFP derived fluorescence (**Fig. 5.2**). This is concordant with previous reports that AAV2/8 shows a fairly rapid onset of transgene expression after subretinal delivery [96, 145].

Unfixed sections provided evidence of RPGR expression and localisation to the connecting cilium in *Rpgr*$^{-/y}$ mice. This is the first evidence for a successful application of a codon optimised RPGR vector sequence. Other groups have previously been successful to restore full length or abbreviated *Rpgr* in *Rpgr*$^{-/y}$ mice [121, 152]. Wild type or mutated human RPGR has also been successfully expressed in in *Rpgr*$^{-/y}$ mice [121, 122] and dogs with XLPRA1 and XLPRA2 (see chapter 1.2.4 and [153]). However, in some of those studies, mutations during the development of the vector used for transgene expression caused alternative protein products, while this work provides evidence for expression and correct localisation of RPGR based on a codon optimised sequence, which translates into a wild type RPGR protein product.

Interestingly, this study confirmed previous observations (above) that transgenic and heterologous RPGR localises to the connecting cilium in mice or dogs, which may be surprising given a sequence homology of only 55% (amino acid sequence) between *Homo sapiens* and *Canis lupus familiaris* or *Mus musculus*. On the other hand, key motifs of RPGR^{ORF15} (e.g. RLD, C-terminus) are fairly conserved across species [49], which may help to explain correct localisation and a functional rescue by RPGR replacement in mice or dogs. Given the successful pilot trial with AAV2/8.RK.coRPGR, we planned a more thorough study (next chapter) to investigate the safety and efficacy of AAV2/8.RK.coRPGR as a potential treatment option for XLRP3.

CHAPTER 6 SAFETY AND EFFICACY OF RPGR GENE THERAPY

6.1 Introduction

Developing gene therapy for XLRP has remained a challenge for a number of reasons. One is the purine rich, repetitive sequence of *RPGR*^{ORF15}, which makes it difficult to clone without encountering spontaneous mutations. Confirming the integrity of the sequence by Sanger sequencing is also problematic as the frequent poly-guanine runs cause DNA polymerases to stall or stop.

A second problem is the mild phenotype in murine disease models such as *Rpgr*$^{-/y}$ and *C57BL/6J*$^{Rd9/Boc}$ mice [76, 77]. With relatively small structural and functional differences between these disease models and wild type controls, it is difficult to reach a statistical significance level in a treatment cohort.

To address the first point, we applied the principle of codon optimisation to change the primary nucleotide sequence of the *RPGR*^{ORF15} coding sequence. Because only synonymous codons were used, the resulting amino acid sequence remained unchanged while the codon optimised *RPGR* construct featured superior sequence stability and translational efficiency compared to the wild type *RPGR* construct. This benefit was evident *in vitro* when using plasmid transfections and transduction experiments with AAV constructs. The same AAV constructs were then used in a pilot trial to demonstrate their potential to transduce photoreceptors. Resulting RPGR protein was localised to the connecting cilium, its physiological compartment in photoreceptors.

To address the second issue with small differences between cohorts with and without disruptive *Rpgr* mutations, we performed a sample size and power calculation based on relevant, objective and quantitative outcome measures.

6.2 Aims

The aim of this work was to test the efficacy of AAV.RK.coRPGR as gene therapeutic agent for XLRP3 in two relevant animal models (*Rpgr*$^{-/y}$ and *C57BL/6J*$^{Rd9/Boc}$ mice) and to explore any potential toxic effects in wild type animals (*C57BL/6J*). The study design was chosen to provide robust statistical evidence with the potential to serve as a basis for regulatory approval of a clinical phase I trial.

6.3 Materials and methods

6.3.1 Sample size and power calculations

Sample size and power calculations were performed using a JavaScript based algorithm provided by Rollin Brant from the University of California, San Francisco Department of Epidemiology & Biostatistics, Division of Biostatistics (http://www.stat.ubc.ca/~rollin/stats/ssize/). Primary outcome measure used for this was the a-wave amplitude [μV] after a dark-adapted single flash stimulus at 0.01cd.s/m^2, which reflects the physiology of the vast majority of photoreceptors in the mouse retina, the target cell population in this study.

These electroretinographic (ERG) responses were measured as detailed in chapter 2.5 and mean and standard deviations for n = 4 per cohort (*C57BL/6J*, *C57BL/6J*$^{Rd9/Boc}$, and *Rpgr*$^{-/y}$ mice) calculated in Excel. Before calculating the sample size, difference of mean a-wave amplitude between *C57BL/6J* (target normal value) and *C57BL/6J*$^{Rd9/Boc}$ (baseline before treatment) and between *C57BL/6J* and *Rpgr*$^{-/y}$ was calculated and ½ of this added to the current mean of the respective disease models assuming a 50% gain due to treatment. This provided values for μ_0 (mean of untreated cohort) and μ_1 (mean of treated cohort). Value for σ (standard deviation of the sampled population) was set to the standard deviation of the a-wave amplitude in the respective disease model. A one-sided test design was assumed, the type I error

rate set to $\alpha = 0.05$ and the desired power defined as 90% for the sample size calculation.

A comparable sample size was then used to calculate the power to detect toxic effects in *C57BL/6J* mice. For this, a loss of 10% of the mean a-wave amplitude at baseline was assumed as toxic effect and the baseline standard deviation entered as σ.

6.3.2 Trial design

ERG responses were chosen as primary outcome measure as objective and quantitative biomarker of retinal function that is relevant to the disease process and an appropriate readout for potential therapeutic and/or toxic effect of the test item, AAV.RK.coRPGR. Due to relatively high inter-individual variability within cohorts, a intra-individual testing paradigm was chosen: one eye would be treated with AAV.RK.coRPGR (*verum*) while the contralateral eye would serve as control. In order to capture the natural disease process and have a control injection with an inactive substance (AAV.control) in such a design, two parallel trials were run: one (necessarily) open label trial with unilateral treatment of randomised eyes with AAV.RK.coRPGR was used to compare treatment effect vs. natural disease process. The second design was a masked trial with a random selection of eyes receiving AAV.RK.coRPGR or AAV.control. The latter trial was used to control for the effect of surgery and AAV exposure. All 129 animals were treated with weaning at postnatal day P22±2 and tested at three subsequent time points: postnatal month 2 (PM2), PM4

and PM6 before sacrifice (**Fig. 6.1**). ERG was recorded at all three time points and the cSLO was performed additionally at the last time point PM6.

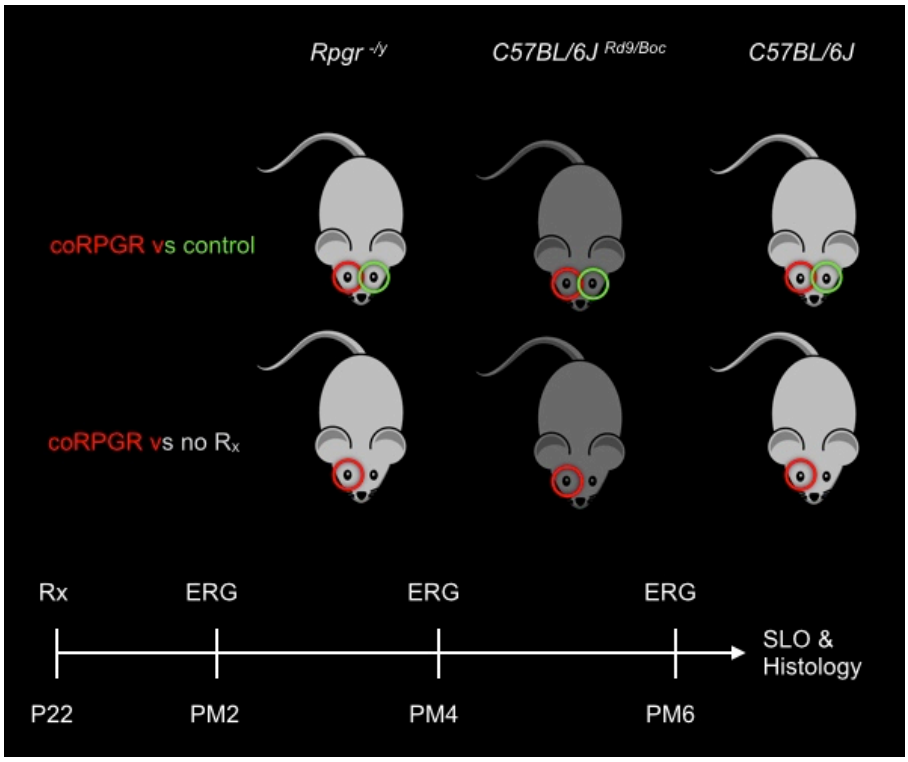

Fig. 6.1 Design of the efficacy and toxicology study. *Rpgr*$^{-/y}$, *C57BL/6J*$^{Rd9/Boc}$, and *C57BL/6J*, mice are subjected to either a masked bilateral treatment testing AAV.RK.coRPGR vs. AAV.control (top) or an unilateral treatment with AAV.RK.coRPGR alone. All eyes were randomly assigned to *verum* vs. sham treatment or treatment vs. no treatment. Surgery was performed at postnatal day 22 (P22) and followed up at postnatal month 2 (PM2), PM4 and PM6 with electroretinography (ERG). At PM6, scanning laser ophthalmoscopy (SLO) was performed before sacrifice and processing of eyes for histology or Western blotting.

6.3.3 C57BL/6J wild type mice

A total of n=47 *C57BL/6J* mice were treated in the two trials (**Fig. 6.1**) to explore potential toxic effects of subretinal AAV2/8.RK.coRPGR delivery. 24 animals received unmasked unilateral treatment, where the eye was chosen in a

randomised fashion. Treatment consisted of a single subretinal injection of $1.5x10^9$vg AAV2/8.RK.coRPGR diluted in BSS® with 0.001% PF-68. The remaining 23 animals received bilateral injections in a masked and randomised fashion. Treatment in the *verum* group was as above, while the control group received $1.5x10^9$vg AAV2/8.control diluted in the same vehicle (BSS® with 0.001% PF-68). Both vectors are described in detail in chapter 4.

Subretinal injections were performed with weaning at 3 weeks of age as detailed in chapter 2.4 and 5. A grading system (0-10) was used by the surgeon to indicate quality of the subretinal injection, where 0/10 denotes no vector delivery and 10/10 full vector delivery without any form of complication such external (e.g. subconjunctival) or internal (e.g. intra-retinal /-vitreal) haemorrhage during or after the subretinal injection. A grade 9/10 was for example given in case of complete vector delivery, but minor subconjunctival bleed (see **Table 6.1**). Poor injections were defined as a grade ≤ 7 and were excluded from the trial (indicated grey in **Table 6.1**).

Table 6.1 Overview of parameters leading to surgical classification.

% vector delivered	no bleed	minor external bleed	major ex- / minor internal bleed	major internal bleed
100	10/10	9/10	8/10	7/10
90	9/10	8/10	7/10	6/10
80	8/10	7/10	6/10	5/10
70	7/10	6/10	5/10	4/10
60	6/10	5/10	4/10	3/10
50	5/10	4/10	3/10	2/10
40	4/10	3/10	2/10	1/10
30	3/10	2/10	1/10	0/10
20	2/10	1/10	0/10	0/10
10	1/10	0/10	0/10	0/10
0	0/10	0/10	0/10	0/10

Table 6.1 Point system from 0-10 was used to semi-quantitatively assess quality of surgical procedure. Parameters taken into account were % of vector suspension delivered (left) and amount and location of bleeding. Only good (8/10) to excellent (10/10) surgical results (all in light grey) were considered as successful vector delivery.

Surgical intervention was followed by longitudinal observation of intra-individual changes in ERG recordings (protocol described in detail in chapter 2.5 and **Fig. 6.1**) at postnatal month two (PM2) and PM4. At PM6, additional SLO imaging of the retina was performed (protocol in chapter 2.6) immediately after ERG recordings.

Mice were sacrificed at the last time point (PM6), and eyes dissected for transgene detection by Western blot or immunohistochemistry (details in chapter 2.7.3-4).

6.3.4 C57BL/6J$^{Rd9/Boc}$ mice

A total of n=36 *C57BL/6J*$^{Rd9/Boc}$ mice were treated in both trials (**Fig. 6.1**). 19 animals received unmasked unilateral treatment, while 17 animals were enrolled to receive masked and randomised bilateral injections with *verum* or control as described above for *C57BL/6J* mice. This was done to assess efficacy of AAV based RPGR gene replacement gene therapy. Follow-up was scheduled as above.

6.3.5 Rpgr$^{-/y}$ mice

Rpgr$^{-/y}$ mice were used to assess efficacy of AAV based RPGR gene replacement gene therapy in a second animal model of XLRP. For this, a total of n=46 were treated in the two separate trials described above (**Fig. 6.1**). 25 animals received

unmasked unilateral treatment, while 21 animals were treated in both eyes (*verum* and control) as described above. Post-interventional readout was scheduled as above for *C57BL/6J* mice.

6.4 Results

6.4.1 Sample size and power calculations

Calculated sample size was based on ERG data collected from four eyes (two animals) per cohort (*C57BL/6J*, *C57BL/6J*$^{Rd9/Boc}$, and *Rpgr*$^{-/y}$ mice). The average a-wave amplitude of n = 9 trials was recorded (see table below) for each eye.

Table 6.2 Electroretinography results from six adult mice.

Dark adapted single flash [0.01 cd.s/m^2]	**a-wave amplitude [µV]**
C57BL/6J #1 OS	84.84
C57BL/6J #1 OD	76.60
C57BL/6J #2 OS	73.61
C57BL/6J #2 OD	89.20
Rpgr$^{-/y}$ 8.1.3 OS	80.54
Rpgr$^{-/y}$ 8.1.3 OD	64.47
Rpgr$^{-/y}$ 8.1.5 OS	67.14
Rpgr$^{-/y}$ 8.1.5 OD	76.67
C57BL/6J$^{Rd9/Boc}$ 3.1.1 OS	77.01
C57BL/6J$^{Rd9/Boc}$ 3.1.1 OD	71.68
C57BL/6J$^{Rd9/Boc}$ 3.1.3 OS	54.37
C57BL/6J$^{Rd9/Boc}$ 3.1.3 OD	56.13

Table 6.2 Adult mice (*C57BL/6J*, *C57BL/6J*$^{Rd9/Boc}$, and *Rpgr*$^{-/y}$ at ca. P28) were used to obtain electroretinographic data for sample size calculations. A-wave amplitudes from four eyes (two animals) per cohort were recorded using a dark-adapted single flash stimulus at 0.01 cd.s/m^2 intensity.

After calculating the μ_0, μ_1 and σ values from the data above, the suggested sample sizes ranged from 16 to 21. The *C57BL/6J*$^{Rd9/Boc}$ mice featured the smallest amplitude (65±11µV; mean±standard deviation) compared to the wild type control (81±7µV) and therefore only required an estimated sample size of n=16. The

suggested sample size for *Rpgr*$^{-/y}$ was n=21 due to its higher amplitude at baseline (72±8μV). Power calculations showed that a loss of 10% amplitude from baseline in wild type mice would be detected with a power of 100% using a cohort size of n=20.

6.4.2 *C57BL/6J* wild type mice

Six eyes were excluded from the trial due to poor surgery and one was excluded due to pre-existing anterior segment changes. This resulted in an overall cohort size of n=19 for the unilateral trial and n=22 for the bilateral trial. The average [and range] of the documented surgical quality was very similar in all groups: 9.0 [8-10] for the open label, 9.5 [8-10] for the *verum* and 9.3 [8-10] in the control group. Representative images from the surgery are shown in **Fig. 6.2**. All mice recovered

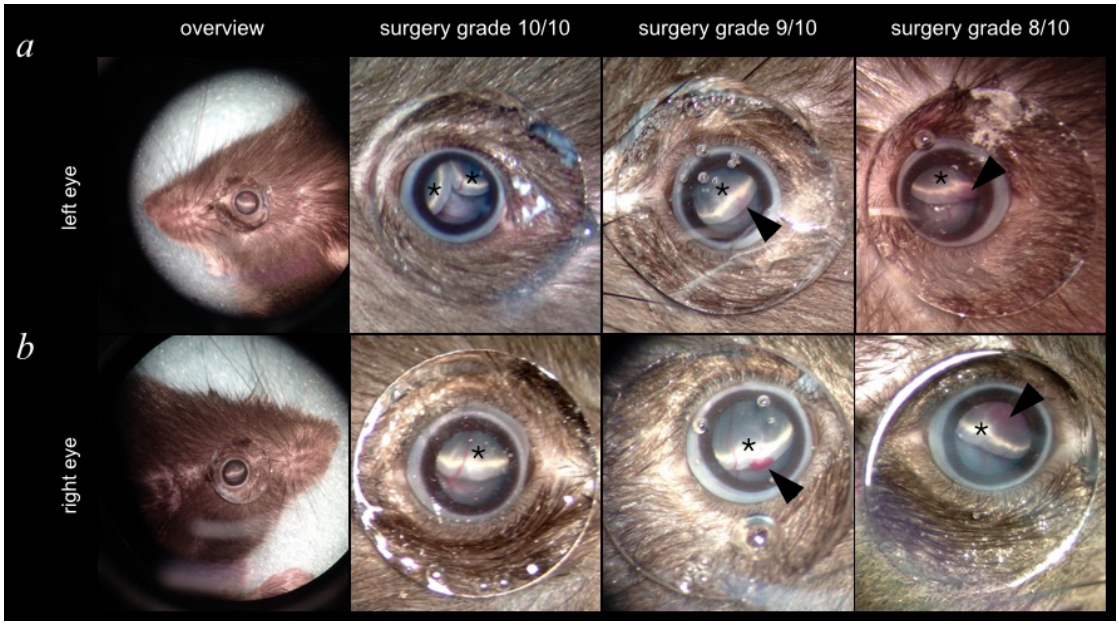

Fig. 6.2 Representative images from surgery in *C57BL/6J* mice. Top panel shows examples from injections in the left eye, bottom panel shows injections in the right eye. Overviews on the left are from low power magnification views through the surgical microscope. During surgery, a higher magnification level is chosen as depicted in the other images, which show typical surgical outcomes rated 10/10 in absence of any complication, 9/10 in case of minimal bleeding and 8/10 in case of slightly more substantial epi-/intraretinal (top right) or subretinal (bottom right) bleeding. Asterisks indicate detachments and arrowheads point to haemorrhages.

quickly after surgery and were kept under standard conditions (see chapter 2.3) until the appropriate timepoint for follow up ERG recordings at PM2, PM4 and PM6.

Due to software issues, a total of four ERG data sets (individual mice at individual time points) were lost. Two of those concerned animals from the unilateral trial (one at PM2 and one at PM4) and two from the bilateral trial (both at PM2). One animal from the bilateral trial did not recover from anaesthesia at PM2. All other recordings (n=120 ERG data sets from 40 mice at three time points) were successfully recorded and saved for further analysis.

None of the recorded signal intensity series either under dark or light adapted conditions showed a significant difference between treated vs. untreated (**Fig. 6.3**) or between *verum* vs. control group (**Fig. 6.4**) at any time point. Retinal imaging with scanning laser ophthalmoscopy (SLO) also confirmed that there was no toxic effect to be observed on retinal structure up to 6 months after subretinal application of AAV.RK.coRPGR (**Fig. 6.5**).

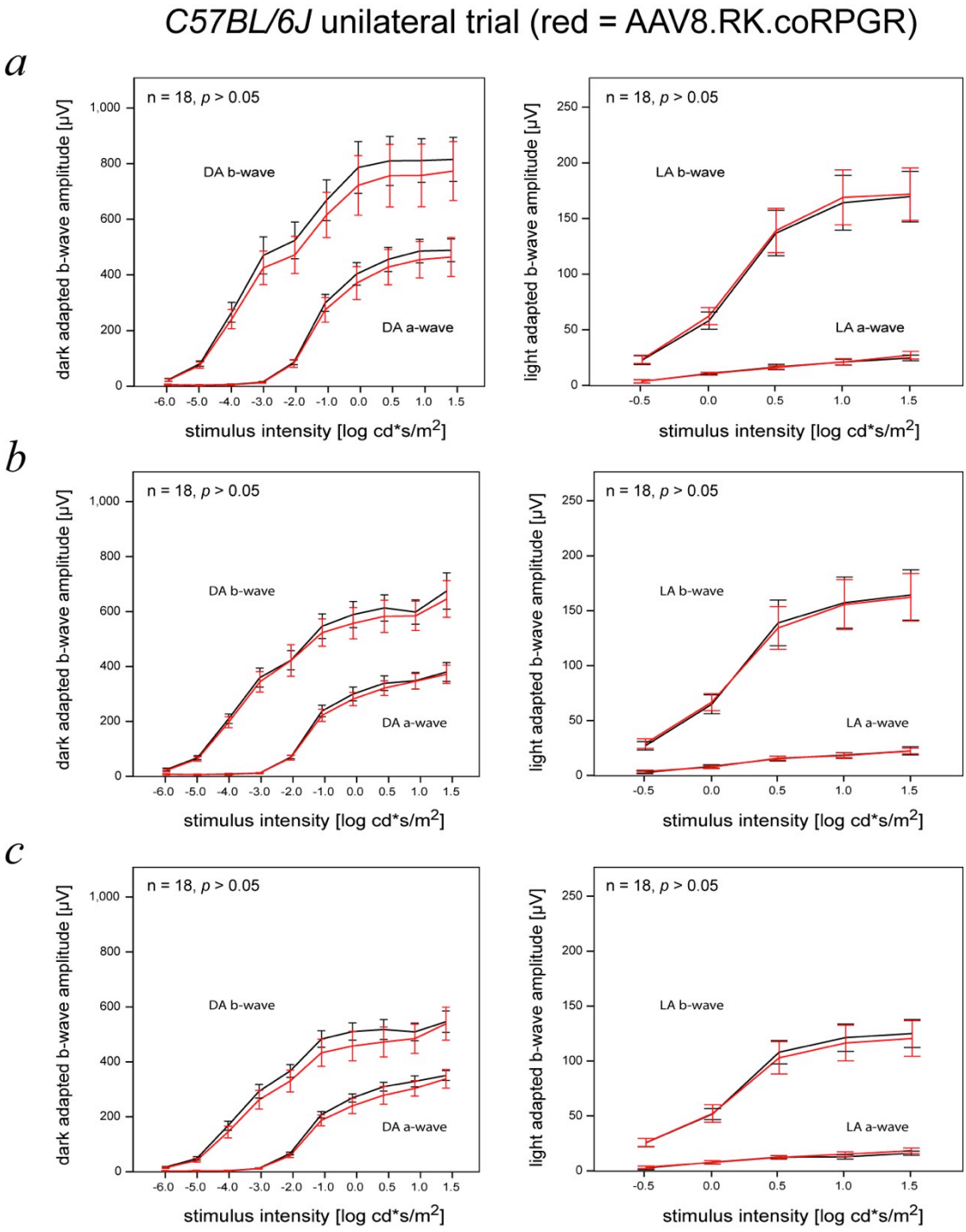

Fig. 6.3 ERG recordings in *C57BL/6J* mice after unilateral subretinal injection of AAV.RK.coRPGR. Red lines represent data from treated eyes, black from untreated eyes. a) shows data from PM2, b) from PM4 and c) from PM6, the last time point tested. Factorial ANOVA for repeated measures retained the null hypothesis (no difference) in all analyses. Lines indicate mean amplitudes ± 95% confidence interval (whiskers).

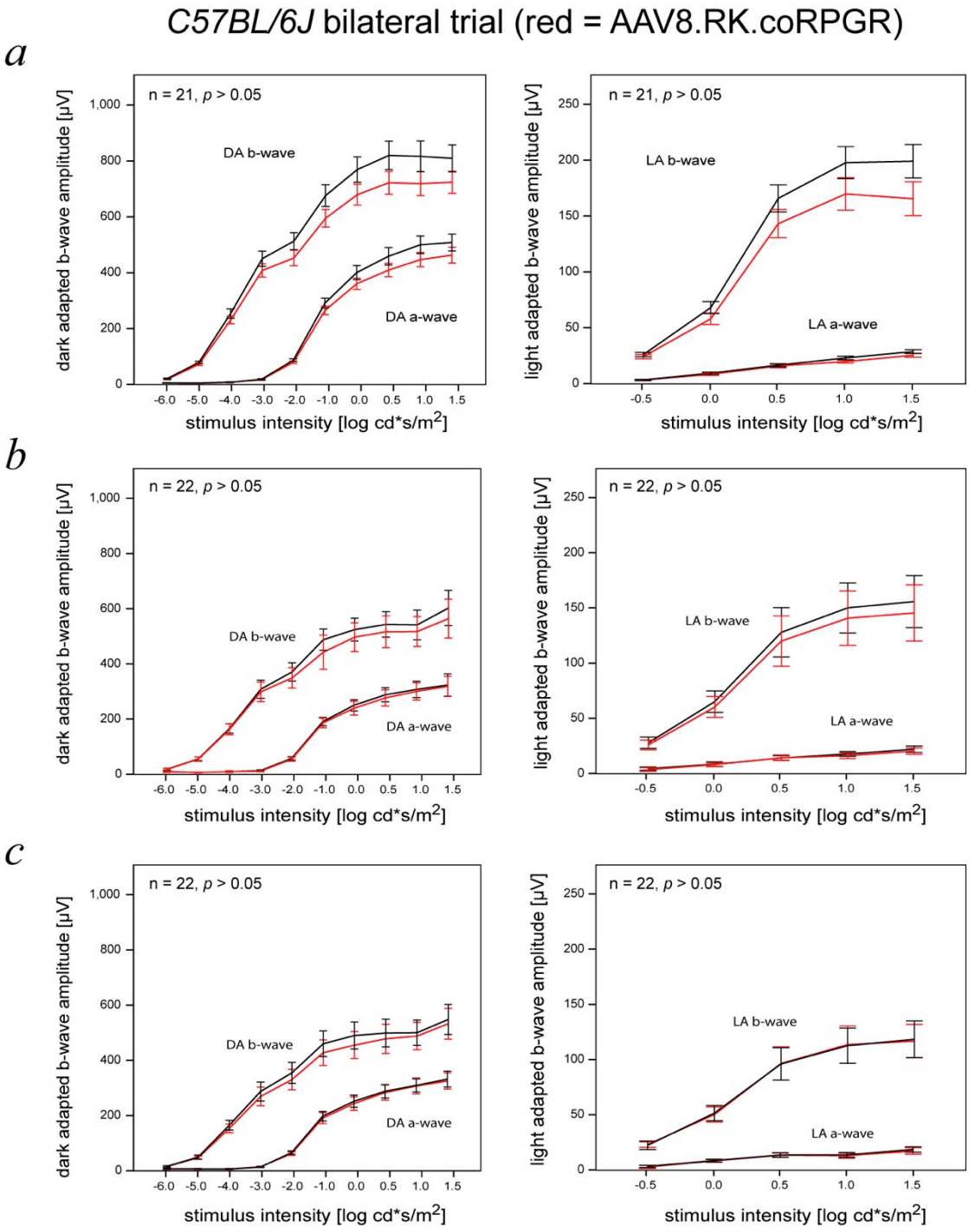

Fig. 6.4 ERG recordings in *C57BL/6J* mice after bilateral subretinal injection of AAV.RK.coRPGR (red) or AAV.control (black). a) shows data from PM2, b) from PM4 and c) from PM6, the last time point tested. Factorial ANOVA for repeated measures retained the null hypothesis (no difference) in all analyses. Lines indicate mean amplitudes ± 95% confidence interval (whiskers).

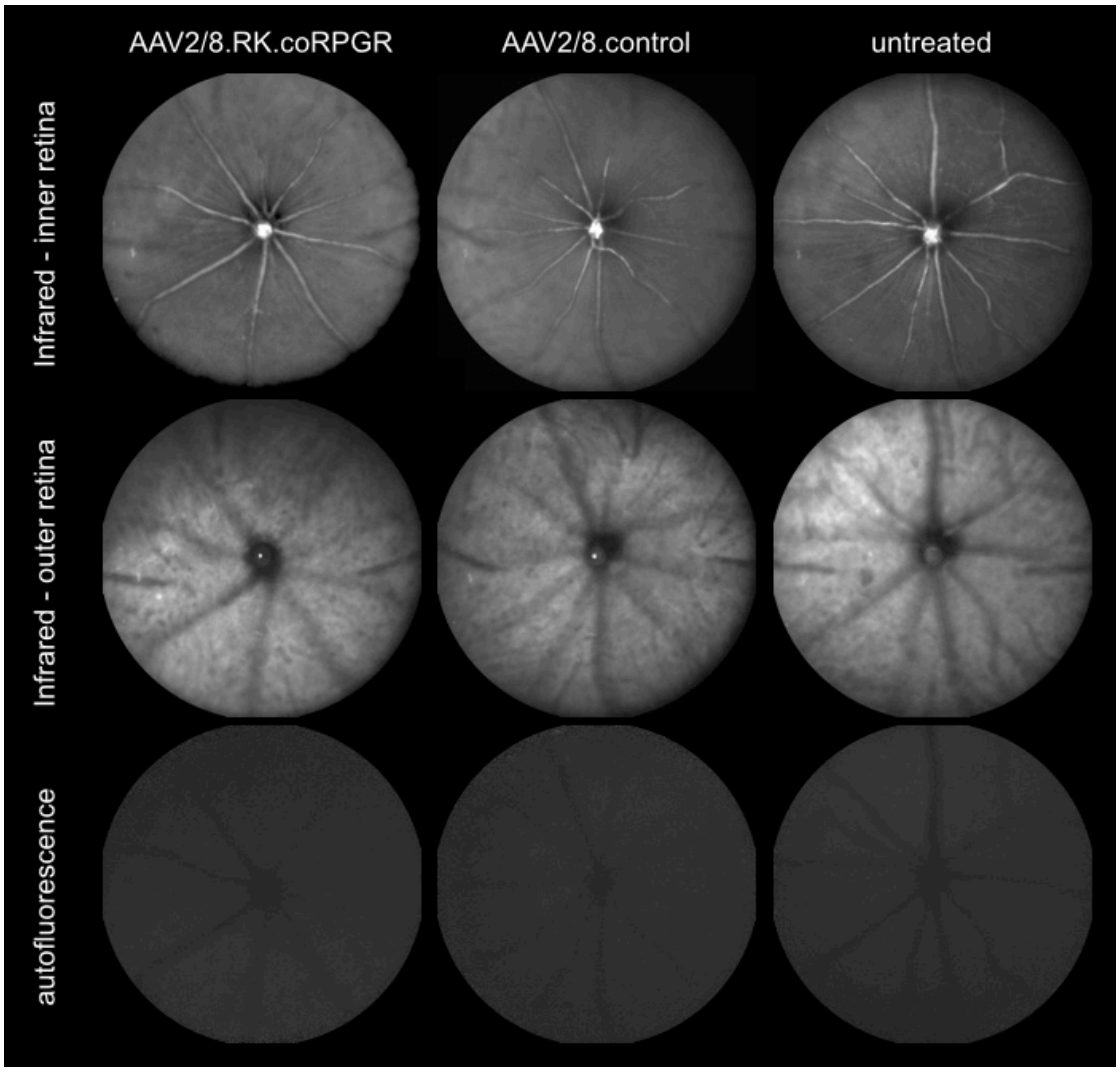

Fig. 6.5 Representative retinal images of *C57BL/6J* mice at postnatal month 6 (PM6). Three columns represent eyes of the treatment group (left), sham control group (middle) and untreated group (right). Using scanning laser ophthalmoscopy imaging in the infrared mode, focal plane was set to inner retina (top row) or outer retina (middle row). Bottom row demonstrates the physiologically weak autofluorescence in wild type mice.

Western blot of whole retinal lysate confirmed RPGR transgene expression in the treated, but not in the control eye (**Fig. 6.6**). The band showed the predicted molecular weight and no extra bands were apparent. Immunohistochemistry of unfixed cryosections also demonstrated RPGR transgene expression and co-localisation with native RPGRIP (**Fig. 6.7**) in the treated eye, but not the untreated control eye.

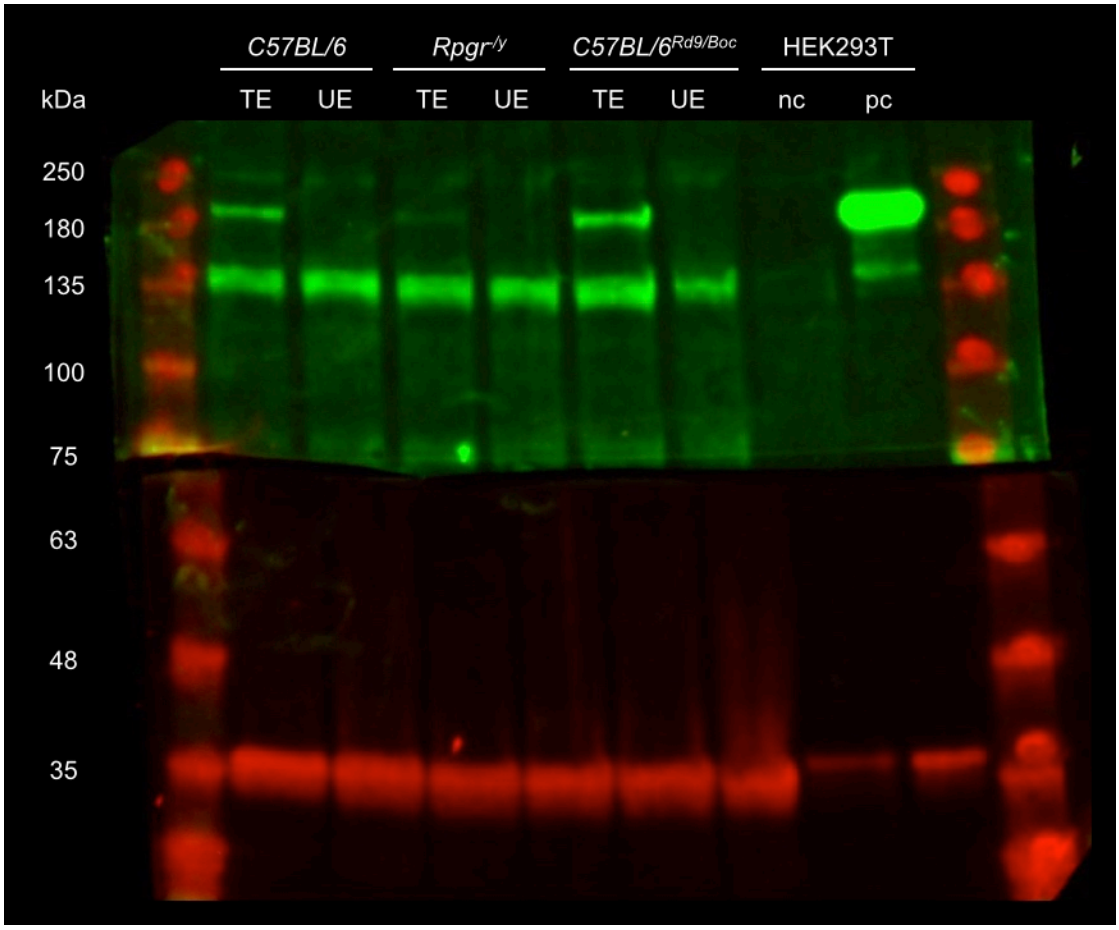

Fig. 6.6 Representative Western blot of whole retinal lysates from treated vs. untreated eyes of *C57BL/6J*, *C57BL/6J*$^{Rd9/Boc}$, and *Rpgr*$^{-/y}$ mice. Rpgr^{ORF15} expression is limited to the treated eyes (TE) and shows a band at ca. 200kDa. The strongest band is visible in *C57BL/6J*$^{Rd9/Boc}$, followed by *C57BL/6J*, while the *Rpgr*$^{-/y}$ sample shows weakest expression, which might be due to variability e.g. in surgery or transduction efficiency. GAPDH was used as loading control (red). Naïve HEK293T cells were used as negative control (nc) and HEK293T cells transfected with a coRPGR expression plasmid as positive control (pc).

Hematoxylin and eosin (H&E) staining in retinal sections from treated eyes (TE) and untreated eyes (UE) revealed normal retinal anatomy in both cohorts (**Fig. 6.8**). As suggested by these representative images, neither of the cohorts showed any sign of inflammation or degeneration in any of the sections.

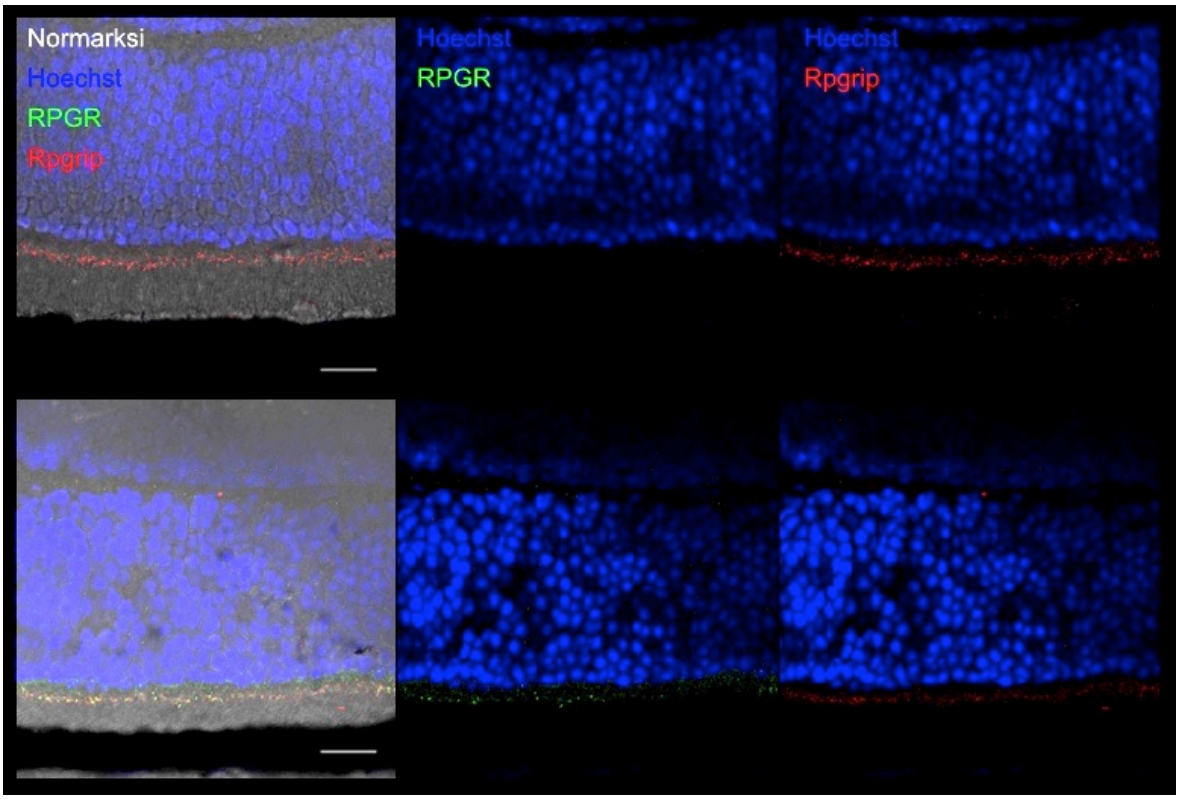

Fig. 6.7 Immunohistochemistry in *C57BL/6J* mice. Representative sections from control-treated (top panels) and AAV.coRPGR treated eyes in *C57BL/6J* mice were stained with Hoechst (blue) and antibodies against human RPGR (SIGMA n-terminal; green) and mouse Rpgrip (red). Top panels show no human RPGR expression in a control-treated eye, while Rpgr (red) indicates location of the connecting cilia. Treatment with AAV.coRPGR resulted in RPGR expression (bottom panels) and co-localisation of human RPGR with Rpgrip (red). Scale bar indicates 20µm.

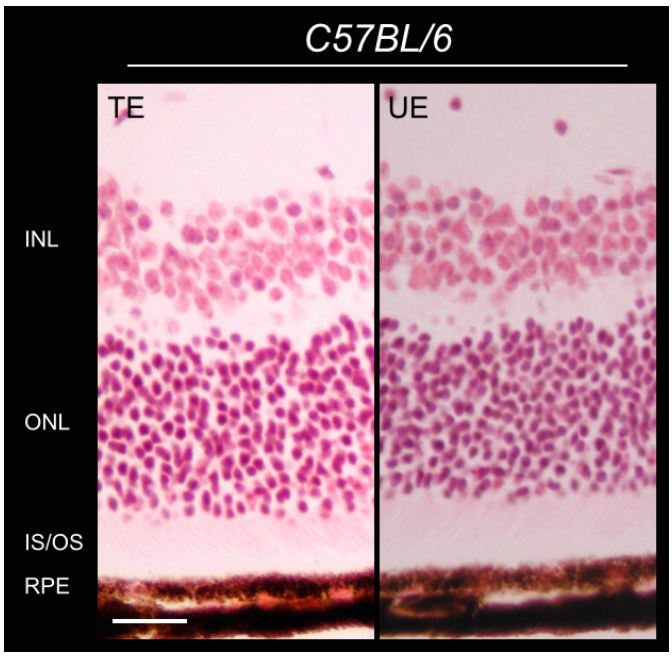

Fig. 6.8 Haematoxylin and eosin staining in *C57BL/6J* mice. Left panel shows a representative retinal section from a treated eye (TE), in the right panel from an untreated eye (UE). There were no signs of inflammation or degeneration visible in any section. Normal anatomy was observed as indicated to the left: INL = inner nuclear layer; ONL = outer nuclear layer; IS/OS = inner and outer segments of photoreceptors; RPE = retinal pigment epithelium. Scale bar indicates 20µm.

6.4.3 *C57BL/6J*$^{Rd9/Boc}$ mice

One mouse of the unilateral open label trial had to be excluded due to a pre-existing corneal infiltrate with associated microphthalmus in the untreated control eye. The microphthalmus may have led to false low ERG recordings in the untreated eye. This resulted in a total of n=18 for the unilateral trial, and n=17 animals for bilateral injections. None of the treated animals had to be excluded due to surgical complications and all animals received injections rated good or excellent with mean (range was 8-10 in all groups) of 9.7 for the open label, 9.1 for the *verum* and 9.0 in the control group.

In the longitudinal follow up, two animals from the unilateral trial did not recover from anaesthesia at PM4. A total of 102 bilateral ERG data sets from three time points were successfully recorded and saved for further analysis.

In the open label, unilateral trial, factorial ANOVA for repeated measures retained the null hypothesis (no difference) at the first time point (PM2), but showed a trend for larger amplitudes for the treated eyes at higher intensities in both dark- and light adapted intensity series (**Fig. 6.9**). At PM4, the treated eyes responded with significantly higher amplitudes across the dark adapted intensity series regarding both a-wave (p = 0.001) and b-wave (p = 0.002). The light adapted responses were not significantly different. This pattern was sustained until the last time point (PM6).

In the masked bilateral trial null hypothesis was retained at all time points. However, *verum* treated eyes always showed a trend for higher amplitudes again especially at higher stimulus intensities (**Fig. 6.10**).

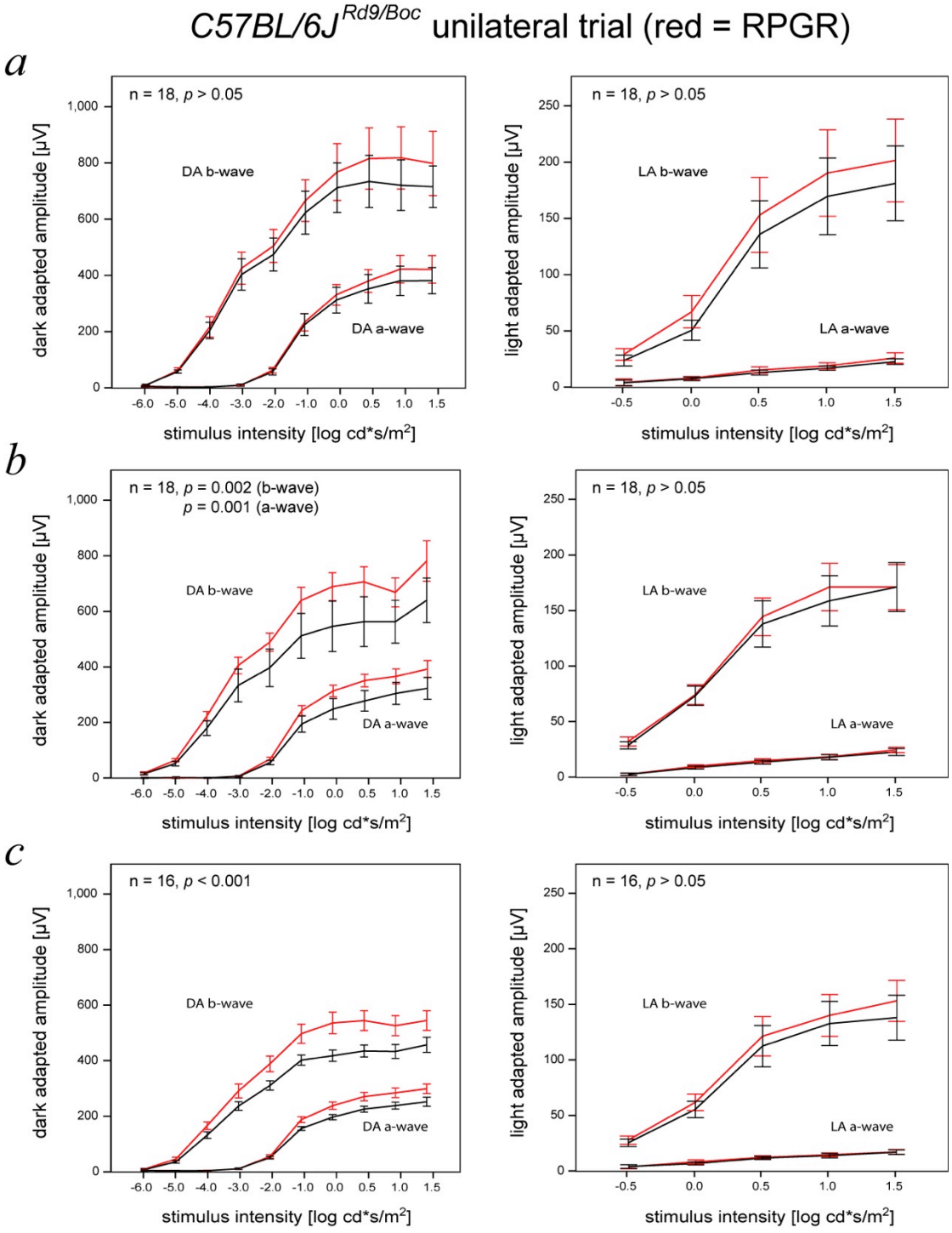

Fig. 6.9 ERG recordings in *C57BL/6J*$^{Rd9/Boc}$ mice after unilateral subretinal injection of AAV.RK.coRPGR. Red lines represent data from treated eyes, black from untreated eyes. a) shows data from PM2, b) from PM4 and c) from PM6, the last time point tested. Factorial ANOVA for repeated measures retained the null hypothesis (no difference) at PM2, but treated eyes (red) showed larger amplitudes in the dark adapted intensity series (left panels) at PM4 and PM6. Lines indicate mean amplitudes ± 95% confidence interval (whiskers).

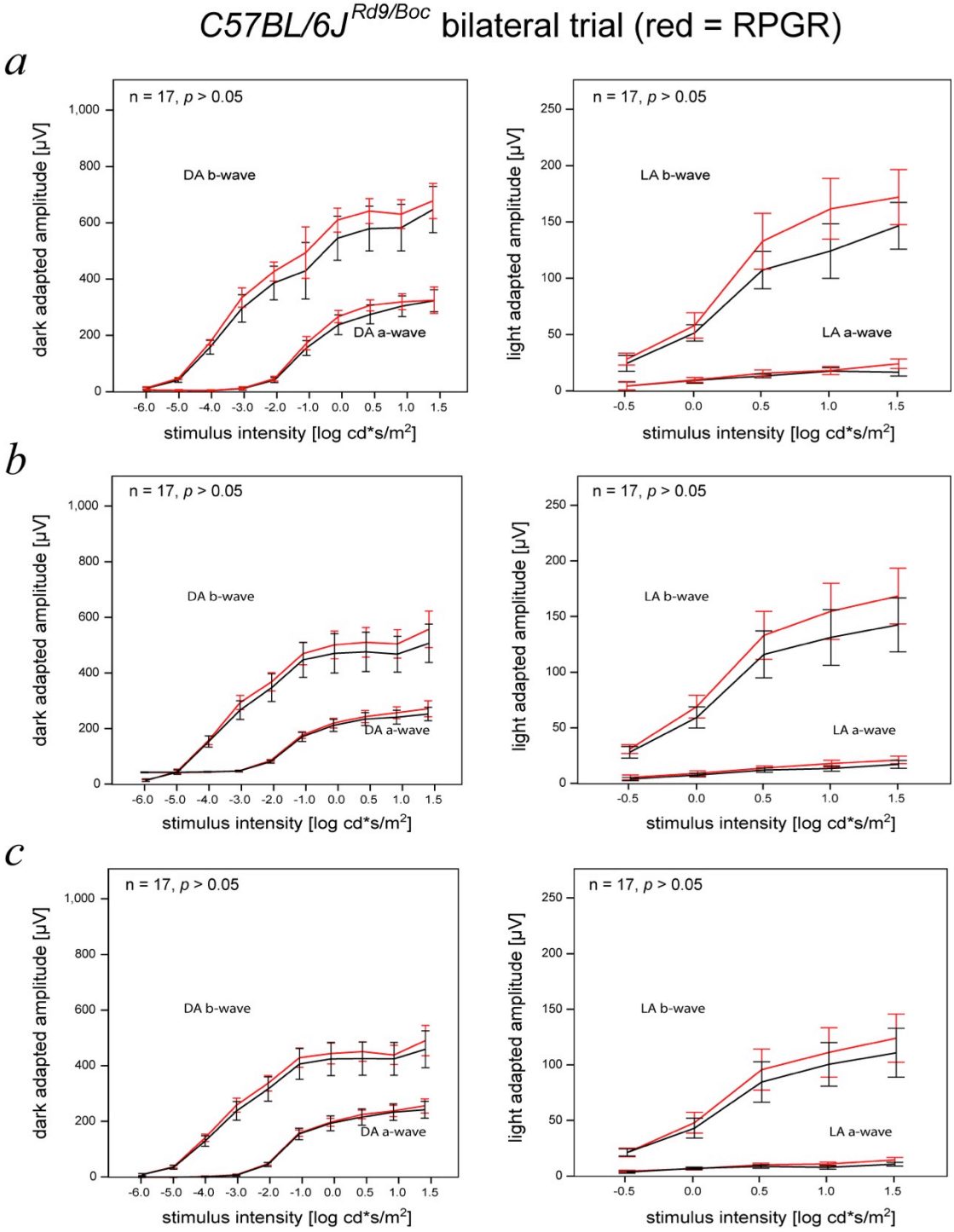

Fig. 6.10 ERG recordings in *C57BL/6J*$^{Rd9/Boc}$ mice after bilateral subretinal injection of AAV.RK.coRPGR (red) or AAV.control (black). a) shows data from PM2, b) from PM4 and c) from PM6, the last time point tested. Factorial ANOVA for repeated measures retained the null hypothesis (no difference) in all analyses. This might indicate a sham effect of the control injection on ERG. Lines indicate mean amplitudes ± 95% confidence interval (whiskers).

Retinal imaging with scanning laser ophthalmoscopy (SLO) also confirmed that there was no toxic effect to be observed on retinal structure up to 6 month after subretinal application of AAV.RK.coRPGR (**Fig. 6.11**). However, autofluorescence imaging revealed a change in the disease presentation in treated *C57BL/6J*$^{Rd9/Boc}$ mice: We showed previously that lack of *Rpgr* expression in mice is associated with hyperfluorescent dots across the retina visible in autofluorescence, while wild type mice only have minimal, homogenous autofluorescence signal (**Fig. 6.5**). Interestingly, imaging in the *verum* treated eyes at PM6 showed a reduction of these hyperfluorescent dots in the superior hemiretina, where the vector was initially applied. Hemiretinal fields were significantly different within the treated eyes: 13±14 (mean±standard deviation) in the treated superior hemiretina vs. 59±40 in the ipsilateral inferior retina (p=0.005; n=6, paired t-test). Comparing the superior hemiretina of the treated vs. the contralateral untreated retina (65±56) produced a similar result (p=0.037; n=6, paired t-test, **Fig. 6.12**).

Western blot of whole retinal lysate confirmed RPGR transgene expression in the treated, but not in the control eye (**Fig. 6.6**). The band showed the predicted molecular weight and no extra bands were apparent. Immunohistochemistry of unfixed cryosections also demonstrated RPGR transgene expression and co-localisation with native Rpgrip (**Fig. 6.13**) in the treated eye, but not the control eye.

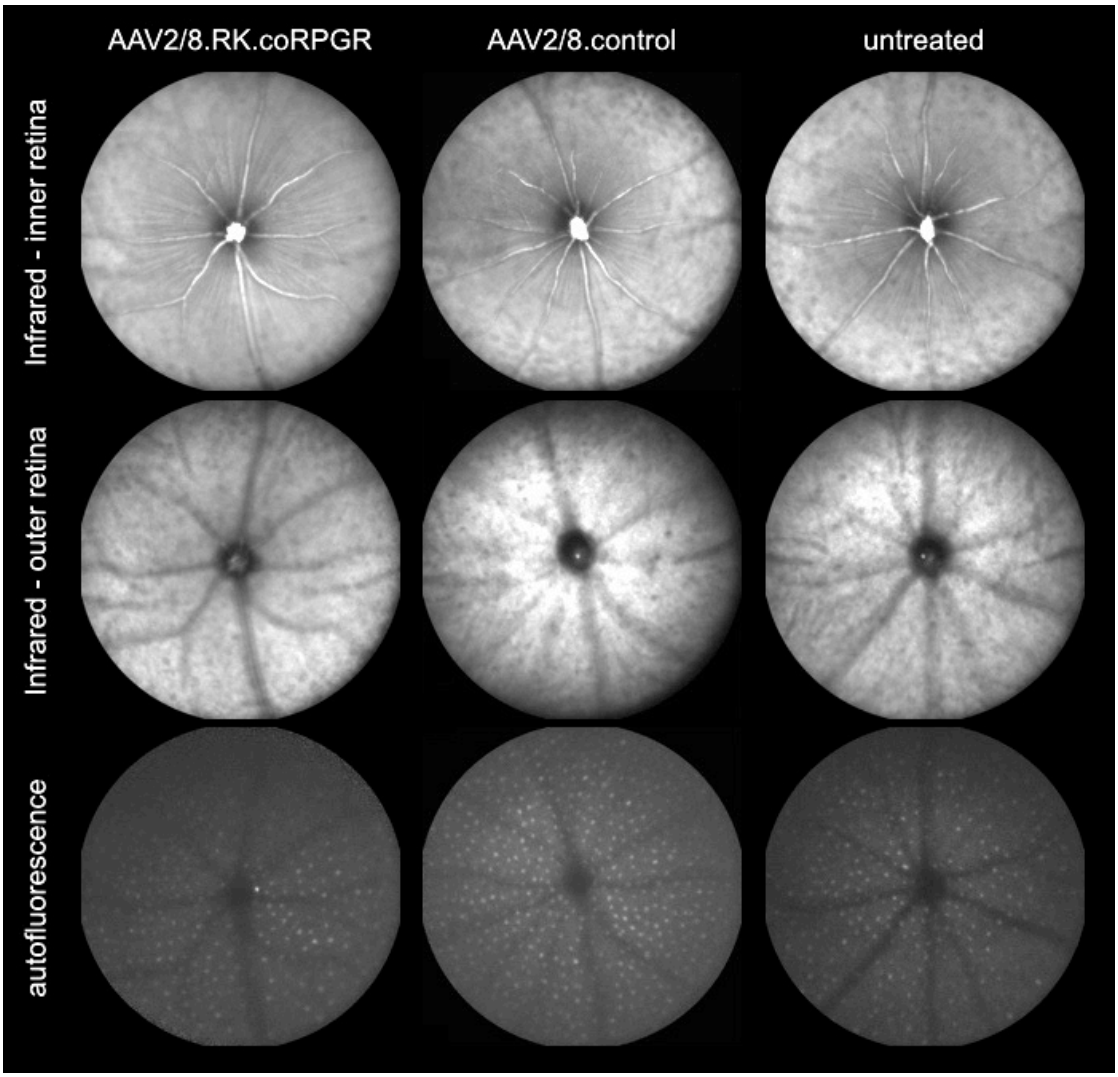

Fig. 6.11 Representative retinal images of *C57BL/6J*$^{Rd9/Boc}$ mice at postnatal month 6 (PM6). Three columns represent eyes of the treatment group (left), sham control group (middle) and untreated group (right). Using scanning laser ophthalmoscopy imaging in infrared mode, focal plane was set to inner retina (top row) or outer retina (middle row). Bottom row demonstrates a distinctly different autofluorescence pattern between the treated (left) and sham (middle) or control (right) eyes: The treated eye shows fewer hyperfluorescent dots in the superior hemiretina – the area of AAV2/8.RK.coRPGR application.

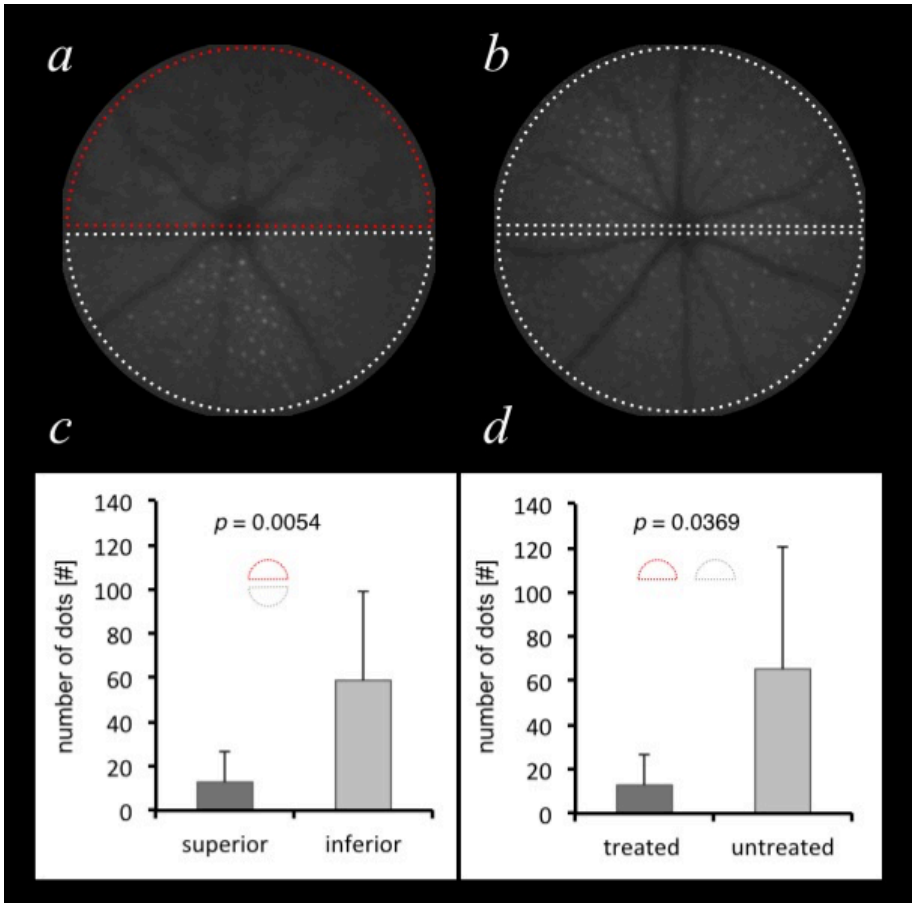

Fig. 6.12 Quantitative analysis of treatment effect on hyperfluorescent dots in *C57BL/6J*$^{Rd9/Boc}$ mice. a) Representative autofluorescence image 6 months after subretinal injection of AAV.RK.coRPGR in the superior hemiretina (red), which shows few hyperfluorescent dots. The inferior hemiretina (white) was not directly exposed to AAV.RK.coRPGR and shows a large number of hyperfluorescent dots. b) Representative autofluorescence image taken at the same time point but in the untreated control eye of the same animal. c) Bar graph following quantitative analysis of number of hyperfluorescent dots in the superior (treated, red) hemiretina vs. the ipsilateral inferior hemiretina (white) from image a). d) Comparison between number of hyperfluorescent dots in the superior (treated) hemiretina (red in a) vs. the contralateral superior hemiretina of the control eye (in b). Significance levels were tested by paired Student's t-test (n = 6).

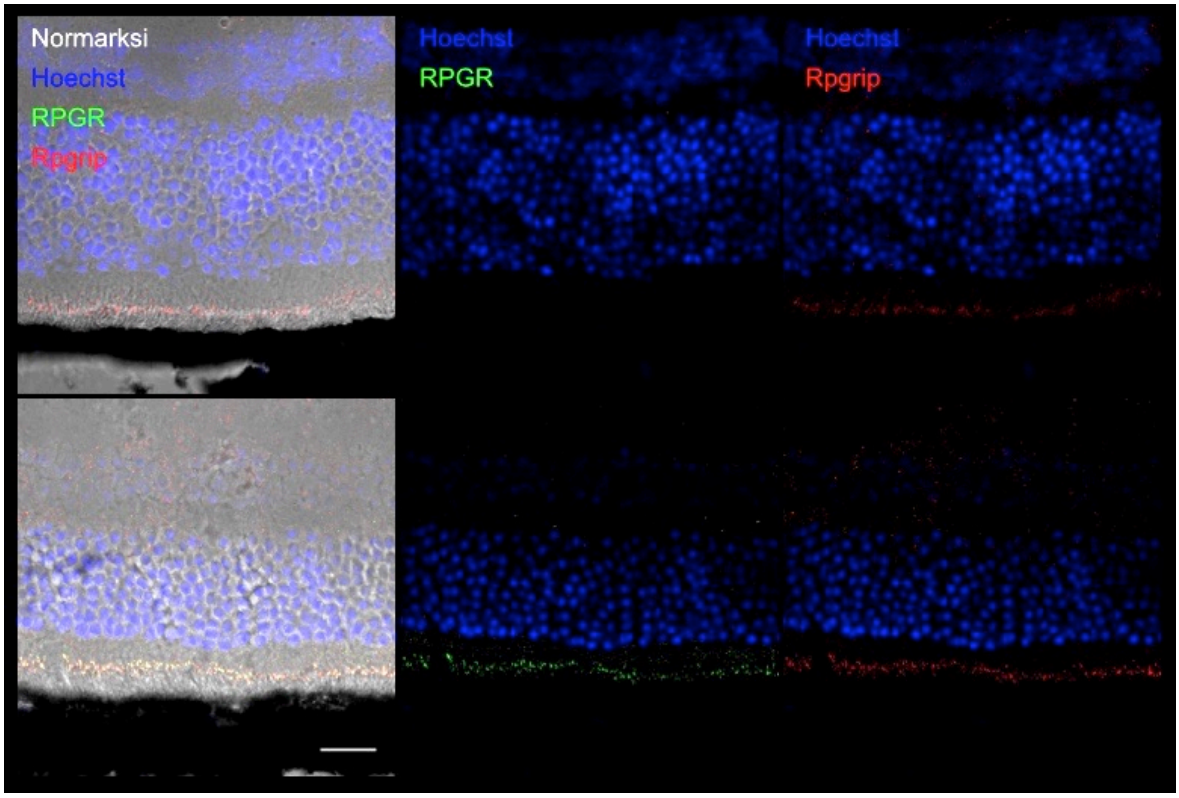

Fig. 6.13 Immunohistochemistry in *C57BL/6J*$^{Rd9/Boc}$ mice. Representative sections from control-treated (top panels) and AAV.coRPGR treated eyes in *C57BL/6J*$^{Rd9/Boc}$ mice were stained with Hoechst (blue) and antibodies against human RPGR (SIGMA n-terminal; green) and mouse Rpgrip (red). Top panels show no human RPGR expression in a control-treated eye, while Rpgr (red) indicates location of the connecting cilia. Treatment with AAV.coRPGR (bottom panels) resulted in RPGR expression and co-localisation of human RPGR with Rpgrip (red). Scale bar indicates 20µm.

6.4.4 *Rpgr*$^{-/y}$ mice

One mouse of the unilateral open label trial had to be excluded due to pre-existing microphthalmus in the untreated eye, that was noticed only after surgical intervention of the contralateral eye and would have led to false low ERG recordings in the untreated eye. Additionally, one animal from the bilateral trial of the treated animals had to be excluded due to surgical complications (part intravitreal injection with intravitreal haemorrhage). This resulted in a total of n=24 for the unilateral trial,

and n=20 animals for bilateral injections. The surgical success rate was high in all cohorts: Mean [range] ratings were 9.3 [8-10] for the open label, 9.5 [9-10] for the *verum* and 9.4 [8-10] in the control group. In the longitudinal follow up, one bilaterally injected animal at PM2 and two animals with unilateral injections at PM4 did not recover from anaesthesia. A total of 128 bilateral ERG data sets from three time points were successfully recorded and saved for further analysis.

In the open label, unilateral trial, there was no apparent difference between eyes at the earliest time point (PM2), but a robust treatment effect visible in the dark adapted ERG responses at PM4 ($p<0.001$) and PM6 ($p<0.001$) in both a- and b-wave amplitudes. Photopic b-wave responses were significantly greater at PM6 ($p=0.004$, **Fig. 6.14**). The masked bilateral trial showed significantly increased amplitudes of dark-adapted b-wave responses at PM6, and light adapted b-wave amplitude was significantly increased at PM4 (but not at PM6, **Fig. 6.15**).

Eyes of *Rpgr*$^{-/y}$ mice treated with AAV.RK.coRPGR showed a reduction of hyperfluorescent dots in the superior hemiretina, as also seen in treated *C57BL/6J*$^{Rd9/Boc}$ mice. In contrast, untreated or sham treated eyes of *Rpgr*$^{-/y}$ mice showed the ubiquitous pattern of hyperfluorescent dots associated with Rpgr-null mutations (**Fig. 6.16**).

Western blot of whole retinal lysate confirmed RPGR transgene expression in the treated, but not in the control eye (**Fig. 6.6**). The band showed the predicted molecular weight and no extra bands were apparent. However the western blot signal in the treated knockout mouse was weaker then in the other mouse lines treated. This might have been due to variability in the surgery and/or transduction efficiency. Immunohistochemistry of unfixed cryosections also demonstrated RPGR transgene

expression and co-localisation with native Rpgrip (**Fig. 6.17**) in the treated eye, but not the control eye.

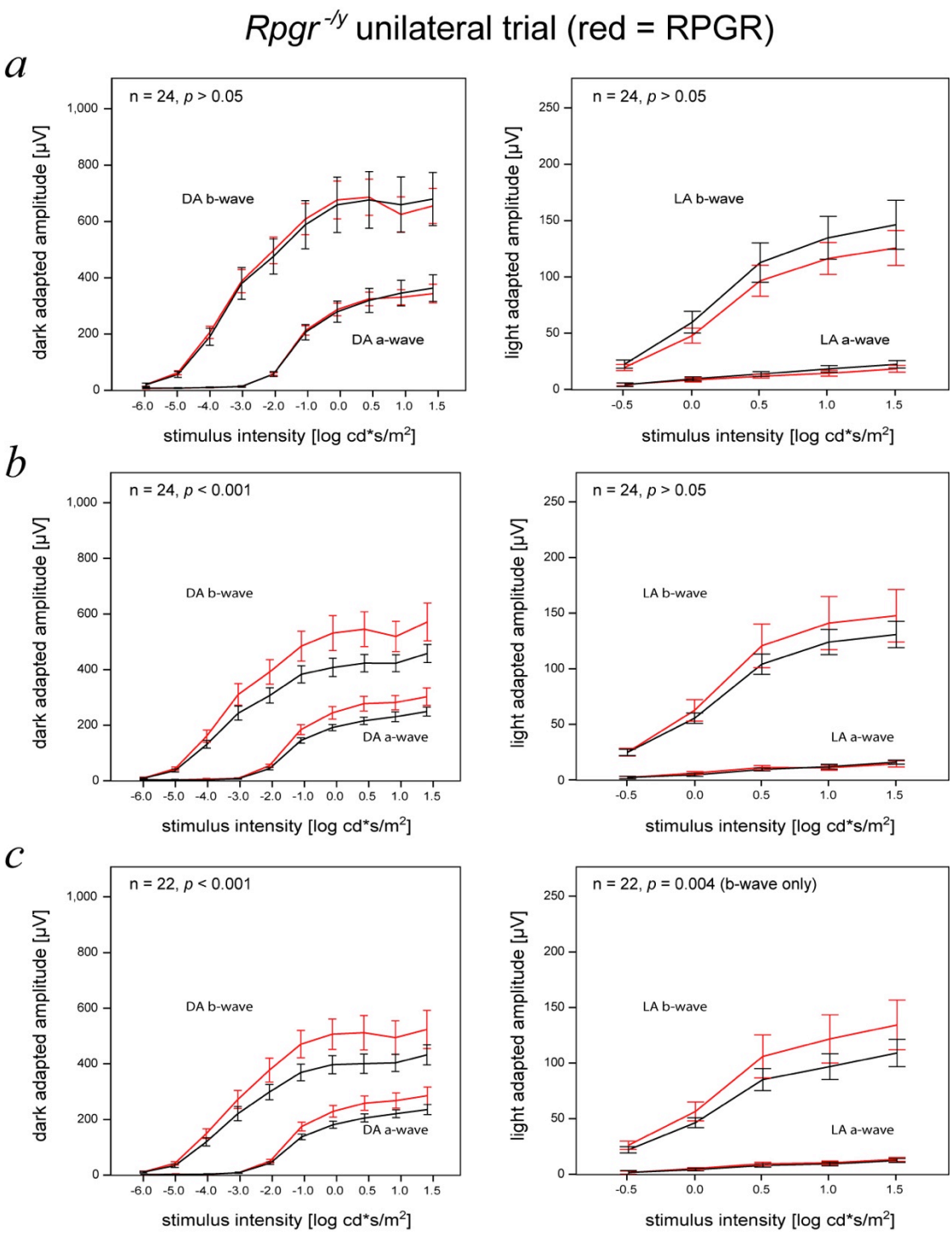

Fig. 6.14 ERG recordings in *Rpgr*$^{-/y}$ mice after unilateral subretinal injection of AAV.RK.coRPGR. Red lines represent data from treated eyes, black from untreated eyes. a) shows data from PM2, b) from PM4 and c) from PM6, the last time point tested. Treatment with AAV.RK.coRPGR led to significant improvement of dark adapted ERG amplitudes (left panels in b-c) and light adapted b-wave amplitudes (right panel in c). Lines indicate mean amplitudes ± 95% confidence interval (whiskers).

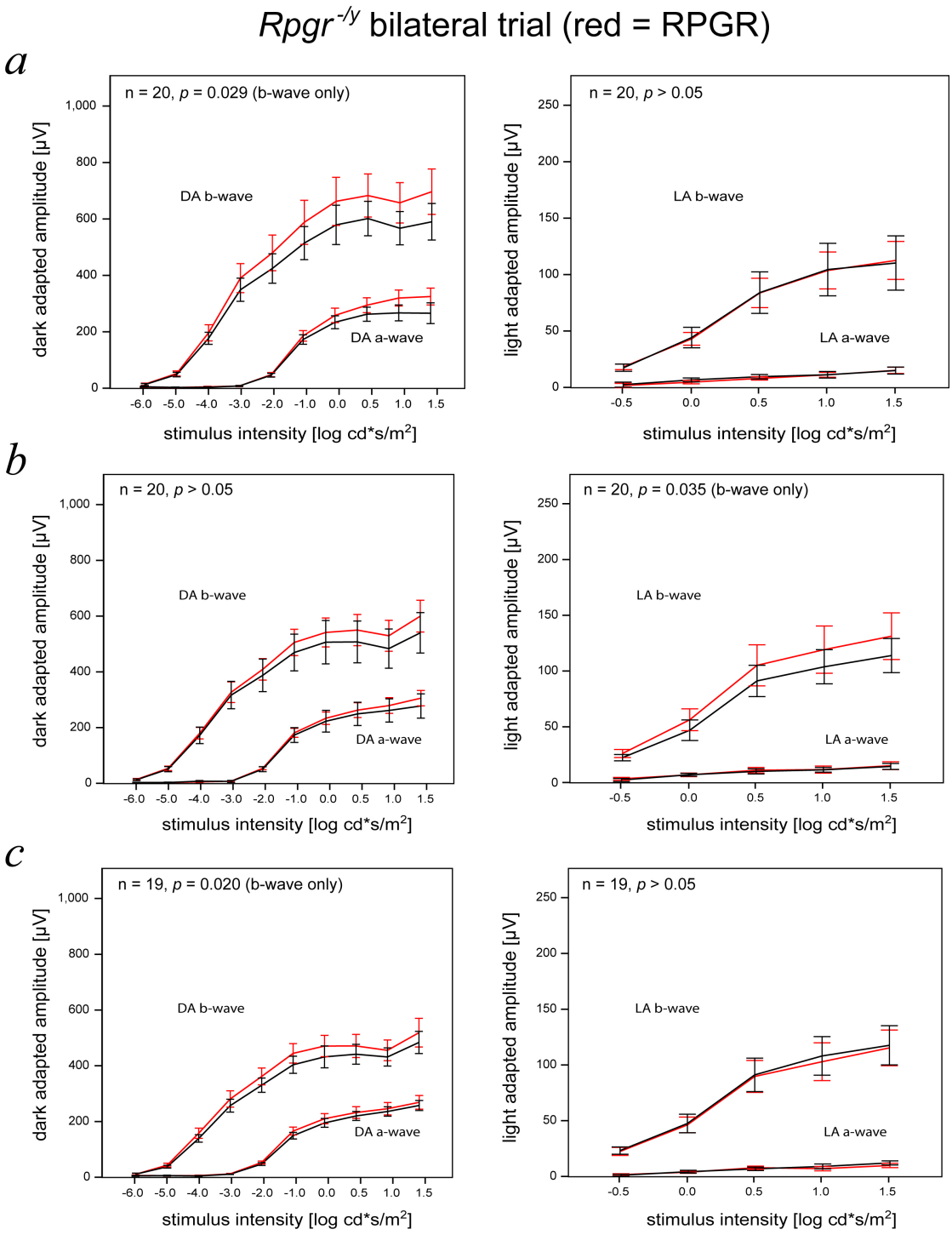

Fig. 6.15 ERG recordings in *Rpgr*$^{-/y}$ mice after bilateral subretinal injection of AAV.RK.coRPGR (red) or AAV.control (black). a) shows data from PM2, b) from PM4 and c) from PM6, the last time point tested. Treatment with AAV.RK.coRPGR led to significant improvement of dark adapted ERG amplitudes (left panel in c). The treatment effect in the light adapted b-wave amplitudes (right panel in b) was not sustained at PM6 (right panels in c). Lines indicate mean amplitudes ± 95% confidence interval (whiskers).

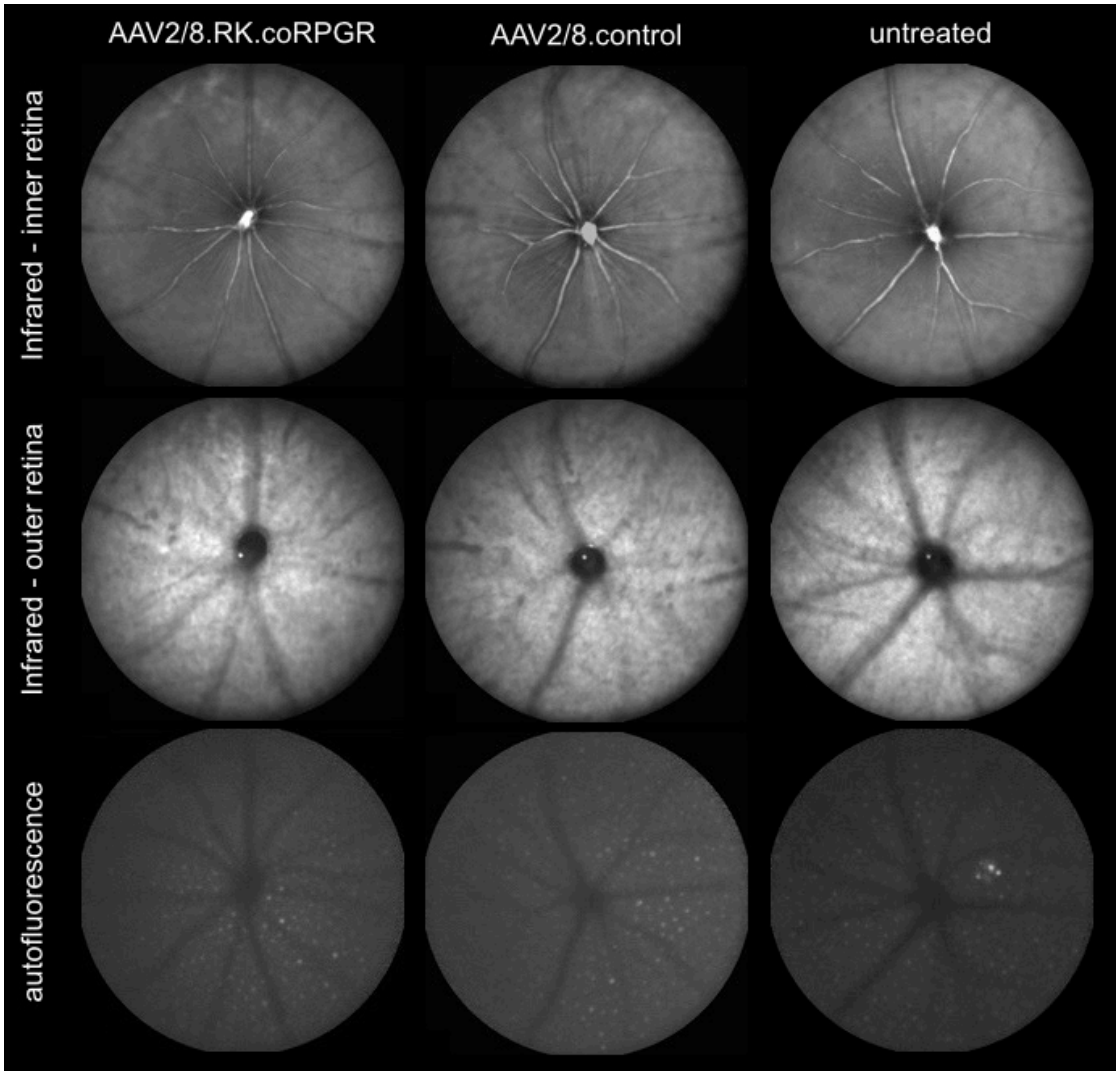

Fig. 6.16 Representative retinal images of *Rpgr*$^{-/y}$ mice at postnatal month 6 (PM6). Three columns represent eyes of the treatment group (left), sham control group (middle) and untreated group (right). Using scanning laser ophthalmoscopy imaging in the infrared mode, focal plane was set to inner retina (top row) or outer retina (middle row). Bottom row demonstrates a different autofluorescence pattern between the treated (left) and sham (middle) or control (right) eyes: The treated eye shows fewer hyperfluorescent dots in the superior hemiretina – the area of AAV.RK.coRPGR application.

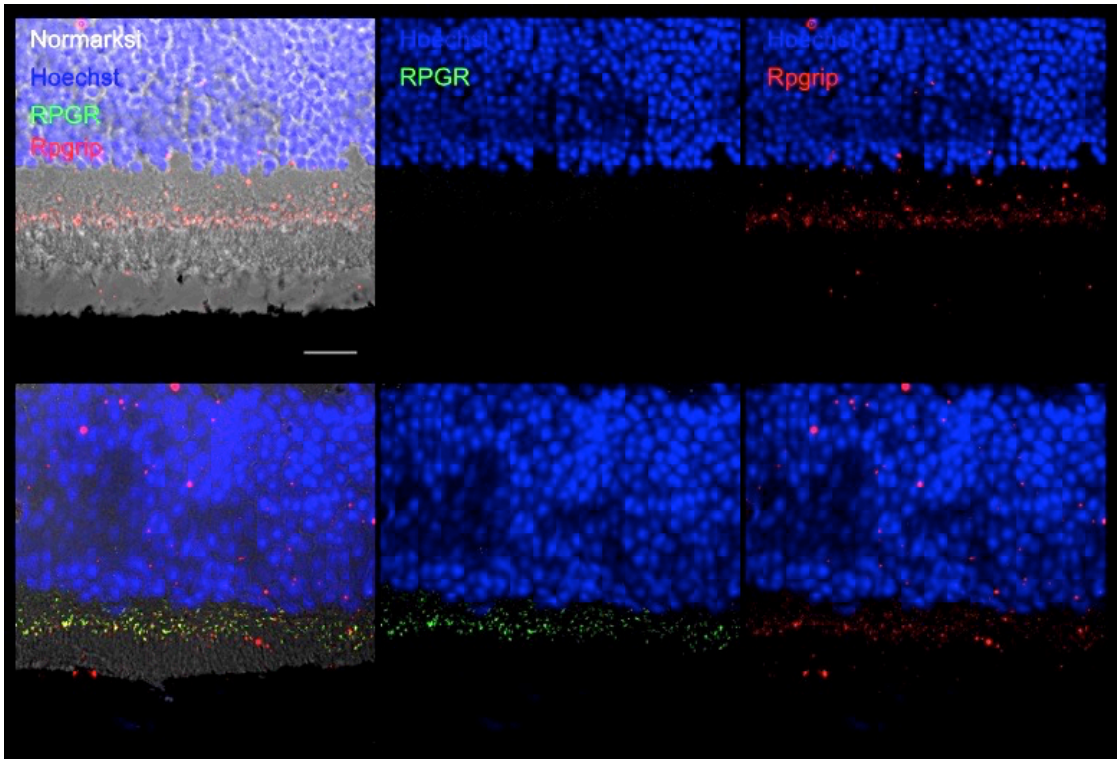

Fig. 6.17 Immunohistochemistry in *Rpgr*$^{-/y}$ mice. Top panels show no RPGR (green) expression in a control-treated eye. Treatment with AAV.coRPGR resulted in RPGR expression and co-localisation of human RPGR with Rpgrip (red). Scale bar indicates 20µm.

6.5 Discussion

RPGR replacement therapy by AAV has been a goal for the scientific community since the characterisation of RPGR as the genetic cause for XLRP3. The fact that it still is a goal that has not translated into a clinical trial is mainly due to the fact that RPGR is a complex gene with high propensity for mutational changes. This has caused serious delays in the development of datasets for the support of clinical trial applications. And even with regulatory approval for a safety trial, production of clinical grade AAV for RPGR gene therapy will be a significant challenge.

Here we present evidence regarding the safety (no toxic effects in wild type animals, *C57BL/6J*) and efficacy of a new type of vector construct for RPGR gene therapy in two relevant animal models (*Rpgr*$^{-/y}$ and *C57BL/6J*$^{Rd9/Boc}$ mice). This rAAV vector features a codon optimised coding sequence of *RPGR*^{ORF15}, which makes the construct more genetically stable while leading to the identical protein product, RPGR^{ORF15}. After extensive *in vitro* analyses (chapters 3-4) and a pilot trial in *Rpgr*$^{-/y}$ mice (chapter 5), the present evidence now shows that a single subretinal application of AAV.RK.coRPGR is safe and may stop or slow down the progression of retinal degeneration due to mutations in *Rpgr*.

6.5.1 Safety

To explore potential toxic effects of AAV.RK.coRPGR, we tested the same dose ($1.5x10^9$ vg in 1.5 µl) in forty-one *C57BL/6J* mice. Nineteen mice were treated

in one eye only, while 22 received masked bilateral treatment with either AAV.RK.coRPGR or AAV.control. There were no significant differences between measures of retinal function in ERG at any time point of either trial between the *verum* group and the control or untreated group (**Fig. 6.3-6.4**). Additionally, *in vivo* retinal imaging suggests that there was no impact of AAV.RK.coRPGR treatment on retinal structure (**Fig. 6.5**). H&E staining showed no toxic effects of the treatment and immunohistochemistry and Western blotting demonstrated $RPGR^{ORF15}$ expression and localisation in treated animals, but not in untreated or control treated animals (**Fig. 6.6-6.8**). Taken together, single treatment of wild type mice with AAV.RK.coRPGR did not seem to induce any toxic effects and showed a good safety profile. This is in line with similar reports from the literature, where different constructs also lead to safe expression of wild type or variants of $RPGR^{ORF15}$ in wild type mice [121, 122]. Toxic effects can principally be observed with some truncated versions of Rpgr [54] or with overexpression of RPGR [121, 122]. The trial design, cohort size and assessment protocols would have allowed to find even relatively mild negative effects. We therefore conclude that treatment with AAV.RK.coRPGR at the chosen dose is safe.

6.5.2 Efficacy

The therapeutic effect of AAV.RK.coRPGR was demonstrated in two well-characterised mouse models of XLRP3: The transgenic model $Rpgr^{-/y}$ (kindly provided by Tiansen Li) and $C57BL/6J^{Rd9/Boc}$ featuring a naturally occurring mutation

in Rpgr. Both models have been shown to lack $Rpgr^{ORF15}$ expression in the retina and hence were chosen as relevant animal models for XLRP3. However, there are some caveats with using these animal models. Most importantly, the disease phenotype is surprisingly mild, which necessitates relatively large cohorts in a trial to gain the necessary statistical power. As a consequence, we conducted trials in a total of ca. 80 animals and provided evidence of efficacy as indicated by significant rescue of electrophysiological measurements in *Rpgr*$^{-/y}$ and *C57BL/6J*$^{Rd9/Boc}$ mice (**Fig. 6.9-6.10** and **Fig. 6.14-6.15**). The treatment did not become evident at the first time point most likely due to the slow disease progression in both animal models. However, AAV.RK.coRPGR treatment was associated with significant ERG rescue in both animal models at PM4 and PM6. This rescue was more evident in the dark adapted intensity series, which reflects the sum potential of rod photoreceptors in the lower intensity range (single flashes up to ca. 0.01cd./m^2) [154]. Higher flash intensities are thought to stimulate a mixed cone-rod response. The biggest difference between the treated and sham-/untreated eyes were seen at intensities around 1cd.s/m^2 indicating that both rod and cone photoreceptors might have gained from AAV.RK.coRPGR transduction. Data from light adapted intensity series were less consistent with some therapeutic efficacy evident at PM4, which could not be reproduced at PM6. Interestingly, the natural disease progression e.g. in *C57BL/6J*$^{Rd9/Boc}$ mice was described with a relative rebound of dark and light adapted amplitudes from PM4 to PM6 [155]. Such a longitudinal development might explain loss of significant differences between a treated and sham-/untreated group from PM4 to PM6. Alternative explanations might be an only temporary nature of any treatment effect or a false positive significance call. The false discovery rate associated with multiple

testing of ERG data was controlled for by the False Discovery method published by Benjamini *et al.* [141]. A temporary treatment effect of AAV.RK.coRPGR seems unlikely in view of the persistent effects in the dark-adapted intensity series. Also, previous studies have indicated that RPGR expression in in *Rpgr*$^{-/y}$ mice leads to sustained treatment effects [121, 122]. The discrepancy between the unilateral, open label trials and the bilateral, sham controlled trials may indicate the possibility that the sham treatment also had an effect on ERG. There is some evidence in other animal models that surgical intervention in the eye induces a therapeutic effect [156]. This is thought to be initiated by injury induced paracrine release of neurotrophic factors e.g. from activated glia cells {LaVail, 1998 #998}. While we can not completely rule out such a sham effect, there were significant differences between AAV.RK.coRPGR treated and sham treated eyes in the dark and light adapted ERG responses e.g. in *Rpgr*$^{-/y}$ mice at different time points.

Taken together, treatment with AAV.RK.coRPGR seems to be safe and effective. Successful transduction of photoreceptors with AAV.RK.coRPGR in wild type mice did not lead to toxic effects, which might have been associated with the expression of RPGR^{ORF15}. Furthermore, treatment of animal models of XLRP3 showed a statistically significant rescue of ERG responses in the treated, but not in the untreated eyes. These data are the first evidence that a codon optimised coding sequence of *RPGR*^{ORF15} can be used to safely treat eyes, which lack expression of this important ciliary protein.

CHAPTER 7 GENERAL DISCUSSION

7.1 Retinal gene therapy

The eye is particularly suited for gene therapy. It is unique in its propensity towards monogenetic diseases while at the same time offering ways to observe and test the affected tissue with or close to single cell resolution *in vivo*. The small size, compartmentalisation with its relative immune privilege and the fact that it is a paired organ (intra-individual control) all contributed to the success of retinal gene therapy. First and foremost, three pivotal trials in London and Philadelphia to treat Leber congenital amaurosis type 2 (OMIM 204100) with AAV2.RPE65 paved the way for many gene therapy programs currently active and/or planned [88, 89, 157]. RPE65 is an isomerase found in the RPE and is responsible for recycling Vitamin A derivatives, which in turn are necessary for light detection in the photoreceptors (chapter 1.1.2). Mutations in RPE65 lead to drastically decreased sensitivity of the retina to light stimuli, degeneration of RPE and photoreceptor cells and ultimately blindness.

These phase I/II trials were successful in showing the safety of gene addition in patients with missense as well as predicted null mutations [158, 159]. This was important as it was previously not clear, whether patients with null mutations would stage an immune response against the therapeutic transgene product as it would be new to the immune system. Jean Bennett and colleagues were the first to demonstrate lack of a clinically significant immune response after second administration of AAV2.RPE65 to the contralateral eye years after the first injection [160]. Based on this pioneering work several conclusions could be drawn:

- High numbers of AAV particles can be administered in the subretinal space without clinically evident toxic effects.
- Subretinal AAV does not lead to a clinical significant immune response.
- Gene addition to RPE cells can restore metabolic activity to clinically relevant levels.

However, some of the more optimistic expectations of restoring vision in LCA2 patients were not met in these first trials. These had been fuelled by the exceptional results from pre-clinical studies on animal models of LCA2 with Lancelot being the most prominent recipient having visited the US Senate [161]. Lancelot was one of the Briard dogs with a naturally occurring mutation in RPE65 that were treated using AAV2.RPE65. The therapeutic effect was remarkable with robust electro-physiological evidence of efficacy and very apparent behavioural change. While most patients from the first trials showed some form of improvement in psychophysical tests measuring retinal sensitivity under mesopic or scotopic conditions, no patient was demonstrated to have gained an objective electrophysiological response. This can be seen as difficult given the unmasked nature of the trial design.

Fig. 7.1 Lancelot, the Briard dog on promotional tour at Washington DC.
Picture courtesy: Foundation Fighting Blindness

The long-term follow up of the patients from the first trials additionally point towards a possible decline of initial functional improvement [158, 159]. Several potential explanations were put forward on why the therapeutic benefit was not more obvious and why there was an indication of continued degeneration. One maintains that the intervention had come too late to effectively stop degeneration of remaining retinal tissue. Support comes from observations in animal models, where treatment success was highly dependent on the timing of intervention [162, 163]. Treatment at very early disease stages showed functional and structural rescue, while later intervention showed only transient functional improvements with continuous structural degeneration eventually leading to complete blindness. Some authors argue that the disease stage found in the enrolled patients equated to the second group and thus only allowed for transient functional benefit. Data published by Maguire *et al.* support this line of argument with greater treatment effect seen in younger patients [164]. However, Bainbridge *et al.* and Jacobson *et al.* could not find a clear correlation between age of participant and response to treatment. In fact, Bainbridge et al report greatest improvements in older participants [158, 159].

Indirectly, this leads to the second line of argument: the applied dose might not have reached the required therapeutic threshold. Greater success in older participants could be related to less tissue being left at later disease stages, thus increasing the ratio of AAV particles applied vs. cells available for transduction (i.e. increasing the multiplicity of infection, MOI). Further support for this hypothesis comes from canine studies, which demonstrate that sub-threshold doses of AAV2.REP65 can lead to

limited functional rescue without ERG improvements (as observed in patients), while higher doses would lead to robust measurable responses on ERG, which were also associated with protection against continuous degeneration [159, 163].

A third hypothesis focused on secondary structural changes in retinal tissue of LCA2 patients: Cideciyan *et al.* suggested that the therapeutic effect of a restored recycling of all-*trans* retinyl esters into 11-*cis* retinal by the RPE65 isomerase transgene product could be limited by pathological alteration of the degenerating retinal tissue, such as disorganised photoreceptor outer segments and accumulating lipid droplets forming a "resistive barrier" [157].

A fourth possible explanation of limited functional rescue is the prolonged and extensive deprivation of the visual cortex in LCA2 patients, who typically experience severe vision loss from birth (hence the name congenital). One could therefore argue that even with the best possible restoration of the recycling activity of RPE65 and phototransduction in the remaining photoreceptors, the perception of light on a cognitive level might be dictated by a limited cortical plasticity. An often cited example is the development of amblyopia in patients in which strabismus is not treated until at least their early teens. Correction of such a strabismus in adults usually does not achieve significant improvement of vision in the amblyopic eye. However, Ashtari *et al.* have demonstrated significantly enhanced activity in the visual cortex in LCA2 patients following gene therapy. The activity was specifically found in the cortical area corresponding to the treatment area in the retina and correlated with improvement of other clinical outcome measures [165]. Maybe more importantly, the

improvement was clearly evident even 3 years after gene therapy, suggesting a sustained beneficial effect.

Another clinical trial also shows a more optimistic picture. Using AAV2.REP1 MacLaren *et al.* have successfully treated circa 12 patients with choroideremia to date [166]. Preliminary data showed good safety and an unexpected increase in visual function in some of the patients. This is remarkable as most previous reports emphasized the preservation of visual acuity until the very last stages [167] and most trial participants went into the operation with (near) normal visual acuity. Hence, the initial goal was to show safety and efficacy in terms of preventing further deterioration of vision. For ethical reasons, the worse eye was treated. Latest follow-up data of trial participants now suggest that the visual function of the treated (initially worse) eye has now become the functionally better eye in the majority of patients. With a follow up of more than 3 years, this suggests that gene therapy can lead to a sustained treatment effect in human patients just as we have seen in animal models.

Taken together, there are a number of reasons, which might explain why some of the first trials were 'only' successful in showing the safety of subretinal AAV gene therapy but limited in demonstrating efficacy. It is important to acknowledge the enormous contributions made by these groups for the field of retinal gene therapy. In their wake, a large number of gene therapy trials have started or are planned and an unprecedented investment from the financial sector in gene therapy companies such as Oxford BioMedica plc., Spark Therapeutics, NightStaRx Ltd., Avalanche

Biotechnologies etc. has made the translation of current (pre-) clinical gene therapy programs into an approved treatment more likely.

7.2 Potential roadblocks and solutions for gene therapy programs

Some potential roadblocks can be identified, which could possibly delay the development of retinal gene therapy. These can be divided in practical aspects and more abstract issues.

One practical bottleneck for retinal gene therapy is the surgical application of vector suspension in order to transduce the target cell population efficiently. Most retinal gene therapies are geared towards photoreceptor and/or RPE cells. Both cell populations are immediately adjacent to the potential subretinal space, which can be filled with balanced salt solutions using fine needles with minimal trauma. This route of delivery has several advantages over intravitreal or intracameral injections, including greater transduction efficiency and greater control of biodistribution. Additionally, the subretinal space has been shown to feature a deviant immune response similar to the anterior chamber-associated immune deviation (ACAID) [92, 168]. By actively suppressing potentially harmful immune responses ACAID may have played a role in the success of subretinal gene therapy in the second eye 1.7–3.3 years after treatment of the contralateral eye [160].

Subretinal delivery of therapeutic agents is an established procedure in vitreoretinal surgery; one example being solutions containing recombinant tissue plasminogen activator (rTPA) for the treatment of submacular haemorrhages in neovascular AMD [169, 170]. The microsurgical procedures and instruments for subretinal delivery are therefore available, but a number of unique factors, such as small injection volumes (~100-500 µl) and minimal surplus solution for priming and flushing, need to be considered as well as biomechanical alterations of ocular tissue due to the underlying disease.

The different retinal gene therapy trials so far have all applied the vector suspension into the subretinal space - each using protocols with small but important differences: Bainbridge used 1000 µl with gas-fluid exchanges to push the bleb into the target area. Maguire injected 150 µl vector suspension with 0.001% PF-68 directly into the subretinal space of the target area and a similar approach was used in the Jacobson *et al.* trial with a volume of 150-300 µl applied directly using a 39-gauge cannula. Bennicelli *et al.* have pointed out that without addition of 0.001% of PF-68, 90% of the AAV2 particles are retained in the injection system [171]. Therefore, the actual dose given in the trial by Bainbridge *et al.* (which did not use PF-68) is likely one log unit below what is nominally reported. Additionally, a bleb with 1000 µl volume is predicted to cause significant strain (large ∂l in $\varepsilon = \partial l / l_0$, where ε is strain, ∂ indicates change and l is length with l_0 indicating length at baseline) on the remaining neuroretinal tissue. Maybe not surprisingly then, this trial reported long-term thinning of retinal thickness [159]. One of the first Philadelphia patients developed a full thickness macular hole and another was reported to have lost a substantial amount of

outer nuclear layer thickness, indicating photoreceptor loss, after subretinal delivery of AAV [89, 172]. Careful review of these cases suggests that the needle penetration site should be well outside the area of foveal thinning and that the biomechanical properties of each patient's retinal architecture should be considered to minimise the mechanical strain ($\varepsilon = \partial l/l_0$) and stress ($\sigma = F/A$, where σ is stress, F is force applied and A indicates cross sectional area) that the retinal tissue is subjected to. Taking elasticity theory into account, it seems prudent i) to minimise stress (σ) by inducing the detachment at the site of greatest retinal thickness (A = cross-sectional area), ii) using minimal total volume to reduce strain (minimising change in length, ∂l) and iii) injecting slowly, thereby limiting the strain rate $\varepsilon(t) = v(t)/l_0$ of the delicate neuronal tissue [$\varepsilon(t)$ is the strain ε at each time t and v(t) is the speed at which the ends are moving away from each other].

Surprisingly, another bottleneck can be lack of robust clinical data on the natural history of disease progression, degree of symmetry, test/re-test variability and/or comparison of relevant outcome measure analyses. Most existing papers field retrospective case series type clinical studies, where the cohort might be defined based on clinical diagnosis alone. However, data from prospective trials are much more appropriate to design a sound interventional trial with suitably defined in/exclusion criteria, follow-up schedules and primary/secondary outcome measures.

A more abstract hazard in the way of gene therapeutic development is the effort needed to actually reach trial (let alone market-) approval by various regulatory bodies in relation to the financial and human resources available to the academic

investigator. The Orphan Drug Designation programs by FDA and EMA are only one part of the solution. More lobbying by patient interest groups seems necessary to streamline regulatory procedures and make investigational new drug (IND) applications more economical for academic investigators. For example, it might be possible to provide biodistribution data on e.g. AAV8 after subretinal application in non-human primates and use these data in trials with different transgene constructs as long as the capsid, vector solution and delivery methods are identical. Consolidating regulatory requirements across national borders (e.g. within EU) would make a lot of sense – especially when dealing with orphan diseases, where large trials would benefit from multiple centres participating due to the low prevalence within each country. The regulatory bodies and patient interest organisations are key stakeholders, but it will be the responsibility of the academic investigator to point out ways to improve current practice.

7.3 X-linked retinitis pigmentosa - an obvious target for retinal gene therapy

X-linked retinitis pigmentosa stands out from all the other forms of hereditary retinal dysfunction and degeneration for three reasons. One is the high prevalence that can be attributed to mutations in one single gene, RPGR (chapters 1.2.1 and 1.2.2). Even by a conservative estimate of only 10% of all RP cases being due to RPGR

mutations, more then 10,000 patients would be expected to live in the European Union alone.

Secondly, XLRP is associated with a very severe form of retinal dysfunction and rapid disease progression. This not only poses an ethical impetus, but also promises clinical trial results within a reasonable short time frame as differences between treated and untreated eyes are likely to become apparent relatively quickly. This is not only an economic argument, but should also aid the analysis of clinical outcome measures: the greater the expected difference between treated and untreated eye, the higher the statistical power to determine efficacy. Last but not least, XLRP is relatively straightforward to diagnose. The inheritance pattern gives important clues and while the clinical presentation can be variable, the vast majority of cases present with classic features of retinitis pigmentosa [59]. Sequencing RPGR for molecular diagnosis is readily available in reference centres of genomic medicine such as in Manchester. More and more countries in the EU provide molecular diagnostic techniques as standard health care service, a trend that can be expected to continue with sequencing techniques becoming more affordable over time.

More then 240 mutations in RPGR have been described to cause disease [173]. Gene therapy with AAV.coRPGR may provide all those patients with one efficient treatment option. This is in contrast to some of the gene editing strategies currently *en vogue* [174], which mostly require a mutation specific guidance nucleotide. This might potentially have to be developed for each of those 240 patient populations individually with subsequent or parallel IND applications each costing the equivalent of a state of the art confocal microscope.

The fact that XLRP is an obvious target is also underlined by the number of research groups publishing on this subject [42, 153, 175-185]. The most recent publications, however, have highlighted the difficulties to produce RPGR gene therapy without generating new mutations in the treatment vector [121, 122]. Here we present a novel approach, which bypasses this problem by using codon optimisation. The dramatically increased genetic stability and additional benefits of codon optimisation are predicted to make translation into clinical reality more likely.

7.4 Codon optimisation as key innovation towards RPGR gene therapy

Codon optimisation makes use of the redundancy of the genetic code and the codon bias (see chapter 3.1). By using synonymous codons, the change on nucleotide level maintains the sequence information for translation. This silent nucleotide substitution results in the identical amino acid chain as from the respective wild type nucleic acid sequence. Use of species-specific major codons has been shown to increase translational efficiency in heterologous and homologous expression systems [138, 139]. Based on these observations, Nathwani *et al.* used codon optimisation to enhance the factor IX transgene cassette in a clinical AAV gene therapy safety trial for haemophilia [186]. In case of haemophilia, the increased expression levels were of crucial importance as only a small fraction of successfully transduced and viable hepatocytes had to produce and secrete large amounts of the transgene to reach a

therapeutic level (e.g. ≥ 5% of normal). This is in contrast to XLRP, where only relatively minute amounts of protein within the transduced photoreceptor would likely be needed. This assumption is based on the observation that the connecting cilium is a stable cellular compartment, i.e. it does not undergo constant regeneration as the adjacent outer segment. Studies on the transcriptional level of $Rpgr^{ORF15}$ have demonstrated an increase of $Rpgr^{ORF15}$ expression in the first 14 days after birth in wild type mice, followed by low and stable levels [75]. This coincides with the known anatomical development of the mouse retina, where photoreceptors form connecting cilia and outer segments around eye opening (day 14), and continue to mature until day 28 [187]. Maybe not surprisingly then, overexpression of RPGR can also have deleterious effects in the eye and elsewhere [121, 122, 188].

Nevertheless, an increased translational efficiency of $coRPGR^{ORF15}$ could benefit RPGR gene therapy by reducing the number of virus particles necessary to reach a therapeutic level. Vandenberghe *et al.* have shown that AAV8 can lead to dose dependent toxic effects in non-human primate retina at high titres [96], suggesting that lower titres of AAV might have a better safety profile. Apart from local effects, the number of virus particles available for biodistribution and shedding could also be reduced if each AAV would be more effective in producing the therapeutic protein due to codon optimisation of its expression cassette. Our data (chapter 3) are in concordance with a higher translational efficiency of $wtRPGR^{ORF15}$ vs. $coRPGR^{ORF15}$ and several independent experimental approaches (Western, immunocytochemistry, and FACS) have indicated greater levels of $RPGR^{ORF15}$ protein originating from the codon optimised construct.

The greatest benefit of codon optimising RPGR^{ORF15}, however, lies in its increased sequence fidelity or genetic stability. For instance, Deng *et al.* noted the following in their work towards RPGR gene therapy using wild-type RPGR^{ORF15} cds: "*The ORF15 sequence contained within this AAV vector, however, has ORF15 DNA sequence variations compared to the published sequence that are likely due to its unusual composition of repetitive purine nucleotides. This mutability is a concern for AAV vector production and safety when contemplating a human trial.*" [122]. In an independent approach to develop RPGR gene therapy towards a clinical safety trial, Wu *et al.* described: "*A set of proteins with lower molecular weights indicating the truncated or alternatively spliced forms of the protein were also detected.*" [121]. Evidence on the superior sequence stability of the codon optimised RPGR^{ORF15} cds is presented in chapter 3. Side by side SDS-PAGE analysis with whole protein staining showed no difference between the wild type and codon optimised RPGR^{ORF15} banding patterns suggesting that there were no additional protein products. Additionally, LC-MS/MS analysis provided direct evidence of the protein products correct peptide sequence (**Fig. 3.12**). No mutations were found in any of the consecutive cloning steps and independent sequencing experiments performed using Sanger sequencing. The National Genetics Reference Laboratory in Manchester independently sequenced the coding sequence and also found no mutation in the coRPGR^{ORF15} construct. In contrast, the wild type RPGR^{ORF15} sequence showed similar genetic instability as described by Wu *et al.* and Deng *et al.* [121, 122].

The underlying problem of the genetic instability is most likely explained by properties of the mutational hotspot, the ORF15 region. It contains far fewer T and C nucleotides than would be predicted in the genome, for instance, the 750 base pair sequence between positions 2410 and 3160 contains no C nucleotides at all in the wildtype sequence. This leads to many repeating sequences that may recombine incorrectly during cloning and vector production. Since most codons start with G at position 1 in this region, the addition of C nucleotides to position 3 of the preceding codon during codon optimisation has been done with consideration of limiting the number of CpG dinucleotides to no more than would be predicted in the eukaryotic exon. This is because too many of these sequences may be identified and become prone to methylation of the C nucleotide. For instance, in the 750 base pair sequence between positions 2410 and 3160, a total of 45 C nucleotides have been added through the codon optimisation process, resulting in 45 CpG dinucleotides (6.00%). This compares favourably to the predicted wildtype frequency of these dinucleotides (6.25%). Furthermore, the C codon optimisation has been applied where possible to the four fold degenerate codon 'GGN', encoding glycine. This is because any subsequent methylation of the C nucleotide of the CpG dinucleotide within the transgene and subsequent deamination to thymine (T), even if it did occur, would not change the RPGR protein sequence because GGC and GGT both encode glycine.

Insertion of T nucleotides within the GA rich region of RPGR has also been limited to avoid creating anomalous polyA signals (e.g. AATAAA) and possible splice donor sites (GT). The latter is a consideration as this region contains many splice acceptor (AG) sequences with repeating G pyrimidine bases and potential A

nucleotide branch points in the 5' direction. The codon optimisation pattern was extensively modelled *in silico* to determine the optimal modification to reduce the GA repeats and also to reduce the risk of anomalous splicing and creation of premature polyA signals. The codon optimised gene is therefore more stable than the wildtype cDNA sequence, which may generate alternatively spliced variants and truncated proteins when reintroduced into the transcriptional machinery through gene therapy [121].

7.5 Preclinical evidence for safety and efficacy of RPGR gene therapy

Hong and colleagues not only generated the *Rpgr*$^{-/y}$ mouse model [76], but also provided first evidence that the reconstitution of *Rpgr* might principally be able to reverse the phenotype [72]. However, these early experiments were performed with a truncated construct and the 'treatment' involved generating transgenic chimera and cross breeding.

The first evidence for successful gene therapy in XLRP came from William Beltran and colleagues at UPenn [123]. In this elegant study, two dog models (XLPRA1 and XLPRA2, for details see chapter 1.2.4) were successfully treated by AAV based gene therapy (reviewed in Chapter 1.3.1). In a follow up study by Deng *et al.* it was revealed that the AAV constructs used carried mutated RPGR coding sequences, which translate into an altered protein product [122]. However, they

demonstrate no toxic effects when treating wild type mouse models with these constructs and argue "*(...) the hRPGR-ORF15 variant in our AAV vectors appears to be a more stable form than the endogenous hRPGR cDNA when propagated in vitro. Its safety profile presented here in combination with its proven efficacy support future gene therapy clinical trials.*"

In a different study by Deng *et al.* (also reviewed in Chapter 1.3.1) the authors provided a vast amount of data from murine Rpgr and human RPGR transgene cassettes packaged into AAV8 and AAV9 and treated *Rpgr*$^{-/y}$ mice with different dosing regimes and at different stages of the disease. They then conclude that there is an optimal dose with their vector, which shows a good safety profile and evidence of efficacy also in animals treated at advanced age: "*Our long-term dose-efficacy study should facilitate the design of human trials with human RPGR-ORF15 vector as a clinical candidate.*" However, even in this carefully planned and executed study, two out of five AAV preparations showed deletions, further highlighting the fact that the wtRPGR^{ORF15} cds is prone to mutations not only as mutational hotspot in patients, but also *in vitro* e.g. in the preparation of putatively therapeutic constructs.

7.6 Perspective towards clinical translation of RPGR gene therapy

The concept of gene replacement therapy is to provide the target cell (e.g. photoreceptor) with a normal copy of the affected gene. However, in case of RPGR

gene therapy, using wtRPGR^{ORF15} cds carries the risk of introducing abnormal copies of the affected gene due to its high frequency of spontaneous mutation. It is difficult to see, how regulatory bodies would accept a strategy, which harbours such risks during the production of the investigational medicinal product (IMP) according to good manufacturing practice (GMP) guidelines. One could argue that GMP guidelines will ensure that such mutations would be picked up during required quality control analyses. But as the IMP production is one of the highest costing factors when running a clinical phase I trial, this leaves considerable risks in terms of time and financial planning, both highly relevant for any potential sponsor. Our evidence that coRPGR^{ORF15} leads to the same results (safe transgene expression and functional efficacy) but in a much more efficient manner, may help to gather momentum to initiate the translation of RPGR gene therapy towards a clinical phase I trial.

A patent application to protect the intellectual property of this work has been filed on behalf of the University of Oxford by Isis Innovation Ltd, a subsidiary owned by the University of Oxford. This may be an advantage in attracting funding for a clinical phase I trial with the goal to develop AAV.coRPGR into a marketed product in future. The basic building blocks of such an endeavour are i) patients with XLRP3, ii) clinical centres with expertise in ocular gene therapy, and iii) the viral vector product.

We have already started to analyse retrospectively ca. 150 patients with XLRP for their genetic and clinical characteristics from the Oxford Eye Hospital and University Eye Hospital Tübingen (Bellingrath *et al.* unpublished). Together with the

existing literature, this multimodal approach will allow us to find the best outcome measures and time points for intervention. It will also highlight, which of the patients already in our care might benefit most from gene therapy and what kind of subgroup we might need to actively recruit in future to prepare for a phase I trial.

Secondly, clinical centres with expertise in retinal gene therapy have already been identified. Next to the Oxford Eye Hospital, where patients of the Choroideremia gene therapy trial (NCT01461213) undergo surgery and follow up by Robert MacLaren as Principal Investigator (PI), the University Eye Hospital Tübingen has all the facilities and expertise to conduct such a trial. In fact, two independent investigational new drug applications for retinal gene therapy trials have recently been submitted by this centre (PI: Dominik Fischer). One was approved on September 14th 2015 (EudraCT: 2014-001874-32) and will apply AAV8.CNGA3 in patients with achromatopsia (OMIM 600053). Provided the second IND application reaches approval as well, both gene therapy trials are due to start in 2015.

Lastly, virus production for a clinical trial will have to be outsourced to a contractor for GMP grade AAV preparations. Quotes have been received in order to support a respective funding application. The success of seminal work by multiple groups in the UK and US [88, 89, 142, 166] is currently met with a lot of interest due to its recognised potential as evident from phase I and II trials [189]. And while the only licensed gene therapeutic product so far (Glybera) targets a metabolic condition, FDA and/or EMA authorised gene therapeutic compounds for retinal disorders seem to become visible on the horizon.

Given the evidence presented in this work, we like to think that treatment with AAV.coRPGR is safe and has a good potential to prove efficacious in patients with XLRP3. We hope that the translation into a clinical trial can be achieved swiftly and successfully to the benefit of our patients.

Acknowledgement

First and foremost, I would like to express my gratitude to my supervisor, Professor Robert E. MacLaren. His encouragement and support has been truly exceptional ever since our first conversation at a busy ARVO poster session in 2011. It has been a remarkable time in his lab and an inspiration on both personal and professional level.

I also wish to thank my colleagues at the Nuffield Laboratory of Ophthalmology for their camaraderie and guidance, in particular Alun Barnard and Michelle McClements. But also Doron Hickey, Alona Cramer, Daniyar Dauletbekov, Mandeep Singh, Camiel Boon, Samantha De Silva, Sher Aslam, Jasleen Jolly, Shaun Wood, Maria Moreira Patricio Rodrigues, Jasmin Balmer, Tom Edwards, Matthew Simunovic, Mark Hassal and Marco Bellini.

Professor Bartz-Schmidt and Professor Marius Ueffing have been instrumental in paving my way to take an extended leave from the University Eye Hospital Tübingen in order to learn more about gene therapy. I thank them for their confidence in my work and for their assistance in the past, present and future.

Lastly and most importantly, I thank my dear wife, for her generous support, for being ready to move to a different country and start our own family. Lovingly yours.

References

1. Llinas RR (2003) The contribution of Santiago Ramon y Cajal to functional neuroscience. Nature reviews Neuroscience 4: 77-80 DOI 10.1038/nrn1011
2. Osterberg G (1935) Topography of the layer of rods and cones in the human retina. Acta Ophthalmol Suppl.: 1–103
3. Hecht S, Shlaer S, Pirenne MH (1942) Energy, Quanta, and Vision. J Gen Physiol 25: 819-840
4. Jeon CJ, Strettoi E, Masland RH (1998) The major cell populations of the mouse retina. J Neurosci 18: 8936-8946
5. Ahnelt PK, Kolb H (2000) The mammalian photoreceptor mosaic-adaptive design. Prog Retin Eye Res 19: 711-777
6. Hendrickson AE, Yuodelis C (1984) The morphological development of the human fovea. Ophthalmology 91: 603-612
7. Curcio CA, Sloan KR, Jr., Packer O, Hendrickson AE, Kalina RE (1987) Distribution of cones in human and monkey retina: individual variability and radial asymmetry. Science 236: 579-582
8. Yau KW, Lamb TD, Baylor DA (1977) Light-induced fluctuations in membrane current of single toad rod outer segments. Nature 269: 78-80
9. Biel M, Seeliger M, Pfeifer A, Kohler K, Gerstner A, Ludwig A, Jaissle G, Fauser S, Zrenner E, Hofmann F (1999) Selective loss of cone function in mice lacking the cyclic nucleotide-gated channel CNG3. Proc Natl Acad Sci U S A 96: 7553-7557

10. Kolb H (1970) Organization of the outer plexiform layer of the primate retina: electron microscopy of Golgi-impregnated cells. Philosophical transactions of the Royal Society of London Series B, Biological sciences 258: 261-283

11. Vardi N, Morigiwa K (1997) ON cone bipolar cells in rat express the metabotropic receptor mGluR6. Vis Neurosci 14: 789-794

12. Wassle H (2004) Parallel processing in the mammalian retina. Nature reviews Neuroscience 5: 747-757 DOI 10.1038/nrn1497

13. Kolb H, Linberg KA, Fisher SK (1992) Neurons of the human retina: a Golgi study. J Comp Neurol 318: 147-187 DOI 10.1002/cne.903180204

14. Prusky GT, Douglas RM (2004) Characterization of mouse cortical spatial vision. Vision Res 44: 3411-3418 DOI 10.1016/j.visres.2004.09.001

15. Campbell FW, Green DG (1965) Optical and retinal factors affecting visual resolution. J Physiol 181: 576-593

16. Gotch F (1903) The time relations of the photo-electric changes in the eyeball of the frog. J Physiol 29: 388-410

17. Frishman LJ (2006) Origins of the Electroretinogram. In: Heckenlively JR, Arden GB (eds) Principles and practice of clinical electrophysiology of vision. The MIT Press, Cambridge, Massachusetts, pp. 139-184.

18. Donders FC (1857) Betrage zur pathollogischen Anatomie des Auges: Pigmentbildung in der Netzhaut. Graefes Arch Clin Exp Ophthalmol 3: 139-150

19. Wright AF, Chakarova CF, Abd El-Aziz MM, Bhattacharya SS (2010) Photoreceptor degeneration: genetic and mechanistic dissection of a complex trait. Nat Rev Genet 11: 273-284 DOI 10.1038/nrg2717

20. Haim M (2002) Epidemiology of retinitis pigmentosa in Denmark. Acta ophthalmologica Scandinavica Supplement: 1-34

21. Daiger SP, Bowne SJ, Sullivan LS, Blanton SH, Weinstock GM, Koboldt DC, Fulton RS, Larsen D, Humphries P, Humphries MM, Pierce EA, Chen R, Li Y (2014) Application of next-generation sequencing to identify genes and mutations causing autosomal dominant retinitis pigmentosa (adRP). Adv Exp Med Biol 801: 123-129 DOI 10.1007/978-1-4614-3209-8_16

22. Birch DG (2006) Retinitis Pigmentosa. In: Heckenlively JR, Arden GB (eds) Principles and Practice of Clinical Electrophysiology of Vision. The MIT Press, Cambridge, pp. 781-794.

23. Heckenlively JR (2006) Cone Dystrophies and Degenerations. In: Heckenlively JR, Arden GB (eds) Principles and Practice of Clinical Electrophysiology of Vision. The MIT Press, Cambridge, pp. 795-802.

24. Hamel CP (2007) Cone rod dystrophies. Orphanet journal of rare diseases 2: 7 DOI 10.1186/1750-1172-2-7

25. Young RW (1967) The renewal of photoreceptor cell outer segments. J Cell Biol 33: 61-72

26. Parks JM, Ames A, 3rd, Nesbett FB (1976) Protein synthesis in central nervous tissue: studies on retina in vitro. Journal of neurochemistry 27: 987-997

27. Jaissle GB, May CA, van de Pavert SA, Wenzel A, Claes-May E, Giessl A, Szurman P, Wolfrum U, Wijnholds J, Fischer MD, Humphries P, Seeliger MW (2009) Bone spicule pigment formation in retinitis pigmentosa: insights from a mouse model. Graefes Arch Clin Exp Ophthalmol 248: 1063-1070 DOI 10.1007/s00417-009-1253-9

28. Cronin T, Leveillard T, Sahel JA (2007) Retinal degenerations: from cell signaling to cell therapy; pre-clinical and clinical issues. Curr Gene Ther 7: 121-129

29. Bovolenta P, Cisneros E (2009) Retinitis pigmentosa: cone photoreceptors starving to death. Nat Neurosci 12: 5-6 DOI 10.1038/nn0109-5

30. Ripps H (2002) Cell death in retinitis pigmentosa: gap junctions and the 'bystander' effect. Exp Eye Res 74: 327-336 DOI 10.1006/exer.2002.1155

31. Ross MT, Grafham DV, Coffey AJ, Scherer S, McLay K, Muzny D, Platzer M, Howell GR, Burrows C, Bird CP, Frankish A, Lovell FL, Howe KL, Ashurst JL, Fulton RS, Sudbrak R, Wen G, Jones MC, Hurles ME, Andrews TD, Scott CE, Searle S, Ramser J, Whittaker A, Deadman R, Carter NP, Hunt SE, Chen R, Cree A, Gunaratne P, Havlak P, Hodgson A, Metzker ML, Richards S, Scott G, Steffen D, Sodergren E, Wheeler DA, Worley KC, Ainscough R, Ambrose KD, Ansari-Lari MA, Aradhya S, Ashwell RI, Babbage AK, Bagguley CL, Ballabio A, Banerjee R, Barker GE, Barlow KF, Barrett IP, Bates KN, Beare DM, Beasley H, Beasley O, Beck A, Bethel G, Blechschmidt K, Brady N, Bray-Allen S, Bridgeman AM, Brown AJ, Brown MJ, Bonnin D, Bruford EA, Buhay C, Burch P, Burford D, Burgess J, Burrill W, Burton J, Bye JM, Carder C, Carrel L, Chako J, Chapman JC, Chavez D, Chen E, Chen G, Chen Y, Chen Z, Chinault C, Ciccodicola A, Clark SY, Clarke G, Clee CM, Clegg S, Clerc-Blankenburg K, Clifford K, Cobley V, Cole CG, Conquer JS, Corby N, Connor RE, David R, Davies J, Davis C, Davis J, Delgado O, Deshazo D, Dhami P, Ding Y, Dinh H, Dodsworth S, Draper H, Dugan-Rocha S, Dunham A, Dunn M, Durbin KJ, Dutta I, Eades T, Ellwood M, Emery-Cohen A, Errington H, Evans KL, Faulkner L, Francis F, Frankland J, Fraser AE, Galgoczy P, Gilbert J, Gill R, Glockner G, Gregory SG, Gribble S, Griffiths C, Grocock R, Gu Y, Gwilliam R, Hamilton C, Hart EA, Hawes A, Heath PD, Heitmann K, Hennig S, Hernandez J, Hinzmann B, Ho S, Hoffs M, Howden PJ, Huckle EJ, Hume J, Hunt PJ, Hunt AR,

Isherwood J, Jacob L, Johnson D, Jones S, de Jong PJ, Joseph SS, Keenan S, Kelly S, Kershaw JK, Khan Z, Kioschis P, Klages S, Knights AJ, Kosiura A, Kovar-Smith C, Laird GK, Langford C, Lawlor S, Leversha M, Lewis L, Liu W, Lloyd C, Lloyd DM, Loulseged H, Loveland JE, Lovell JD, Lozado R, Lu J, Lyne R, Ma J, Maheshwari M, Matthews LH, McDowall J, McLaren S, McMurray A, Meidl P, Meitinger T, Milne S, Miner G, Mistry SL, Morgan M, Morris S, Muller I, Mullikin JC, Nguyen N, Nordsiek G, Nyakatura G, O'Dell CN, Okwuonu G, Palmer S, Pandian R, Parker D, Parrish J, Pasternak S, Patel D, Pearce AV, Pearson DM, Pelan SE, Perez L, Porter KM, Ramsey Y, Reichwald K, Rhodes S, Ridler KA, Schlessinger D, Schueler MG, Sehra HK, Shaw-Smith C, Shen H, Sheridan EM, Shownkeen R, Skuce CD, Smith ML, Sotheran EC, Steingruber HE, Steward CA, Storey R, Swann RM, Swarbreck D, Tabor PE, Taudien S, Taylor T, Teague B, Thomas K, Thorpe A, Timms K, Tracey A, Trevanion S, Tromans AC, d'Urso M, Verduzco D, Villasana D, Waldron L, Wall M, Wang Q, Warren J, Warry GL, Wei X, West A, Whitehead SL, Whiteley MN, Wilkinson JE, Willey DL, Williams G, Williams L, Williamson A, Williamson H, Wilming L, Woodmansey RL, Wray PW, Yen J, Zhang J, Zhou J, Zoghbi H, Zorilla S, Buck D, Reinhardt R, Poustka A, Rosenthal A, Lehrach H, Meindl A, Minx PJ, Hillier LW, Willard HF, Wilson RK, Waterston RH, Rice CM, Vaudin M, Coulson A, Nelson DL, Weinstock G, Sulston JE, Durbin R, Hubbard T, Gibbs RA, Beck S, Rogers J, Bentley DR (2005) The DNA sequence of the human X chromosome. Nature 434: 325-337 DOI 10.1038/nature03440

32. Wu H, Luo J, Yu H, Rattner A, Mo A, Wang Y, Smallwood PM, Erlanger B, Wheelan SJ, Nathans J (2014) Cellular resolution maps of X chromosome

inactivation: implications for neural development, function, and disease. Neuron 81: 103-119 DOI 10.1016/j.neuron.2013.10.051

33. Helena Mangs A, Morris BJ (2007) The Human Pseudoautosomal Region (PAR): Origin, Function and Future. Current genomics 8: 129-136

34. Alberts B, Johnson AK, Lewis J, Raff M, Roberts K, Walter P (2008) DNA Replication, Repair, and RecombinationMolecular biology of the cell. Garland Science, Abingdon, UK.

35. Bhattacharya SS, Wright AF, Clayton JF, Price WH, Phillips CI, McKeown CM, Jay M, Bird AC, Pearson PL, Southern EM, et al. (1984) Close genetic linkage between X-linked retinitis pigmentosa and a restriction fragment length polymorphism identified by recombinant DNA probe L1.28. Nature 309: 253-255

36. Schwahn U, Lenzner S, Dong J, Feil S, Hinzmann B, van Duijnhoven G, Kirschner R, Hemberger M, Bergen AA, Rosenberg T, Pinckers AJ, Fundele R, Rosenthal A, Cremers FP, Ropers HH, Berger W (1998) Positional cloning of the gene for X-linked retinitis pigmentosa 2. Nat Genet 19: 327-332 DOI 10.1038/1214

37. Ott J, Bhattacharya S, Chen JD, Denton MJ, Donald J, Dubay C, Farrar GJ, Fishman GA, Frey D, Gal A, et al. (1990) Localizing multiple X chromosome-linked retinitis pigmentosa loci using multilocus homogeneity tests. Proc Natl Acad Sci U S A 87: 701-704

38. Gieser L, Fujita R, Goring HH, Ott J, Hoffman DR, Cideciyan AV, Birch DG, Jacobson SG, Swaroop A (1998) A novel locus (RP24) for X-linked retinitis pigmentosa maps to Xq26-27. Am J Hum Genet 63: 1439-1447 DOI 10.1086/302121

39. Melamud A, Shen GQ, Chung D, Xi Q, Simpson E, Li L, Peachey NS, Zegarra H, Hagstrom SA, Wang QK, Traboulsi EI (2006) Mapping a new genetic locus for X linked retinitis pigmentosa to Xq28. J Med Genet 43: e27 DOI 10.1136/jmg.2005.031518

40. Iannaccone A, Breuer DK, Wang XF, Kuo SF, Normando EM, Filippova E, Baldi A, Hiriyanna S, MacDonald CB, Baldi F, Cosgrove D, Morton CC, Swaroop A, Jablonski MM (2003) Clinical and immunohistochemical evidence for an X linked retinitis pigmentosa syndrome with recurrent infections and hearing loss in association with an RPGR mutation.J Med Genet, pp. e118.

41. Churchill JD, Bowne SJ, Sullivan LS, Lewis RA, Wheaton DK, Birch DG, Branham KE, Heckenlively JR, Daiger SP (2013) Mutations in the X-Linked Retinitis Pigmentosa Genes RPGR and RP2 Found in 8.5% of Families with a Provisional Diagnosis of Autosomal Dominant Retinitis Pigmentosa.Invest Ophthalmol Vis Sci, pp. 1411-1416.

42. Hosch J, Lorenz B, Stieger K (2011) RPGR: role in the photoreceptor cilium, human retinal disease, and gene therapy. Ophthalmic Genet 32: 1-11 DOI 10.3109/13816810.2010.535889

43. Zahid S, Khan N, Branham K, Othman M, Karoukis AJ, Sharma N, Moncrief A, Mahmood MN, Sieving PA, Swaroop A, Heckenlively JR, Jayasundera T (2013) Phenotypic Conservation in Patients With X-Linked Retinitis Pigmentosa Caused by RPGR Mutations. JAMA ophthalmology 131: 1016-1025 DOI 10.1001/jamaophthalmol.2013.120

44. Mears AJ, Hiriyanna S, Vervoort R, Yashar B, Gieser L, Fahrner S, Daiger SP, Heckenlively JR, Sieving PA, Wright AF, Swaroop A (2000) Remapping of the RP15 locus for X-linked cone-rod degeneration to Xp11.4-p21.1, and

identification of a de novo insertion in the RPGR exon ORF15. Am J Hum Genet 67: 1000-1003 DOI 10.1086/303091

45. Meindl A, Dry K, Herrmann K, Manson F, Ciccodicola A, Edgar A, Carvalho MR, Achatz H, Hellebrand H, Lennon A, Migliaccio C, Porter K, Zrenner E, Bird A, Jay M, Lorenz B, Wittwer B, D'Urso M, Meitinger T, Wright A (1996) A gene (RPGR) with homology to the RCC1 guanine nucleotide exchange factor is mutated in X-linked retinitis pigmentosa (RP3). Nature genetics 13: 35-42 DOI 10.1038/ng0596-35

46. Wright AF, Shu X (2007) Focus on Molecules: RPGR. Experimental eye research 85: 1-2 DOI 10.1016/j.exer.2006.03.006

47. Shu X, Black GC, Rice JM, Hart-Holden N, Jones A, O'Grady A, Ramsden S, Wright AF (2007) RPGR mutation analysis and disease: an update. Human mutation 28: 322-328 DOI 10.1002/humu.20461

48. Vervoort R, Lennon A, Bird AC, Tulloch B, Axton R, Miano MG, Meindl A, Meitinger T, Ciccodicola A, Wright AF (2000) Mutational hot spot within a new RPGR exon in X-linked retinitis pigmentosa. Nature genetics 25: 462-466 DOI 10.1038/78182

49. Megaw RD, Soares DC, Wright AF (2015) RPGR: Its role in photoreceptor physiology, human disease, and future therapies. Exp Eye Res DOI 10.1016/j.exer.2015.06.007

50. Wright AF, Shu X (2007) Focus on Molecules: RPGR. Exp Eye Res 85: 1-2 DOI 10.1016/j.exer.2006.03.006

51. Sharon D, Sandberg MA, Rabe VW, Stillberger M, Dryja TP, Berson EL (2003) RP2 and RPGR mutations and clinical correlations in patients with X-linked retinitis pigmentosa. Am J Hum Genet 73: 1131-1146 DOI 10.1086/379379

52. Fahim AT, Bowne SJ, Sullivan LS, Webb KD, Williams JT, Wheaton DK, Birch DG, Daiger SP (2011) Allelic heterogeneity and genetic modifier loci contribute to clinical variation in males with X-linked retinitis pigmentosa due to RPGR mutations. PLoS One 6: e23021 DOI 10.1371/journal.pone.0023021

53. Beltran WA, Hammond P, Acland GM, Aguirre GD (2006) A frameshift mutation in RPGR exon ORF15 causes photoreceptor degeneration and inner retina remodeling in a model of X-linked retinitis pigmentosa. Invest Ophthalmol Vis Sci 47: 1669-1681 DOI 10.1167/iovs.05-0845

54. Hong DH, Pawlyk BS, Adamian M, Li T (2004) Dominant, gain-of-function mutant produced by truncation of RPGR. Investigative ophthalmology & visual science 45: 36-41

55. Bird AC (1975) X-linked retinitis pigmentosa. Br J Ophthalmol 59: 177-199

56. Ayyagari R, Demirci FY, Liu J, Bingham EL, Stringham H, Kakuk LE, Boehnke M, Gorin MB, Richards JE, Sieving PA (2002) X-linked recessive atrophic macular degeneration from RPGR mutation. Genomics 80: 166-171

57. Birch DG, Locke KG, Felius J, Klein M, Wheaton DK, Hoffman DR, Hood DC (2015) Rates of decline in regions of the visual field defined by frequency-domain optical coherence tomography in patients with RPGR-mediated X-linked retinitis pigmentosa. Ophthalmology 122: 833-839 DOI 10.1016/j.ophtha.2014.11.005

58. Ayton LN, Apollo NV, Varsamidis M, Dimitrov PN, Guymer RH, Luu CD (2014) Assessing residual visual function in severe vision loss. Invest Ophthalmol Vis Sci 55: 1332-1338 DOI 10.1167/iovs.13-12657

59. Zahid S, Khan N, Branham K, Othman M, Karoukis AJ, Sharma N, Moncrief A, Mahmood MN, Sieving PA, Swaroop A, Heckenlively JR, Jayasundera T

(2013) Phenotypic Conservation in Patients With X-Linked Retinitis Pigmentosa Caused by RPGR Mutations.JAMA ophthalmology, pp. 1-10.

60. Fumoto S, Hosoi K, Ohnishi H, Hoshina H, Yan K, Saji H, Oka A (2014) Chimerism of buccal membrane cells in a monochorionic dizygotic twin. Pediatrics 133: e1097-1100 DOI 10.1542/peds.2013-1938

61. Walia S, Fishman GA, Swaroop A, Branham KE, Lindeman M, Othman M, Weleber RG (2008) Discordant phenotypes in fraternal twins having an identical mutation in exon ORF15 of the RPGR gene. Arch Ophthalmol 126: 379-384 DOI 10.1001/archophthalmol.2007.72

62. Watzlich D, Vetter I, Gotthardt K, Miertzschke M, Chen YX, Wittinghofer A, Ismail S (2013) The interplay between RPGR, PDEdelta and Arl2/3 regulate the ciliary targeting of farnesylated cargo. EMBO reports 14: 465-472 DOI 10.1038/embor.2013.37

63. Hattula K, Furuhjelm J, Arffman A, Peranen J (2002) A Rab8-specific GDP/GTP exchange factor is involved in actin remodeling and polarized membrane transport. Molecular biology of the cell 13: 3268-3280 DOI 10.1091/mbc.E02-03-0143

64. Moritz OL, Tam BM, Hurd LL, Peranen J, Deretic D, Papermaster DS (2001) Mutant rab8 Impairs docking and fusion of rhodopsin-bearing post-Golgi membranes and causes cell death of transgenic Xenopus rods. Molecular biology of the cell 12: 2341-2351

65. Murga-Zamalloa C, Swaroop A, Khanna H (2010) Multiprotein complexes of Retinitis Pigmentosa GTPase regulator (RPGR), a ciliary protein mutated in X-linked Retinitis Pigmentosa (XLRP). Adv Exp Med Biol 664: 105-114 DOI 10.1007/978-1-4419-1399-9_13

66. Hameed A, Abid A, Aziz A, Ismail M, Mehdi SQ, Khaliq S (2003) Evidence of RPGRIP1 gene mutations associated with recessive cone-rod dystrophy. J Med Genet 40: 616-619

67. Dryja TP, Adams SM, Grimsby JL, McGee TL, Hong DH, Li T, Andreasson S, Berson EL (2001) Null RPGRIP1 alleles in patients with Leber congenital amaurosis. Am J Hum Genet 68: 1295-1298 DOI 10.1086/320113

68. Remans K, Burger M, Vetter IR, Wittinghofer A (2014) C2 domains as protein-protein interaction modules in the ciliary transition zone. Cell reports 8: 1-9 DOI 10.1016/j.celrep.2014.05.049

69. Gerner M, Haribaskar R, Putz M, Czerwitzki J, Walz G, Schafer T (2010) The retinitis pigmentosa GTPase regulator interacting protein 1 (RPGRIP1) links RPGR to the nephronophthisis protein network. Kidney international 77: 891-896 DOI 10.1038/ki.2010.27

70. Zhao Y, Hong DH, Pawlyk B, Yue G, Adamian M, Grynberg M, Godzik A, Li T (2003) The retinitis pigmentosa GTPase regulator (RPGR)- interacting protein: subserving RPGR function and participating in disk morphogenesis. Proc Natl Acad Sci U S A 100: 3965-3970 DOI 10.1073/pnas.0637349100

71. Linari M, Ueffing M, Manson F, Wright A, Meitinger T, Becker J (1999) The retinitis pigmentosa GTPase regulator, RPGR, interacts with the delta subunit of rod cyclic GMP phosphodiesterase.Proc Natl Acad Sci USA, pp. 1315-1320.

72. Hong DH, Pawlyk BS, Adamian M, Sandberg MA, Li T (2005) A single, abbreviated RPGR-ORF15 variant reconstitutes RPGR function in vivo. Investigative ophthalmology & visual science 46: 435-441 DOI 10.1167/iovs.04-1065

73. Patil H, Tserentsoodol N, Saha A, Hao Y, Webb M, Ferreira PA (2012) Selective loss of RPGRIP1-dependent ciliary targeting of NPHP4, RPGR and SDCCAG8 underlies the degeneration of photoreceptor neurons.Cell death & disease, pp. e355.

74. Shu X, Fry AM, Tulloch B, Manson FD, Crabb JW, Khanna H, Faragher AJ, Lennon A, He S, Trojan P, Giessl A, Wolfrum U, Vervoort R, Swaroop A, Wright AF (2005) RPGR ORF15 isoform co-localizes with RPGRIP1 at centrioles and basal bodies and interacts with nucleophosmin. Human molecular genetics 14: 1183-1197 DOI 10.1093/hmg/ddi129

75. Wright RN, Hong DH, Perkins B (2012) RpgrORF15 connects to the usher protein network through direct interactions with multiple whirlin isoforms. Invest Ophthalmol Vis Sci 53: 1519-1529 DOI 10.1167/iovs.11-8845

76. Hong DH, Pawlyk BS, Shang J, Sandberg MA, Berson EL, Li T (2000) A retinitis pigmentosa GTPase regulator (RPGR)-deficient mouse model for X-linked retinitis pigmentosa (RP3). P Natl Acad Sci USA 97: 3649-3654 DOI 10.1073/pnas.060037497

77. Thompson DA, Khan NW, Othman MI, Chang B, Jia L, Grahek G, Wu Z, Hiriyanna S, Nellissery J, Li T, Khanna H, Colosi P, Swaroop A, Heckenlively JR (2012) Rd9 is a naturally occurring mouse model of a common form of retinitis pigmentosa caused by mutations in RPGR-ORF15. PLoS One 7: e35865 DOI 10.1371/journal.pone.0035865

78. Mowat FM, Petersen-Jones SM, Williamson H, Williams DL, Luthert PJ, Ali RR, Bainbridge JW (2008) Topographical characterization of cone photoreceptors and the area centralis of the canine retina. Mol Vis 14: 2518-2527

79. Zhang Q, Acland GM, Wu WX, Johnson JL, Pearce-Kelling S, Tulloch B, Vervoort R, Wright AF, Aguirre GD (2002) Different RPGR exon ORF15 mutations in Canids provide insights into photoreceptor cell degeneration. Hum Mol Genet 11: 993-1003

80. Zeiss CJ, Acland GM, Aguirre GD (1999) Retinal pathology of canine X-linked progressive retinal atrophy, the locus homologue of RP3.Invest Ophthalmol Vis Sci, pp. 3292-3304.

81. Beltran WA (2006) A Frameshift Mutation in RPGR Exon ORF15 Causes Photoreceptor Degeneration and Inner Retina Remodeling in a Model of X-Linked Retinitis PigmentosaInvest Ophthalmol Vis Sci, pp. 1669-1681.

82. Wright AF, Jacobson SG, Cideciyan AV, Roman AJ, Shu X, Vlachantoni D, McInnes RR, Riemersma RA (2004) Lifespan and mitochondrial control of neurodegeneration. Nat Genet 36: 1153-1158 DOI 10.1038/ng1448

83. Avery OT, Macleod CM, McCarty M (1944) Studies on the Chemical Nature of the Substance Inducing Transformation of Pneumococcal Types : Induction of Transformation by a Desoxyribonucleic Acid Fraction Isolated from Pneumococcus Type Iii. J Exp Med 79: 137-158

84. Sambrook J, Westphal H, Srinivasan PR, Dulbecco R (1968) The integrated state of viral DNA in SV40-transformed cells. Proc Natl Acad Sci U S A 60: 1288-1295

85. Rogers S, Pfuderer P (1968) Use of viruses as carriers of added genetic information. Nature 219: 749-751

86. Bennett J (2014) My career path for developing gene therapy for blinding diseases: the importance of mentors, collaborators, and opportunities. Hum Gene Ther 25: 663-670 DOI 10.1089/hum.2014.2529

87. Ali RR, Reichel MB, Thrasher AJ, Levinsky RJ, Kinnon C, Kanuga N, Hunt DM, Bhattacharya SS (1996) Gene transfer into the mouse retina mediated by an adeno-associated viral vector. Hum Mol Genet 5: 591-594

88. Bainbridge JW, Smith AJ, Barker SS, Robbie S, Henderson R, Balaggan K, Viswanathan A, Holder GE, Stockman A, Tyler N, Petersen-Jones S, Bhattacharya SS, Thrasher AJ, Fitzke FW, Carter BJ, Rubin GS, Moore AT, Ali RR (2008) Effect of gene therapy on visual function in Leber's congenital amaurosis. N Engl J Med 358: 2231-2239 DOI 10.1056/NEJMoa0802268

89. Maguire AM, Simonelli F, Pierce EA, Pugh EN, Jr., Mingozzi F, Bennicelli J, Banfi S, Marshall KA, Testa F, Surace EM, Rossi S, Lyubarsky A, Arruda VR, Konkle B, Stone E, Sun J, Jacobs J, Dell'Osso L, Hertle R, Ma JX, Redmond TM, Zhu X, Hauck B, Zelenaia O, Shindler KS, Maguire MG, Wright JF, Volpe NJ, McDonnell JW, Auricchio A, High KA, Bennett J (2008) Safety and efficacy of gene transfer for Leber's congenital amaurosis. N Engl J Med 358: 2240-2248

90. Hauswirth WW, Aleman TS, Kaushal S, Cideciyan AV, Schwartz SB, Wang L, Conlon TJ, Boye SL, Flotte TR, Byrne BJ, Jacobson SG (2008) Treatment of leber congenital amaurosis due to RPE65 mutations by ocular subretinal injection of adeno-associated virus gene vector: short-term results of a phase I trial. Hum Gene Ther 19: 979-990 DOI 10.1089/hum.2008.107

91. Samulski RJ, Berns KI, Tan M, Muzyczka N (1982) Cloning of adeno-associated virus into pBR322: rescue of intact virus from the recombinant plasmid in human cells.Proc Natl Acad Sci USA, pp. 2077-2081.

92. Willett K, Bennett J (2013) Immunology of AAV-Mediated Gene Transfer in the Eye. Frontiers in immunology 4: 261 DOI 10.3389/fimmu.2013.00261

93. Igarashi T, Miyake K, Asakawa N, Miyake N, Shimada T, Takahashi H (2013) Direct Comparison of Administration Routes for AAV8-mediated Ocular Gene Therapy. Curr Eye Res 38: 569-577 DOI 10.3109/02713683.2013.779720

94. Marangoni D, Wu Z, Wiley HE, Zeiss CJ, Vijayasarathy C, Zeng Y, Hiriyanna S, Bush RA, Wei LL, Colosi P, Sieving PA (2014) Preclinical Safety Evaluation of a Recombinant AAV8 Vector for X-linked Retinoschisis after Intravitreal Administration in Rabbits. Human gene therapy Clinical development DOI 10.1089/humc.2014.067

95. Pang J-J, Dai X, Boye SE, Barone I, Boye SL, Mao S, Everhart D, Dinculescu A, Liu L, Umino Y, Lei B, Chang B, Barlow R, Strettoi E, Hauswirth WW (2011) Long-term retinal function and structure rescue using capsid mutant AAV8 vector in the rd10 mouse, a model of recessive retinitis pigmentosa.Molecular Therapy, pp. 234-242.

96. Vandenberghe LH, Bell P, Maguire AM, Cearley CN, Xiao R, Calcedo R, Wang L, Castle MJ, Maguire AC, Grant R, Wolfe JH, Wilson JM, Bennett J (2011) Dosage thresholds for AAV2 and AAV8 photoreceptor gene therapy in monkey. Science translational medicine 3: 88ra54 DOI 10.1126/scitranslmed.3002103

97. Buning H, Bolyard CM, Hallek M, Bartlett JS (2011) Modification and labeling of AAV vector particles. Methods Mol Biol 807: 273-300 DOI 10.1007/978-1-61779-370-7_12

98. Lux K, Goerlitz N, Schlemminger S, Perabo L, Goldnau D, Endell J, Leike K, Kofler DM, Finke S, Hallek M, Buning H (2005) Green fluorescent protein-tagged adeno-associated virus particles allow the study of cytosolic and

nuclear trafficking. Journal of virology 79: 11776-11787 DOI 10.1128/JVI.79.18.11776-11787.2005

99. Perabo L, Goldnau D, White K, Endell J, Boucas J, Humme S, Work LM, Janicki H, Hallek M, Baker AH, Buning H (2006) Heparan sulfate proteoglycan binding properties of adeno-associated virus retargeting mutants and consequences for their in vivo tropism. Journal of virology 80: 7265-7269 DOI 10.1128/JVI.00076-06

100. Daya S, Berns KI (2008) Gene therapy using adeno-associated virus vectors. Clinical microbiology reviews 21: 583-593 DOI 10.1128/CMR.00008-08

101. Bartlett JS, Wilcher R, Samulski RJ (2000) Infectious entry pathway of adeno-associated virus and adeno-associated virus vectors. Journal of virology 74: 2777-2785

102. Atchison RW, Casto BC, Hammon WM (1965) Adenovirus-Associated Defective Virus Particles. Science 149: 754-756

103. Henry CJ (1973) Adenovirus-associated (satellite) viruses. Progress in experimental tumor research 18: 273-293

104. Hermonat PL (1994) Adeno-associated virus inhibits human papillomavirus type 16: a viral interaction implicated in cervical cancer. Cancer research 54: 2278-2281

105. Su PF, Wu FY (1996) Differential suppression of the tumorigenicity of HeLa and SiHa cells by adeno-associated virus. British journal of cancer 73: 1533-1537

106. Hermonat PL, Plott RT, Santin AD, Parham GP, Flick JT (1997) Adeno-associated virus Rep78 inhibits oncogenic transformation of primary human keratinocytes by a human papillomavirus type 16-ras chimeric. Gynecologic oncology 66: 487-494 DOI 10.1006/gyno.1997.4789

107. Schlehofer JR, Ehrbar M, zur Hausen H (1986) Vaccinia virus, herpes simplex virus, and carcinogens induce DNA amplification in a human cell line and support replication of a helpervirus dependent parvovirus. Virology 152: 110-117

108. Salo RJ, Mayor HD (1979) Adenovirus-associated virus polypeptides synthesized in cells coinfected with either adenovirus or herpesvirus. Virology 93: 237-245

109. Buller RM, Janik JE, Sebring ED, Rose JA (1981) Herpes simplex virus types 1 and 2 completely help adenovirus-associated virus replication. Journal of virology 40: 241-247

110. Kotin RM, Siniscalco M, Samulski RJ, Zhu XD, Hunter L, Laughlin CA, McLaughlin S, Muzyczka N, Rocchi M, Berns KI (1990) Site-specific integration by adeno-associated virus. Proc Natl Acad Sci U S A 87: 2211-2215

111. Samulski RJ, Zhu X, Xiao X, Brook JD, Housman DE, Epstein N, Hunter LA (1991) Targeted integration of adeno-associated virus (AAV) into human chromosome 19. The EMBO journal 10: 3941-3950

112. Kotin RM, Menninger JC, Ward DC, Berns KI (1991) Mapping and direct visualization of a region-specific viral DNA integration site on chromosome 19q13-qter. Genomics 10: 831-834

113. Tenenbaum L, Lehtonen E, Monahan PE (2003) Evaluation of risks related to the use of adeno-associated virus-based vectors.Curr Gene Ther, pp. 545-565.

114. Penaud-Budloo M, Le Guiner C, Nowrouzi A, Toromanoff A, Cherel Y, Chenuaud P, Schmidt M, von Kalle C, Rolling F, Moullier P, Snyder RO (2008) Adeno-associated virus vector genomes persist as episomal chromatin

in primate muscle. Journal of virology 82: 7875-7885 DOI 10.1128/JVI.00649-08

115. Schnepp BC, Jensen RL, Chen CL, Johnson PR, Clark KR (2005) Characterization of adeno-associated virus genomes isolated from human tissues. Journal of virology 79: 14793-14803 DOI 10.1128/JVI.79.23.14793-14803.2005

116. Goncalves MA (2005) Adeno-associated virus: from defective virus to effective vector. Virology journal 2: 43 DOI 10.1186/1743-422X-2-43

117. Samulski RJ, Chang LS, Shenk T (1989) Helper-free stocks of recombinant adeno-associated viruses: normal integration does not require viral gene expression. Journal of virology 63: 3822-3828

118. Bell P, Wang L, Lebherz C, Flieder DB, Bove MS, Wu D, Gao GP, Wilson JM, Wivel NA (2005) No evidence for tumorigenesis of AAV vectors in a large-scale study in mice. Mol Ther 12: 299-306 DOI 10.1016/j.ymthe.2005.03.020

119. Li H, Malani N, Hamilton SR, Schlachterman A, Bussadori G, Edmonson SE, Shah R, Arruda VR, Mingozzi F, Wright JF, Bushman FD, High KA (2011) Assessing the potential for AAV vector genotoxicity in a murine model. Blood 117: 3311-3319 DOI 10.1182/blood-2010-08-302729

120. Balaggan KS, Duran Y, Georgiadis A, Thaung C, Barker SE, Buch PK, MacNeil A, Robbie S, Bainbridge JW, Smith AJ, Ali RR (2012) Absence of ocular malignant transformation after sub-retinal delivery of rAAV2/2 or integrating lentiviral vectors in p53-deficient mice. Gene Ther 19: 182-188 DOI 10.1038/gt.2011.194

121. Wu Z, Hiriyanna S, Qian H, Mookherjee S, Campos MM, Gao C, Fariss R, Sieving PA, Li T, Colosi P, Swaroop A (2015) A long-term efficacy study of

gene replacement therapy for RPGR-associated retinal degeneration. Hum Mol Genet 24: 3956-3970 DOI 10.1093/hmg/ddv134

122. Deng WT, Dyka FM, Dinculescu A, Li J, Zhu P, Chiodo V, Boye SL, Conlon TJ, Erger KE, Cossette T, Hauswirth WW (2015) Stability and Safety of an AAV Vector for Treating RPGR-ORF15 X-linked Retinitis Pigmentosa. Hum Gene Ther DOI 10.1089/hum.2015.035

123. Beltran WA, Cideciyan AV, Lewin AS, Iwabe S, Khanna H, Sumaroka A, Chiodo VA, Fajardo DS, Román AJ, Deng W-T, Swider M, Alemán TS, Boye SL, Genini S, Swaroop A, Hauswirth WW, Jacobson SG, Aguirre GD (2012) Gene therapy rescues photoreceptor blindness in dogs and paves the way for treating human X-linked retinitis pigmentosa.Proc Natl Acad Sci USA, pp. 2132-2137.

124. Graham FL, Smiley J, Russell WC, Nairn R (1977) Characteristics of a human cell line transformed by DNA from human adenovirus type 5. The Journal of general virology 36: 59-74

125. Lin YC, Boone M, Meuris L, Lemmens I, Van Roy N, Soete A, Reumers J, Moisse M, Plaisance S, Drmanac R, Chen J, Speleman F, Lambrechts D, Van de Peer Y, Tavernier J, Callewaert N (2014) Genome dynamics of the human embryonic kidney 293 lineage in response to cell biology manipulations. Nature communications 5: 4767 DOI 10.1038/ncomms5767

126. Patel AK, Tikoo SK (2006) 293T cells expressing simian virus 40 T antigen are semi-permissive to bovine adenovirus type 3 infection. The Journal of general virology 87: 817-821 DOI 10.1099/vir.0.81305-0

127. Gama-Norton L, Botezatu L, Herrmann S, Schweizer M, Alves PM, Hauser H, Wirth D (2011) Lentivirus production is influenced by SV40 large T-antigen

and chromosomal integration of the vector in HEK293 cells. Hum Gene Ther 22: 1269-1279 DOI 10.1089/hum.2010.143

128. Biedler JL, Roffler-Tarlov S, Schachner M, Freedman LS (1978) Multiple neurotransmitter synthesis by human neuroblastoma cell lines and clones. Cancer research 38: 3751-3757

129. Biedler JL, Helson L, Spengler BA (1973) Morphology and growth, tumorigenicity, and cytogenetics of human neuroblastoma cells in continuous culture. Cancer research 33: 2643-2652

130. You Q, Brown LA, McClements M, Hankins MW, Maclaren RE (2012) Tetradecanoylphorbol-13-acetate (TPA) significantly increases AAV2/5 transduction of human neuronal cells in vitro. Exp Eye Res 97: 148-153 DOI 10.1016/j.exer.2011.12.009

131. Tan E, Ding XQ, Saadi A, Agarwal N, Naash MI, Al-Ubaidi MR (2004) Expression of cone-photoreceptor-specific antigens in a cell line derived from retinal tumors in transgenic mice. Invest Ophthalmol Vis Sci 45: 764-768

132. Birnboim HC, Doly J (1979) A rapid alkaline extraction procedure for screening recombinant plasmid DNA. Nucleic acids research 7: 1513-1523

133. Li E, Bestor TH, Jaenisch R (1992) Targeted mutation of the DNA methyltransferase gene results in embryonic lethality.Cell, pp. 915-926.

134. Sagdullaev BT, DeMarco PJ, McCall MA (2004) Improved contact lens electrode for corneal ERG recordings in mice. Doc Ophthalmol 108: 181-184

135. Charbel Issa P, Singh MS, Lipinski DM, Chong NV, Delori FC, Barnard AR, MacLaren RE (2012) Optimization of in vivo confocal autofluorescence imaging of the ocular fundus in mice and its application to models of human retinal degeneration. Invest Ophthalmol Vis Sci 53: 1066-1075 DOI 10.1167/iovs.11-8767

136. Fiers W, Grosjean H (1979) On codon usage. Nature 277: 328

137. Sharp PM, Li W-H (1987) The codon adaptation index-a measure of directional synonymous codon usage bias, and its potential applications.

138. Daniell H, Ruiz G, Denes B, Sandberg L, Langridge W (2009) Optimization of codon composition and regulatory elements for expression of human insulin like growth factor-1 in transgenic chloroplasts and evaluation of structural identity and function. BMC biotechnology 9: 33 DOI 10.1186/1472-6750-9-33

139. Inouye S, Sahara-Miura Y, Sato J, Suzuki T (2015) Codon optimization of genes for efficient protein expression in mammalian cells by selection of only preferred human codons. Protein expression and purification 109: 47-54 DOI 10.1016/j.pep.2015.02.002

140. Charbel Issa P, De Silva SR, Lipinski DM, Singh MS, Mouravlev A, You Q, Barnard AR, Hankins MW, During MJ, Maclaren RE (2013) Assessment of tropism and effectiveness of new primate-derived hybrid recombinant AAV serotypes in the mouse and primate retina. PLoS One 8: e60361 DOI 10.1371/journal.pone.0060361

141. Benjamini Y, Hochberg Y (1995) Controlling the false discovery rate: A practical and powerful approach to multiple testing. Journal of the Royal Statistical Society 57: 289-300

142. Jacobson SG, Cideciyan AV, Ratnakaram R, Heon E, Schwartz SB, Roman AJ, Peden MC, Aleman TS, Boye SL, Sumaroka A, Conlon TJ, Calcedo R, Pang JJ, Erger KE, Olivares MB, Mullins CL, Swider M, Kaushal S, Feuer WJ, Iannaccone A, Fishman GA, Stone EM, Byrne BJ, Hauswirth WW (2012) Gene therapy for leber congenital amaurosis caused by RPE65 mutations: safety and efficacy in 15 children and adults followed up to 3 years. Arch Ophthalmol 130: 9-24 DOI 10.1001/archophthalmol.2011.298

143. Pang JJ, Dai X, Boye SE, Barone I, Boye SL, Mao S, Everhart D, Dinculescu A, Liu L, Umino Y, Lei B, Chang B, Barlow R, Strettoi E, Hauswirth WW (2011) Long-term retinal function and structure rescue using capsid mutant AAV8 vector in the rd10 mouse, a model of recessive retinitis pigmentosa. Mol Ther 19: 234-242 DOI 10.1038/mt.2010.273

144. Nathwani AC, Tuddenham EG, Rangarajan S, Rosales C, McIntosh J, Linch DC, Chowdary P, Riddell A, Pie AJ, Harrington C, O'Beirne J, Smith K, Pasi J, Glader B, Rustagi P, Ng CY, Kay MA, Zhou J, Spence Y, Morton CL, Allay J, Coleman J, Sleep S, Cunningham JM, Srivastava D, Basner-Tschakarjan E, Mingozzi F, High KA, Gray JT, Reiss UM, Nienhuis AW, Davidoff AM (2011) Adenovirus-associated virus vector-mediated gene transfer in hemophilia B. N Engl J Med 365: 2357-2365 DOI 10.1056/NEJMoa1108046

145. Allocca M, Mussolino C, Garcia-Hoyos M, Sanges D, Iodice C, Petrillo M, Vandenberghe LH, Wilson JM, Marigo V, Surace EM, Auricchio A (2007) Novel adeno-associated virus serotypes efficiently transduce murine photoreceptors. Journal of virology 81: 11372-11380 DOI 10.1128/JVI.01327-07

146. Aguirre GD, Yashar BM, John SK, Smith JE, Breuer DK, Hiriyanna S, Swaroop A, Milam AH (2002) Retinal histopathology of an XLRP carrier with a mutation in the RPGR exon ORF15. Exp Eye Res 75: 431-443

147. Khani SC, Pawlyk BS, Bulgakov OV, Kasperek E, Young JE, Adamian M, Sun X, Smith AJ, Ali RR, Li T (2007) AAV-mediated expression targeting of rod and cone photoreceptors with a human rhodopsin kinase promoter. Invest Ophthalmol Vis Sci 48: 3954-3961 DOI 10.1167/iovs.07-0257

148. Davies WL, Carvalho LS, Hunt DM (2007) SPLICE: a technique for generating in vitro spliced coding sequences from genomic DNA. BioTechniques 43: 785-789

149. Shu X (2005) RPGR ORF15 isoform co-localizes with RPGRIP1 at centrioles and basal bodies and interacts with nucleophosminHuman Molecular Genetics, pp. 1183-1197.

150. Gao K, Li M, Zhong L, Su Q, Li J, Li S, He R, Zhang Y, Hendricks G, Wang J, Gao G (2014) Empty Virions In AAV8 Vector Preparations Reduce Transduction Efficiency And May Cause Total Viral Particle Dose-Limiting Side-Effects. Molecular therapy Methods & clinical development 1: 20139 DOI 10.1038/mtm.2013.9

151. Luhmann UFO, Robbie S, Munro PMG, Barker SE, Duran Y, Luong V, Fitzke FW, Bainbridge JWB, Ali RR, MacLaren RE (2009) The drusenlike phenotype in aging Ccl2-knockout mice is caused by an accelerated accumulation of swollen autofluorescent subretinal macrophages.Invest Ophthalmol Vis Sci, pp. 5934-5943.

152. Hong DH (2005) A Single, Abbreviated RPGR-ORF15 Variant Reconstitutes RPGR Function In VivoInvest Ophthalmol Vis Sci, pp. 435-441.

153. Beltran WA, Cideciyan AV, Lewin AS, Iwabe S, Khanna H, Sumaroka A, Chiodo VA, Fajardo DS, Roman AJ, Deng WT, Swider M, Aleman TS, Boye SL, Genini S, Swaroop A, Hauswirth WW, Jacobson SG, Aguirre GD (2012) Gene therapy rescues photoreceptor blindness in dogs and paves the way for treating human X-linked retinitis pigmentosa. Proc Natl Acad Sci U S A 109: 2132-2137 DOI 10.1073/pnas.1118847109

154. Tanimoto N, Muehlfriedel RL, Fischer MD, Fahl E, Humphries P, Biel M, Seeliger MW (2009) Vision tests in the mouse: Functional phenotyping with electroretinography. Front Biosci 14: 2730-2737 DOI 3409 [pii]

155. Thompson DA, Khan NW, Othman MI, Chang B, Jia L, Grahek G, Wu Z, Hiriyanna S, Nellissery J, Li T, Khanna H, Colosi P, Swaroop A, Heckenlively JR (2012) Rd9 Is a Naturally Occurring Mouse Model of a Common Form of Retinitis Pigmentosa Caused by Mutations in RPGR-ORF15PLoS ONE, pp. e35865.

156. Faktorovich EG, Steinberg RH, Yasumura D, Matthes MT, LaVail MM (1992) Basic fibroblast growth factor and local injury protect photoreceptors from light damage in the rat. The Journal of neuroscience : the official journal of the Society for Neuroscience 12: 3554-3567

157. Cideciyan AV, Aleman TS, Boye SL, Schwartz SB, Kaushal S, Roman AJ, Pang JJ, Sumaroka A, Windsor EA, Wilson JM, Flotte TR, Fishman GA, Heon E, Stone EM, Byrne BJ, Jacobson SG, Hauswirth WW (2008) Human gene therapy for RPE65 isomerase deficiency activates the retinoid cycle of vision but with slow rod kinetics. Proc Natl Acad Sci U S A 105: 15112-15117 DOI 0807027105 [pii]

158. Jacobson SG, Cideciyan AV, Roman AJ, Sumaroka A, Schwartz SB, Heon E, Hauswirth WW (2015) Improvement and decline in vision with gene therapy in childhood blindness. N Engl J Med 372: 1920-1926 DOI 10.1056/NEJMoa1412965

159. Bainbridge JW, Mehat MS, Sundaram V, Robbie SJ, Barker SE, Ripamonti C, Georgiadis A, Mowat FM, Beattie SG, Gardner PJ, Feathers KL, Luong VA, Yzer S, Balaggan K, Viswanathan A, de Ravel TJ, Casteels I, Holder GE, Tyler N, Fitzke FW, Weleber RG, Nardini M, Moore AT, Thompson DA,

Petersen-Jones SM, Michaelides M, van den Born LI, Stockman A, Smith AJ, Rubin G, Ali RR (2015) Long-term effect of gene therapy on Leber's congenital amaurosis. N Engl J Med 372: 1887-1897 DOI 10.1056/NEJMoa1414221

160. Bennett J, Ashtari M, Wellman J, Marshall KA, Cyckowski LL, Chung DC, McCague S, Pierce EA, Chen Y, Bennicelli JL, Zhu X, Ying G-S, Sun J, Wright JF, Auricchio A, Simonelli F, Shindler KS, Mingozzi F, High KA, Maguire AM (2012) AAV2 gene therapy readministration in three adults with congenital blindness.Science translational medicine, pp. 120ra115.

161. Acland GM, Aguirre GD, Ray J, Zhang Q, Aleman TS, Cideciyan AV, Pearce-Kelling SE, Anand V, Zeng Y, Maguire AM, Jacobson SG, Hauswirth WW, Bennett J (2001) Gene therapy restores vision in a canine model of childhood blindness. Nat Genet 28: 92-95 DOI 10.1038/88327

162. Cideciyan AV, Jacobson SG, Beltran WA, Sumaroka A, Swider M, Iwabe S, Roman AJ, Olivares MB, Schwartz SB, Komaromy AM, Hauswirth WW, Aguirre GD (2013) Human retinal gene therapy for Leber congenital amaurosis shows advancing retinal degeneration despite enduring visual improvement. Proc Natl Acad Sci U S A DOI 10.1073/pnas.1218933110

163. Mowat FM, Breuwer AR, Bartoe JT, Annear MJ, Zhang Z, Smith AJ, Bainbridge JW, Petersen-Jones SM, Ali RR (2013) RPE65 gene therapy slows cone loss in Rpe65-deficient dogs. Gene Ther 20: 545-555 DOI 10.1038/gt.2012.63

164. Maguire AM, High KA, Auricchio A, Wright JF, Pierce EA, Testa F, Mingozzi F, Bennicelli JL, Ying GS, Rossi S, Fulton A, Marshall KA, Banfi S, Chung DC, Morgan JI, Hauck B, Zelenaia O, Zhu X, Raffini L, Coppieters F, De Baere E, Shindler KS, Volpe NJ, Surace EM, Acerra C, Lyubarsky A,

Redmond TM, Stone E, Sun J, McDonnell JW, Leroy BP, Simonelli F, Bennett J (2009) Age-dependent effects of RPE65 gene therapy for Leber's congenital amaurosis: a phase 1 dose-escalation trial. Lancet 374: 1597-1605 DOI 10.1016/S0140-6736(09)61836-5

165. Ashtari M, Cyckowski LL, Monroe JF, Marshall KA, Chung DC, Auricchio A, Simonelli F, Leroy BP, Maguire AM, Shindler KS, Bennett J (2011) The human visual cortex responds to gene therapy-mediated recovery of retinal function.J Clin Invest, pp. 2160-2168.

166. MacLaren RE, Groppe M, Barnard AR, Cottriall CL, Tolmachova T, Seymour L, Clark KR, During MJ, Cremers FP, Black GC, Lotery AJ, Downes SM, Webster AR, Seabra MC (2014) Retinal gene therapy in patients with choroideremia: initial findings from a phase 1/2 clinical trial. Lancet 383: 1129-1137 DOI 10.1016/S0140-6736(13)62117-0

167. Roberts MF, Fishman GA, Roberts DK, Heckenlively JR, Weleber RG, Anderson RJ, Grover S (2002) Retrospective, longitudinal, and cross sectional study of visual acuity impairment in choroideraemia. Br J Ophthalmol 86: 658-662

168. Bennett J (2003) Immune response following intraocular delivery of recombinant viral vectors. Gene Ther 10: 977-982 DOI 10.1038/sj.gt.3302030

169. Treumer F, Roider J, Hillenkamp J (2012) Long-term outcome of subretinal coapplication of rtPA and bevacizumab followed by repeated intravitreal anti-VEGF injections for neovascular AMD with submacular haemorrhage. Br J Ophthalmol 96: 708-713 DOI 10.1136/bjophthalmol-2011-300655

170. Vander JF (1992) Tissue plasminogen activator irrigation to facilitate removal of subretinal hemorrhage during vitrectomy. Ophthalmic surgery 23: 361-363

171. Bennicelli J, Wright JF, Komaromy A, Jacobs JB, Hauck B, Zelenaia O, Mingozzi F, Hui D, Chung D, Rex TS, Wei Z, Qu G, Zhou S, Zeiss C, Arruda VR, Acland GM, Dell'Osso LF, High KA, Maguire AM, Bennett J (2008) Reversal of blindness in animal models of leber congenital amaurosis using optimized AAV2-mediated gene transfer. Mol Ther 16: 458-465 DOI 10.1038/sj.mt.6300389

172. Jacobson SG, Cideciyan AV, Ratnakaram R, Heon E, Schwartz SB, Román AJ, Peden MC, Alemán TS, Boye SL, Sumaroka A, Conlon TJ, Calcedo R, Pang J-J, Erger KE, Olivares MB, Mullins CL, Swider M, Kaushal S, Feuer WJ, Iannaccone A, Fishman GA, Stone EM, Byrne BJ, Hauswirth WW (2012) Gene therapy for leber congenital amaurosis caused by RPE65 mutations: safety and efficacy in 15 children and adults followed up to 3 years.Arch Ophthalmol, pp. 9-24.

173. Shu X, Black GC, Rice JM, Hart-Holden N, Jones A, O'Grady A, Ramsden S, Wright AF (2007) RPGRmutation analysis and disease: an updateHum Mutat, pp. 322-328.

174. Sander JD, Joung JK (2014) CRISPR-Cas systems for editing, regulating and targeting genomes. Nat Biotechnol 32: 347-355 DOI 10.1038/nbt.2842

175. Megaw RD, Soares DC, Wright AF (2015) RPGR: Its role in photoreceptor physiology, human disease, and future therapies. Exp Eye Res 138: 32-41 DOI 10.1016/j.exer.2015.06.007

176. Beltran WA, Cideciyan AV, Lewin AS, Hauswirth WW, Jacobson SG, Aguirre GD (2015) Gene augmentation for X-linked retinitis pigmentosa caused by mutations in RPGR. Cold Spring Harbor perspectives in medicine 5: a017392 DOI 10.1101/cshperspect.a017392

177. Raghupathy RK, McCulloch DL, Akhtar S, Al-mubrad TM, Shu X (2013) Zebrafish model for the genetic basis of X-linked retinitis pigmentosa. Zebrafish 10: 62-69 DOI 10.1089/zeb.2012.0761

178. Huang WC, Wright AF, Roman AJ, Cideciyan AV, Manson FD, Gewaily DY, Schwartz SB, Sadigh S, Limberis MP, Bell P, Wilson JM, Swaroop A, Jacobson SG (2012) RPGR-associated retinal degeneration in human X-linked RP and a murine model. Invest Ophthalmol Vis Sci 53: 5594-5608 DOI 10.1167/iovs.12-10070

179. Glaus E, Schmid F, Da Costa R, Berger W, Neidhardt J (2011) Gene therapeutic approach using mutation-adapted U1 snRNA to correct a RPGR splice defect in patient-derived cells. Mol Ther 19: 936-941 DOI 10.1038/mt.2011.7

180. Pawlyk BS, Bulgakov OV, Liu X, Xu X, Adamian M, Sun X, Khani SC, Berson EL, Sandberg MA, Li T (2010) Replacement gene therapy with a human RPGRIP1 sequence slows photoreceptor degeneration in a murine model of Leber congenital amaurosis. Hum Gene Ther 21: 993-1004 DOI 10.1089/hum.2009.218

181. Veltel S, Wittinghofer A (2009) RPGR and RP2: targets for the treatment of X-linked retinitis pigmentosa? Expert opinion on therapeutic targets 13: 1239-1251 DOI 10.1517/14728220903225016

182. Pawlyk BS, Smith AJ, Buch PK, Adamian M, Hong DH, Sandberg MA, Ali RR, Li T (2005) Gene replacement therapy rescues photoreceptor degeneration in a murine model of Leber congenital amaurosis lacking RPGRIP. Invest Ophthalmol Vis Sci 46: 3039-3045 DOI 10.1167/iovs.05-0371

183. Hong DH, Pawlyk BS, Adamian M, Sandberg MA, Li T (2005) A single, abbreviated RPGR-ORF15 variant reconstitutes RPGR function in vivo. Invest Ophthalmol Vis Sci 46: 435-441 DOI 10.1167/iovs.04-1065

184. Wang DY, Chan WM, Tam PO, Baum L, Lam DS, Chong KK, Fan BJ, Pang CP (2005) Gene mutations in retinitis pigmentosa and their clinical implications. Clinica chimica acta; international journal of clinical chemistry 351: 5-16 DOI 10.1016/j.cccn.2004.08.004

185. Breuer DK, Yashar BM, Filippova E, Hiriyanna S, Lyons RH, Mears AJ, Asaye B, Acar C, Vervoort R, Wright AF, Musarella MA, Wheeler P, MacDonald I, Iannaccone A, Birch D, Hoffman DR, Fishman GA, Heckenlively JR, Jacobson SG, Sieving PA, Swaroop A (2002) A comprehensive mutation analysis of RP2 and RPGR in a North American cohort of families with X-linked retinitis pigmentosa. Am J Hum Genet 70: 1545-1554 DOI 10.1086/340848

186. Nathwani AC, Tuddenham EGD, Rangarajan S, Rosales C, McIntosh J, Linch DC, Chowdary P, Riddell A, Pie AJ, Harrington C, O'Beirne J, Smith K, Pasi J, Glader B, Rustagi P, Ng CYC, Kay MA, Zhou J, Spence Y, Morton CL, Allay J, Coleman J, Sleep S, Cunningham JM, Srivastava D, Basner-Tschakarjan E, Mingozzi F, High KA, Gray JT, Reiss UM, Nienhuis AW, Davidoff AM (2011) Adenovirus-associated virus vector-mediated gene transfer in hemophilia B.N Engl J Med, pp. 2357-2365.

187. Lamb TD, Collin SP, Pugh EN, Jr. (2007) Evolution of the vertebrate eye: opsins, photoreceptors, retina and eye cup. Nature reviews Neuroscience 8: 960-976 DOI 10.1038/nrn2283

188. Brunner S, Colman D, Travis AJ, Luhmann UF, Shi W, Feil S, Imsand C, Nelson J, Grimm C, Rulicke T, Fundele R, Neidhardt J, Berger W (2008)

Overexpression of RPGR leads to male infertility in mice due to defects in flagellar assembly. Biology of reproduction 79: 608-617 DOI 10.1095/biolreprod.107.067454

189. Cheever TR, Berkley D, Braun S, Brown RH, Byrne BJ, Chamberlain JS, Cwik V, Duan D, Federoff HJ, High KA, Kaspar BK, Klinger KW, Larkindale J, Lincecum J, Mavilio F, McDonald CL, McLaughlin J, Weiss McLeod B, Mendell JR, Nuckolls G, Stedman HH, Tagle DA, Vandenberghe LH, Wang H, Wernett PJ, Wilson JM, Porter JD, Gubitz AK (2015) Perspectives on best practices for gene therapy programs. Hum Gene Ther 26: 127-133 DOI 10.1089/hum.2014.147